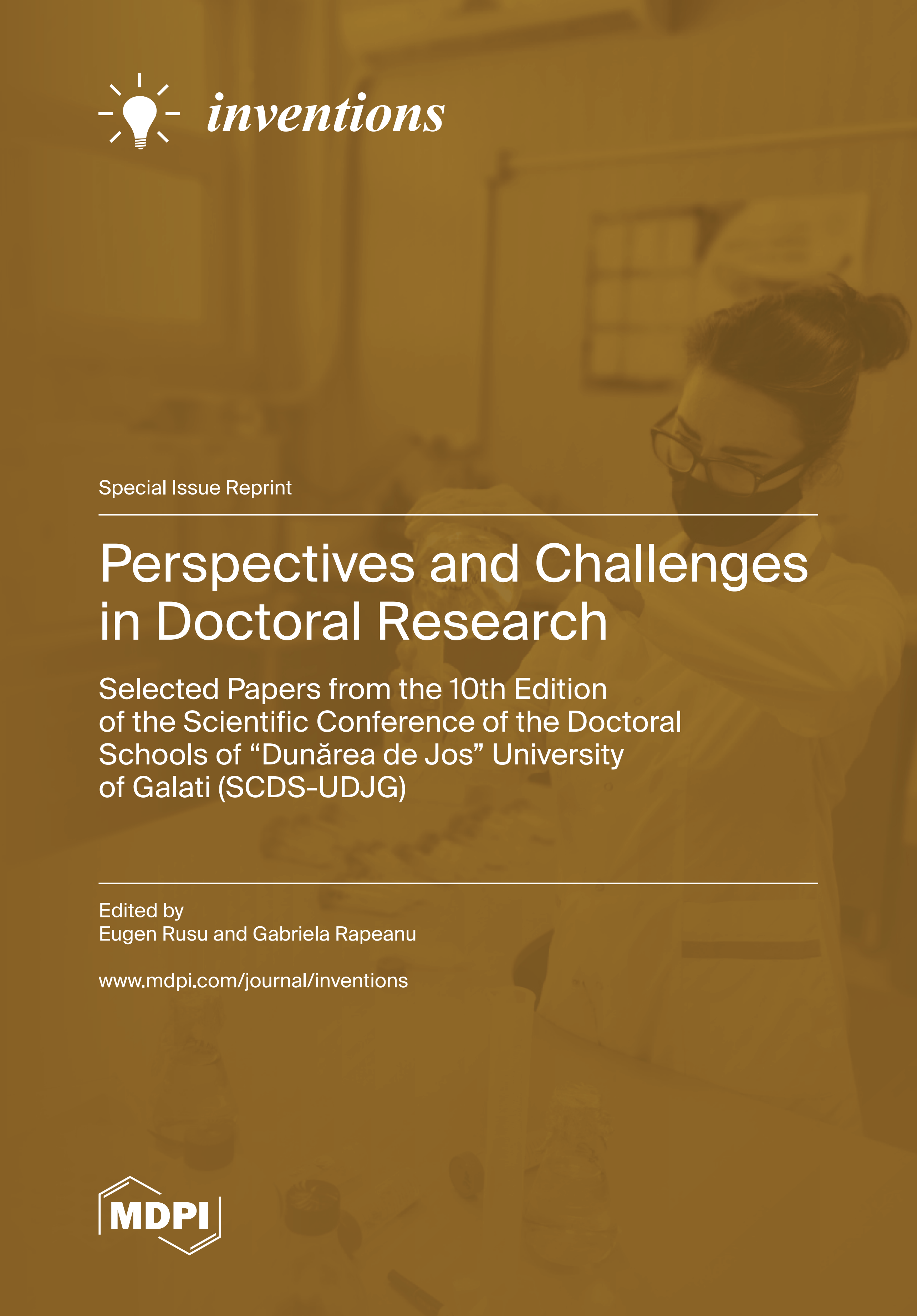

inventions

Special Issue Reprint

Perspectives and Challenges in Doctoral Research

Selected Papers from the 10th Edition of the Scientific Conference of the Doctoral Schools of “Dunărea de Jos” University of Galati (SCDS-UDJG)

Edited by
Eugen Rusu and Gabriela Rapeanu

www.mdpi.com/journal/inventions

MDPI

Perspectives and Challenges in Doctoral Research—Selected Papers from the 10th Edition of the Scientific Conference of the Doctoral Schools of “Dunărea de Jos” University of Galati (SCDS-UDJG)

Perspectives and Challenges in Doctoral Research—Selected Papers from the 10th Edition of the Scientific Conference of the Doctoral Schools of "Dunărea de Jos" University of Galati (SCDS-UDJG)

Editors

Eugen Rusu
Gabriela Rapeanu

MDPI • Basel • Beijing • Wuhan • Barcelona • Belgrade • Manchester • Tokyo • Cluj • Tianjin

Editors

Eugen Rusu	Gabriela Rapeanu
“Dunarea de Jos” University of Galati	“Dunarea de Jos” University of Galati
Galați	Galați
Romania	Romania

Editorial Office
MDPI
St. Alban-Anlage 66
4052 Basel, Switzerland

This is a reprint of articles from the Special Issue published online in the open access journal *Inventions* (ISSN 2411-5134) (available at: https://www.mdpi.com/journal/inventions/special_issues/10th_Doctoral_Research).

For citation purposes, cite each article independently as indicated on the article page online and as indicated below:

LastName, A.A.; LastName, B.B.; LastName, C.C. Article Title. *Journal Name* **Year**, *Volume Number*, Page Range.

ISBN 978-3-0365-7892-7 (Hbk)
ISBN 978-3-0365-7893-4 (PDF)

Cover image courtesy of Gabriela Rapeanu

© 2023 by the authors. Articles in this book are Open Access and distributed under the Creative Commons Attribution (CC BY) license, which allows users to download, copy and build upon published articles, as long as the author and publisher are properly credited, which ensures maximum dissemination and a wider impact of our publications.
The book as a whole is distributed by MDPI under the terms and conditions of the Creative Commons license CC BY-NC-ND.

Contents

About the Editors

Eugen Rusu

Eugen Rusu received a diploma in Naval Architecture (1982) and a Ph.D. in Mechanical Engineering (1997). Between 1999 and 2004, he worked as a post-doc fellow at the at Hydrographical Institute of the Portuguese Navy, where he was responsible for wave modelling and provided environmental support for some major situations, such as the accident of the M/V Prestige (2002) and the NATO exercises Unified Odyssey (2002) and 'Swordfish' (2003). Eugen Rusu worked as a consulting Scientist at the NATO Centre for Maritime Research and Experimentation, La Spezia, Italy (2005), having modelling coastal waves and surf zone processes.

Starting in 2006, in parallel with his activity as a professor at the University Dunarea de Jos of Galati, he has been working as a professor collaborator at CENTEC (Centre for Marine Technology and Ocean Engineering), University of Lisbon, Portugal. Since 2012, he has also acted as an expert for the European Commission. Eugen Rusu has published more than 150 works in the fields of renewable energy and marine engineering and has received awards including Doctor Honoris Causa (2015) from the Maritime University of Constanta, Romania; Outstanding Contribution in Reviewing from *Renewable Energy* (2015) and *Ocean Engineering* (2016) journals; and Top 1% World Reviewers in the field of engineering (2018 and 2019). He is also the President of the Council of the Doctoral Schools of Galati University and of the Romanian National Commission of Mechanical Engineering. Since 2018, he has been a corresponding member of the Romanian Academy, the highest-level scientific and cultural forum in Romania.

Gabriela Rapeanu

Gabriela Rapeanu is a Professor at the Faculty of Food Science and Engineering, Dunarea de jos University of Galati. She received a diploma in Food Technology (1997) and a Ph.D. in 2005. Her PhD topic was to investigate the thermal and/or high-pressure inactivation of PPO from white grapes. The research was partially funded by an EU Project (FP5 - EU-Marie Curie Training Site: *Enzyme kinetics during thermal and non-thermal food processing* QLK1-CT-2000-60014) during the period 2003–2004 at the Laboratory of Food Technology, Katholieke Universiteit Leuven, Belgium. During the last 26 years, she has published a number of works in journals with high impact factors, as well as books and chapters in books published in prestigious international publishing houses. She has been involved in collaborative projects merging food science, functional foods, food safety, food quality and biotechnology.

She is also member of the National Research Council (CNCS) (Chair of the Life Sciences and Biotechnology Committee (2011–2013 and 2020–present) and the Director of the Doctoral School of Fundamental Sciences and Engineering, Dunarea de Jos University of Galati, Galați, Romania.

Preface to “Perspectives and Challenges in Doctoral Research—Selected Papers from the 10th Edition of the Scientific Conference of the Doctoral Schools of “Dunărea de Jos” University of Galati (SCDS-UDJG)"

This Special Issue of the journal *Inventions* includes papers from different research fields reflecting the sectional talks presented at the 10th edition of the Scientific Conference of the Doctoral Schools of “Dunărea de Jos” University of Galaţi, which took place in June 2022. The objective of the 2022 Conference was to bring together perspectives and challenges in doctoral research in a common forum and to provide a platform enabling doctoral researchers to meet and share state-of-the-art developments in their fields.

The Special Issue includes 13 papers presented at the conference from several fields, including mechanical and industrial engineering, food science and biotechnology, electrical/electronic engineering, systems engineering and information technologies, chemistry, and economic models and strategies.

Eugen Rusu and Gabriela Rapeanu
Editors

inventions

Editorial

Editorial Note for the Special Issue: Perspectives and Challenges in Doctoral Research—Selected Papers from the 10th Edition of the Scientific Conference of the Doctoral Schools from the "Dunărea de Jos"

Eugen Rusu [1] and Gabriela Rapeanu [2,*]

[1] Department of Mechanical Engineering, Dunărea de Jos University of Galati, 47 Domnească Street, 800201 Galati, Romania; eugen.rusu@ugal.ro
[2] Faculty of Food Science and Engineering, Dunărea de Jos University of Galati, 111 Domnească Street, 800201 Galati, Romania
* Correspondence: gabriela.rapeanu@ugal.ro

Citation: Rusu, E.; Rapeanu, G. Editorial Note for the Special Issue: Perspectives and Challenges in Doctoral Research—Selected Papers from the 10th Edition of the Scientific Conference of the Doctoral Schools from the "Dunărea de Jos". *Inventions* **2023**, *8*, 73. https://doi.org/10.3390/inventions8030073

Received: 6 April 2023
Accepted: 11 May 2023
Published: 17 May 2023

Copyright: © 2023 by the authors. Licensee MDPI, Basel, Switzerland. This article is an open access article distributed under the terms and conditions of the Creative Commons Attribution (CC BY) license (https://creativecommons.org/licenses/by/4.0/).

This editorial note is dedicated to the 10th Scientific Conference which was held on June 2022 in Galati, Romania, and was organized by the Council of Doctoral Schools of the "Dunărea de Jos" University of Galati (SCDS-UDJG). The papers in this Special Issue, which reflect the sectional talks exhibited at the SCDS-UDJG, originate from a relatively variety of research fields. The goal of this conference and Special Issue was to present the most recent innovations in doctoral research while bringing together new perspectives and challenges.

This Special Issue contains a total of 13 scientific works that were presented at the SCDS-UDJG conference and includes topics including artificial intelligence technologies, mechanical and industrial engineering, mechatronics, materials system engineering, food science and bio-resources engineering.

Four articles present studies related to artificial intelligence technologies, representing the majority of papers published in this Special Issue. In article [1], the authors attempted to identify the most effective multivariate model for screening for main drugs of abuse, including opioids, cannabinoids, and hallucinogenic amphetamines (2C-x, DOx, and NBOMe) based on their ATR-FTIR spectra. Several machine learning methods, including Support Vector Machines (SVMs), eXtreme Gradient Boosting (XGB), Gradient Boosting, Random Forest, and K-Nearest Neighbors (KNN), were used to assess the drug class membership.

In article [2], the authors presented alternative training methods that were evaluated for an Artificial Neural Network (ANN) intended to identify JWH synthetic cannabinoids. The authors employed the Python programming language along with the Neural Designer data science and machine learning platform to improve the model's performance in terms of output sensitivity.

In the study reported in article [3], a technique based on deep learning and machine learning was used to help doctors to more accurately categorize breast cancers as benign or malignant utilizing BUS photographs. The authors suggested a technique that incorporates Hu's moments as handcrafted and significant aspects in the analysis of breast tumors. This technique may be applied to aid in the clinical diagnosis of breast cancers after detection by offering a good combination of segmentation and Hu's moments.

Last but not least, A CNN (convolutional neural network) version along with full photographs from four digital databases were considered in article [4] to describe a method for fingerprint categorization. The suggested model has three stages: a preprocessing stage that handles edge enhancement operations, data resizing and data augmentation, and a post-processing stage that concentrates on classification tasks.

Three articles in this Special Issue present findings in the field of mechanical and industrial engineering. Thus, articles [5,6] take wind energy as their main objects of research. The objective of article [5] was to provide a parallel assessment of the wind resources from the Black Sea's onshore and offshore regions, taking into account some significant local sites such as the harbors.

Article [6] uses weather information from the Maritime Hydrographic Directorate collected over a 13-year period (2009–2021) to present a general survey of the wind energy potential of the Black Sea coast of Romania. Furthermore, in article [7], information and design options appropriate to the entire shipping industry are presented along with an overview of the development of the modern low-speed marine two-stroke diesel engine from the perspective of the technical water-cooling plant, taking into consideration and starting from the market requirements for power and speed.

In the domain of mechatronics, two articles, [8,9], were also published. The flexible assembly, disassembly, and repair of a mechatronic line (A/D/RML) supported by an autonomous robotic system (ARS), two robotic manipulators (RM), and a visual servoing system (VSS) are the subject of the article [8], which describes modeling and control techniques used in this field of study.

The A/D/RML comprises a flexible cell (FC) with a 6-DOF ABB industrial robotic manipulator (IRM) and an ARS for manipulation and transport, along with six workstations (WS) on a mechatronics line (ML) attached to the flexible cell (WS). The work in question also covers the question of how to synchronize data between different types of industry-standard field equipment and control systems. With the aim of obtaining precise positioning in a processing technology applied to a laboratory mechatronics line (ML), the essential contribution of article [9] is the modeling and control of a complex autonomous system (CAS) outfitted with a robotic manipulator (RM) and a mobile vision sensor (MVS).

The next two research articles cover topics related to materials system engineering. Thus, article [10] describes an event-based PID controller equipped in a conveyor transportation system. PID control is one of the most widely researched methods of control used for controlling the event trigger transportation system. Article [11] also studies the corrosion rate indicated in the material loss per unit of time and the surface characteristics of the carbon steel type S235JR blasted with different types of materials (quartz, alumina, and red garnet with a particle size between 60 and 80 mesh (0.25–0.60 mm)). The corrosion rate was estimated using electrochemical techniques such as the open circuit potential, corrosion rate, polarization resistance, and gravimetric process.

Finally, the other two articles included in this Special Issue focus on various bioactive compounds from plant matrices used to enhance the extraction process and acquisition of by-products and value-added extracts for the design of functional food products. The extraction optimization of biologically active compounds, especially anthocyanin compounds and polyphenol compounds, and the antioxidant activity from red grape (*Băbească Neagră*) peels is discussed in article [12], while article [13] investigates the optimization of the parameters impacting on the concentration of anthocyanins in red onion skins and their antioxidant activity. These two studies are based on the idea that natural food additives should take the place of synthetic ones in the food system while also controlling the food industry's economic value chain by exploiting various valuable byproducts.

At this final point, it has to be highlighted that the works discussed above reflect the most recent advancements in the fields of artificial intelligence technologies, mechanical and industrial engineering (wave and wind energy), mechatronics, materials system engineering, food science, and bio-resources engineering. In the opinion of this Special Issue's Guest Editors, these papers represent a starting point for further studies and open new research directions.

Acknowledgments: This scientific event was supported by a grant from the Romanian Ministry of National Education.

Conflicts of Interest: The authors declare no conflict of interest.

References

1. Darie, I.-F.; Anton, S.R.; Praisler, M. Machine Learning Systems Detecting Illicit Drugs Based on Their ATR-FTIR Spectra. *Inventions* **2023**, *8*, 56. [CrossRef]
2. Burlacu, C.M.; Burlacu, A.C.; Praisler, M. Sensitivity Analysis of Artificial Neural Networks Identifying JWH Synthetic Cannabinoids Built with Alternative Training Strategies and Methods. *Inventions* **2022**, *7*, 82. [CrossRef]
3. Anghelache Nastase, I.-N.; Moldovanu, S.; Moraru, L. Image Moment-Based Features for Mass Detection in Breast US Images via Machine Learning and Neural Network Classification Models. *Inventions* **2022**, *7*, 42. [CrossRef]
4. Dincă Lăzărescu, A.-M.; Moldovanu, S.; Moraru, L. A Fingerprint Matching Algorithm Using the Combination of Edge Features and Convolution Neural Networks. *Inventions* **2022**, *7*, 39. [CrossRef]
5. Yildirir, V.; Rusu, E.; Onea, F. Wind Variation near the Black Sea Coastal Areas Reflected by the ERA5 Dataset. *Inventions* **2022**, *7*, 57. [CrossRef]
6. Nedelcu, L.-I.; Tanase, V.-M.; Rusu, R. An Evaluation of the Wind Energy along the Romanian Black Sea Coast. *Inventions* **2023**, *8*, 48. [CrossRef]
7. Faitar, C.; Rusu, E. Study on the Design Stage from a Dimensional and Energetic Point of View for a Marine Technical Water Generator Suitable for a Medium Size Container Ship. *Inventions* **2023**, *8*, 22. [CrossRef]
8. Ionescu, D.; Filipescu, A.; Simion, G.; Mincă, E.; Cernega, D.; Șolea, R.; Filipescu, A. Communication and Control of an Assembly, Disassembly and Repair Flexible Manufacturing Technology on a Mechatronics Line Assisted by an Autonomous Robotic System. *Inventions* **2022**, *7*, 43. [CrossRef]
9. Simion, G.; Filipescu, A.; Ionescu, D.; Șolea, R.; Cernega, D.; Mincă, E.; Filipescu, A. Mobile Visual Servoing Based Control of a Complex Autonomous System Assisting a Manufacturing Technology on a Mechatronics Line. *Inventions* **2022**, *7*, 47. [CrossRef]
10. Duca, O.; Minca, E.; Filipescu, A.; Cernega, D.; Solea, R.; Bidica, C. Event-Based PID Control of a Flexible Manufacturing Process. *Inventions* **2022**, *7*, 86. [CrossRef]
11. Bogatu, N.; Muresan, A.C.; Mardare, L.; Ghisman, V.; Ravoiu, A.; Dima, F.M.; Buruiana, D.L. The Influence of Different Type Materials of Grit Blasting on the Corrosion Resistance of S235JR Carbon Steel. *Inventions* **2023**, *8*, 39. [CrossRef]
12. Serea, D.; Constantin, O.E.; Horincar, G.; Stănciuc, N.; Aprodu, I.; Bahrim, G.E.; Râpeanu, G. Optimization of Extraction Parameters of Anthocyanin Compounds and Antioxidant Properties from Red Grape (Băbească Neagră) Peels. *Inventions* **2023**, *8*, 59. [CrossRef]
13. Stoica, F.; Constantin, O.E.; Stănciuc, N.; Aprodu, I.; Bahrim, G.E.; Râpeanu, G. Optimization of the Parameters Influencing the Antioxidant Activity and Concentration of Anthocyanins Extracted from Red Onion Skins Using a Central Composite Design. *Inventions* **2022**, *7*, 89. [CrossRef]

Disclaimer/Publisher's Note: The statements, opinions and data contained in all publications are solely those of the individual author(s) and contributor(s) and not of MDPI and/or the editor(s). MDPI and/or the editor(s) disclaim responsibility for any injury to people or property resulting from any ideas, methods, instructions or products referred to in the content.

inventions

Article

Optimization of Extraction Parameters of Anthocyanin Compounds and Antioxidant Properties from Red Grape (*Băbească neagră*) Peels

Daniela Serea, Oana Emilia Constantin, Georgiana Horincar, Nicoleta Stănciuc, Iuliana Aprodu, Gabriela Elena Bahrim and Gabriela Râpeanu *

Faculty of Food Science and Engineering, Dunărea de Jos University of Galati, 111 Domnească Street, 800201 Galati, Romania
* Correspondence: gabriela.rapeanu@ugal.ro; Tel.: +4-0336-130-177

Abstract: Using a Central Composite Design, the extraction of bioactive compounds from red grape *Băbească neagră* peels was optimized by applying a conventional solvent extraction. On the anthocyanin content, total phenolic content, and antioxidant activity (using the DPPH method), the effects of extraction factors, including ethanol and citric acid concentrations, extraction temperature, and duration, were investigated. For each of the investigated parameters, a quadratic model was suggested. The maximum and minimum variables investigated in the coded form of the experimental plan are the concentrations of citric acid (0.10–2.64%), ethanol (38.06–96.93%), operating temperature (13.06–71.90 °C), and extraction time (11.36–78.63 min). The optimal mixture for recovering the most significant amount of polyphenol content and antioxidant activity was 85% ethanol, 0.85% citric acid, 52.14 min, and 57 °C. Based on the experimental approach, the anthocyanin content ranged from 1.71 to 2.74 mg C3G/g DW, the total phenolic content ranged from 24.67 to 43.97 mg/g, and the antioxidant activity ranged from 15.95 to 20.98 mM TE/g DW. Overall, it should be stressed that establishing operating factors to maximize model responses can improve the extraction process and the obtaining of red grape peel value-added extracts for creating functional food products.

Keywords: anthocyanins; antioxidant; red grape; citric acid; ethanol; temperature; time; CCD

Citation: Serea, D.; Constantin, O.E.; Horincar, G.; Stănciuc, N.; Aprodu, I.; Bahrim, G.E.; Râpeanu, G. Optimization of Extraction Parameters of Anthocyanin Compounds and Antioxidant Properties from Red Grape (*Băbească neagră*) Peels. *Inventions* **2023**, *8*, 59. https://doi.org/10.3390/inventions8020059

Academic Editors: Monique Lacroix and Yves Wache

Received: 30 December 2022
Revised: 10 February 2023
Accepted: 22 March 2023
Published: 27 March 2023

Copyright: © 2023 by the authors. Licensee MDPI, Basel, Switzerland. This article is an open access article distributed under the terms and conditions of the Creative Commons Attribution (CC BY) license (https://creativecommons.org/licenses/by/4.0/).

1. Introduction

Nowadays, due to the high content of valuable compounds, the wine industry is responsible for the generation of by-products used, in various branches of industry such as animal feed, composting, or ethanol production [1]. About 75% of cultivated grapes are intended for wine production, of which 20–30% represent residual products [2,3]. This waste represents grape pomace which consists of skin, remaining pulp, seeds, and bunch fragments [4]. Grape pomace represents a valuable source of important nutrients. Different studies have presented the use of dried pomace powder for directly fortifying food products such as dairy, meat, and fish [2]. The research on grape pomace may be relevant for industrial reasons due to the rising need for nutraceutical and antioxidant compounds [5]. Increasing demand and production of wines have begun generating increased amounts of grape by-products during the winemaking process such as peel/skin, and their disposal poses a burden on the environment. However, grape skin/peels are stocked with bioactive compounds, favoring the use of these by-products as functional ingredients. The major bioactive compounds in grapes are phenolic acids, flavonoids, anthocyanins, proanthocyanins, and stilbenes [6,7], most concentrated in the skin [8]. The composition of grape peel/skin is variable based on varietal diversity, agronomic conditions of the region in which they were cultivated, and the extraction techniques used [9]. Despite these environmental factors, the bioactive chemicals that remain in the grape skins after winemaking can be extracted [10–12]. Those compounds are evaluated as potential antioxidants [13] and food colorants [14]. Given the antioxidant characteristics of grape skin/peel, these compounds can be useful in many foods' industrial aspects where the prevention of oxidative damage or free radical formation is involved. Therefore, food quality, shelf-life extension, and intelligent packaging could be improved or maintained by developing these characteristics [13].

Among the phenolic compounds present in grapes, flavonoids (flavonols, anthocyanins, flavan-ols, and their derivative proanthocyanidins) are the most abundant physiologically active phytonutrients in grapes with major grape skins and seeds and are involved in the biological activities of grape products [15,16]. Due to their dual functions, anthocyanin pigments play a significant role in grapes and wines. Firstly, their concentration, forms, and derivatives directly affect the finished wine's color, making them a crucial component of sensory qualities. Secondly, they are thought to possess a variety of biological qualities, such as antioxidant properties, which protect against neurological disorders and exhibit anti-inflammatory, anti-hepatotoxicity, cardioprotective, chemotherapeutic, hepatoprotective, and neuroprotective activity [17–19]. The anthocyanins profile from red grapes consists of 3-O-monoglucosides of delphinidin, cyanidin, petunidin, peonidin, and malvidin [20]. Therefore, their extraction and application in different food matrices represent a way of valorizing grape by-products (skins) by obtaining value-added ingredients (natural colorants and antioxidants) in order to replace synthetic food additives [21]. Additionally, phenolic acids can be found in grapes, free or conjugated with sugars, anthocyanins, or condensed tannins [22]. Proanthocyanidins, also known as condensed tannins, are released from both grape skins and seeds and are what give wine its astringent and bitter characteristics [23,24].

Optimizing the extraction process efficiently to maximize the amount of biologically active compounds from the by-products of the food industry is still a scientific concern [9]. Over time, many studies have highlighted different methods of extracting bioactive compounds from the skin of grapes through different extraction techniques [9,25], among them solid–liquid extractions, such as mechanical agitation and solvent extraction (ethanol and methanol extraction). The solvent selection used for the extraction can increase extraction efficiency, time, quality, and solvent consumption. The development and optimization of efficient extraction procedures are essential to improve the extraction of valuable compounds. To improve the extraction process, the following parameters are usually taken into account: matrix, solvent, temperature, pH, liquid–solid ratio, and extraction time [26]. Common methods for extracting phenolic compounds from fruit and vegetables include Soxhlet extraction, maceration, and hydrodistillation, which rely on the effectiveness of various solvents as extractants as well as the use of heat and/or mixing. The selection of a solvent is based on several factors, such as its physicochemical properties, cost, and toxicity. Some solvents, such as ethanol, water, and their mixtures, are designated as "generally recognized as safe"). Moreover, the preferred solvent systems are currently used for natural products [27].

Using a central composite design and response surface methodology (RSM), this study sought to maximize the extraction of phenolic antioxidants from grape skins. A conventional single-factor experiment, which does not consider the interactive effects among the analyzed variables, could not fully show the effects of the parameters on the responses. The screening of a wide variety of factors is possible with response surface methodology based on a central composite design (RSM-CCD), which provides information on the cumulative impact of the factors while helping to lower the cost of the analysis, in addition to evaluating the contribution of each factor [28]. The study used ethanol concentration, acid type, duration, and temperature as our extraction parameters. The dependent variables included total phenolic content (mg GAE/g), total monomeric anthocyanins (mg G3G/g), and DPPH radical scavenging levels (responses). Data on extraction factors having notable impacts on the phenolic antioxidants in grape skins were obtained from single-factor trials. The ideal extraction condition was then more precisely determined by the RSM-CCD analysis of these components. The CCD offers a decent quantity of information for inconsistency testing without requiring many design points, making it perfect for sequential experimentation [29].

2. Materials and Methods

2.1. Reagents and Chemicals

For the chemical characterization of biologically active compounds from red grape skins, we used 96% ethanol, Folin–Ciocâlteu reagent (FC), DPPH (2,2-diphenyl-1-picrylhydrazyl), Trolox (6-hydroxy-2,5,7,8-tetramethylchroman-2-carboxylic acid), methanol (MeOH), potassium chloride solution (KCl), sodium acetate solution (CH_3COONa), sodium carbonate (Na_2CO_3) 20%, and Gallic acid solution which were obtained from Sigma Aldrich (St. Louis, MO, USA).

2.2. Red Grape Skins Preparation

Red grapes from the *Băbească neagră* variety were purchased from a local market in Galati, Romania (from the 2020 harvest). The grape skins were manually separated, washed with cold water, and rinsed with distilled water at a ratio of 1:2 (*w/w*). Then, they were wiped with paper towels to remove any residual pulp. The collected skins were freeze-dried using Alpha 1–4 LD plus equipment (CHRIST, Osterode am Harz, Germany) at −42 °C under a pressure of 10 Pa for 48 h. Finally, the dried skins were grounded and stored at 4 °C in a hermetically closed jar until further analysis.

2.3. Extraction of Biologically Active Compounds

A total of 1 g of dried peel grape powder was utilized for the extraction along with 9 mL of the solvent (38.06–96.93% ethanol) and 1 mL of citric acid with a range of concentrations from 0.01 to 2.64%. The extractions took place at 13.06–71.9 °C for 11.36 to 78.6 min using a sonication water bath (MRC Scientific 193 Instruments, Holon, Israel), followed by centrifugation at 5000 rpm for 10 min at 4 °C, and the supernatant was phytochemically analyzed.

2.4. Determination of the Total Anthocyanins Content (TAC)

In order to estimate the total monomeric anthocyanins content (TAC), a modified pH differential method was used [30]. Before the analysis, the samples were diluted (D = 1:10). Then, 200 µL of vegetable extract, and 800 µL of a buffer solution with a pH of 1.0/4.5 were used, and the absorbance of diluted extracts was measured at two distinct wavelengths: 520 nm and 700 nm. The results were expressed as milligrams of cyanidin-3-glucoside (C3G) per gram of dry weight (DW).

2.5. Total Phenolic Compounds Determination

The total phenolic compounds content (TPC) was achieved using the modified method of Dewanto et al. [31]. Briefly, a mixture was obtained by adding 200 µL extract, 15.8 mL ultrapure water, and 1 mL of Folin-Ciocâlteu reagent. After 10 min, a volume of 3 mL of 20% Na_2CO_3 was added, and the mixture was maintained in a dark place for 60 min at 25 °C. The mixture absorbance was measured at a wavelength of 765 nm. The results obtained were expressed as mg gallic acid equivalents GAE/g DW. The gallic acid concentration for the standard curve was 10–100 ppm, and the equation obtained was $y = 1.6991x - 0.0256$.

2.6. Antioxidant Activity—DPPH Assay (AOA)

The antiradical activity of red grape skin extracts was determined using 2,2-diphenyl-1-picrylhydrazyl (DPPH) according to Castro-Vargas et al. [32] and Turturică et al. [30]. Briefly, a mixture was obtained by adding a 200 µL extract and a 3.9 mL DPPH solution 0.1M. The mixture was maintained in a dark place for 90 min at 25 °C. The mixture absorbance was measured at a wavelength of 515 nm. A control was prepared by adding 200 µL methanol and 3.9 mL DPPH solution 0.1 M, and the absorbance mixture was also measured. The results obtained were expressed as mM Trolox/g DW. The Trolox concentration for the standard curve was 10–100 ppm, and the equation obtained was $y = 0.45x + 0.0075$.

2.7. Experimental Design

The antioxidant activity of the red grape skin extract was experimentally determined, and the TAC, TPC, and AOA were optimized using the Central Composite Design (CCD) approach. An experimental factorial model was created using the design of 21 experimental variants, 3 central points, and a core component of 5 variables. The experimental plan's variables' maximum and lowest values are shown in Table 1 in both their present and coded forms. Additionally, the CCD develops a quadratic model for the response variables.

Table 1. Range of values for the variables examined and values encoded.

Code	Independent Variables	Units	Minimum	Maximum	Coded Low	Coded High
A	Citric acid	%	0.0100	2.64	−1 = 0.10	+1 = 2.00
B	Ethanol	%	38.06	96.93	−1 = 50.00	+1 = 85.00
C	Temperature	°C	13.06	71.90	−1 = 25.00	+1 = 60.00
D	Time	min	11.36	78.63	−1 = 25.00	+1 = 65.00

The experimental conditions can be represented by a second-order polynomial model (1):

$$R = b_0 + \sum_i^n b_i \cdot x_i + \sum_{i=1}^n b_{ii} \cdot x_{ii}^2 + \sum b_{ij} \cdot x_i \cdot x_{jd} \qquad (1)$$

where R is the predicted response, b_0 is the intercept, b_i, b_{ii}, and b_{ij} are the regression coefficients, x_i and x_{jd} are the independent variables analyzed, and n is the number of factors.

2.8. Statistical Analysis

To assess the experimental model in the study, we used the statistical program Design Expert (v. 13) from Design-Expert® (Stat-Ease, Inc., Minneapolis, MN, USA). The results of each analysis were performed in triplicate, and they are shown as mean standard deviation.

3. Results and Discussion

In order to find the optimized parameters for the extraction process, a Central Composite Design (CCD) and surface response modeling were used to establish the ideal parameters for optimizing the extraction process. In this respect, the content of total anthocyanins, total polyphenolic compounds, and antioxidant activity were measured.

The four independent variables (citric acid concentration, ethanol concentration, temperature, and time of extraction) were used to optimize the extraction parameters modeled by CCD in this study (Table 2).

Table 2. The CCD matrix with the measured values in terms of TAC, TPC, and AOA.

Run	Factor 1 A: Citric Acid %	Factor 2 B: Ethanol %	Factor 3 C: Temperature °C	Factor 4 D: Time min	Response 1 (R1) TAC mg/g	Response 2 (R2) TPC mg/g	Response 3 (R3) AOA mM/g
1	0.1	85	25	65	2.09 ± 0.08	29.01 ± 1.70	19.76 ± 0.25
2	1	67	13.06	45	2.15 ± 0.11	29.97 ± 1.55	18.24 ± 0.13
3	1	67	71.9	45	2.29 ± 0.02	40.97 ± 1.70	15.95 ± 0.39
4	1	67	42	45	2.24 ± 0.02	36.94 ± 1.67	17.26 ± 0.14
5	1	67	42	45	2.25 ± 0.18	37.04 ± 1.49	17.25 ± 0.16
6	0.1	50	25	25	2.45 ± 0.03	29.93 ± 0.38	19.65 ± 0.66
7	2	50	25	65	2.64 ± 0.18	30.12 ± 1.71	19.05 ± 0.89
8	0.1	85	60	65	2.4 ± 0.39	31.09 ± 0.56	18.91 ± 0.50
9	2	50	60	65	2.17 ± 0.22	31.92 ± 0.89	19.31 ± 0.24
10	0.01	67	42	45	2.1 ± 0.09	30.86 ± 1.23	20.16 ± 0.64
11	0.1	50	60	25	2.53 ± 0.29	43.97 ± 0.94	18.38 ± 0.20
12	1	67	42	11.36	2.05 ± 0.10	31.41 ± 1.39	18.77 ± 0.29
13	2.64	67	42	45	2.49 ± 0.15	35.88 ± 0.98	20.49 ± 0.55
14	2	85	25	25	1.71 ± 0.08	24.67 ± 1.11	20.98 ± 0.40
15	1	67	42	78.63	2.32 ± 0.11	26.45 ± 1.92	18.72 ± 0.18
16	2	85	60	25	2.07 ± 0.07	31.1 ± 0.56	17.47 ± 0.50

Table 2. *Cont.*

Run	Factor 1 A: Citric Acid %	Factor 2 B: Ethanol %	Factor 3 C: Temperature °C	Factor 4 D: Time min	Response 1 (R1) TAC mg/g	Response 2 (R2) TPC mg/g	Response 3 (R3) AOA mM/g
17	1	67	42	45	2.24 ± 0.02	37.12 ± 1.94	17.26 ± 0.27
18	1	67	42	45	2.25 ± 0.00	37.01 ± 1.15	17.26 ± 0.13
19	1	96.93	42	45	2.59 ± 0.10	42.07 ± 1.66	16.35 ± 1.25
20	1	38.06	42	45	2.03 ± 0.16	32.25 ± 1.44	17.61 ± 0.80
21	1	67	42	45	2.25 ± 0.11	37.14 ± 1.96	17.35 ± 0.21

3.1. Effect of the Extraction Parameters on TAC

As can be seen in Table 2, the total anthocyanins content varied from 1.71 to 2.64 mg/g DW as a function of the various variables. Considering the extraction environment's variables, the values of TAC from red grape skins were explained using regression equations developed after the ANOVA analysis (Table 3). The Model F-value of 1003.34 for TAC from red grape peels suggests that the model is significant. Model terms are significant if the determined *p*-values are less than the value of 0.0500, according to the results. In this situation, the following terms, such as A, B, C, D, AB, AC, AD, BC, BD, CD, B^2, C^2, and D^2, are significant model terms.

$$\text{R1 (TAC)} = 2.26 + 0.1375\text{A} + 0.1722\text{B} + 0.0380\text{C} + 0.1043\text{D} + 0.0368\text{AB} - 0.06\text{AC} + 0.3622\text{AD} + 0.1324\text{BC} + 0.2475\text{BD} - 0.0750\text{CD} + 0.0038\text{A}^2 + 0.0225\text{B}^2 - 0.008\text{C}^2 - 0.0200\text{D}^2 \tag{2}$$

Table 3. ANOVA for the reduced quadratic model calculated for TAC and TPC extraction and AOA.

	TAC					TPC					AOA				
Source	**SS**	**df**	**MS**	**F-Value**	***p*-Value**	**SS**	**df**	**MSquare**	**F-Value**	***p*-Value**	**SS**	**df**	**MS**	**F-Value**	***p*-Value**
Model [a]	0.9492	14	0.0678	1003.34	<0.0001	518.33	13	39.87	2495.65	<0.0001	37.31	14	2.67	1241.30	<0.0001
A-Citric acid	0.0547	1	0.0547	809.95	<0.0001	29.58	1	29.58	1851.33	<0.0001	2.06	1	2.06	960.80	<0.0001
B-Ethanol	0.1661	1	0.1661	2457.72	<0.0001	46.57	1	46.57	2915.05	<0.0001	0.8648	1	0.8648	402.78	<0.0001
C-Temperature	0.0197	1	0.0197	290.88	<0.0001	131.49	1	131.49	8230.00	<0.0001	6.37	1	6.37	2967.68	<0.0001
D-Time	0.0606	1	0.0606	896.65	<0.0001	6.78	1	6.78	424.19	<0.0001	0.0137	1	0.0137	6.40	0.0447
AB	0.0044	1	0.0044	65.51	0.0002	0.0853	1	0.0853	5.34	0.0541	0.0459	1	0.0459	21.39	0.0036
AC	0.0314	1	0.0314	465.24	<0.0001	7.84	1	7.84	490.84	<0.0001	0.1584	1	0.1584	73.76	0.0001
AD	0.4312	1	0.4312	6380.64	<0.0001	95.57	1	95.57	5982.19	<0.0001	0.7707	1	0.7707	358.95	<0.0001
BC	0.1403	1	0.1403	2076.49	<0.0001	6.74	1	6.74	422.14	<0.0001	1.40	1	1.40	652.50	<0.0001
BD	0.1302	1	0.1302	1926.32	<0.0001	57.93	1	57.93	3626.06	<0.0001	1.56	1	1.56	728.21	<0.0001
CD	0.0450	1	0.0450	665.91	<0.0001	34.40	1	34.40	2153.40	<0.0001	2.19	1	2.19	1022.08	<0.0001
A^2	0.0001	1	0.0001	1.57	0.2568	44.28	1	44.28	2771.33	<0.0001	20.60	1	20.60	9596.00	<0.0001
B^2	0.0076	1	0.0076	112.10	<0.0001	-	-	-	-	-	0.1771	1	0.1771	82.50	<0.0001
C^2	0.0010	1	0.0010	14.16	0.0094	5.49	1	5.49	343.61	<0.0001	0.0642	1	0.0642	29.90	0.0016
D^2	0.0060	1	0.0060	88.49	<0.0001	125.06	1	125.06	7827.78	<0.0001	3.91	1	3.91	1820.54	<0.0001
Residual	0.0004	6	0.0001			0.1118	7	0.0160			0.0129	6	0.0021		
Lack of Fit [b]	0.0003	2	0.0001	4.76	0.0876	0.085	3	0.0283	4.23	0.0986	0.0060	2	0.0030	1.72	0.2885
Pure Error	0.0001	4	0.000			0.0268	4	0.0067			0.0069	4	0.0017		
Cor Total	0.9496	20				518.44	20				37.33	20			

Sum of Squares—SS; Mean Square—MS; [a] Significant; [b] Not significant. Equation (2) presents the relationship between the TAC (R1) and the variables expressed in coded units.

The ethanol (B) had the most positive impact on the anthocyanins content according to the regression equation's b coefficients. Furthermore, citric acid concentration (A), and extraction time (D) all improved the TAC of the extracts. The extraction of TAC from red grape skins was negatively influenced, as shown in equation 1, by interactions between citric acid concentration and temperature (AC), temperature and time of extraction (CD), and a quadratic time of extraction (C^2) and temperature (D^2).

There was a moderate effect on the TAC from the interactions between citric acid and ethanol concentration (AB), citric acid concentration and time (AD), and ethanol concentration and time (BD) of TAC extraction from red grape skins.

In analyzing Figure 1(Aa–Ad), a synergistic effect of the independent variables (citric acid concentration, ethanol concentration, temperature, and time) on the TAC of the extract was found. Figure 1A depicts the correlation between the independent and dependent variables which was predicted using second-order contour plots. The three-dimensional response reveals the impact of the selected parameters on the extract's TAC. Figure 1(Ab) shows that citric acid concentration and extraction time are the main parameters impacting

TAC extraction. The maximum value for TAC was achieved at 2% citric acid concentration and about 65 min extraction time. The negative effect of interaction between time and temperature was also identified by Li et al. [9], who observed that from 40 to 51 °C, there was a significant rise in TAC extraction yield, but above 51 °C, the yield began to decline. Furthermore, as shown in Figure 1(Ad), lower extraction times (25 min) and higher concentrations of ethanol (85%) led to a decreased TAC value. The contour plots showed that the concentration of anthocyanins was affected by ethanol concentration rather than temperature variation (Figure S1(Aa,Ac)).

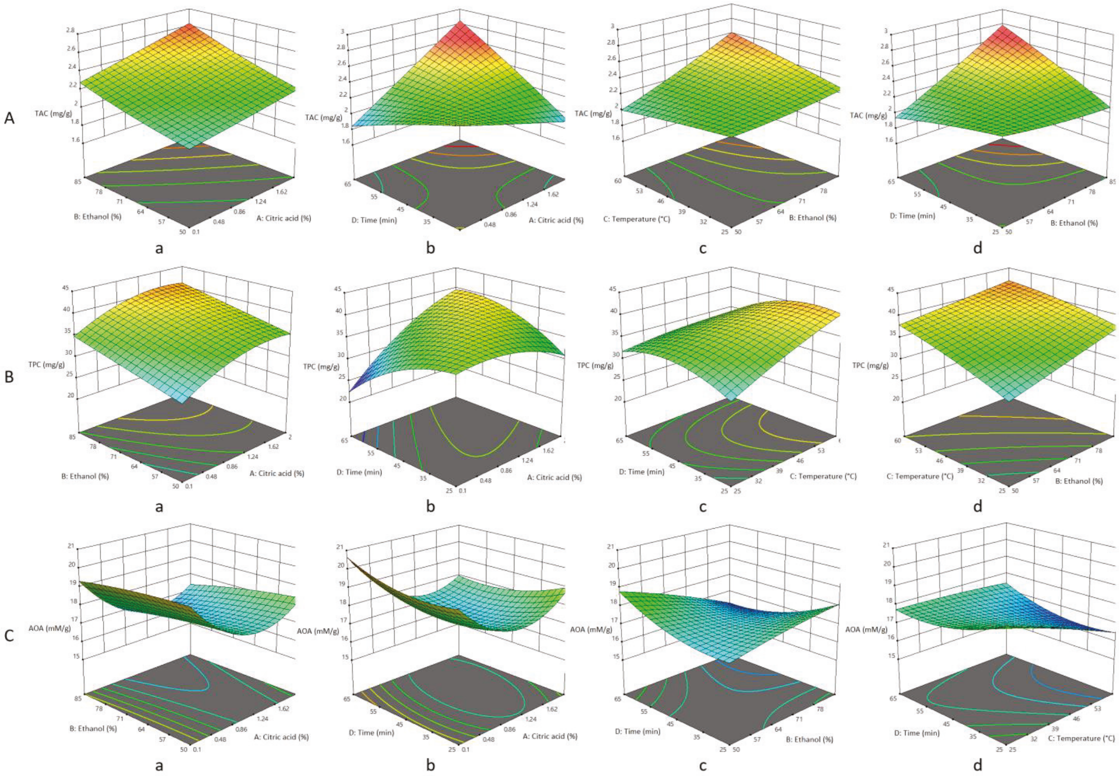

Figure 1. Three-dimensional surface plots screening the effect of the variables on the TAC ((**A**)—(**a**): citric acid–ethanol; (**b**): citric acid–time; (**c**): ethanol–temperature; (**d**): ethanol–time), TPC ((**B**)—(**a**): citric acid–ethanol; (**b**): citric acid–time; (**c**): temperature–time; (**d**): ethanol–temperature) and AOA ((**C**)—(**a**): citric acid–ethanol; (**b**): citric acid–time; (**c**): ethanol–time; (**d**): temperature–time).

Several parameters' perturbation plots show how each impacted the current response (Figure 2A). The perturbation plot compares the effects of all factors in the design space and is used to determine which factors have the greatest impact on the response. A steep slope or curvature in a factor indicates the sensitivity of the response to that factor, whereas a relatively flat line indicates a factor's insensitivity to change [33]. Thereby, curve B in the perturbation graph looks crucial in determining TAC, showing how significantly the ethanol value affected the result. Curves A and D, which represented time and citric acid, respectively, showed that these variables had a less significant impact on the extraction than ethanol.

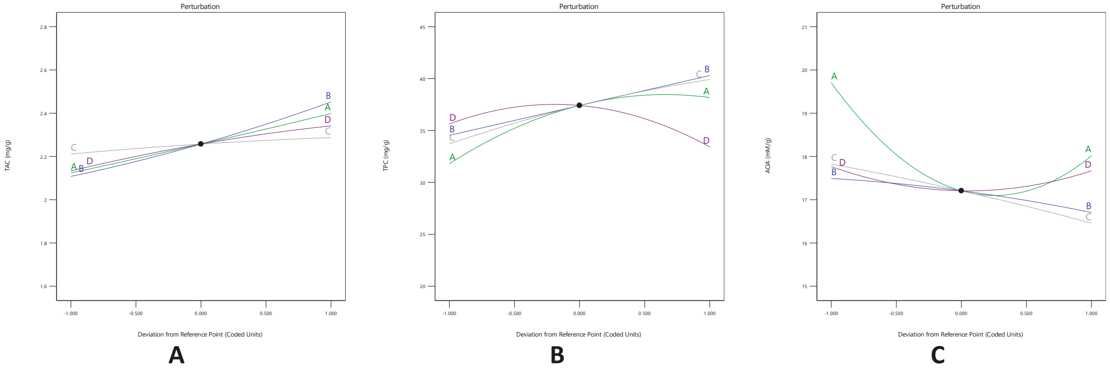

Figure 2. Perturbation graphs of each independent variable on TAC (**A**), TPC (**B**), and AOA (**C**) of the red grape peel extracts. A: citric acid (%); B: ethanol (%); C: temperature (°C); D: time (min).

Table 2 shows the concentrations of anthocyanins extracted from the skin of *Băbească neagră* grapes obtained by varying the parameters of the conventional extraction method using a CCD model. The highest concentration of anthocyanins TAC (2.64 mg/g) corresponds to the extracts obtained with EtOH 50% acidified with citric acid 2% at 25 °C, for 65 min of extraction. Therefore, the yields of anthocyanin extraction may be increased by mixing water with ethanol, and the extracts are easy to introduce into biological systems. The results corroborate those of Khazaei et al. [34], who used RSM with Box–Behnken to discover that increasing the solvent ratio to the solute improved anthocyanin extractions by raising TAC. Similar results were obtained by de Andrade et al. [35] who reported in the skin of *Syrah* grapes an anthocyanin content of 3.25 ± 0.03 mg M3G/g DW. Yammine [36] used an extraction ratio of 50% ethanol and extracted from the *Cabernet Franc* grape an anthocyanin content of 11.67 ± 1.67 mg/g DW from the pomace of the Cabernet Franc grape. With the help of the maceration method, Arozarena et al. [37] extracted a concentration of anthocyanins from the skins of the grape variety *Cabernet Sauvignon* of 23.3 ± 0.3 g M3G/kg DW. The same approach was used to obtain, from the skins of the *Graciano* grape variety, an amount of 22.6 ± 0.4 g M3G/kg DW. Rockenbach et al. [12] observed a total anthocyanin content value between 2.89 and 9.34 mg/g DW in six red grape (*Vitis vinifera* and *Vitis labrusca*) extracts from Brazil. These differences between the anthocyanin contents in the grape can be explained by the factors involved in the vine cultivation and also between varieties.

3.2. Effect of the Extraction Parameters on TPC

This study aimed to find the ideal parameters for extracting phenolic compounds from red grape skins. The TPC ranged from 24.67 to 43.97 mg/g DW based on the experimental design depicted in Table 2. Data presented in Table 3 revealed that for TPC, a Model F-value of 2495.65 implies that the model is significant, and *p*-values less than 0.05 imply that the model terms were significant. Model terms are considered significant if their *p*-values are less than 0.0500. In this case, A, B, C, D, AC, AD, BC, BD, CD, A^2, C^2, and D^2 are significant model terms.

$$\begin{aligned}\mathrm{R2\ (TPC)} = +37.41 + 3.19A + 2.88B + 3.10C - 1.10D - 0.1614AB - 0.9895AC + 5.39AD - 0.9180BC + 5.21\,BD - \\ 2.07CD - 2.42A^2 - 0.6054C^2 - 2.89D^2\end{aligned} \tag{3}$$

The model equation presenting the correlation between the R2 (TPC) and the variables in coded units is revealed in Equation 3. The regression equation's b coefficients showed that the ethanol concentration and extraction time positively affected the phenolic compounds extraction.

The interactions between citric acid concentration and time of extraction (AD) and between ethanol concentration and extraction time (BD) had an appreciably positive effect on TPC extraction. On the contrary, citric acid concentration (A^2) and extraction time (D^2) had an appreciably negative contribution. Furthermore, interactions between citric acid concentration and ethanol concentration (AB) and acid citric concentration and temperature (AC) of extraction, as well as ethanol concentration and temperature (BC), had a moderately negative effect on the TPC yield.

Figure 1(Ba–Bf) shows the tridimensional surface plots and 3D surfaces of the interactions between the concentrations of citric acid and ethanol, temperature, and extraction time that have the greatest influence on the extraction of TPC. The TPC increased when the ethanol concentration approached 85% and the citric acid concentration reached over 2%, according to an analysis of the impacts of ethanol concentration and citric acid concentration (Figure 1(Ba)). According to the surface graphs, citric acid concentration and ethanol concentration had a greater impact on polyphenol concentration than did extraction duration. A decrease in phenolic compounds content is observed at an increased concentration of citric acid and extraction time (Figure 1(Bb)). Additionally, the increase in TPC with an increasing temperature was observed at low (<25 min) and moderate (35 min) extraction time concentrations. However, the effect of the temperature almost disappeared at a higher extraction time (>65 min) (Figure 1(Bc)). Figure 1(Bd) demonstrates a considerable increase in TPC with a decreasing temperature and increasing ethanol concentration in the solvent composition.

Moreover, the perturbations graph (Figure 2B) exhibiting the effects of each independent variable on the TPC revealed that both citric acid and ethanol concentration had a significant influence on increasing the TPC.

Following the conventional extraction, the highest content of total phenolic compounds, 43.97 mg EAG/g DW, was obtained for the extraction with 50% ethanol and 0.1% citric acid after 25 min of extraction at 60 °C. Katalinić et al. [38] reported content of 45.0 ± 26.3 mg EAG/g grape skin following a conventional extraction with ethanol (ethanol/water 80/20, at 60 °C, for 60 min). On the other hand, Negro et al. [39] obtained a content of 33.3 ± 0.3 mg EAG /100 g DW in the skin of red grapes by extraction with 80% ethanol with acetic acid. Poudel et al. [40] determined a content of 8.47 ± 0.20 (mg/g EAG) in the skin of the *Ebizuru* grape variety by 80% methanol extraction with 1N HCl. Tournour et al. [41] reported a content ranging from 69.30 to 131.70 mg/g EAG for different grape cultivars following a conventional magnetic stirring extraction for 48 h using an 80% ethanolic solution.

3.3. Effect of Extraction Parameters on AOA

The recorded values of antioxidant activity ranged from 15.95 to 20.98 mM TE/g DW according to the influence of various variables (Table 2). For the AA parameter, the model is suggested to be significant by the model's Model F-value of 1241.30, and *p*-values less than 0.0500 indicate that model terms are significant. In this case, A, B, C, D, AB, AC, AD, BC, BD, CD, A^2, B^2, C^2, and D^2 are significant model terms.

Equation (4) reveals the model equation for the relationship between the antioxidant activity (R3) and variables expressed in coded units.

$$\begin{aligned} \text{R3 (AOA)} = {} & +17.21 - 0.8438\text{A} - 0.3931\text{B} - 0.6835\text{C} - 0.0497\text{D} - 11.84\text{AB} - 0.4843\text{AD} - 0.4184\text{BC} - \\ & 0.8576\text{BD} + 0.5237\text{CD} + 1.66\text{A}^2 - 0.1089\text{B}^2 - 0.0656\text{C}^2 + 0.5114\text{D}^2 \end{aligned} \tag{4}$$

The regression equation's b coefficients showed that among all the variables, the time of extraction had a minor negative effect on antioxidant activity. The interaction between citric acid concentration and ethanol concentration (AB) significantly negatively impacted the AOA of the red grape skin extract. The interactions between citric acid concentration and time of extraction (AD), ethanol concentration and temperature (BC), ethanol concentration and time of extraction (BD), quadratic ethanol concentration (B^2), and quadratic temperature (BD) were all found to have a small negative impact (C^2).

Additionally, the interaction between temperature and time (CD) and quadratic extraction duration had a moderate impact on the extract's antioxidant activity (D^2). Additionally, the antioxidant activity of the red grape skins extract is significantly positively influenced by quadratic citric acid content (A^2).

The second-order contour plots were designed to predict the correlation between the independent and dependent variables, as seen in Figure 1C. The same correlation is used to highlight the synergistic effects of the studied independent variables on the values of antioxidant activity for the red grape skin extract. The correlative effect of the selected independent three-dimensional response area can describe the extract's antioxidant activity. Figure 1(Ca–Cd) shows the extraction parameters that affect antioxidant activity. The maximum antioxidant activity was obtained after 25 min of extraction at a concentration of ethanol of about 85%. Antioxidant activity increases as citric acid concentrations increase (Figure 1(Ca,Cb)). Shorter extraction times and higher citric acid concentrations also positively impacted the DPPH free radical-scavenging capacity, as evidenced by the plots. AOA decrease was observed at an increased ethanol concentration (Figure 1(Cc)). However, at higher extraction times (≥45 min) and at a moderate ethanol concentration (64%) an increase in AOA was observed (Figure S1(Cc)). Higher temperatures increase the solubility of phenolic compounds, leading to an increase in AOA. Nonetheless, using higher extraction temperatures and a longer extraction time, the extracted phenolic compounds began to degrade and, after reaching equilibrium, reduced AOA concentrations (Figure 1(Cd)). Similar results were obtained by Li et al. [9] who found a negative correlation between increasing ethanol concentration and increasing temperature, indicating that the antioxidant activity of AOA decreased as the ethanol concentration and temperature increased. Moreover, curve D from the perturbations graph has played a significant role in the determination of AOA in the perturbation graph, demonstrating the sizeable influence of the time of extraction value. Additionally, curves B and C will have less impact on extraction than curve A (Figure 2C).

After 25 min of extraction at 25 °C, the extraction with 85% ethanol and 2% citric acid produced the highest AOA of 24.67 mM TE/g DW. For the same grape variety but harvested in 2012, Constantin et al. [42] reported 4.89 ± 0.02 μM TE/g DW by the ABTS assay. Rockenbach et al. [12] obtained an average of 2.076 mM TE/100 g DW for different grape varieties from Brazil. The pinot noir and Isabel varieties had the highest levels of antioxidant activity. In a study conducted by Kupe et al. [43], nine '*Karaerik*' grape clones' peel samples showed DPPH radical scavenging between 1.08 and 1.34 mM TE /100 g FW. After model validation, for extraction, Li et al. [9] used the following parameters: 49% ethanol/51 C/15 min and obtained an AOA of 41.78 ± 1.13 mg TE/g.

3.4. Extraction Parameter Optimization and Validation

To verify the model equation, the model suggested the best factors based on maximizing response desirability (Figure 3, Table 4). The ramp graphs are labeled with a specific point that represents the optimal level for the variable under study. The value of the desirability function varies from the value zero, outside the imposed limits, to the value 1 or a value close to 1. The program's objective is to maximize the function, starting at a random point and aiming for the steepest slope possible [44]. A score of 1 (0.926) meant that all chosen conditions were true. The ideal conditions for maximizing phenolic compounds extraction and antioxidant activity were 0.85% citric acid, 85% ethanol, a temperature of 57.39 °C, and an extraction time of 52.14 min.

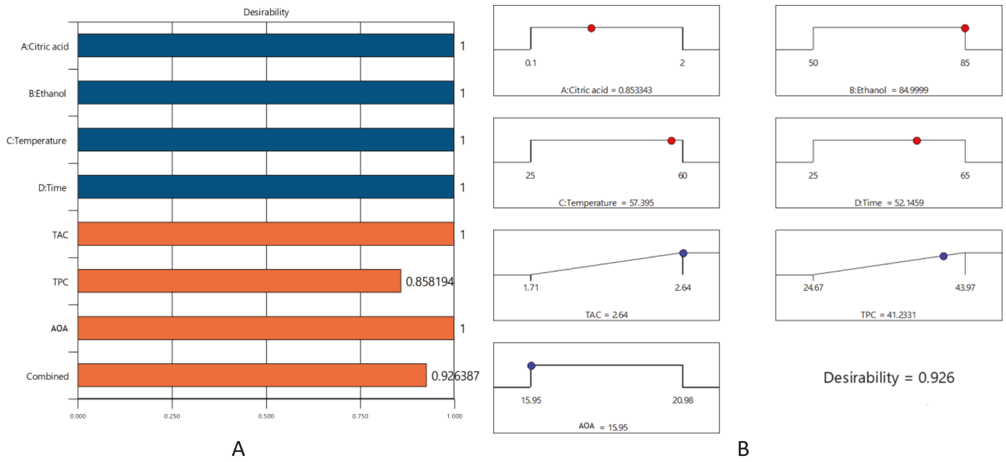

Figure 3. The optimization desirability bar chart (**A**) and ramps (**B**).

Table 4. The mathematical model's validation.

Dependent Variable	Predicted Value	95% Confidence Intervals	Experimental Value
TAC (mg C3G/g DW)	2.25	2.23–2.27	2.26
TPC (mg GAE/g DW)	37.41	37.09–37.73	37.22
AOA (mM TE/g DW)	17.20	17.08–17.32	17.11

According to the model, the maximal levels of anthocyanins, total phenolic compounds, and antioxidant activity were 2.25 mg C3G/g DW, 37.41 mg GAE/g DW, and 17.2 mM TE/g DW, respectively. The experimental findings (Table 4) demonstrated fast responses to the model's predictions. Three extractions were carried out under those predicted variables to verify the model. In a study conducted by Li et al. [9], using a Box–Behnken design by RSM optimized the extraction parameters (48.80% ethanol at 50.79 °C for 14.82 min) of grape skin for obtaining the highest yields of the TPC (15.24 mg GAE/g) and TAC (3.46 mg CGE/100 g).

4. Conclusions

To obtain peel extracts from *Băbească neagră* grapes with a high yield of phenolic compounds and high levels of antioxidant activity, the conventional solvent extraction process variables (citric acid concentration—0.85%, ethanol concentration—85%, temperature—57.39 °C, and extraction time—52.14 min) were optimized using a CCD and response surface methodology. The maximum concentrations of anthocyanins (2.25 mg C3G/g DW), total phenolic compounds (37.41 mg GAE/g DW), and DPPH radical scavenging activity (17.2 mM TE/g DW) in the experiment were obtained from the interaction of time, temperature, acid, and solvent concentrations. The optimized extraction process may be a potentially efficient way to obtain valuable extracts from affordable, natural sources like grape skins with potential antioxidants and a high yield of anthocyanins and other phenolic compounds. These results demonstrate proper factor combinations and a unique solvent mixture for obtaining a high yield of phenolic compounds and, particularly, anthocyanins.

Supplementary Materials: The following supporting information can be downloaded at: https://www.mdpi.com/article/10.3390/inventions8020059/s1.

Author Contributions: Conceptualization, D.S., O.E.C. and G.R.; methodology, D.S., G.H. and O.E.C.; software, O.E.C. and I.A.; validation, O.E.C. and I.A.; formal analysis, G.H. and D.S.; investigation, D.S.; resources, G.E.B.; data curation G.R. and N.S.; writing—original draft preparation D.S. and I.A.; writing—review and editing, G.R. and N.S.; visualization, N.S.; supervision, G.E.B. All authors have read and agreed to the published version of the manuscript.

Funding: This research received no external funding.

Institutional Review Board Statement: Not applicable.

Informed Consent Statement: Not applicable.

Data Availability Statement: The data supporting this study's findings are available from the corresponding author (G.R.) upon reasonable request.

Acknowledgments: The results of this work have been presented to the 10th edition of the Scientific Conference organized by the Doctoral Schools of "Dunărea de Jos" University of Galati (SCDS-UDJG) http://www.cssd-udjg.ugal.ro/ (accessed on 9 April 2022) that will be held on the 9–10 June 2022, in Galati, Romania.

Conflicts of Interest: The authors declare no conflict of interest.

References

1. Djilas, S.M.; Canadanović-Brunet, J.; Ćetković, G. By-Products of Fruits Processing as a Source of Phytochemicals. *Chem. Ind. Chem. Eng. Q.* **2009**, *15*, 191–202. [CrossRef]
2. Antonić, B.; Jančíková, S.; Dordević, D.; Tremlová, B. Grape Pomace Valorization: A Systematic Review and Meta-Analysis. *Foods* **2020**, *9*, 1627. [CrossRef] [PubMed]
3. García-Lomillo, J.; González-SanJosé, M.L. Applications of Wine Pomace in the Food Industry: Approaches and Functions. *Compr. Rev. Food Sci. Food Saf.* **2017**, *16*, 3–22. [CrossRef] [PubMed]
4. Balbinoti, T.C.V.; Stafussa, A.P.; Haminiuk, C.W.I.; Maciel, G.M.; Sassaki, G.L.; de Matos Jorge, L.M.; Jorge, R.M.M. Addition of Grape Pomace in the Hydration Step of Parboiling Increases the Antioxidant Properties of Rice. *Int. J. Food Sci. Technol.* **2020**, *55*, 2370–2380. [CrossRef]
5. Jara-Palacios, M.J.; Hernanz, D.; Cifuentes-Gomez, T.; Escudero-Gilete, M.L.; Heredia, F.J.; Spencer, J.P.E. Assessment of White Grape Pomace from Winemaking as Source of Bioactive Compounds, and Its Antiproliferative Activity. *Food Chem.* **2015**, *183*, 78–82. [CrossRef]
6. Nassiri-Asl, M.; Hosseinzadeh, H. Review of the Pharmacological Effects of Vitis Vinifera (Grape) and Its Bioactive Constituents: An Update. *Phytother. Res.* **2016**, *30*, 1392–1403. [CrossRef]
7. Sabra, A.; Netticadan, T.; Wijekoon, C. Grape Bioactive Molecules, and the Potential Health Benefits in Reducing the Risk of Heart Diseases. *Food Chem. X* **2021**, *12*, 100149. [CrossRef]
8. Rebello, L.P.G.; Lago-Vanzela, E.S.; Barcia, M.T.; Ramos, A.M.; Stringheta, P.C.; Da-Silva, R.; Castillo-Muñoz, N.; Gómez-Alonso, S.; Hermosín-Gutiérrez, I. Phenolic Composition of the Berry Parts of Hybrid Grape Cultivar BRS Violeta (BRS Rubea × IAC 1398-21) Using HPLC–DAD–ESI-MS/MS. *Food Res. Int.* **2013**, *54*, 354–366. [CrossRef]
9. Li, J.; Zhang, S.; Zhang, M.; Sun, B. Novel Approach for Extraction of Grape Skin Antioxidants by Accelerated Solvent Extraction: Box–Behnken Design Optimization. *J. Food Sci. Technol.* **2019**, *56*, 4879–4890. [CrossRef]
10. Brazinha, C.; Cadima, M.; Crespo, J.G. Optimization of Extraction of Bioactive Compounds from Different Types of Grape Pomace Produced at Wineries and Distilleries. *J. Food Sci.* **2014**, *79*, E1142–E1149. [CrossRef]
11. Caldas, T.W.; Mazza, K.E.L.; Teles, A.S.C.; Mattos, G.N.; Brígida, A.I.S.; Conte-Junior, C.A.; Borguini, R.G.; Godoy, R.L.O.; Cabral, L.M.C.; Tonon, R.V. Phenolic Compounds Recovery from Grape Skin Using Conventional and Non-Conventional Extraction Methods. *Ind. Crops Prod.* **2018**, *111*, 86–91. [CrossRef]
12. Rockenbach, I.I.; Gonzaga, L.V.; Rizelio, V.M.; de Souza Schmidt Gonçalves, A.E.; Genovese, M.I.; Fett, R. Phenolic Compounds and Antioxidant Activity of Seed and Skin Extracts of Red Grape (Vitis Vinifera and Vitis Labrusca) Pomace from Brazilian Winemaking. *Food Res. Int.* **2011**, *44*, 897–901. [CrossRef]
13. Kumar, M.; Barbhai, M.D.; Hasan, M.; Punia, S.; Dhumal, S.; Radha; Rais, N.; Chandran, D.; Pandiselvam, R.; Kothakota, A.; et al. Onion (*Allium cepa* L.) Peels: A Review on Bioactive Compounds and Biomedical Activities. *Biomed. Pharmacother.* **2022**, *146*, 112498. [CrossRef]
14. Giusti, M.M.; Wrolstad, R.E. Acylated Anthocyanins from Edible Sources and Their Applications in Food Systems. *Biochem. Eng. J.* **2003**, *14*, 217–225. [CrossRef]
15. Georgiev, V.; Ananga, A.; Tsolova, V. Recent Advances and Uses of Grape Flavonoids as Nutraceuticals. *Nutrients* **2014**, *6*, 391–415. [CrossRef]
16. Gouot, J.C.; Smith, J.P.; Holzapfel, B.P.; Walker, A.R.; Barril, C. Grape Berry Flavonoids: A Review of Their Biochemical Responses to High and Extreme High Temperatures. *J. Exp. Bot.* **2019**, *70*, 397–423. [CrossRef]

17. Putta, S.; Yarla, N.S.; Peluso, I.; Tiwari, D.K.; Reddy, G.V.; Giri, P.V.; Kumar, N.; Malla, R.; Rachel, V.; Bramhachari, P.V.; et al. Anthocyanins: Multi-Target Agents for Prevention and Therapy of Chronic Diseases. *Curr. Pharm. Des.* **2017**, *23*, 6321–6346. [CrossRef]
18. Ren, K.-W.; Li, Y.-H.; Wu, G.; Ren, J.-Z.; Lu, H.-B.; Li, Z.-M.; Han, X.-W. Quercetin Nanoparticles Display Antitumor Activity via Proliferation Inhibition and Apoptosis Induction in Liver Cancer Cells. *Int. J. Oncol.* **2017**, *50*, 1299–1311. [CrossRef]
19. Rasines-Perea, Z.; Teissedre, P.-L. Grape Polyphenols' Effects in Human Cardiovascular Diseases and Diabetes. *Molecules* **2017**, *22*, 68. [CrossRef]
20. Costa, E.; Cosme, F.; Jordão, A.M.; Mendes-Faia, A. Anthocyanin Profile and Antioxidant Activity from 24 Grape Varieties Cultivated in Two Portuguese Wine Regions. *OENO One* **2014**, *48*, 51–62. [CrossRef]
21. Samota, M.K.; Sharma, M.; Kaur, K.; Sarita; Yadav, D.K.; Pandey, A.K.; Tak, Y.; Rawat, M.; Thakur, J.; Rani, H. Onion Anthocyanins: Extraction, Stability, Bioavailability, Dietary Effect, and Health Implications. *Front. Nutr.* **2022**, *9*, 917617. [CrossRef]
22. Kumar, N.; Goel, N. Phenolic Acids: Natural Versatile Molecules with Promising Therapeutic Applications. *Biotechnol. Rep.* **2019**, *24*, e00370. [CrossRef]
23. Sun, B.; de Sá, M.; Leandro, C.; Caldeira, I.; Duarte, F.L.; Spranger, I. Reactivity of Polymeric Proanthocyanidins toward Salivary Proteins and Their Contribution to Young Red Wine Astringency. *J. Agric. Food Chem.* **2013**, *61*, 939–946. [CrossRef] [PubMed]
24. Kyraleou, M.; Kallithraka, S.; Theodorou, N.; Teissedre, P.-L.; Kotseridis, Y.; Koundouras, S. Changes in Tannin Composition of Syrah Grape Skins and Seeds during Fruit Ripening under Contrasting Water Conditions. *Molecules* **2017**, *22*, 1453. [CrossRef] [PubMed]
25. Machado, A.P.D.F.; Pasquel-Reátegui, J.L.; Barbero, G.F.; Martínez, J. Pressurized Liquid Extraction of Bioactive Compounds from Blackberry (*Rubus Fruticosus* L.) Residues: A Comparison with Conventional Methods. *Food Res. Int.* **2015**, *77*, 675–683. [CrossRef]
26. Martiny, T.R.; Raghavan, V.; de Moraes, C.C.; da Rosa, G.S.; Dotto, G.L. Optimization of Green Extraction for the Recovery of Bioactive Compounds from Brazilian Olive Crops and Evaluation of Its Potential as a Natural Preservative. *J. Environ. Chem. Eng.* **2021**, *9*, 105130. [CrossRef]
27. da Silva Meirelles, L.; Fontes, A.M.; Covas, D.T.; Caplan, A.I. Mechanisms Involved in the Therapeutic Properties of Mesenchymal Stem Cells. *Cytokine Growth Factor Rev.* **2009**, *20*, 419–427. [CrossRef]
28. Mei, Z.; Zhang, R.; Zhao, Z.; Zheng, G.; Xu, X.; Yang, D. Extraction Process and Method Validation for Bioactive Compounds from Citrus Reticulata Cv. Chachiensis: Application of Response Surface Methodology and HPLC–DAD. *Acta Chromatogr.* **2020**, *33*, 270–280. [CrossRef]
29. Weremfo, A.; Abassah-Oppong, S.; Adulley, F.; Dabie, K.; Seidu-Larry, S. Response Surface Methodology as a Tool to Optimize the Extraction of Bioactive Compounds from Plant Sources. *J. Sci. Food Agric.* **2022**, *103*, 26–36. [CrossRef]
30. Turturică, M.; Stănciuc, N.; Bahrim, G.; Râpeanu, G. Effect of Thermal Treatment on Phenolic Compounds from Plum (Prunus Domestica) Extracts—A Kinetic Study. *J. Food Eng.* **2016**, *171*, 200–207. [CrossRef]
31. Dewanto, V.; Wu, X.; Adom, K.K.; Liu, R.H. Thermal Processing Enhances the Nutritional Value of Tomatoes by Increasing Total Antioxidant Activity. *J. Agric. Food Chem.* **2002**, *50*, 3010–3014. [CrossRef]
32. Castro-Vargas, H.I.; Rodríguez-Varela, L.I.; Ferreira, S.R.S.; Parada-Alfonso, F. Extraction of Phenolic Fraction from Guava Seeds (*Psidium guajava* L.) Using Supercritical Carbon Dioxide and Co-Solvents. *J. Supercrit. Fluids* **2010**, *51*, 319–324. [CrossRef]
33. Anderson, M.J.; Whitcomb, P.J. *RSM Simplified: Optimizing Processes Using Response Surface Methods for Design of Experiments*, 2nd ed.; Productivity Press: London, UK, 2016.
34. Khazaei, K.M.; Jafari, S.M.; Ghorbani, M.; Kakhki, A.H.; Sarfarazi, M. Optimization of Anthocyanin Extraction from Saffron Petals with Response Surface Methodology. *Food Anal. Methods* **2016**, *9*, 1993–2001. [CrossRef]
35. de Andrade, R.B.; Machado, B.A.S.; de Abreu Barreto, G.; Nascimento, R.Q.; Corrêa, L.C.; Leal, I.L.; Tavares, P.P.L.G.; Ferreira, E.d.S.; Umsza-Guez, M.A. Syrah Grape Skin Residues Has Potential as Source of Antioxidant and Anti-Microbial Bioactive Compounds. *Biology* **2021**, *10*, 1262. [CrossRef]
36. Yammine, S. Extraction of High-Value Added Compounds by Subcritical Water and Fractionation by Membrane Processes: Valorization of Vine and Wine by-Products by Eco-Innovative Processes. Ph.D. Thesis, Université de Bordeaux, Bordeaux, France, 2016.
37. Arozarena, I.; Casp, A.; Marín, R.; Navarro, M. Multivariate Differentiation of Spanish Red Wines According to Region and Variety. *J. Sci. Food Agric.* **2000**, *80*, 1909–1917. [CrossRef]
38. Katalinić, V.; Možina, S.S.; Skroza, D.; Generalić, I.; Abramovič, H.; Miloš, M.; Ljubenkov, I.; Piskernik, S.; Pezo, I.; Terpinc, P.; et al. Polyphenolic Profile, Antioxidant Properties and Antimicrobial Activity of Grape Skin Extracts of 14 Vitis Vinifera Varieties Grown in Dalmatia (Croatia). *Food Chem.* **2010**, *119*, 715–723. [CrossRef]
39. Negro, C.; Tommasi, L.; Miceli, A. Phenolic Compounds and Antioxidant Activity from Red Grape Marc Extracts. *Bioresour. Technol.* **2003**, *87*, 41–44. [CrossRef]
40. Poudel, P.R.; Tamura, H.; Kataoka, I.; Mochioka, R. Phenolic Compounds and Antioxidant Activities of Skins and Seeds of Five Wild Grapes and Two Hybrids Native to Japan. *J. Food Compos. Anal.* **2008**, *21*, 622–625. [CrossRef]
41. Tournour, H.H.; Segundo, M.A.; Magalhães, L.M.; Barreiros, L.; Queiroz, J.; Cunha, L.M. Valorization of Grape Pomace: Extraction of Bioactive Phenolics with Antioxidant Properties. *Ind. Crops Prod.* **2015**, *74*, 397–406. [CrossRef]
42. Constantin, O.; Skrt, M.; Ulrih, N.; Rapeanu, G. Anthocyanins Profile, Total Phenolics and Antioxidant Activity of Two Romanian Red Grape Varieties: Feteasca Neagra and Babeasca Neagra (Vitis Vinifera). *Chem. Pap.* **2015**, *69*, 1573–1581. [CrossRef]

43. Kupe, M.; Karatas, N.; Unal, M.S.; Ercisli, S.; Baron, M.; Sochor, J. Phenolic Composition and Antioxidant Activity of Peel, Pulp and Seed Extracts of Different Clones of the Turkish Grape Cultivar 'Karaerik. ' *Plants* **2021**, *10*, 2154. [CrossRef] [PubMed]
44. De, B.; Bhandari, K.; Katakam, P.; Goswami, T.K. Development of a Standardized Combined Plant Extract Containing Nutraceutical Formulation Ameliorating Metabolic Syndrome Components. *SN Appl. Sci.* **2019**, *1*, 1484. [CrossRef]

Disclaimer/Publisher's Note: The statements, opinions and data contained in all publications are solely those of the individual author(s) and contributor(s) and not of MDPI and/or the editor(s). MDPI and/or the editor(s) disclaim responsibility for any injury to people or property resulting from any ideas, methods, instructions or products referred to in the content.

inventions

Article

Machine Learning Systems Detecting Illicit Drugs Based on Their ATR-FTIR Spectra

Iulia-Florentina Darie [1,2], Stefan Razvan Anton [3] and Mirela Praisler [4,*]

[1] Department of Mathematics and Computer Sciences, "Dunarea de Jos" University of Galati, 47 Domneasca Street, 800008 Galati, Romania
[2] "Paul Dimo" High School, Str. 1 Decembrie 1918 nr. 27, 800566 Galati, Romania
[3] Center for Research and Training in Innovative Techniques of Applied Mathematics in Engineering, Polytechnic University of Bucharest, 060042 Bucharest, Romania
[4] Department of Chemistry, Physics and Environment, "Dunarea de Jos" University of Galati, 47 Domneasca Street, 800008 Galati, Romania
* Correspondence: mirela.praisler@ugal.ro

Abstract: We present a comparative study aiming to determine the most efficient multivariate model screening for the main drugs of abuse based on their ATR-FTIR spectra. A preliminary statistical analysis of selected spectra data extracted from the public SWGDRUG IR Library was first performed. The results corroborated those of an exploratory analysis that was based on several dimensionality reduction methods, i.e., Principal Component Analysis (PCA), Independent Component Analysis (ICA), and autoencoders. Then, several machine learning methods, i.e., Support Vector Machines (SVM), eXtreme Gradient Boosting (XGB), Random Forest, Gradient Boosting, and K-Nearest Neighbors (KNN), were used to assign the drug class membership. In order to account for the stochastic nature of these machine learning methods, both models were evaluated 10 times on a randomly distributed subset of the whole SWGDRUG IR Library, and the results were compared in detail. Finally, their performance in assigning the class identity of three classes of drugs of abuse, i.e., hallucinogenic (2C-x, DOx, and NBOMe) amphetamines, cannabinoids, and opioids, were compared based on confusion matrices and various classification parameters, such as balanced accuracy, sensitivity, and specificity. The advantages of each of the illicit drug-detecting systems and their potential as forensic screening tools used in field scenarios are also discussed.

Keywords: amphetamines; cannabinoids; opioids; ATR-FTIR spectra; PCA; ICA; autoencoders; SVM; XGB; random forest; gradient boosting; K-Nearest Neighbors (KNN)

Citation: Darie, I.-F.; Anton, S.R.; Praisler, M. Machine Learning Systems Detecting Illicit Drugs Based on Their ATR-FTIR Spectra. *Inventions* **2023**, *8*, 56. https://doi.org/10.3390/inventions8020056

Academic Editor: Cristian Manzoni

Received: 7 December 2022
Revised: 6 February 2023
Accepted: 6 March 2023
Published: 13 March 2023

Copyright: © 2023 by the authors. Licensee MDPI, Basel, Switzerland. This article is an open access article distributed under the terms and conditions of the Creative Commons Attribution (CC BY) license (https://creativecommons.org/licenses/by/4.0/).

1. Introduction

Amphetamines are a class of psychotropic compounds that became popular in recent decades for their stimulant, euphoric, and hallucinogenic effects. In recent decades, many such new psychotropic substances have emerged in the black market [1]. Among these, three important groups of hallucinogenic amphetamines have been noticed in recent years, i.e., 2C-x, DOx, and NBOMe amphetamines.

The 2C-x class of drugs owes its name to Alexander Shulgin and refers to the two carbon atoms that bind the amino group to the benzene ring [2]. The compounds included in the DOx class of hallucinogenic amphetamines are characterized by the presence of methoxy groups in the phenyl ring at the 2 and 5 positions, and a substituent at the 4-position of the phenyl ring [3]. The NBOMe amphetamines, which are analogs of the 2C-x drugs, emerged in the early 2000s when they were first synthesized [4,5].

Cannabinoids are a class of drugs similar in structure to the chemical compounds found in the natural products of *Cannabis sativa*. With the accessibility of cannabinoids expanding, especially of synthetic ones, public concern about these compounds is rising [6].

Opioids represent a class of drugs of abuse with important effects for the treatment of pain, used in a medical but also in an illicit scope [7,8].

Such illicit drugs constantly emerging in the black market represent a current problem of our days. From this point of view, it is important to develop models which can be able to automatically detect the class membership of these new compounds.

2. Related Work

Machine learning and statistical methods have been successfully applied to detect various types of drugs. Pereira et al. [9] applied PCA followed by PLS-DA (Partial Least Squares Discriminant Analysis) and ATR-FTIR spectra to identify the presence of different illegal drugs in seized ecstasy tablets. In a recent study [10], Koshute et al. developed a machine-learning model based on various techniques, such as random forests, neural networks, or logistic regression, in order to identify fentanyl analogs based on mass spectra. Lee et al. [11] developed machine learning models applied to LC-MS-MS (High-Resolution Liquid Chromatography Mass Spectrometry) in order to identify unknown controlled substances and new psychoactive substances (NPS). For this purpose, Artificial Neural Networks (ANN), Support Vector Machine (SVM), and K-Nearest Neighbors (KNN) models were developed for the classification of 13 subgroups, including the 2C series, opiates, and classical cannabinoids. Wong et al. [12] analyzed the detection of some novel psychoactive substances based on Gas Chromatography–Mass Spectrometry (GC-MS). In this scope, three machine learning models were applied, namely ANN, Convolutional Neural Networks (CNN) and Balanced Random Forest (BRF).

The aim of our study is to develop a machine learning system that can be used for the detection of various drugs of abuse, namely 2C-x, DOx, and NBOMe amphetamines, opioids, and cannabinoids, based on their ATR-FTIR (Attenuated Total Reflectance–Fourier-Transform Infrared Spectroscopy) spectra.

3. Materials and Methods

3.1. Dataset Preparation

Attenuated Total Reflectance–Fourier Transform Infrared (ATR-FTIR) spectrometers are increasingly used for in-field screening for illicit drugs, as they are portable instruments and do not require sample preparation [13]. The ATR-FTIR spectra used in this study were extracted from the SWGDRUG public spectral library [14]. They consist of 95 spectra of the targeted illicit drugs and of randomly selected negatives of forensic interest, as shown in Table 1. In order to perform statistical analysis, the spectra were divided into four classes: Class 1—amphetamines (including 2C-x, DOx, and NBOMe hallucinogens); Class 2—opioids; Class 3—cannabinoids; and Class 4—negatives. The class of amphetamines contains the spectra of 25 substances, the class of opioids includes the spectra of 36 compounds, the class of cannabinoids consists of the spectra of 18 substances, and the class of negatives was formed with the spectra of 16 different (randomly selected) compounds. The statistical analysis, autoencoders, and machine learning modeling were performed by using the Python packages numpy 1.24.1, scipy 1.10.0, scikit-learn 1.2.1, and sequitur 1.2.4.

3.2. Exploratory Data Analysis

In order to identify patterns and anomalies, an exploratory investigation based on statistics and graphical representations was first performed on the dataset. Two types of exploratory data analysis methods were used, i.e., statistical and dimensionality-reduction methods.

3.2.1. Statistical Measures

To gain a better understanding of the trends in our dataset, we used a series of statistical parameters. The mean was used to assess the central tendency of the data, while the standard deviation was used to measure the amount of dispersion of the data. A low value of the standard deviation indicates that the data values tend to be close to the true value of the set, and a higher value indicates that the data values are spread out on a larger interval.

Table 1. Compounds included in the database.

Nr. crt.	Amphetamines	Opioids	Cannabinoids	Negatives
1	2C-B HCl	4′-Methyl acetyl fentanyl HCl	JWH-018 N-(5-chloropentyl) analog	4-Acetoxy-N,N-Dimethyltryptamine oxalate
2	2C-C HCl	para-Methyl acetyl fentanyl HCl	JWH-203	Cocaine base
3	2C-E HCl	Benzylfentanyl HCl	JWH-250	Sertraline HCl
4	2C-T-7 HCl	Acryl fentanyl HCl	JWH-122	Trenbolone Hexahydro benzylcarbonate
5	2C-T-2 HCl	2-Furanylbenzyl fentanyl	JWH-018 adamantyl-carboxamide	4-estren-3beta, 17beta-diol
6	2C-I HCl	2R,4S-2-Methyl fentanyl HCl	JWH-018	Butalbital
7	2,5-Dimethoxy-4-Chloro-amphetamine HCl	Despropionyl para-fluorofentanyl	JWH-307	Boldenone Acetate
8	2,5-Dimethoxy phenethylamine HCl	Despropionyl ortho-fluorofentanyl	JWH-081	Cocaine HCl
9	3,4-Dimethoxy amphetamine HCl	cis-3-Methyl fentanyl HCl	JWH-022	Safrole
10	2,5-Dimethoxyamphetamine HCl	Norfentanyl	JWH-210	Phenazepam
11	DOI HCl	trans-3-Methyl fentanyl HCl	JWH-019	Methenolone
12	d,l-4-Bromo-2,5-dimethoxyamphetamine HCl	para-Methoxy fentanyl HCl	JWH-073	Methaqualone base
13	4-Chloro-2,5-dimethoxyamphetamine HCl (DOC)	para-Chloroisobutyryl fentanyl HCl	JWH-018 Benzimidazole	MBZP HCl
14	25B-NBOMe HCl	ortho-Methylacetyl fentanyl HCl	FUB-JWH-018	Diazepam
15	25C-NBOMe HCl	Heptanoyl fentanyl HCl	JWH-249	Etaqualone HCl
16	25I-NBOMe Base	beta-Hydroxy fentanyl HCl	JWH-018 indazole	Oxazepam
17	25E-NBOMe HCl	3-Methyl butyryl fentanyl HCl	AB-FUBICA	
18	25D-NBOMe HCl	beta′-Phenyl fentanyl	ADB-PINACA	
19	25H-NBOMe HCl	ortho-Fluoroisobutyryl fentanyl HCl		
20	25N-NBOMe HCl	para-Fluoroacetyl fentanyl HCl		
21	25C-NB3OMe HCl	meta-Fluoroisobutyryl fentanyl HCl		
22	25C-NB4OMe HCl	Tetrahydrofuran fentanyl 3-tetrahydrofurancarboxamide HCl		
23	25I-NBOMe HCl	para-Methyl cyclopropyl fentanyl HCl		
24	25I-NB3OMe HCl	para-Methoxy furanyl fentanyl HCl		
25	25I-NB4OMe HCl	ortho-Methyl cyclopropyl fentanyl HCl		

Table 1. *Cont.*

Nr. crt.	Amphetamines	Opioids	Cannabinoids	Negatives
26		ortho-Fluoro furanyl fentanyl HCl		
27		N-benzyl para-fluoro norfentanyl HCl		
28		N-Benzyl para-fluoro cyclopropyl norfentanyl HCl		
29		Despropionyl meta-Fluorofentanyl		
30		para-Fluoro fentanyl HCl		
31		ortho-Methoxy furanyl fentanyl		
32		Heroin Hydrochloride Monohydrate		
33		W-18		
34		W-15		
35		06-Monoacetyl morphine HCl		
36		Morphine HCl trihydrate		

The skewness considers the extremes of the dataset. A distribution is considered symmetrical if the skewness is between −0.5 and 0.5, moderately skewed if the skewness is between −1 and −0.5 or 0.5 and 1, and highly skewed if the skewness is less than −1 or greater than 1. In his paper on series analysis, Grigoletto [15] argued that the more skewed the data, either positive or negative, the less accurate the analysis is.

Excess kurtosis indicates how much the dataset resembles a normal distribution. This parameter has been successfully used by Loperfido [16] for outlier detection. Distributions similar to the normal distribution are called mesokurtic; those with positive excess kurtosis are referred to as leptokurtic, while distributions with negative excess kurtosis are called platykurtic [17]. Minimum and maximum values were also calculated to account for the peaks of the spectra.

3.2.2. Principal Component Analysis (PCA)

PCA is a multivariate technique [18] that accomplishes dimensionality reduction by linearly transforming the data into a new coordinate system, where the variation in the data can be described with a set of new orthogonal variables, called principal components (PCs). Its advantage is the ability to plot combinations of PC scores in order to identify clusters of closely related data points. PCA was also used as an exploratory analysis method, in order to evaluate to what extent the chosen classes form well-defined clusters.

3.2.3. Independent Component Analysis (ICA)

ICA is a technique often used in signal processing and presumes to separate a multivariate signal into additive subcomponents by making the hypothesis that one subcomponent is Gaussian and all other subcomponents are statistically independent of each other [19]. ICA can also be used for signals that are not generated by mixing, such as our case, where we consider each ATR-FTIR spectrum as a complex multivariate signal. This technique also uses graphical tools to plot combinations of components to identify clusters of similar objects (compounds in our case).

Similarly to PCA, ICA was used as an exploratory method. Even if PCA and ICA have the same role, they differentiate one from another. An important difference is that PCA is focused on dimension reduction, while ICA concentrates on separating information into independent components [20].

3.2.4. Autoencoders

Autoencoders represent a subset of ANN used to obtain efficient representations of data. The algorithm extracts several features and then attempts to recreate the original input from these features [21]. The autoencoder is defined by two functions, i.e., the encoder function and the decoder function. The first step in using these networks is to train both the encoder and the decoder at the same time through gradient descent. The second step consists of removing the decoder part of the model, leaving only the encoder. Thus, the output of a model consists of the key features of the input. Those features can be used in the same way as with PCA or ICA for a two-dimensional representation of spectra. In our paper, we used a linear autoencoder trained on the whole dataset with an encoding dimension of 10. For the graphical representation, we chose the best features for cluster formation.

3.3. Machine Learning Methods (MLM)

Multiclass classification of the analyzed spectra was then performed with five machine learning models, i.e., SVM [22], eXtreme Gradient Boosting (XGB) [23], Random Forest [24], Gradient Boosting [25], and KNN [26]. These models were chosen due to their efficiency, simplicity, and their fast implementation. Such models have been successfully used to classify counterfeit drugs based on their infrared spectra [27].

For all the models, the dataset was randomly split into two partitions, summing up 60% of all spectra for training and 40% for testing. Each model was then trained on the training set and evaluated on the testing set. The model, training, and test datasets were then deleted. We define this process as a training session. Although the initial dataset for each session was the same, the training and testing sets were different at each iteration, because the entries were randomly selected each time. In other words, the models were trained and evaluated each time on different selections of the same dataset. Each training session was repeated 10 times. Furthermore, the hyperparameter selection was performed using the Optuna 3.1.0 hyperparameter optimization framework.

The following parameters were calculated in order to assess and compare the performances of the models:

$$\text{Sensitivity}(\text{TPR}) = \frac{\text{TP}}{\text{TP} + \text{FN}} \tag{1}$$

$$\text{Specificity}(\text{TNR}) = \frac{\text{TN}}{\text{TN} + \text{FP}} \tag{2}$$

$$\text{Balanced accuracy}(\text{TNR}) = \frac{\text{TPR} + \text{TNR}}{2} \tag{3}$$

$$\text{Matthews correlation coefficient} = \frac{\text{TP} \times \text{TN} - \text{FP} \times \text{FN}}{\sqrt{(\text{TP} + \text{FP})(\text{TP} + \text{FN})(\text{TN} + \text{FP})(\text{TN} + \text{FN})}} \tag{4}$$

where TP is the number of true positives, TN is the number of true negatives, FP is the number of false positives, and FN is the number of false negatives.

4. Results and Discussions

4.1. Exploratory Data Analysis

4.1.1. Statistical Measures

The purpose of the statistical analysis was to better understand the relationship between the three classes of drugs of abuse and the class of negatives. First, the mean ATR-FTIR spectrum was calculated for each class for the qualitative assessment of the data. The results, illustrated in Figure 1, indicate that all the targeted classes have the main peak near 2800 cm^{-1}. The strongest peak characterizes the amphetamines, followed by the cannabinoids, opioids, and negatives. Although the peak at 2800 cm^{-1} of opioids and negatives have nearly the same intensity, their mean spectra can be easily differentiated because the opioids have a second relatively strong peak at 2400 cm^{-1}.

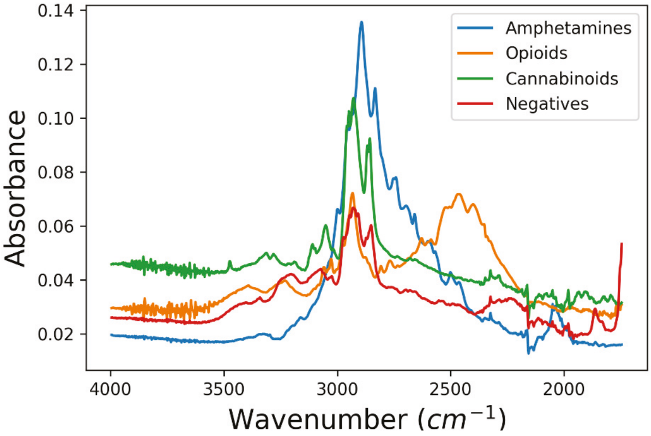

Figure 1. Mean ATR-FTIR spectrum calculated for the amphetamines (blue), opioids (orange), cannabinoids (green), and negatives (red) included in the database.

The statistical parameters calculated for the mean spectra are presented in Table 2. In terms of the central tendency of the spectra, the mean values vary only between 0.0338 and 0.0452. The data dispersion shows that the class of amphetamines stands out with a standard deviation of 0.0263, almost double of the next one, determined for the class of cannabinoids. The relatively large standard deviation of the class of amphetamines indicates that the spectra of these compounds are less similar than those included in the other classes. This is probably due to the fact that the class of hallucinogenic amphetamines is formed by three subclasses of compounds, i.e., 2C-x, DOx, and NBOMe amphetamines.

Table 2. Statistical parameters calculated based on the mean ATR-FTIR spectra of the targeted classes of compounds, between 1500 and 4000 cm^{-1}, with a resolution of 1.92 cm^{-1}.

	Amphetamines	**Opioids**	**Cannabinoids**	**Negatives**
Mean	0.0338	0.0393	0.0452	0.0341
Standard Deviation	0.0263	0.0126	0.0128	0.0105
Skewness	1.877	1.261	2.567	0.7721
Excess Kurtosis	2.760	1.276	8.098	0.2311
Minimum	0.0126	0.0254	0.0258	0.0186
Maximum	0.135	0.0744	0.1072	0.0678

The skewness of the spectra of each class indicates that none ranges between −0.5 and 0.5, so none of the analyzed classes of compounds has a symmetrical distribution. The class of negatives is a moderately skewed dataset, as its skewness ranges between 0.5 and 1. The sets formed by the spectra of the three modeled classes of positives have skewness values larger than 1, so they are highly skewed.

The distributions of the spectra of the three classes of positives are leptokurtic, as they have large excess kurtosis. The largest excess kurtosis is recorded for the cannabinoids. The negatives have a mesokurtic distribution. The excess kurtosis of this group being very small (close to zero), their distribution may be considered practically normal. The results obtained for the negatives are consistent with the fact that it contains the highest diversity of substances, with the rest of the classes consisting of substances with very similar molecular structures and hence very similar ATR-FTIR spectra.

4.1.2. Principal Component Analysis

A two-component PCA was then performed as a preliminary exploratory analysis. Figure 2 displays the score plot obtained for the first two PCs, which indicates that the amphetamines form the most compact cluster. The points associated with the opioid and cannabinoid compounds are much more spread out. Many of the points associated with the negatives are overlying the clusters formed by the positives, especially the cluster of opioids.

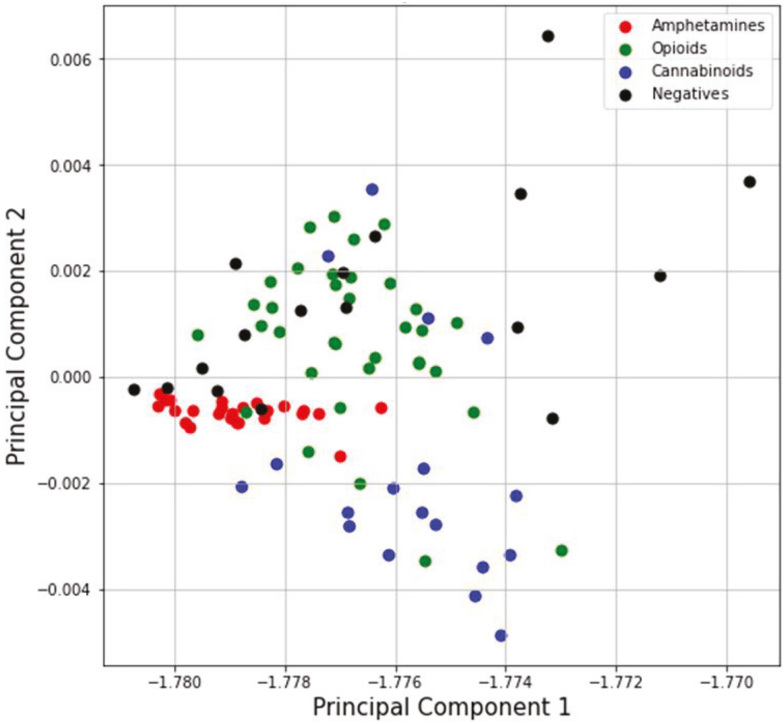

Figure 2. Score plot of the first two principal components of a two-component PCA displaying the class of amphetamines (red), opioids (green), cannabinoids (blue), and negatives (black).

4.1.3. Independent Component Analysis

The score plot obtained with a three-component ICA is displayed in Figure 3. It indicates that ICA leads to better clustering, especially for the class of amphetamines. The opioids and the cannabinoids also show a better grouping than in the case of PCA. There is practically no improvement in the group of negatives, their associated points being scattered on nearly the whole plot.

4.1.4. Transformers

The results obtained with 10 component transformers are presented in Figure 4. For the class of amphetamines, this method leads to results similar to those obtained with ICA. However, there is an improvement in the other three modeled classes: the opioid and cannabinoid classes are more clearly separated, and the negatives tend to be better discriminated as well.

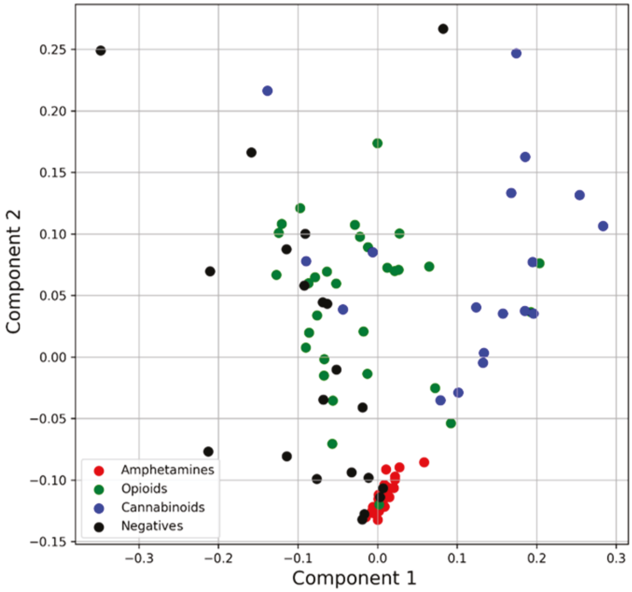

Figure 3. Score plot of the first two components of a three-component ICA displaying the class of amphetamines (red), opioids (green), cannabinoids (blue), and negatives (black).

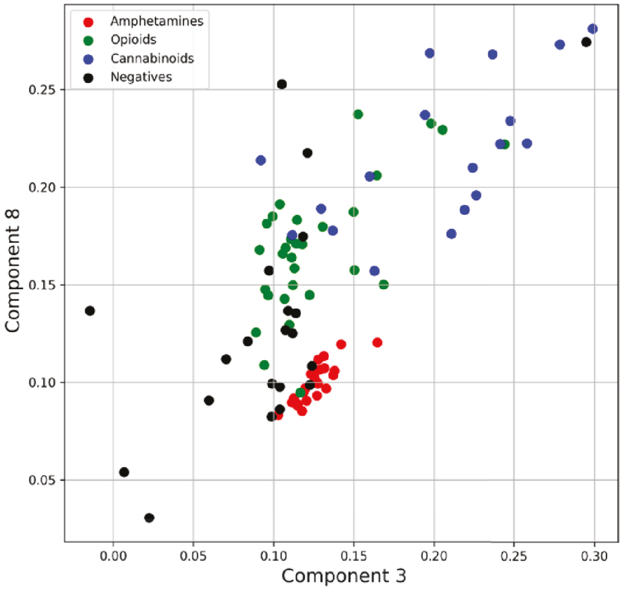

Figure 4. Score plot of the 3rd and 8th components of a ten-component transformed operation displaying the class of amphetamines (red), opioids (green), cannabinoids (blue), and negatives (black).

4.2. Classification Models

SVM, XGB, Random Forest, Gradient Boosting, and KNN were then used for classification purposes. In order to assess the overall performances of the models, as measured based on the average values obtained for 10 runs, it is useful to analyze Table 3 in conjunction with the confusion matrices that were determined for each model, which are displayed in Figures 5–9. Table 3 indicates that the SVM and the XGB models are the most accurate, their accuracy being nearly the same. At the same time, SVM has the highest specificity, while XGB is the most sensitive model, all other models being significantly less specific or sensitive. SVM and XGB have the best (and comparable) Matthews correlation coefficient, while the coefficient determined for the other models is significantly smaller. The value of this coefficient is positive for all the models, which indicates positive correlations in all cases. The SVM and XGB models also have the highest ROC AUC, which has the same value (of 0.91) for both models. The ROC AUC being very high (very close to 1), we may conclude that these two models have a very good prediction rate.

Table 3. Standard performance metrics calculated for the machine learning models.

Model	Balanced Accuracy (%)	Sensitivity (%)	Specificity (%)	Matthews Correlation Coefficient	ROC AUC
SVM	92.08 ± 5.41	87.91 ± 5.16	96.25 ± 4.13	0.86 ± 0.04	0.91
XGBoost	91.99 ± 7.33	95.29 ± 7.59	88.69 ± 6.11	0.81 ± 0.05	0.91
Random forest	81.57 ± 8.66	71.15 ± 7.55	92.00 ± 8.74	0.67 ± 0.09	0.81
Gradient Boosting	76.46 ± 5.86	64.64 ± 4.95	88.28 ± 5.47	0.53 ± 0.05	0.76
K-Nearest Neighbors	66.88 ± 10.20	69.84 ± 10.20	90.64 ± 9.66	0.49 ± 0.12	0.80

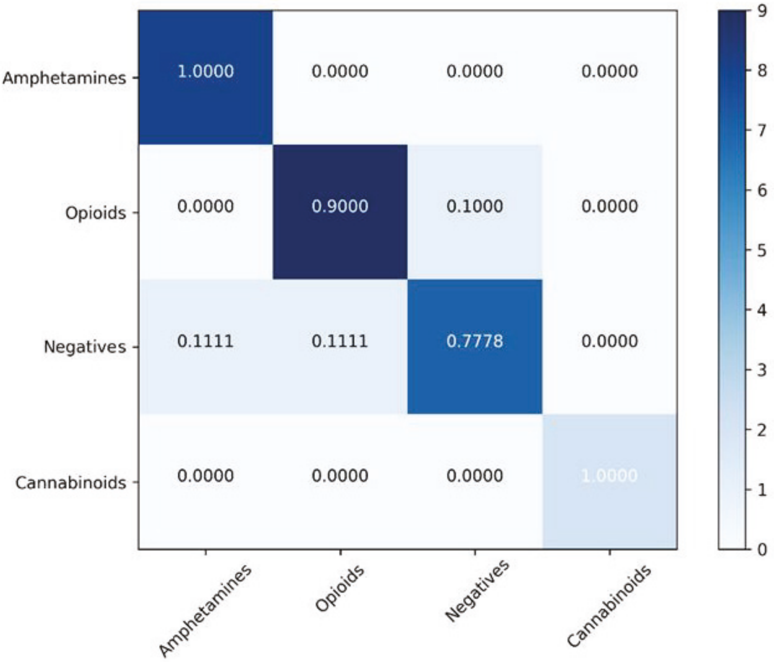

Figure 5. Confusion matrix for the SVM model.

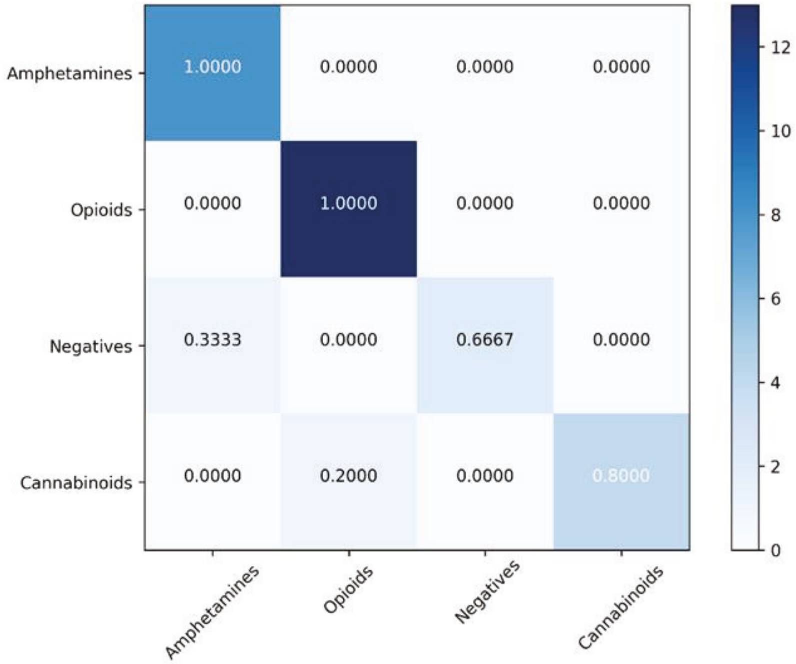

	Amphetamines	Opioids	Negatives	Cannabinoids
Amphetamines	1.0000	0.0000	0.0000	0.0000
Opioids	0.0000	1.0000	0.0000	0.0000
Negatives	0.3333	0.0000	0.6667	0.0000
Cannabinoids	0.0000	0.2000	0.0000	0.8000

Figure 6. Confusion matrix for the XGB model.

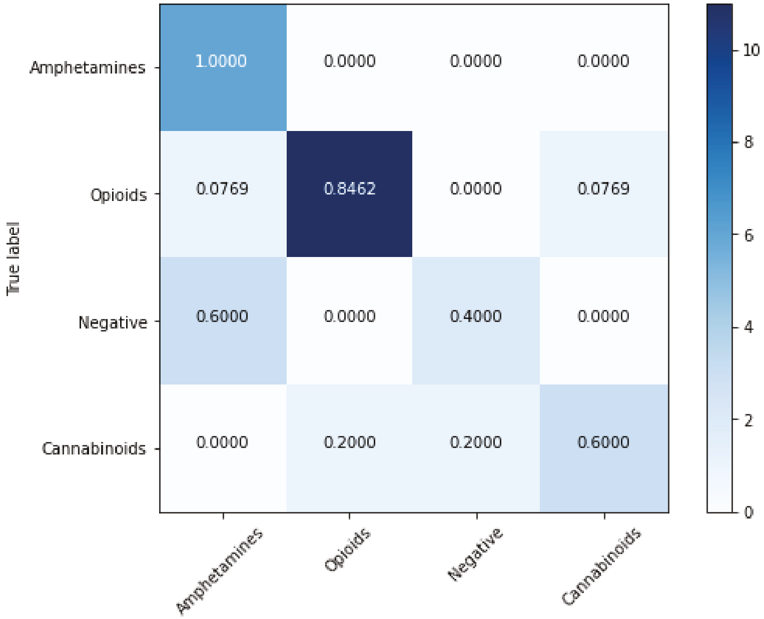

	Amphetamines	Opioids	Negative	Cannabinoids
Amphetamines	1.0000	0.0000	0.0000	0.0000
Opioids	0.0769	0.8462	0.0000	0.0769
Negative	0.6000	0.0000	0.4000	0.0000
Cannabinoids	0.0000	0.2000	0.2000	0.6000

Figure 7. Confusion matrix for the Random Forest model.

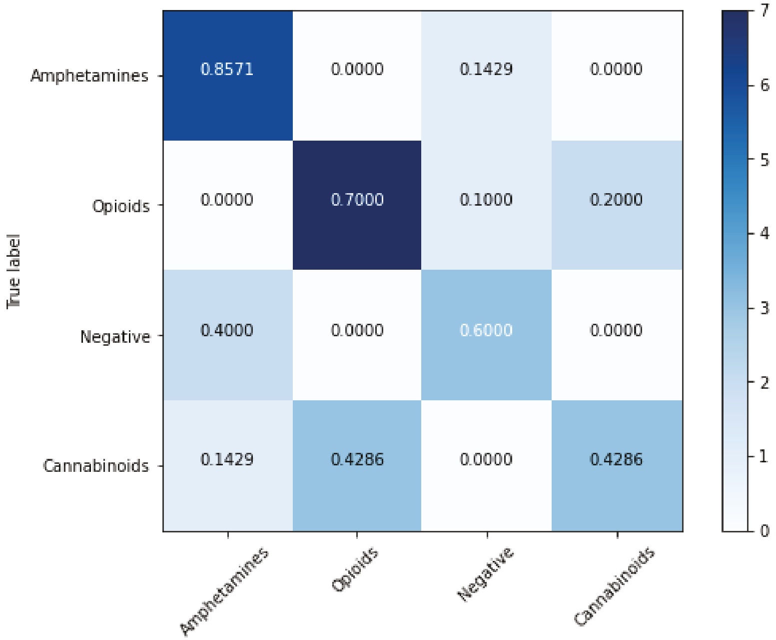

Figure 8. Confusion matrix for the Gradient Boosting model.

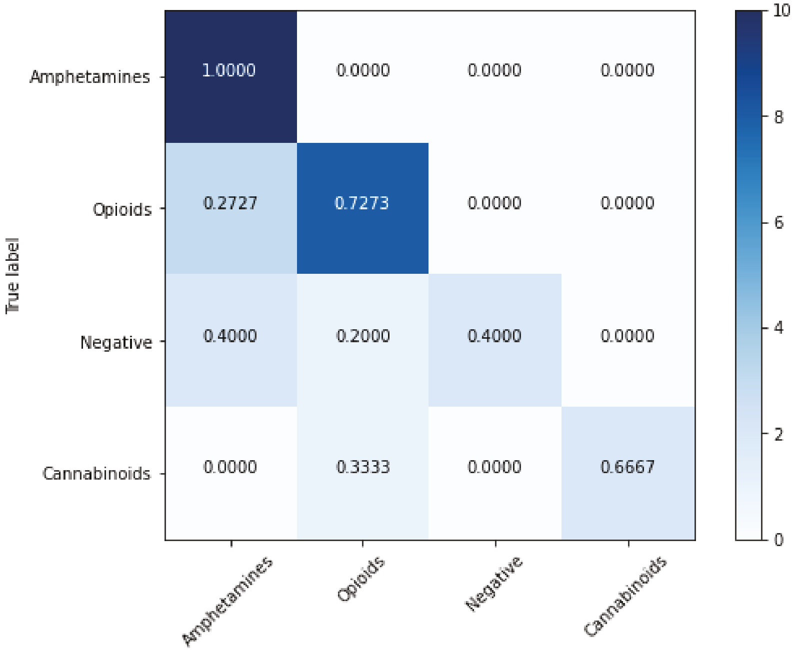

Figure 9. Confusion matrix for the KNN model.

If we take into account that the tested models are tree-based models (XGB, Random Forest, and Gradient Boosting), decision boundary models (SVM), and non-parametric models (KNN), we may conclude that the decision boundary models performed best, followed by the tree-based models and the non-parametric models.

The confusion matrices (Figures 5–9) indicate that, except for the Gradient Boosting model, all the models classify the amphetamines with 100% accuracy. The Gradient Boosting model is not that far behind, with an accuracy of 85.71%. The main difference between the models, regarding the class of amphetamines, is related to the rate of false positives, which is 11.11% for the SVM model, 33.33% for the XGB model, 60% for the Random Forest model, 50.29% for the Gradient Boosting model, and 67.27% for the KNN model. In other words, the classification of amphetamines with the Random Forest, Gradient Boosting, and KNN models is only marginally better than a random guess.

The opioids are 100% correctly classified by the XGB model. The second-best correct classification rate (90%) is recorded for the SVM model, with 10% of the opioids being misclassified as negatives. The other models fail to assign the correct class identity for a significant number of opioids.

The cannabinoids are recognized as such with 100% accuracy only by the SVM model. The second-best model is the XGB model, the rest of the models often failing to distinguish them, especially from the opioids. The other models have significantly lower performances in the case of the cannabinoids as well.

Taking into account both the accuracy and the misclassification rates, the negatives seem to be the hardest to classify correctly for all models, most probably because of the large variety of substances that are forming this class in the dataset.

The availability of screening tools able to screen for illicit substances harmful to humans in a fast and reliable way is essential for public safety. The models presented in this paper can work in harmony with the currently recommended methodology of designer drug detection.

We explored the use of five distinct and highly different multivariate models and discussed their classification performance, next to the interpretation of the confusion matrix for addressing the specifics of each class of substances used in the classification. All the models are more specific than sensitive (see Table 3).

Both SVM and XGB models yielded accuracy results close to other systems previously built for screening for drugs of abuse [28,29]. However, it should be noted that the later systems were built to detect only one (cannabinoids) [28] or two (hallucinogenic amphetamines and cannabinoids [29]) classes of illicit drugs. In our case, the balanced accuracy is calculated for three classes of positives (amphetamines, opioids, and cannabinoids). Hence, the results obtained with SVM and XGB may be considered very good, as both models screen simultaneously for a larger number of classes of drugs of abuse, i.e., (2C-x, DOx, and NBOMe) hallucinogenic amphetamines, cannabinoids, and opioids. Moreover, it is reasonable to expect that their accuracy will increase once more ATR-FTIR spectra of substances belonging to the targeted classes of compounds become available.

From the point of view of overall accuracy, the best-performing model was SVM. As forensic screening systems designed to operate ATR-FTIR field (portable) analytical instruments, the developed models should be able to perform cost-effective, non-destructive, real-time, direct, on-site tests. However, the main objective of these models is to narrow down the number of samples further subjected to in-depth analysis with more sophisticated stationary analytical instruments in the laboratory. Only the samples tested on-site and assigned a positive class identity (hallucinogenic amphetamines, cannabinoids, and opioids) will be analyzed in the laboratory in order to determine their individual identity (not only their class membership).

Hence, the essential feature of such a screening system is its efficiency in detecting positives. In our case, no hallucinogenic amphetamine, cannabinoid, or opioid should be misclassified as a (false) negative. For this reason, XGB is a better fit for the purpose than SVM, as XGB yields no false negatives. While 10% of the opioids are erroneously classified as negatives by SVM, no amphetamine, opioid, or cannabinoid is misclassified as a negative by XGB.

It is true that XGB has a higher rate of misclassified positives than the SVM model. XGB misclassifies 33% of the negatives as amphetamines and 20% of the cannabinoids as opioids, while SVM misclassifies only 11.11% of the negatives as amphetamines and 11.11% as opioids. However, the false positives (false hallucinogenic amphetamines, cannabinoids, and opioids), although also not desirable, are less important. As mentioned before, their individual identity (molecular structure) will be determined during the tests subsequently performed in the laboratory, based on a series of analytical methods that are recommended for each class of drugs of abuse by specialized international agencies such as the United Nations Office on Drugs and Crime [30,31]. In conclusion, SVM performs better than the other tested models, but XGB is a better choice from a forensic point of view.

5. Conclusions

The high classification accuracy of the presented models indicates that artificial intelligence-based strategies represent an important route to follow in the context of automatizing the processing of ATR-FTIR spectra during field operations. The model which performs best under the classification strategy that takes into account only the overall accuracy is SVM. However, as these are forensic tools, the classification strategy should also consider the false negative rate. For this reason, XGB was found to be the best choice, as it has a significantly lower false negative rate, while its overall accuracy is only very slightly lower than that of SVM.

We believe that the screening systems presented in this paper still have an important potential for improvement, especially in terms of distinguishing better between the classes of positives (amphetamines, cannabinoids, and opioids). We aim to continue our work by using strategies such as the following: increasing the number of positives included in the training set; applying the classification algorithms not to their spectra, but to the PCA or ICA scores derived from these spectra [32]; preprocessing the input with a feature weight that enhances the variables having the largest modeling and/or discriminating power [33]; and using as input only the most relevant variables, as selected with techniques such as Genetic Algorithms (GA) [29].

Author Contributions: Conceptualization, I.-F.D., S.R.A. and M.P.; methodology I.-F.D., S.R.A. and M.P.; software, I.-F.D. and S.R.A.; validation, I.-F.D., S.R.A. and M.P.; formal analysis, I.-F.D., S.R.A. and M.P.; investigation, I.-F.D., S.R.A. and M.P.; resources, I.-F.D. and S.R.A.; data curation, I.-F.D.; writing—original draft preparation, I.-F.D., S.R.A. and M.P.; writing—review and editing, I.-F.D., S.R.A. and M.P.; visualization, I.-F.D., S.R.A. and M.P.; supervision, M.P.; project administration, M.P. All authors have read and agreed to the published version of the manuscript.

Funding: This research received no external funding.

Data Availability Statement: The ATR-FTIR spectra used in this study were extracted from the Scientific Working Group for the Analysis of Seized Drugs (SWGDRUG) public spectral library (www.swgdrug.org).

Acknowledgments: The authors appreciate the "Wiley Online Library" and the forensic spectral data science platform SWGDRUG, important and useful tools used to develop the system architectures presented in this paper.

Conflicts of Interest: The authors declare no conflict of interest.

References

1. Carvalho, M.; Carmo, H.; Costa, V.M.; Capela, J.P.; Pontes, H.; Remião, F.; Carvalho, F.; Bastos, M.d.L. Toxicity of amphetamines: An update. *Arch. Toxicol.* **2012**, *86*, 1167–1231. [CrossRef]
2. Dean, B.V.; Stellpflug, S.J.; Burnett, A.M.; Engebretsen, K.M. 2C or not 2C: Phenethylamine designer drug review. *J. Med. Toxicol.* **2013**, *9*, 172–178. [CrossRef] [PubMed]
3. Trachsel, D.; Lehmann, D.; Enzensperger, C. *Phenethylamine: Von der Struktur zur Funktion*; Nachtschatten-Verlag: Solothurn, Switzerland, 2013.

4. Herrmann, E.S.; Johnson, P.S.; Johnson, M.W.; Vandrey, R. Novel drugs of abuse: Cannabinoids, stimulants, and hallucinogens. In *Neuropathology of Drug Addictions and Substance Misuse*; Elsevier: Amsterdam, The Netherlands, 2016; pp. 893–902.
5. Zawilska, J.B.; Kacela, M.; Adamowicz, P. NBOMes–highly potent and toxic alternatives of LSD. *Front. Neurosci.* **2020**, *14*, 78. [CrossRef] [PubMed]
6. Shi, V.Y.J.; Hsiao, M.; Loves, I.; Hamsavi, A. *Comprehensive Guide to Hidradenitis Suppurativa*; Elsevier: Amsterdam, The Netherlands, 2021; pp. 273–282.
7. Kerrigan, S.; Goldberger, B.A. Opioids. In *Principles of Forensic Toxicology*; Springer: Berlin/Heidelberg, Germany, 2020; pp. 347–369.
8. Zöllner, C.; Stein, C. Opioids. In *Analgesia. Handbook of Experimental Pharmacology*; Stein, C., Ed.; Springer: Berlin/Heidelberg, Germany, 2006; pp. 31–63.
9. Pereira, L.S.; Lisboa, F.L.; Neto, J.C.; Valladão, F.N.; Sena, M.M. Screening method for rapid classification of psychoactive substances in illicit tablets using mid infrared spectroscopy and PLS-DA. *Forensic Sci. Int.* **2018**, *288*, 227–235. [CrossRef] [PubMed]
10. Koshute, P.; Hagan, N.; Jameson, N.J. Machine learning model for detecting fentanyl analogs from mass spectra. *Forensic Chem.* **2022**, *27*, 100379. [CrossRef]
11. Lee, S.Y.; Lee, S.T.; Suh, S.; Ko, B.J.; Oh, H.B. Revealing unknown controlled substances and new psychoactive substances using high-resolution LC–MS-MS machine learning models and the hybrid similarity search algorithm. *J. Anal. Toxicol.* **2022**, *46*, 732–742. [CrossRef] [PubMed]
12. Wong, S.L.; Tan, J.; Ng, L.T.; Pan, J. Screening Unknown Novel Psychoactive Substances Using GC-MS Based Machine Learning. *ChemRxiv* **2022**. [CrossRef]
13. Piorunska-Sedlak, K.; Stypulkowska, K. Strategy for identification of new psychoactive substances in illicit samples using attenuated total reflectance infrared spectroscopy. *Forensic Sci. Int.* **2020**, *312*, 110262. [CrossRef] [PubMed]
14. Scientific Working Group for the Analysis of Seized Drugs (SWGDRUG). Available online: www.swgdrug.org (accessed on 20 January 2023).
15. Grigoletto, M.; Lisi, F. Looking for skewness in financial time series. *Econom. J.* **2009**, *12*, 310–323. [CrossRef]
16. Loperfido, N. Kurtosis-based projection pursuit for outlier detection in financial time series. *Eur. J. Financ.* **2020**, *26*, 142–164. [CrossRef]
17. McAlevey, L.G.; Stent, A.F. Kurtosis: A forgotten moment. *Int. J. Math. Educ. Sci. Technol.* **2018**, *49*, 120–130. [CrossRef]
18. Deconinck, E.; Duchateau, C.; Balcaen, M.; Gremeaux, L.; Courselle, P. Chemometrics and infrared spectroscopy—A winning team for the analysis of illicit drug products. *Rev. Anal. Chem.* **2022**, *41*, 228–255. [CrossRef]
19. Stone, J.V. Independent component analysis: An introduction. *Trends Cogn. Sci.* **2002**, *6*, 59–64. [CrossRef] [PubMed]
20. Himberg, J.; Mantyjarvi, J.; Korpipaa, P. Using PCA and ICA for exploratory data analysis in situation awareness. In Proceedings of the Conference Documentation International Conference on Multisensor Fusion and Integration for Intelligent Systems. MFI 2001 (Cat. No. 01TH8590), Baden-Baden, Germany, 20–22 August 2001; pp. 127–131.
21. Kunapuli, S.S.; Bhallamudi, P.C. A review of deep learning models for medical diagnosis. In *Machine Learning, Big Data, and IoT for Medical Informatics*; Elsevier: Amsterdam, The Netherlands, 2021; pp. 389–404.
22. Rodríguez-Pérez, R.; Bajorath, J. Evolution of Support Vector Machine and Regression Modeling in Chemoinformatics and Drug Discovery. *J. Comput. Aided Mol. Des.* **2022**, *36*, 355–362. [CrossRef] [PubMed]
23. Wade, C. *Hands-On Gradient Boosting with XGBoost and Scikit-Learn: Perform Accessible Machine Learning and Extreme Gradient Boosting with Python*; Packt Publishing: Birmingham, UK, 2020.
24. Smith, C.; Koning, M. *Decision Trees and Random Forests: A Visual Introduction For Beginners*; Blue Windmill Media: Chicago, IL, USA, 2017.
25. Bentéjac, C.; Csörgő, A.; Martínez-Muñoz, G. A comparative analysis of gradient boosting algorithms. *Artif. Intell. Rev.* **2021**, *54*, 1937–1967. [CrossRef]
26. Vitola, J.; Pozo, F.; Tibaduiza, D.A.; Anaya, M. A Sensor Data Fusion System Based on K-Nearest Neighbor Pattern Classification for Structural Health Monitoring Applications. *Sensors* **2017**, *17*, 417. [CrossRef]
27. Scafi, S.H.F.; Pasquini, C. Identification of counterfeit drugs using near-infrared spectroscopy. *Analyst* **2001**, *126*, 2218–2224. [CrossRef]
28. Burlacu, C.M.; Burlacu, A.C.; Praisler, M. Sensitivity analysis of artificial neural networks identifying JWH synthetic cannabinoids built with alternative training strategies and methods. *Inventions* **2022**, *7*, 82. [CrossRef]
29. Negoita, C.; Praisler, M.; Ion, A. Artificial intelligence application designed to screen for new psychoactive drugs based on their ATR-FTIR spectra. In *AIP Conference Proceedings*; Mishonov, T.M., Varonov, A.M., Eds.; AIP Publishing: Melville, NY, USA, 2019.
30. United Nations Office on Drugs and Crime. *Recommended Methods for the Identification and Analysis of Amphetamine, Methamphetamine and Their Ring-Substituted Analogues in Seized Materials*; United Nations Publications: New York, NY, USA, 2006.
31. United Nations Office on Drugs and Crime. *Recommended Methods for the Identification and Analysis of Synthetic Cannabinoid Receptor Agonists in Seized Materials*; United Nations Publications: New York, NY, USA, 2013.

32. Gosav, S.; Praisler, M.; Birsa, M.L. Principal Component Analysis Coupled with Artificial Neural Networks—A Combined Technique Classifying Small Molecular Structures Using a Concatenated Spectral Database. *Int. J. Mol. Sci. Spec. Issue Adv. Comput. Toxicol.* **2011**, *12*, 6668–6684. [CrossRef]
33. Ciochina, S.; Praisler, M.; Coman, M.M. Choosing Between Quantum Cascade Lasers (QCL) Equipping a New Hollow Fiber Infrared Scanner Designed to Detect New Psychoactive Substances (NPS). In *AIP Conference Proceedings*; Mishonov, T.M., Varonov, A.M., Eds.; AIP Publishing: Melville, NY, USA, 2019.

Disclaimer/Publisher's Note: The statements, opinions and data contained in all publications are solely those of the individual author(s) and contributor(s) and not of MDPI and/or the editor(s). MDPI and/or the editor(s) disclaim responsibility for any injury to people or property resulting from any ideas, methods, instructions or products referred to in the content.

inventions

MDPI

Article

An Evaluation of the Wind Energy along the Romanian Black Sea Coast

Laura-Ionela Nedelcu [1,2,*], Viorel-Mihai Tanase [3] and Eugen Rusu [2]

[1] Department of Navigation and Naval Transport, Faculty of Navigation and Naval Management, “Mircea cel Batran” Naval Academy, 1st Fulgerului Street, 900218 Constanta, Romania
[2] Department of Mechanical Engineering, Faculty of Engineering, “Dunarea de Jos” University of Galati, 47th Domneasca Street, 800008 Galati, Romania
[3] Maritime Hydrographic Directorate, 1st Fulgerului Street, 900218 Constanta, Romania
* Correspondence: laura.nedelcu@anmb.ro

Abstract: The present study aims to outline a general overview of the wind energy potential along the Romanian coast of the Black Sea, using the weather data provided by the Maritime Hydrographic Directorate covering a 13-year time interval (2009–2021). The data obtained from seven automatic weather coastal stations distributed along the Romanian perimeter were used to evaluate the wind regime, highlighting the Black Sea’s complex marine environment. The analysis based on the evaluation of the wind parameters per each station registered on the total period revealed that the overall wind characteristics are similar, resulting in no significant variations depending on the station’s location. Moreover, the climatic picture of the Black Sea can be interpreted as two seasons, winter and summer, a conclusion based on the analysis made of the seasonal and monthly variation of the wind aspects. Subsequently, the outcomes obtained in this research imply that the Romanian Black Sea coast has the potential to be a good location for wind energy development due to the strong winds that blow in the region.

Keywords: wind potential; Romanian coast; Black Sea area; weather stations; marine environment

Citation: Nedelcu, L.-I.; Tanase, V.-M.; Rusu, E. An Evaluation of the Wind Energy along the Romanian Black Sea Coast. *Inventions* **2023**, *8*, 48. https://doi.org/10.3390/inventions8010048

Academic Editor: Theocharis Tsoutsos

Received: 30 December 2022
Revised: 28 January 2023
Accepted: 9 February 2023
Published: 13 February 2023

Copyright: © 2023 by the authors. Licensee MDPI, Basel, Switzerland. This article is an open access article distributed under the terms and conditions of the Creative Commons Attribution (CC BY) license (https://creativecommons.org/licenses/by/4.0/).

1. Introduction

Offshore wind energy is considered an important pillar in achieving net greenhouse gas emissions. According to the European Commission, by 2050, Europe must develop between 230 and 450 GW of offshore wind capacity, which will provide up to 30% of Europe’s electricity needs. To date, Romania is the leader of Southeast Europe in terms of onshore development, with an installed capacity of 3 GW [1]. The onshore wind farm development was mainly carried out in the Dobrogea plateau, where almost 80% of the existing wind turbines in Romania are concentrated. The largest onshore wind farm in Europe is Fantanele–Cogealac, in the Dobrogea area, with an installed capacity of 600 MW [2].

Most research regarding the Black Sea wind and wave conditions indicates that the northwestern part presents a higher energy level than the eastern sector [3–8]. The evaluation carried out in [4], Rusu L., Bernardino M., and Guedes Soares C. outlined that the average wind speed value registered at Sulina meteorological station was 7.29 m/s, and at Chonomors’ke was 4.47 m/s, whereas at Gloria platform it was registered a value of 5.16 m/s. The observations provided by the two weather stations were made at a height of 10 m above the water, and those from the Gloria platform at a height of 36 m. In the same research, the wind speed analysis was made indicating that the western part registers significant seasonal variations, whereas the east is characterized by more stable conditions [9,10].

Furthermore, in their paper [10], the authors performed a comparison between the average wind speed from coastal stations and data provided by satellites. The analysis stated the following wind speed average values: 4.9 m/s (coastal stations) and 6 m/s (satellites). Moreover, in [11], based on wind and wave conditions evaluated over a period of 50 years (1958–2007), it is concluded that the wind and wave climate of the western Black Sea basin presents a large spatial and seasonal variability. The authors mentioned that the wind speed exceeded 40 m/s offshore and 25 m/s near the shore.

The analysis carried out in [12,13] indicates that the Romanian coast has a higher energy level during the winter season, with an average wind speed of approximately 9.7 m/s and a power of 870 W/m^2 at a height of 80 m. Moreover, in [12] it is mentioned that during the warm season the wind climate registers values between 5.69–7.17 m/s with a maximum in September and a minimum in August. The cold season has an average wind speed located in the range of 7.67–8.59 m/s, with higher values being registered in January and minimums in October. The average annual wind speed at the height of 10 m is approximately 7.1 m/s.

Myslenkov et al. pointed out in the paper [14] that low-quality wind and wave potential were observed during the summer months. In their article [15], Rusu L., Răileanu A., and Onea F. obtained, based on the data provided by the Gloria platform, speeds of 6–7 m/s at heights of 10 m. In addition, in the papers [16,17], the authors highlighted the fact that in the vicinity of Romania and Ukraine, the wind speed during the winter season reaches an average value of 7.7 m/s and a maximum of 13.2 m/s. Diaconita A., Rusu L., and Andrei G. concluded in their study [18] that the average wind speed at a height of 10 m was 6.7 m/s. According to [19], the average wind speed is between 7–6 m/s in the offshore area and, respectively, near the Romanian coast. Near the Crimean Peninsula, an average wind speed of about 5.5 m/s was recorded.

Likewise, from the analysis carried out in the period 1979–2009, in [20], it was determined that in the December, January, and February season the winds have the highest magnitude, reaching values of approximately 8.1 m/s in the western part of the Black Sea and 8.7 m/s in the Sea of Azov. The authors specify that the Sea of Azov is exposed to strong winds compared to the Black Sea. The strongest wind values registered during summer (June, July, August) are in the Sea of Azov (6.1 m/s), whereas in the northwestern part of the Black Sea there are values around 5.7 m/s, whereas in the southwestern part, the wind reaches speeds of approximately 5.5 m/s. In spring (March–April–May), maximum wind speed values reach 7.0 m/s in the Sea of Azov and 6.3 m/s in the northwestern Black Sea. During autumn, maximum wind values of approximately 7.6 m/s were recorded in the Sea of Azov and 7.2 m/s in the northwestern Black Sea.

Based on the literature review mentioned above, the Black Sea area can be considered a valuable source of renewable energy. Data analyzed in [21] indicate that wind speed increases offshore, with only the central part of the deep-water sector having higher average wind speeds (nearly 7 m/s) compared to the southeastern part of the Exclusive Economic Zone (EEZ), where the wind speed decreases. A large part of Romania's EEZ has deep waters (>50 m), suitable for floating platforms. Whereas deep areas are accessible for floating wind turbines, at depths greater than 150 m the costs of maintenance increase significantly. Moreover, in [21], the authors evaluated the potential of the offshore wind sector in Romania, estimating a total capacity of 94 GW, which means a total annual energy production (AEP) of 239.04 TWh, of which 22 GW (AEP = 54.44 TWh) from fixed turbines and 72 GW (AEP = 184.6 TWh) from offshore wind farms.

This study can be considered an opportunity since there is a significantly growing interest in offshore wind project development on the Romanian coast of the Black Sea. Consequently, this research paper will focus on the analysis of the wind characteristics based on the data provided by the Maritime Hydrographic Directorate over a period of 13 years, indicating the wind potential along the Romanian coast. The elements of the novelty of the present work are defined as follows: (a) the Romanian coast wind regime is assessed by in situ measurements for seven sites located on or near the shoreline, compared to other research that used modeled or satellite data and very few observations; (b) a long-term overview of the wind resources is provided (13 years); (c) the full wind characteristics coverage of the area because of the location of the stations.

2. Materials and Methods

2.1. Target Area

The Black Sea (Figure 1) represents an inland sea located between Europe, Anatolia, and the Caucasus, covering an area of 423,000 km^2. It has a volume of 555,000 km^3, an average depth of 1315 m, and a maximum of 2258 m. It is considered one of the most isolated parts of the planetary ocean, being connected to the Mediterranean Sea through the Bosporus and Dardanelles straits and to the Sea of Azov through the Kerch Strait [22–24].

Figure 1. The Black Sea. Image obtained from [25].

The Black Sea is defined by an irregular shape, having as riparian states Romania, Ukraine, Russia, Georgia, Turkey, and Bulgaria. The largest bay is located in the western part of the sea off the coast of Bulgaria (bays of Bulgaria and Varna), followed by the bays of Odesa and Karkinit (in the northwest) and bays of Kalamit and Feodora in Crimea. In the eastern part of the sea can be seen the bays of Novorossiysk and Gelendzhik, whereas in the south there are Sinop bay and Samsun Bight. Crimea is the largest peninsula in the Black Sea [8].

The bathymetry of the Black Sea is divided between the reef, the continental slope, and the abyssal plain. The reef occupies up to 25% of the total area of the seabed and has average depths between 100–200 m and a width of 200 km. In the remaining area, depths below 2000 m can be found. The configuration of the bathymetric line as well as the presence of depressions and canyons have an important influence on the distribution of water masses and the direction and speed of currents [22–24,26].

The Black Sea region climate is temperate–continental, influenced by the baric centers situated above Southeast Europe: the Azores anticyclone and the Southeast European anticyclone. Furthermore, the Black Sea is roughly encompassed by mountain belts: the Pontics to the south, the Caucasus to the north and east, and the Carpathians to the west. Therefore, the sea climate can be indicated as follows: in the summer the air temperature is relatively uniform, whereas in the winter the air temperature can be described according to the geographical locations (minimums in the northwest corner and maximums in the southeast). Water temperatures vary according to the season: in summer, the surface water warms to 25 °C, (occasional extremes up to 28 °C), whereas in winter the sea temperatures reach 6–8 °C. The northwest coast has ice during winter, whereas the southeast remains around 9 °C [27,28].

One of the most valuable features of the Black Sea is that the water layers cannot mix. The sea's hydrochemical configuration is mainly influenced by basin topography and fluvial inputs, resulting in a strong stratified vertical structure. The first layer, located on the sea surface over 50 m, is less dense, less salty, and broadly cooler, fueled by large river systems. The second layer, the cold one, has a mass of water located at depths from 50 to 180 m. Fluvial inputs represent the European rivers that flow into the Black Sea (Danube, Dnieper, Don) as well as precipitation. Annually, the Black Sea gains an approximate quantity of 350 km^2 of water from the aforementioned rivers and nearly 250 km^2 from precipitation, whereas 350 km^2 of water is evaporated [22,26,29,30].

Black Sea salinity is established by the balance between freshwater received by rivers and the Mediterranean water entering through the Bosporus Strait. At the surface, an average salinity of 16–18 PPT (twice lower than the salinity of the surface waters of the world ocean) was recorded. The bottom layer salinity increases to 21–22.5 PPT at a depth below 120–200 m [31].

Two types of sea currents are present in the Black Sea: the surface currents, caused by the cyclonic wind pattern, and the double currents caused by the Kerch and Bosporus straits. Surface currents form two closed circles: the western and the eastern circles. The first one is opposite the Danube Delta and has a width of 100 km which decreases towards the south, whereas its velocity is around 0.5 km/h. The width of the second circle varies between 50 and 100 km, and the velocity is 1 km/h. The Bosporus double current consists of the water exchange between the Black Sea and the Marmara Sea. At the surface, there is less salty and lighter water that flows into the Marmara Sea at a speed of 2 m/s. At depths of 50–120 m, there is the saltier and denser water of the Marmara Sea which flows into the Black Sea with a speed of 4–6 m/s. Regarding the Kerch Strait, the first current, located at the surface flows from the Sea of Azov to the Black Sea with 1–2 m/s, whereas the bottom current flows in the opposite direction at a depth of about 5 m [22].

The Black Sea circulation is generally driven by the Rim current (cyclonic). This current follows the continental slope in the northwestern and western parts of the Black Sea and presents various cyclonic and anticyclonic whirlwinds within the primary current. The Black Sea has a horizontal circulation defined by gyres (cyclonic and anticyclonic currents directed by the force of the wind). Occasionally, the Rim Current has a width of tens of km and a maximum speed of 0.8–1 Nd or 40–50 cm/s, which sometimes reaches values up to 1.6 Nd or 80–100 cm/s [29,32–36].

The Black Sea tides vary from 1.1 cm near the Crimean Peninsula to 19 cm in the Dnieper–Bug estuary (Kherson and Nikolaev), 13–14 cm in Odesa and Illichivsk, and up to 12.6 cm on the eastern coast (Batumi). In general, semidiurnal tides prevail in the Black Sea [37].

2.2. Wind Dataset

The analysis carried out in this research aims at a comprehensive picture of the wind potential of the Black Sea northwestern part, the Romanian littoral, based on the data and information provided by the Maritime Hydrographic Directorate over a 13-year time period.

The Maritime Hydrographic Directorate is the Romanian Naval Forces specialized structure that provides meteorological, oceanographical, and climate information to the Navy's ships and units [38].

The department responsible for the data that this research relies on is the Climatology Laboratory from the Maritime Hydrographic Directorate (MHD). The purpose of this laboratory is to collect, manage, and analyze Meteorological and Oceanographic (METOC) data from the area of interest. Currently, the Naval Forces Marine Meteorological Surveillance Network (RSMM-FN), includes seven coastal automatic weather stations at the lighthouses subordinated to MHD and five naval automatic weather stations on board some military vessels. The study is based on the data and information collected by the seven automatic stations, located on the entire Romanian coast and distributed from north to south. Their location and metadata can be seen in Figure 2 and Table 1, where the altitude represents the station height above the mean sea level, and the sensor altitude represents the sensor height above ground [38].

Figure 2. Location of weather stations on the Romanian Black Sea coast [39].

Each station is equipped with specific instruments able to process the climate information as detailed in Table 1. Further, the data are transmitted to the MHD headquarters to be registered and analyzed. The system is capable of recording the following data and information: wind speed and direction, air temperature, precipitations, visibility, wind gusts, air pressure, and dew point. The wind parameters which are the key element to our research, are recorded and processed as an average value every 10 min, 24 h a day. The observations were made in the 2009–2021 period.

Table 1. Locations and characteristics of the seven automatic weather coastal stations.

Station	Latitude	Longitude	Altitude	Instruments
Sulina	45.15°	29.76°	1.6 m	• Vaisala WXT520 (10 m altitude) heated multisensor composed of: – WINDCAP ultrasonic wind speed and direction sensor; – RAINCAP precipitation sensor; – PTU module including BAROCAP capacitive pressure, THERMOCAP temperature, and HUMICAP humidity sensors. • Vaisala PWD22 (9.7 m altitude) heated present time and visibility multisensor composed of: – 2 RAINCAP capacitive precipitation sensors; – optical visibility sensor including PWT11 transmitter and PWC22 receiver/processor; – temperature sensor—Pt100 thermistor.
Sf. Gheorghe	44.90°	29.60°	0.5 m	• Vaisala WXT520 (5.5 m altitude) heated multisensor composed of: – WINDCAP ultrasonic wind speed and direction sensor; – RAINCAP precipitation sensor; – PTU module including BAROCAP capacitive pressure, THERMOCAP temperature, and HUMICAP humidity sensors. • Vaisala PWD22 (5.2 m altitude) heated present time and visibility multisensor composed of: – 2 RAINCAP capacitive precipitation sensors; – optical visibility sensor including PWT11 transmitter and PWC22 receiver/processor; – temperature sensor—Pt100 thermistor.
G. Portitei	44.68°	28.99°	0 m	• Vaisala WXT520 (10 m altitude) heated multisensor composed of: – WINDCAP ultrasonic wind speed and direction sensor; – RAINCAP precipitation sensor; – PTU module including BAROCAP capacitive pressure, THERMOCAP temperature, and HUMICAP humidity sensors. • Vaisala PWD22 (9 m altitude) heated present time and visibility multisensor composed of: – 2 RAINCAP capacitive precipitation sensors; – optical visibility sensor including PWT11 transmitter and PWC22 receiver/processor; – temperature sensor—Pt100 thermistor.
Midia	44.32°	28.69°	6.3 m	• Vaisala WXT510 (12.7 m altitude) heated multisensor composed of: – WINDCAP ultrasonic wind speed and direction sensor; – RAINCAP precipitation sensor – PTU module including BAROCAP capacitive pressure, THERMOCAP temperature, and HUMICAP humidity sensors.
Constanta	44.15°	28.67°	5 m	• Vaisala WS425 (11.2 m altitude) heated ultrasonic wind speed and direction sensor. • Temperature and relative air humidity sensor QMH102, based on the Vaisala HMP45D transmitter (8.2 m altitude), composed of: – temperature sensor—thermistor Pt-100 IEC 751; – HUMICAP relative humidity sensor. • Vaisala PWD22 (8.2 m altitude) heated multisensor of present time and visibility composed of: – 2 RAINCAP capacitive precipitation sensors; – optical visibility sensor including PWT11 transmitter and PWC22 receiver/processor; – temperature sensor—Pt100 thermistor. • Vaisala PMT16A pressure sensor—silicon capacitive sensor (7.2 m altitude)
Tuzla	43.99°	28.67°	16 m	• Vaisala WXT520 (5.5 m altitude) heated multisensor composed of: – WINDCAP ultrasonic wind speed and direction sensor; – RAINCAP precipitation sensor; – TU module including BAROCAP capacitive pressure, THERMOCAP temperature and HUMICAP humidity sensors.

Table 1. *Cont.*

Station	Latitude	Longitude	Altitude	Instruments
Mangalia	43.80°	28.60°	3.6 m	• Vaisala WS425 (14.3 m altitude) heated ultrasonic wind speed and direction sensor. • QMH102 air temperature and relative humidity sensor, based on the Vaisala HMP45D transmitter (8.3 m altitude), composed of: – temperature sensor—thermistor Pt-100 IEC 751; – HUMICAP relative humidity sensor. • Vaisala PWD22 (8.2 m altitude) heated multisensor of present time and visibility composed of: – 2 RAINCAP capacitive precipitation sensors; – optical visibility sensor including PWT11 transmitter and PWC22 receiver/processor; – temperature sensor—Pt100 thermistor. • Vaisala PMT16A pressure sensor—silicon capacitive sensor (7.4 m altitude).

3. Results

The present research evaluates the wind data provided by MHD on the 2009–2021 period. Among the reasons for the analysis is to identify an average wind speed value based on the data provided from all seven stations throughout the period. The primary data are represented as average values recorded every day of every month for all 13 years. The evaluation of monthly averaged wind speed data is based on the averages collected from all seven automatic stations each month to analyze the wind patterns and characteristics presented in the Black Sea area. The second analysis was carried out by taking the maximum wind speed value recorded by each station each month during the time interval, then calculating the average of all these maximum values. Additionally, wind roses, which show the frequency and direction of the wind, were created to visualize the data.

Figure 3 and Table 2 provide a first evaluation of the wind speed, emphasizing the distribution of the mean values of each station per month. From the seven stations' data review, we may notice that all data are in the same range, except Sf. Gheorghe, whose values are lower than the averages with approximately 1–2 m/s, because its location is approximately 3 km from the shoreline, the lower wind sensor height (5.5 m), and the higher surface roughness due to surrounding terrain whereas all the other stations are situated on the shoreline (Gura Portitei, Tuzla), or even slightly in the sea (Sulina, Midia, Constanta, Mangalia) and have the sensors at about 10 m.

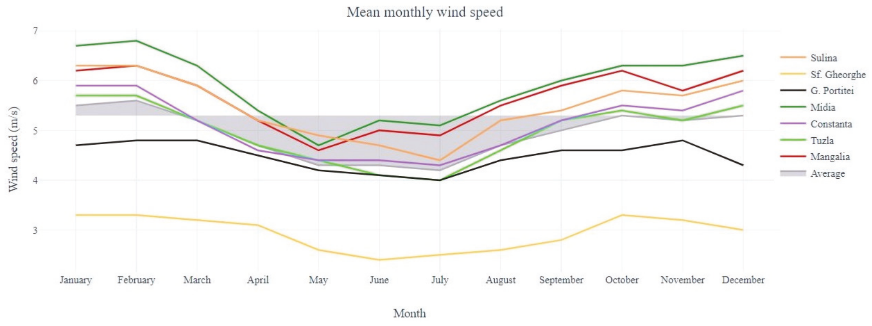

Figure 3. Mean monthly values of the wind speed.

Table 2. Mean monthly values of the wind speed.

	Jan	Feb	Mar	Apr	May	Jun	Jul	Aug	Sep	Oct	Nov	Dec
Constanta	5.9	5.6	5.2	4.6	4.4	4.4	4.3	4.7	5.2	5.5	5.4	5.8
Mangalia	6.2	6.2	5.9	5.2	4.6	5.0	4.9	5.5	5.9	6.2	5.8	6.2
Sulina	6.3	6.3	5.9	5.2	4.9	4.7	4.4	5.2	5.4	5.8	5.7	6.0
G. Portitei	4.7	5.0	4.8	4.5	4.2	4.1	4.0	4.4	4.6	4.6	4.8	4.3
Sf. Gheorghe	3.3	3.6	3.2	3.1	2.6	2.4	2.5	2.6	2.8	3.3	3.2	3.0
Midia	6.7	6.6	6.3	5.4	4.7	5.2	5.1	5.6	6.0	6.3	6.3	6.5
Tuzla	5.7	5.6	5.2	4.7	4.4	4.1	4.0	4.6	5.2	5.4	5.2	5.5
Average	5.5	5.6	5.2	4.7	4.3	4.3	4.2	4.7	5.0	5.3	5.2	5.3

As can be seen, the most energetic month is February, with an average wind speed of 5.6 m/s, followed by January (5.5 m/s), and both December and October, with a value of 5.2 m/s. The outcome of the presented analysis reveals that the most dynamic season is winter. The following season with great value is autumn. As presented earlier, October reported a mean wind speed of 5.3 m/s, close to November (5.2 m/s) and September (5 m/s). Further, the next season evaluated is spring, with the following wind speed recorded: March—5.2 m/s, April—4.7 m/s, and May—4.3 m/s. Lastly, the lowest energetic season is summer; the lowest value registered belongs to July—4.2 m/s, followed by June—4.3 m/s, and August—4.7 m/s.

From the analysis made, based on the entire data collected over the 13-year period, an average wind speed value of 4.9 m/s was obtained.

The highest average values of wind speed were recorded by Midia station (5.9 m/s), situated on the south part of the Romanian coast, followed by Mangalia (5.6 m/s), also located in the south, Sulina—5.5 m/s (north), Constanta—5.1 m/s (south), Tuzla—5 m/s (south), G. Portitei—4.5 m/s (north), and Sf. Gheorghe—3 m/s (north), resulting in greater values registered in the southern part of the Romanian coast.

In Figure 4, a more precise analysis of the average and maximum wind speed of each month can be observed, based on the information collected from all seven automatic stations during the entire period.

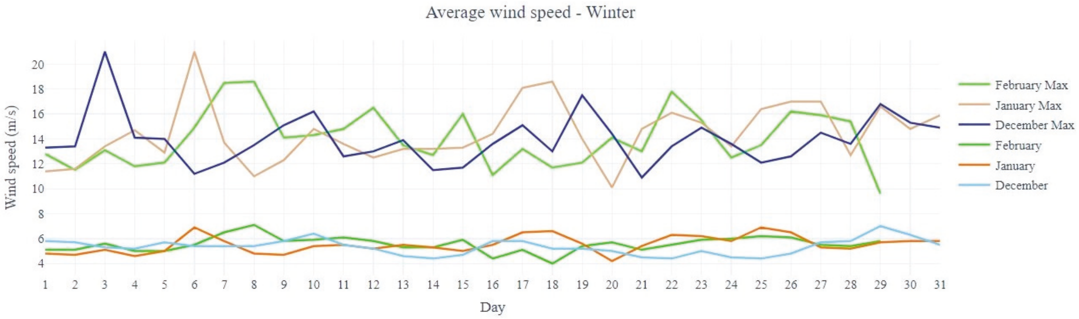

(**a**)

Figure 4. *Cont.*

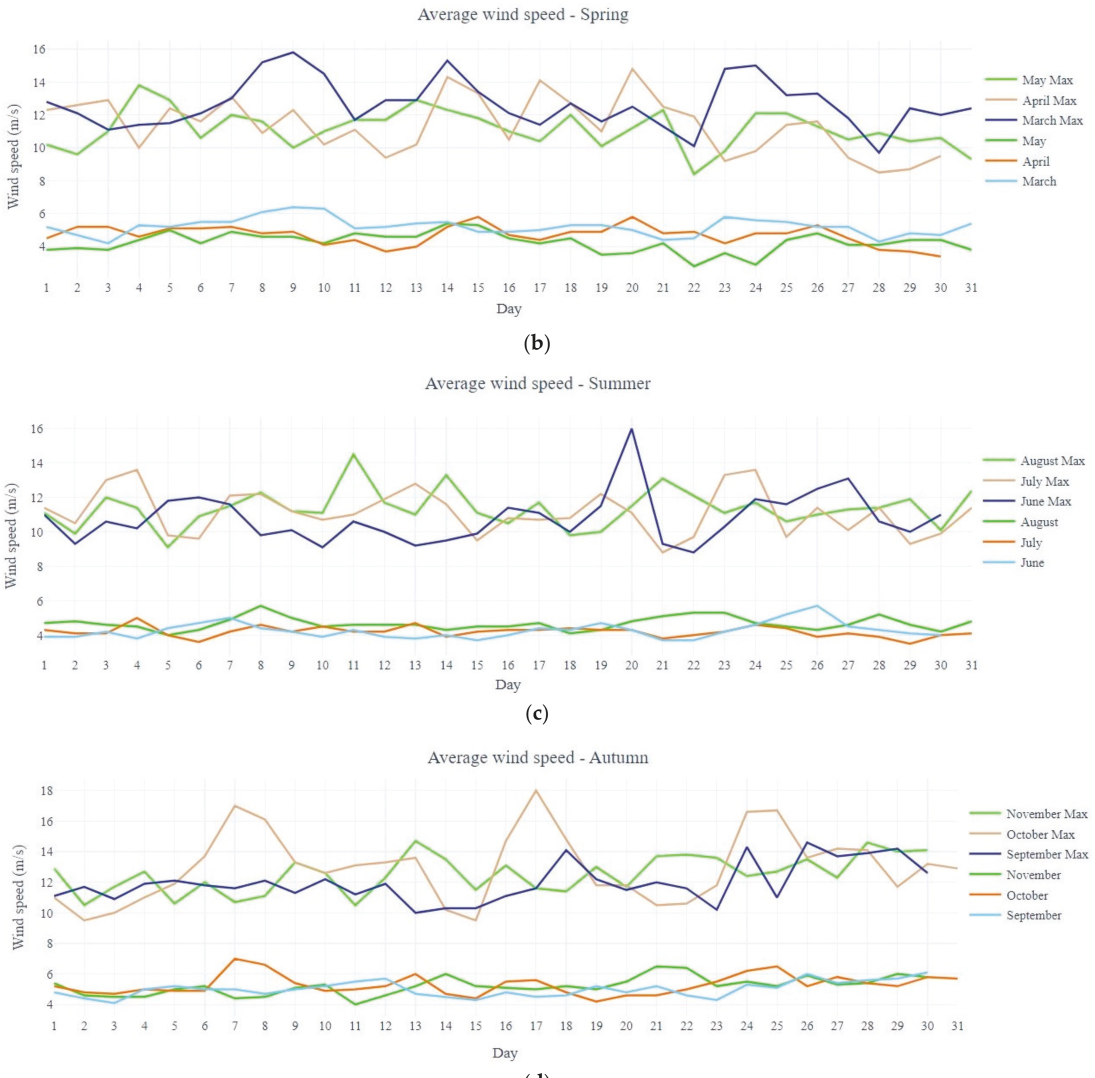

(**b**)

(**c**)

(**d**)

Figure 4. Monthly wind speed analysis; (**a**) winter; (**b**) spring; (**c**) summer; (**d**) autumn.

3.1. Mean Wind Data Analysis per Month

In the present section, the mean wind speeds each month were analyzed to outline in a comprehensive way the climatic picture of the Romanian coast of the Black Sea. As presented above, January is one of the most energetic months of the year, alongside February and December, with a registered wind speed mean value of 5.5 m/s. The values recorded in this month are in good agreement, being in the range of 4.2 m/s (20 Jan) and 6.9 m/s (two observations made on 6 and 25 Jan). Following the same trend, in February, mean wind speeds were recorded in the range of 4 m/s (18 Feb) and 7.1 m/s (8 Feb), having an average wind speed of 5.6 m/s. The maximum average wind speed from February represents the greatest value in this particular analysis. From the evaluation made, February is the most dynamic month; nevertheless, no major variations were observed. The next month presented is March, where an average of 5.2 m/s was recorded. The maximum value was recorded on the 9th—6.4 m/s, whereas the lowest was on the 3rd—4.2 m/s. In the fourth month of the year, values in the range of 3.4 (30 Apr)—5.8 m/s (15 and 20 Apr) with a mean value of 4.7 m/s were registered. Spring season evaluation ends in May, which has an average wind speed data of 4.3 m/s. From the analysis made it can be seen that a maximum value of 5.4 m/s was noticed on the 14th, whereas a minimum of 2.8 m/s was on the 22nd, representing the lowest value recorded regarding the average wind speed. The evaluation of the data collected from the seven stations illustrates a continuous decrease with the summer season, where the lowest values were recorded. Based on the evaluation made, in June a mean wind speed of 4.3 m/s was noticed. In the present month, minimum values of 3.7 m/s (three observations made on 15, 21, and 22) and a maximum of 5.7 m/s on the 26th were registered. July is the lowest energetic month with a wind speed value of 4.2 m/s. Several minimum values were recorded: 3.5 m/s—30th, 3.6 m/s—6th, and also a maximum of 5 m/s on 4th. In terms of wind variations, July is a stable month with differences between the maximum and minimum of 1.4 m/s. In addition, August wind values have differences of 1.7 m/s between the maximum registered (5.7 m/s—8 Aug) and the minimum (4 m/s—6 Aug). The next season discussed is autumn, with the following months: September, October, and November. Firstly, September shows an average of 5 m/s, a minimum of 4.1 m/s at the beginning of the month (3 Sep), and a maximum of 6.1 m/s at the end of the month (30 Sep). Secondly, in October, values in the range of 4.2 m/s (19 Oct) and 7 m/s (7 Oct) were recorded. The average wind speed value noticed was 5.3 m/s, close to the one observed in November—5.2 m/s. It can be noticed that values are increasing as the months approach the end of the year. A minimum observation of 4 m/s was made on 11th November, whereas a maximum observation was made on the 21st—6.5 m/s. The last month of the present analysis, December, shows an average of 5.3 m/s, outlining once more that it is a dynamic month concerning the wind energy potential. The analysis outlines a maximum of 7 m/s on the 29th and minimum values of 4.4 m/s on the 14th, 22nd, and 25th. Based on the evaluation made for each month during the entire period analyzed, it resulted that the values were encountered in the range of 2.8 m/s (22nd of May) and 7.1 m/s (8th of February). Nevertheless, no major variations were encountered, and the values obtained followed either an increasing or decreasing path.

3.2. Maximum Wind Values

The second approach of the present paper represents the analysis of the maximum values obtained from the evaluation of wind speed. The maximum wind values in the Black Sea can vary significantly depending on the season and the specific location. In general, the Black Sea is known for its strong winds, especially during the winter months when storms are more common. The highest wind speeds are typically found in the western part of the Black Sea, whereas in the eastern part of the Black Sea, the winds are generally less strong. It is important to note that the Black Sea is also prone to sudden and severe storms, which can bring strong winds and rough seas. These storms can occur at any time of year, but they are most common in the winter and spring.

In Figure 5 and Table 3, the monthly maximum wind speed broken down by stations is illustrated. The outline revealed from the entire database suggests a mean maximum value of 12.4 m/s. The highest mean value registered was in January—14.5 m/s, followed by February—14.1 m/s and December—14 m/s, resulting again that winter is the most intense season concerning the wind potential. The next season with dynamic conditions is autumn, with the following values: October—13 m/s, November—12.5 m/s, and September—11.9 m/s. Following the same criteria, the third season is spring. In March, a maximum mean wind speed of 12.6 m/s was registered, whereas in April it was 11.4 m/s, and in May 11.1 m/s. The last season discussed is summer with the following recorded values: August—11.4 m/s, July—11.1 m/s, and the lowest high value—10.8 m/s (June). This analysis follows the same trend as the mean wind speed with the same season's order depending on the wind dynamic.

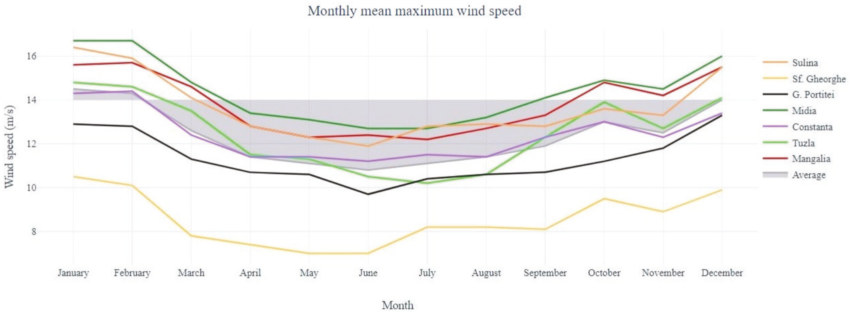

Figure 5. Monthly mean maximum values of the wind speed.

Table 3. Monthly mean maximum values of the wind speed.

	Jan	Feb	Mar	Apr	May	Jun	Jul	Aug	Sep	Oct	Nov	Dec
Constanta	14.3	13.8	12.4	11.4	11.4	11.2	11.5	11.4	12.3	13.0	12.3	13.4
Mangalia	15.6	15.7	14.6	12.8	12.3	12.4	12.2	12.7	13.3	14.8	14.2	15.5
Sulina	16.4	15.8	14.1	12.8	12.3	11.9	12.8	12.9	12.8	13.6	13.3	15.5
G. Portitei	12.9	12.5	11.3	10.7	10.6	9.7	10.4	10.6	10.7	11.2	11.8	13.3
Sf. Gheorghe	10.5	10.1	7.8	7.4	7.0	7.0	8.2	8.2	8.1	9.5	8.9	9.9
Midia	16.7	16.3	14.8	13.4	13.1	12.7	12.7	13.2	14.1	14.9	14.5	16.0
Tuzla	14.8	14.4	13.5	11.5	11.3	10.5	10.2	10.6	12.3	13.9	12.7	14.1
Average	14.5	14.1	12.6	11.4	11.1	10.8	11.1	11.4	11.9	13.0	12.5	14.0

Moreover, it is concluded that the maximum wind speed values recorded from each station are roughly in the same sequence as presented earlier in the highest average values evaluation, reiterating that the southern part presents high values than the northern part: Midia—14.4 m/s, Mangalia—13.8 m/s, Sulina—13.7 m/s, Tuzla—12.5 m/s, Constanta—12.4 m/s, G. Portitei—11.3 m/s, and Sf. Gheorghe—8.6 m/s.

3.3. Maximum Wind Values Recorded per Month

In this section, the averages of the greatest wind speeds recorded per month are analyzed to illustrate the most dynamic periods referred to in this study. As explained earlier, with a value of 14.5 m/s, January is the month with the highest data registered in terms of mean maximum wind speeds. The peak of this analysis is reached on the 6th when a value of 21 m/s was registered. The same value is encountered on the 3rd of December. Considerable great values were seen in January: 18 Jan—18.6 m/s, 17 Jan—18.1 m/s, and 26 and 27 Jan—17 m/s. Close to the monthly maximum mean speed recorded in January is the one registered in February—14.1 m/s. Apart from the peak recorded on the 8th of February (18.6 m/s), other high values were recorded on the dates of the 7th (18.5 m/s) and 22nd (17.8 m/s), but after these values, the lowest data was observed—9.6 m/s (29 Feb). Further, moving to the next season, high values are considerably lower. In March a mean maximum value of 15.8 m/s was marked on the 9th, whereas the average value is 12.6 m/s. Other great values were seen on the following dates: 15.3 m/s—14 Mar, 15.2 m/s—8 Mar, and 15 m/s—24 Mar. Particular attention is paid to April, which presents an extended period with greater values than the rest of the month. In the period of 13–22 April appropriate wind data were observed resulting in stable conditions in terms of weather parameters. Peaks of 14.3 m/s on the 14th, 14.1 m/s on the 17th, and 14.8 m/s on the 20th were recorded, whereas medium values were seen among them in order to smooth the continuous wind trend. In May no major variations were observed. Values between 8.4 m/s (22nd of May) and 13.8 m/s (4th of May) were seen, as in Figure 4b. In June, the lowest mean value concerning the maximum wind speed was observed—10.8 m/s. In this month, a peak of 16 m/s was seen on the 20th, and others in the range of 8.8 m/s (22 Jun) and 13.1 m/s (27 Jun) were recorded. Low values are also detailed in Figure 4c. In July, maximum wind average speeds are considerably lower: 13.6 m/s—4 Jul and 24 Jul. The last month of the summer season, August presents an average maximum wind speed of 11.4 m/s. A maximum value of 14.5 m/s was recorded on the 11th; still, no major variations were observed. The second energetic season is autumn. In September all values are in good agreement, being in the range of 10 m/s (13th Sep) and 14.6 m/s (26th Sep). In October, values are considerably higher, recording a mean maximum wind speed of 13 m/s. Other high values presented in this month can be seen in Figure 4d (18 m/s—17 Oct, 17 m/s—7 Oct, 16.7 m/s—25 Oct). November represents a stable month, illustrating a difference of 4.2 m/s between the lowest value (10.5 m/s—2 Nov and 11 Nov) and 14.7 m/s—13 Nov. Similar wind data are seen in this month with minor ups and downs. The last month analyzed is December. Like February, December presents significant variations in terms of mean maximum wind speeds with differences of 10.1 m/s observed. As presented earlier, a peak of 21 m/s was seen on the 3rd of December, followed by lower values: 17.5 m/s—19 Dec and 16.8 m/s—29 Dec. The analysis made in this section concluded that winter is the most suitable season in terms of dynamic wind parameters, nevertheless unstable conditions are seen in December and February. Stable conditions are located in November and April.

3.4. Wind Directions

The wind direction in the Black Sea can vary greatly depending on the time of year and the specific location within the sea. The Black Sea is generally influenced by the prevailing winds in the region, typically westerly or southwesterly. During the winter months, the winds tend to be stronger and more consistent, whereas, in the summer, the winds are generally lighter and more variable. In addition to the prevailing winds, the Black Sea is also influenced by local weather patterns and topographic features, which can affect wind direction and strength. The purpose of the present section is to evaluate the wind frequencies by direction, depending on the month (Figure 6).

The wind direction is typically from the northwest in the winter and from the southeast in the summer, however, a few exceptions have been found based on the data used on the time interval. The winter months are basically following the same wind frequencies: December—NW (22.7%) and W (22.6%); January—NW (21.8%) and N (19.7%); February—N (22.9%), S—(15.5%). In spring, great wind frequencies are found from the southeast. In March, there are high values both in the north (19.3%) and south (17.4%), representing a transit month from one season to another. In April and May, great values are found from the south (19.4%—Apr, 17%—May), followed by wind frequencies from the southeast (18.3%—Apr, 15.8%—May). In June, winds from the south can be found with a frequency of 16.4%, followed by those from the north—15.8%. In July, the wind shifts to NW (18%) and N (16.1%). August, the last month of summer, has similar values related to July: N (23.6%) and NW (18%). The wind directions presented in autumn are from the northwest: September—N (18.5%), NW (15.9%), October—N (21.1%), NW (16.9%), and November—N (20.6%), NW (16.7%). The analysis highlighted that during winter and autumn seasons the prevailing wind direction is from N–NW–W, whereas in spring the wind blows more frequently from S–SE or N. The summer season presents higher wind direction frequencies from N–NW or S.

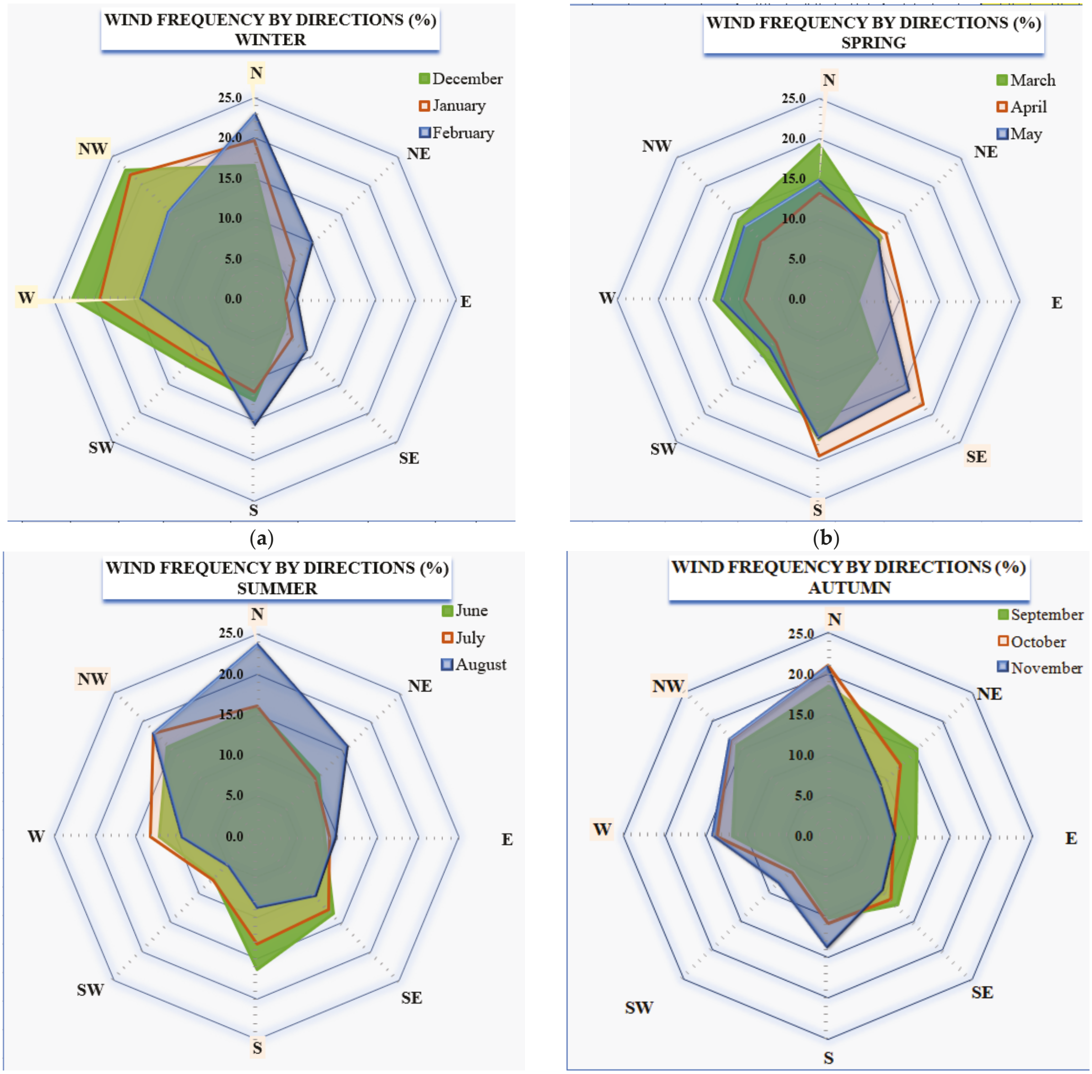
WIND FREQUENCY BY DIRECTIONS (%) WINTER

WIND FREQUENCY BY DIRECTIONS (%) SPRING

WIND FREQUENCY BY DIRECTIONS (%) SUMMER

WIND FREQUENCY BY DIRECTIONS (%) AUTUMN

(**a**) (**b**)

(**c**) (**d**)

Figure 6. Wind frequency by directions; (**a**) winter; (**b**) spring; (**c**) summer; (**d**) autumn.

4. Discussion

This study aimed to assess the climatic wind picture along the western coast of the Black Sea, identifying its mean and maximum wind speed values each month to provide the most suitable periods in terms of wind energy potential. Moreover, the wind directions were analyzed. The outcome of this research is based on the MHD weather data over a 13-year interval (2009–2021) from seven automatic marine stations situated on lighthouses along the Romanian Black Sea coast.

An important aspect that requires more detailed investigation is the storm dynamics presented in the Black Sea. Storm dynamics in the Black Sea are complex phenomena and can be influenced by various factors. One important factor is the contrast in temperature between the sea and the surrounding land, creating instability in the atmosphere, which can lead to the development of storms. Another crucial factor is the movement of air masses. Warm, moist air from the Mediterranean Sea can move northward into the Black Sea, interacting with colder air masses from the east or west, leading to the development of storms, particularly in winter and spring.

The aim of this analysis is to identify the periods that presented storm characteristics (wind speed greater than 14 m/s). The research was based on the average stormy days from all seven stations over the 13-year interval. In January, an average of 28 stormy days was registered, the most significant dates being 3, 6, 17, 18, 22, 25, 26, 27, and 30 January. Midia station reported 52 days in January with great wind values in the evaluated period. In February, a lower value was registered—25 stormy days and once again Midia station recorded the most numerous days (45). The following days were observed with high values: 3, 17, 18, 22, 25, and 26 February. Further, in spring, the number of days with storm aspects decreases: March—12 days, April—8 days (the 20th of April represents the most energetic day concerning the storms occurring), and May—4 days. No extremes were seen in summer. In all three months of this season (June, July, and August) a value of 3 days per month was seen in terms of the average number of stormy days. Moving to the autumn season, the number of stormy days is significantly increasing. In September an average of 8 days with wind speed greater than 14 m/s was registered, Midia being again the station with the most numerous days registered (23). The average value obtained in October was 17 days which fulfilled the storm criteria, and various days were seen with high values (7, 8, 16, 17, 24, and 25 of October). November registered an average number of stormy days of 11 days. Lastly, based on the data from all seven stations, an average of 23 stormy days was obtained in December. Midia registered 45 days, whereas Mangalia obtained 43 days for the total period evaluated. The following days are noticed as dynamic ones (10, 29, 30, and 31 of December). Based on the evaluation, it is concluded that the winter months present the tendency for storms to occur (December—23 days, January—28 days, February—25 days). Moreover, it is revealed that these complex weather conditions are fulfilled in the southern part of the analyzed area. Still, no significant variations are noticed.

5. Conclusions

In the present research, the wind potential of the Romanian coast of the Black Sea was evaluated considering its main parameters (speed and direction). Based on the MHD wind datasets considering a 13-year time interval, the wind climate of the respective area was highlighted, indicating the most suitable months for strong and persistent winds. Relevant trends considering the wind dynamics were outlined, resulting from the evaluation of mean and maximum wind speed values. In addition, the wind directions issue was discussed and a summary regarding the periods in which present storm characteristics was elaborated.

From the analysis made, based on the entire data collected over the 13-year period, an average wind speed value of 4.9 m/s and a mean maximum value of 12.4 m/s were obtained. All the analyses made indicate that during winter, which is the most energetic season, strong winds are encountered and the most numerous days with storms are seen; nevertheless, unstable conditions are noticed in December and February. Moreover, it is revealed that wind speed values recorded from each station are roughly in the same sequence, although greater values were registered in the southern part of the Romanian coast. Concerning the wind directions, it was highlighted that most wind directions are from N or NW regardless of the season (winter, summer, or autumn), whereas other directions (S or SE) were seen in summer.

The Black Sea is known for its variable and sometimes unpredictable weather, including strong winds and storms, particularly during winter. These winds can reach high speeds and can create large waves and rough sea conditions. The wind's direction and strength can affect the sea's navigability and shipping safety. Strong winds and rough seas can make it difficult for vessels to maintain their course and can cause delays in shipping. On the other hand, favorable wind conditions can help to speed up the voyage and make it more efficient [40]. In conclusion, the offshore wind industry presented in

Europe has been rapidly increasing in recent years, with many nations eager to invest heavily in the development of offshore wind farms. However, this area is not considered an ideal location for offshore wind power due to its generally lower wind speeds than those in other European areas where offshore wind power is more prevalent, such as the North Sea and the Baltic Sea. Although, the present research proves that the western coast of the Black Sea has moderate to high wind resources and may be suitable for nearshore wind power generation. To sum up, more research is needed to fully understand the wind characteristics of the Black Sea and the potential for offshore or nearshore wind power in this region.

Author Contributions: Writing—review and editing, methodology, L.-I.N.; data curation, resources V.-M.T.; supervision and project administration, E.R. All authors have read and agreed to the published version of the manuscript.

Funding: This work was carried out in the framework of the research project CLIMEWAR (CLimate change IMpact Evaluation on future WAve conditions at Regional scale for the Black and Mediterranean seas marine system), supported by a grant of the Ministry of Research, Innovation, and Digitization, CNCS—UEFISCDI, project number PN-III-P4-PCE-2021-0015, within PNCDI III.

Institutional Review Board Statement: Not applicable.

Informed Consent Statement: Not applicable.

Data Availability Statement: The data that were used in the present study are available by official statement. The wind data were obtained from the Maritime Hydrographic Directorate.

Conflicts of Interest: The authors declare no conflict of interest.

References

1. Available online: https://www.interregeurope.eu/agrores/news/news-article/10859/opportunities-of-black-sea-offshore-wind/ (accessed on 29 December 2022).
2. Dragomir, G.; Şerban, A.; NĂstase, G.; Brezeanu, A.I. Wind energy in Romania: A review from 2009 to 2016. *Renew. Sustain. Energy Rev.* **2016**, *64*, 129–143. [CrossRef]
3. Aydoĝan, B.; Ayat, B.; Yüksel, Y. Black Sea wave energy atlas from 13 years hindcasted wave data. *Renew. Energy* **2013**, *57*, 436–447. [CrossRef]
4. Rusu, L.; Bernardino, M.; Soares, C.G. Wind and wave modelling in the Black Sea. *J. Oper. Oceanogr.* **2014**, *7*, 5–20. [CrossRef]
5. IslekFulya, Y.Y. Inter-comparison of long-term wave power potential in the Black Sea based on the SWAN wave model forced with two different wind fields. *Dyn. Atmos. Ocean.* **2021**, *93*, 101192.
6. Rusu, L.; Ganea, D.; Mereuta, E. A joint evaluation of wave and wind energy resources in the Black Sea based on 20-year hindcast information. *Energy Explor. Exploit.* **2018**, *36*, 335–351. [CrossRef]
7. Girleanu, A.; Onea, F.; Rusu, E. Assessment of the wind energy potential along the romanian coastal zone. *Inventions* **2021**, *6*, 41. [CrossRef]
8. Davy, R.; Gnatiuk, N.; Pettersson, L.; Bobylev, L. Climate change impacts on wind energy potential in the European domain with a focus on the Black Sea. *Renew. Sustain. Energy Rev.* **2018**, *81*, 1652–1659. [CrossRef]
9. Staneva, J.V.; Stanev, E.V. Oceanic response to atmospheric forcing derived from different climatic data sets. Intercomparison study for the Black Sea. *Oceanol. Acta* **1998**, *21*, 393–417. [CrossRef]
10. Atodiresei, D.; Toma, A.; Cotorcea, A.; Samoilescu, G. Opportunities for harnessing wind potential on board ships in the northwest area of the black sea. *Rev. Roum. des Sci. Tech. Ser. Electrotech. Energ.* **2017**, *62*, 265–268.
11. Valchev, N.; Palazov, A. Estimation of wind wave climate of the Western Black Sea during the last 50 years. In Proceedings of the Ninth International Conference on Marine Sciences and Technologies "Black Sea 2008", Varna, Bulgaria, 23–25 October 2008; pp. 232–239.
12. Onea, F.; Rusu, E. An evaluation of the wind energy in the North-West of the Black Sea. *Int. J. Green Energy* **2014**, *11*, 465–487. [CrossRef]
13. Ganea, D.; Mereuta, E.; Rusu, L. Estimation of the near futurewind power potential in the black sea. *Energies* **2018**, *11*, 3198. [CrossRef]
14. Myslenkov, S.; Zelenko, A.; Resnyanskii, Y.; Arkhipkin, V.; Silvestrova, K. Quality of the wind wave forecast in the black sea including storm wave analysis. *Sustainability* **2021**, *13*, 13099. [CrossRef]
15. Rusu, L.; Raileanu, A.B.; Onea, F. A comparative analysis of the wind and wave climate in the Black Sea along the shipping routes. *Water* **2018**, *10*, 924. [CrossRef]

16. Onea, F.; Raileanu, A.; Rusu, E. Evaluation of the Wind Energy Potential in the Coastal Environment of Two Enclosed Seas. *Adv. Meteorol.* **2015**, *2015*, 808617. [CrossRef]
17. Onea Florin, R.E. Wind energy assessments along the Black Sea basin. *Meteorol. Appl.* **2014**, *21*, 316–329. [CrossRef]
18. Diaconita, A.I.; Rusu, L.; Andrei, G. A local perspective on wind energy potential in six reference sites on the western coast of the black sea considering five different types of wind turbines. *Inventions* **2021**, *6*, 44. [CrossRef]
19. Onea, F.; Rusu, L. Evaluation of some state-of-the-art wind technologies in the nearshore of the black sea. *Energies* **2018**, *11*, 2452. [CrossRef]
20. Akpınar, A.; Bingölbali, B.; Van Vledder, G.P. Wind and wave characteristics in the Black Sea based on the SWAN wave model forced with the CFSR winds. *Ocean Eng.* **2016**, *126*, 276–298. [CrossRef]
21. Bălan, M.; Dudău, R.; Mihnea Cătuți, A.C. *Romania's Offshore Wind Energy Resources: Natural Potential, Regulatory Framework, and Development Prospects*; Energy Policy Group: Bucharest, Romania, 2020.
22. Rusu, E.; Onea, F.; Toderascu, R. Dynamics of the environmental matrix in the Black Sea as reflected by recent measurements and simulations with numerical models. In *The Black Sea: Dynamics, Ecology and Conservation*; Nova Science Publishers, Inc.: New York, NY, USA, 2011; ISBN 9781611228557.
23. Divinsky, B.; Kos'yan, R. Spatiotemporal Variability of the Black Sea Wave Climate in the Last 37 Years. *Cont. Shelf Res.* **2017**, *136*, 10–16. [CrossRef]
24. Nedelcu, L.I.; Rusu, E. An Analysis of the Wind Parameters in the Western Side of the Black Sea. *Inventions* **2022**, *7*, 21. [CrossRef]
25. Available online: https://emodnet.ec.europa.eu/geoviewer/# (accessed on 25 January 2022).
26. Nedelcu, A.T.; Atodiresei, D.; Buzbuchi, N. Oceanographic Research And Recordings Made on the North-West Coast of the Black Sea. *Int. J. Conserv. Sci.* **2020**, *11*, 615–624.
27. Available online: https://ecomareaneagra.wordpress.com/marea-neagra/clima/ (accessed on 29 December 2022).
28. Available online: https://www.fao.org/3/n7372e/N7372E02.htm (accessed on 29 December 2022).
29. Mee, L.; Maiboroda, O. *Black Sea Study Pack: A Resource for Teachers*; GEF Black Sea Ecosystem Recovery Project: Istanbul, Turkey, 2006.
30. Available online: http://www.blackseascene.net/ (accessed on 29 December 2022).
31. Amarioarei, A.; Itcus, C.; Tusa, I.; Sidoroff, M.; Paun, M. Classification of Romanian salt water lakes by statistical methods. *J. Environ. Prot. Ecol.* **2018**, *19*, 1–14.
32. Miladinova, S.; Stips, A.; Garcia-Gorriz, E.; Macias Moy, D. Black Sea thermohaline properties: Long-term trends and variations. *J. Geophys. Res. Ocean.* **2017**, *122*, 5624–5644. [CrossRef]
33. Rusu, E. Strategies in using numerical wave models in ocean/coastal applications. *J. Mar. Sci. Technol.* **2011**, *19*, 58–75. [CrossRef]
34. Stanev, E.V. Understanding Black Sea dynamics: An overview of recent numerical modeling. *Oceanography* **2005**, *18*, 56–75. [CrossRef]
35. Ortiz, C.E. *Mesoscale Circulation in the Black Sea: A Study Combining Numerical Modelling and Observations*; University of Plymouth: Plymouth, UK, 2005.
36. Soffientino, B.; Pilson, M.E.Q. The Bosporus Strait: A special place in the history of Oceanography. *Oceanography* **2005**, *18*, 16–23. [CrossRef]
37. Medvedev, I.P. Tides in the Black Sea: Observations and Numerical Modelling. *Pure Appl. Geophys.* **2018**, *175*, 1951–1969. [CrossRef]
38. Available online: https://www.dhmfn.ro/ (accessed on 29 December 2022).
39. Tanase, V.M.; Chiotoroiu, B.C.; Vatu, N. Wave energy along the Romanian Southern Black Sea coast. *J. Phys. Conf. Ser.* **2018**, *1122*, 012029. [CrossRef]
40. Nedelcu, L.; Rusu, E. Research overview concerning the maritime industry: An evaluation of the trends and topics in the Black Sea area. *Sci. Bull. Nav. Acad.* **2022**, *XXV*, 131–145. [CrossRef]

Disclaimer/Publisher's Note: The statements, opinions and data contained in all publications are solely those of the individual author(s) and contributor(s) and not of MDPI and/or the editor(s). MDPI and/or the editor(s) disclaim responsibility for any injury to people or property resulting from any ideas, methods, instructions or products referred to in the content.

inventions

Article

A Fingerprint Matching Algorithm Using the Combination of Edge Features and Convolution Neural Networks

Andreea-Monica Dincă Lăzărescu [1,2], Simona Moldovanu [1,3] and Luminita Moraru [1,4,*]

[1] The Modelling & Simulation Laboratory, Dunarea de Jos University of Galati, 47 Domneasca Str., 800008 Galati, Romania; andreea.dinca@ugal.ro (A.-M.D.L.); simona.moldovanu@ugal.ro (S.M.)
[2] Mihail Kogălniceanu High School, 161B Brăilei St., 800320 Galați, Romania
[3] Department of Computer Science and Information Technology, Faculty of Automation, Computers, Electrical Engineering and Electronics, Dunarea de Jos University of Galati, 47 Domneasca Str., 800008 Galati, Romania
[4] Department of Chemistry, Physics & Environment, Faculty of Sciences and Environment, Dunarea de Jos University of Galati, 47 Domneasca Str., 800008 Galati, Romania
* Correspondence: luminita.moraru@ugal.ro

Abstract: This study presents an algorithm for fingerprint classification using a CNN (convolutional neural network) model and making use of full images belonging to four digital databases. The main challenge that we face in fingerprint classification is dealing with the low quality of fingerprints, which can impede the identification process. To overcome these restrictions, the proposed model consists of the following steps: a preprocessing stage which deals with edge enhancement operations, data resizing, data augmentation, and finally a post-processing stage devoted to classification tasks. Primarily, the fingerprint images are enhanced using Prewitt and Laplacian of Gaussian filters. This investigation used the fingerprint verification competition with four databases (FVC2004, DB1, DB2, DB3, and DB4) which contain 240 real fingerprint images and 80 synthetic fingerprint images. The real images were collected using various sensors. The innovation of the model is in the manner in which the number of epochs is selected, which improves the performance of the classification. The number of epochs is defined as a hyper-parameter which can influence the performance of the deep learning model. The number of epochs was set to 10, 20, 30, and 50 in order to keep the training time at an acceptable value of 1.8 s/epoch, on average. Our results indicate the overfitting of the model starting with the seventh epoch. The accuracy varies from 67.6% to 98.7% for the validation set, and between 70.2% and 75.6% for the test set. The proposed method achieved a very good performance compared to the traditional hand-crafted features despite the fact that it used raw data and it does not perform any handcrafted feature extraction operations.

Keywords: convolutional neural networks; fingerprint images; data augmentation; fingerprint classification

Citation: Dincă Lăzărescu, A.-M.; Moldovanu, S.; Moraru, L. A Fingerprint Matching Algorithm Using the Combination of Edge Features and Convolution Neural Networks. *Inventions* **2022**, *7*, 39. https://doi.org/10.3390/inventions7020039

Academic Editor: Anastasios Doulamis

Received: 10 May 2022
Accepted: 26 May 2022
Published: 27 May 2022

Publisher's Note: MDPI stays neutral with regard to jurisdictional claims in published maps and institutional affiliations.

Copyright: © 2022 by the authors. Licensee MDPI, Basel, Switzerland. This article is an open access article distributed under the terms and conditions of the Creative Commons Attribution (CC BY) license (https://creativecommons.org/licenses/by/4.0/).

1. Introduction

Various approaches to automatically authenticate fingerprints for personal identification and verification have found important applications in ensuring public security and criminal investigations. A fingerprint represents a graphical pattern on the surface of a human finger expressed by ridges and valleys. Ridges are the upper skin surface parts of the finger that touch a surface, and valleys are the lower parts. In a fingerprint image, ridge lines are the dark areas, and valleys are the bright areas which represent the inter-ridge spaces. Fingerprints are unique and are the most reliable human feature which can be utilized for personal identification [1].

Automatic fingerprint identification uses fingerprint features such as ridge flow, ridge period, ridge ending, and the delta or core points for fingerprint enrollment and verification steps [2]. Matching performance is strongly affected by fingertip surface conditions such as fingerprint deformations or distortions, fingerprint collection conditions, variations in the pressure between the finger and the acquisition sensor, scars, age, race, sex, etc. Additionally, the minutiae extraction can be affected by noise, rotation, and the scale of the images or fingerprint alignment information [1–3]. There is a sinusoidal-shaped wave of ridges with some slow changes in their orientation. This characteristic defines a fingerprint pattern. However, fingerprint images are prone to structural imperfections. In order to create an accurate identification system, an effective enhancement algorithm is necessary. This algorithm can be coupled with a performance classification method [4,5]. A major limitation of fingerprint recognition algorithms is that only small-area fingerprint images are usually available to the algorithm for differential matching. This calls for a model which can solve the restoration of the whole fingerprint image to make the process of fingerprint recognition and matching more effective [6–8]. The enhancement step is based on the obvious directional behavior manifested in a fingerprint image. Some effective enhancement techniques are based on the Prewitt and Laplacian of Gaussian filters [9,10]. Additionally, a robust feature extractor and classifier must be able to deal with augmentation operations such as translation, rotation, or skin distortion.

The process of feature extraction and matching demands some preprocessing operations such as ridge enhancement (for a fingerprint structure clarity), followed by feature extraction using artificial neural networks. Recently, deep convolutional networks have been heavily used in image recognition. Most of these are devoted to a single-frame recognition with an improved classification performance [11–15]. The main advantage of CNN-based classifiers is that they are fully independent of any human actions devoted to feature extraction and classification. For large databases, the computational cost of searching for a fingerprint image is huge, but CNNs drastically reduce this burden.

In the present study, starting from the fact that the existing fingerprint recognition algorithms rely too heavily on the details of the fingerprint, a software solution was proposed to evaluate the quality of fingerprint identification by using a convolutional neural network (CNN) architecture and by calling full images belonging to four digital databases. We did not perform any handcrafted feature extraction operations. The main challenge that we face is the low quality of fingerprints, which can impede or make the identification process difficult.

The main contributions of this work are as follows:

- Despite intense development efforts, there is still one open research problem devoted to the restoration of whole fingerprint images to make the process of fingerprint recognition and matching more effective. We discuss the investigation of whole fingerprint images.
- We aim to validate the edge enhancement operations, data augmentation, and the network structure regarding the potential of a CNN architecture to accurately identify the fingerprints for a further classification task.
- The Prewitt and Laplacian of Gaussian filters are used to enhance the edges that separate the ridges and valleys in the fingerprint images. Moreover, we do not use any skeletonization operations to convert gray-scale fingerprint images to black-and-white images.
- To decrease the training time, we reduce the dimensionality of the fingerprint images from [256 × 256] to [80 × 80] pixels.
- To improve the performance of the proposed model, we use the rotation as a data augmentation technique.
- As CNNs can learn discriminative features from whole fingerprint images and they do not require explicit feature extraction to do so, the deep learning approach is an attractive option in fingerprint identification. Thus, the performance of the proposed CNN model is evaluated based on the accuracies for the training and validation tests with attention paid to the number of epochs, which is considered the hyper-parameter of the CNN that could influence the performance of the deep learning model.

The rest of this paper is organized as follows: Section 2 reviews the related literature and emphasizes the most important sources of our motivation. Also, in Section 2 the adopted methodology, the design of our CNN method, and the used databases are presented. Section 3 shows the results obtained from several experiments, discusses and evaluates the accuracy values provided by the individual systems. Finally, Section 4 provides a summary of our research and sets out our future work intentions.

2. Materials and Methods

2.1. Related Work

Over the last thirty years, there have been important developments in deep learning methods. These developments had a significant impact on a wide range of applications dealing with computer vision and pattern recognition. The research field of automatic fingerprint recognition is among the most interesting topics, due to the requirement to increase the recognition accuracy rate. Additionally, deep learning methods avoid the focus on methods devoted to minutiae extraction as handcrafted features, shifting the interest to the analysis of the whole image. The latest investigations devoted to the field of fingerprint image organization are reviewed in this section.

The most sensitive step in the fingerprint recognition scheme is image improvement. Wang et al. [16] proposed an algorithm for fingerprint image quality enhancement, i.e., to improve the clarity and continuity of ridges, based on the wavelet transform and a mechanism of compensation coefficients for each sub-band based on a Gaussian template. Yang et al. [17] presented an enhancement technique which approached both spatial and frequency domains. A spatial ridge-compensation filter was employed to enhance the fingerprint image in the spatial domain. Then, a frequency bandpass filter performed sharp attenuation of both the radial and angular-frequency domains. Shrein et al. [13] used a convolutional neural network that performed the classification tasks for fingerprints in the IAFIS (integrated automated fingerprint identification system) database with 95.9% accuracy. He has shown that precise image preprocessing, aiming to reduce the dimensionality of the feature vector, greatly decreased the training times, even in networks of moderate depth. Mohamed [14] thoroughly investigated all the factors which may affect fingerprint classification using CNNs. His proposed system consists of a preprocessing stage dealing with increasing the fingerprint quality, and a post-processing step devoted to training and classification. A resized image (its dimensions reduced from 512 × 512 pixels to 200 × 200 pixels) was created in order to reduce the training time. A classification accuracy of 99.2% with a zero rejection rate was reported. Militello et al. [15] used a pre-trained convolutional neural network and two fingerprint databases with heterogeneous characteristics (PolyU and NIST) for classification purposes. The used features were the arch, left loop, right loop, whorl, and three nets: AlexNet, GoogLeNet, and ResNet. The comparative analysis allowed the system to determine the type of classification that should be used for the best performance in terms of precision and model efficiency. Borra et al. [18] reported a method based on a denoising procedure (the wave atom transform technique), image augmentation (based on morphological operations), and an adaptive genetic neural network in order to evaluate the performance of the approach. The networks used the feature values that were extracted from each image. The experiments were performed on the FVC2000 databases. The authors reported better performance values compared to some neural networks and machine learning approaches. Listyalina et al. [19] sought to classify raw fingerprint images. They proposed a deep learning method (i.e., transfer learning GoogLeNet) which transferred the classification steps, such as pre-processing, feature extraction, and classification rather than training a deep CNN architecture. They used fingerprint images from the NIST-4 database and reported performance accuracy measures as follows: 94.7% and 96.2% for the five-class and four-class classification problems, respectively. Tertychnyi et al. [20] proposed an efficient deep neural network algorithm to recognize low-quality fingerprint images. These images are affected by physical damage, dryness, wetness, and/or blurriness. A VGG16 convolutional network model was employed based on transfer learning for training. In addition, both image dimension reduction and data augmentation were performed to improve the computing cost. They reported an average accuracy of 89.4%; this is almost the same accuracy provided by regular CNNs. Finally, Pandya et al. [21] proposed a model which encompasses a pre-processing stage (histogram equalization, enhancement based on a Gabor filter, and ridge thinning) and a classification stage using a CNN architecture. The proposed algorithm achieved a 98.21% classification accuracy with a 0.9 loss for 560 samples (56 users providing 10 images each). Overfitting was avoided by Nur-A-Alam et al. [22] using a combination of the Gabor filtering technique coupled with deep learning techniques and principal component analysis (PCA). The meaningful features that can support an automatic authentication process for the fingerprint for personal identification and verification were extracted using the fusion of CNNs and Gabor filters; PCA reduces the dimensionality of statistical features. The proposed approach reached an accuracy of 99.87%. An efficient unimodal and multimodal biometric system based on CNNs and feature selection for fast palmprint recognition was recently proposed by Trabelsi et al. [23]. Simplified Gabor–PCA convolutional networks, an enhanced feature selection method, and a "reduction of the dimensions" approach were used to achieve a high recognition rate, i.e., 0% equal error rate (meaning the best trade-off between false rejections and false acceptances) and 100% rank-one recognition (meaning the percentage of samples recognized by the system). Oleiwi et al. [24] introduced a fingerprint classification method based on gender techniques, which integrates the Wiener filter and multi-level histogram techniques with three CNNs. They used CNNs to extract the fingerprint features followed by Softmax as a classifier.

2.2. Proposed Methodology

2.2.1. Mathematical Approaches

To improve the quality of fingerprint images, the first- and second-order derivative filters were used. An image is defined by an image function $A(\boldsymbol{x}, \boldsymbol{y})$ that gives the intensity of the gray levels at pixel position (x, y). The gradient vector of the image function is defined as in [25]:

$$\nabla A(\boldsymbol{x},\boldsymbol{y}) = \left[G_x G_y\right] = \left[\frac{\partial A(\boldsymbol{x},\boldsymbol{y})}{\partial x}\ \frac{\partial A(\boldsymbol{x},\boldsymbol{y})}{\partial y}\right] \tag{1}$$

- Prewitt Operator

The Prewitt filter detects the vertical and horizontal directions of the edges of an image by locating those pixel values defined by steep gray values [26]. The Prewitt operator consists of two 3 × 3 convolution masks [25–27]:

$$G_y = \begin{bmatrix} +1 & 0 & -1 \\ +1 & 0 & -1 \\ +1 & 0 & -1 \end{bmatrix} * A(\boldsymbol{x},\boldsymbol{y}) \tag{2}$$

$$G_x = \begin{bmatrix} +1 & +1 & +1 \\ 0 & 0 & 0 \\ -1 & -1 & -1 \end{bmatrix} * A(\boldsymbol{x},\boldsymbol{y}) \tag{3}$$

where A is the image source and * is the 2D convolution operation.

- The Laplacian operator

The Laplace operator is computed using the second-order derivative approximations of the image function $A(\boldsymbol{x}, \boldsymbol{y})$. It is noise sensitive, so it is often combined with a Gaussian filter to decrease the sensitivity to noise [28]. The Laplacian filter searches the zero crossing points of the second-order derivatives of the image function and establishes the rapid changes in adjacent pixel values that belong to an edge [28,29].

$$\nabla^2 A(\boldsymbol{x},\boldsymbol{y}) = \frac{\partial^2 A(\boldsymbol{x},\boldsymbol{y})}{\partial x^2} + \frac{\partial^2 A(\boldsymbol{x},\boldsymbol{y})}{\partial y^2} \tag{4}$$

A zero value indicates the areas of constant intensity, while values < 0 or > 0 are placed in the vicinity of an edge.

- The Laplacian of Gaussian (*LoG*) operator

For an image $A(x, y)$ with pixel intensity values (x, y), a combination of the Laplacian and Gaussian functions generates a new operator *LoG* [20], centered on zero and with a Gaussian standard deviation σ:

$$LoG(x,y) = -\frac{1}{\pi\sigma^4}\left[1 - \frac{x^2+y^2}{2\sigma^2}\right]e^{-\frac{x^2+y^2}{2\sigma^2}} \tag{5}$$

The Gaussian operator suppresses the noise before using the Laplace operator for edge detection. The *LoG* operator detects areas where the intensity changes rapidly, namely the function's values are positive on the darker side (pixel values close to 0) and negative on the brighter side (pixel values close to 255) [30].

2.2.2. Dataset

The analyzed fingerprint images belong to the FVC2004 database, which is the property of the University of Bologna, Italy [31]. The image data are described, in detail, in Table 1.

Table 1. Dataset characteristics.

FVC2004 Datasets	Fingerprint Scanner	Image Size	Fingerprint Images	Total Image Number after Augmentation
BD1	Optical sensor "V300" by CrossMatch	640 × 480	80	720
BD2	Optical sensor "U.are.U 4000"	328 × 364	104	936
BD3	Thermal Sweeping Sensor "FingerChip FCD4B14CB" by Atmel	300 × 480	104	936
BD4	Synthetic fingerprint generator	288 × 384	104	936

In order to enhance the limitations of low-quality fingerprint images, both the Prewitt and *LoG* filters were used to enhance the edges that separate the ridges and valleys in the fingerprint images [9,10]. Figure 1 displays examples of image enhancement from each used database and filter.

2.2.3. Data Augmentation

The optimization of a CNN which uses small datasets means avoiding the network convergence to a local minimum. This issue is overcome using augmentation to extend the training dataset and to prevent the issue of overfitting during training. The number of images has been increased nine times. Data augmentation has been performed by executing ±30° rotations, from 0° to 360°. This provided a total of 3528 images, of which 2469 were used as training samples. Additionally, each image was resized from 256 × 256 pixels to 80 × 80 pixels to be more suitable to be fed into the network and to reduce the training time. Figure 2 shows an example of data augmentation.

2.2.4. Convolutional Neural Network

A CNN architecture aggregates convolutional modules that perform feature extraction, pooling, and fully connected layers [32]. CNNs perform well in recognition of images tasks. To optimize the performance of a CNN model, it has to be trained to extract the most important deep discriminatory features. As a general description of a CNN architecture and its learning strategy, we could mention that a gradual training process designed to solve complex concepts is employed. Thus, the early layers detect the general features of a given image. Furthermore, from layer to layer the convolution filters are trained to detect more and more complex patterns, such as object features (Figure 3). The model architecture is given in Table 2. The parameter settings and some hyperparameters selected for the proposed CNN model are also presented (Table 3). They were established before training. An epoch means the whole dataset passes once forward and backward through the neural network. Usually, the number of epochs is determined when the validation accuracy starts decreasing, even if the training accuracy is still increasing. In addition, one epoch is too large to be run through the model as a whole, so it is divided into several smaller subsamples called batches. A higher number of epochs increases the cost of computational complexity and the risk of overfitting, respectively. The variation in the number of epochs stops when the validation loss no longer improves.

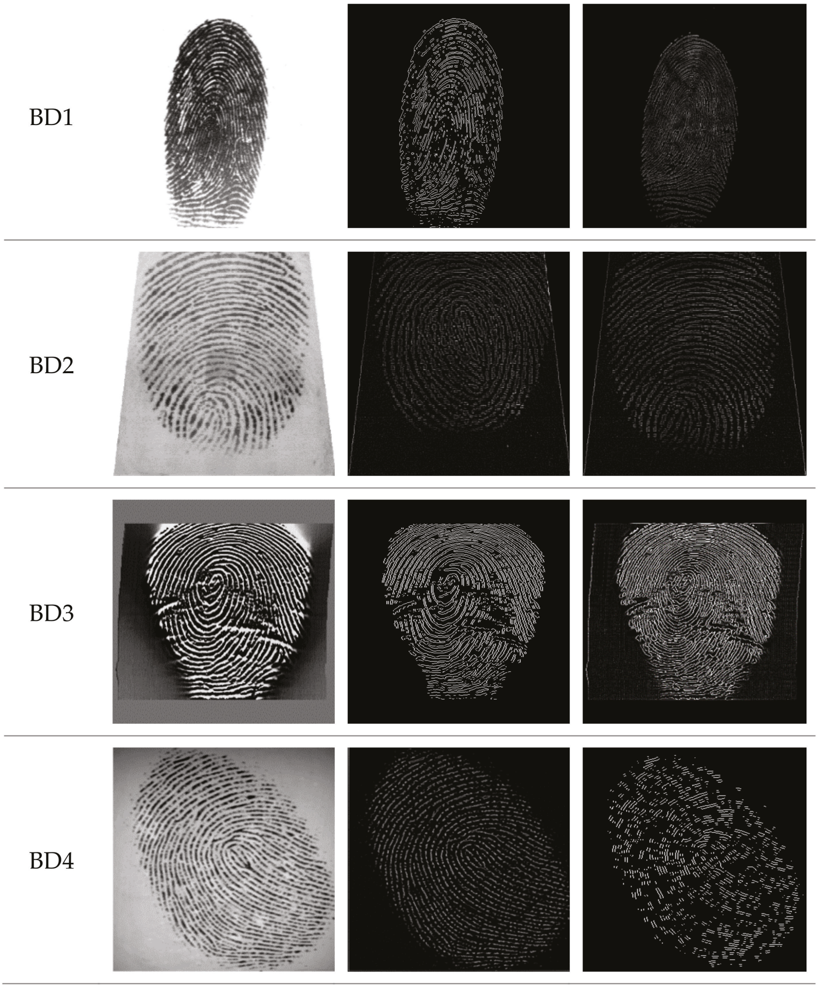

Figure 1. Samples of fingerprints from our evaluation datasets and examples of enhanced fingerprint images. Columns: **left**—raw grayscale images; **middle**—edge enhancement using the Prewitt filter; **right**—edge enhancement using the *LoG* filter.

Figure 2. Data augmentation. Rotated fingerprint on ±30°.

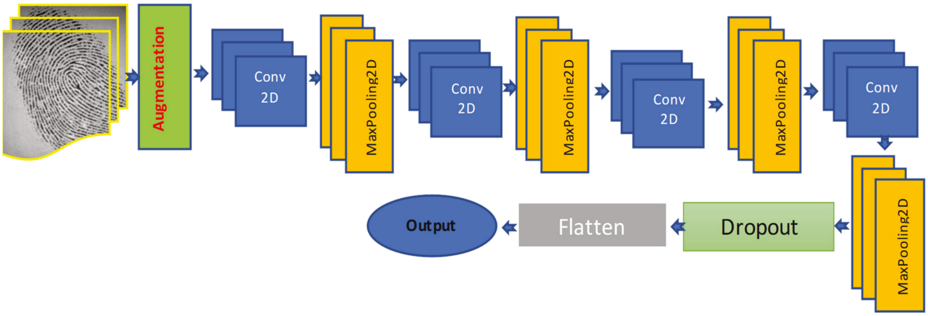

Figure 3. CNN model architecture.

Table 2. Model architecture and parameter settings.

Layer (Type)	Output Shape	Param
sequential_11 (Sequential)	(None, 80, 80, 3)	0
rescaling_7 (Rescaling)	(None, 80, 80, 3)	0
conv2d_27 (Conv2D)	(None, 80, 0, 8)	224
max_pooling2d_27 (MaxPooling2D)	(None, 40, 40, 8)	0
conv2d_28 (Conv2D)	(None, 40, 40, 16)	1168
max_pooling2d_28 (MaxPooling2D)	(None, 20, 20, 16)	0
conv2d_29 (Conv2D)	(None, 20, 20, 32)	4640
max_pooling2d_29 (MaxPooling2D)	(None, 10, 10, 32)	0
conv2d_30 (Conv2D)	(None, 10, 10, 64)	18,496
max_pooling2d_30 (MaxPooling2D)	(None, 5, 5, 64)	0
dropout_7 (Dropout)	(None, 5, 5, 64)	0
flatten_7 (Flatten)	(None, 1600)	0
dense_14 (Dense)	(None, 128)	204,928
dense_15 (Dense)	(None, 3)	387

Total parameters: 229,843; Trainable parameters: 229,843; 'None' indicates that any positive integer may be expected so that the model is able to process batches of any size.

Table 3. The hyper-parameters of the CNN model.

Hyper-Parameters	Name/Dimension
Epochs	10, 20, 30, 50
Batch size	20
Activation function	ReLU
Image size	80 × 80
Time consuming/20 epochs	23 s
Learning rate	0.01

The convolutional layers extract features from the input images. The size of the input image is reduced by the pooling layers. In addition, these pooling layers collect features, and their basic task is to reduce the feature dimensions or to reduce the feature map size by using the ReLU (rectified linear unit) activation function. The ReLU function does not activate all the neurons at the same time. If the output of the linear transformation is negative, the neurons are deactivated. The fully connected or dense layers exploit the learned high-level features and act as classifiers. Additionally, to reduce overfitting and enhance the CNN performance, a large amount of data is required. This issue is overcome by augmentation. To evaluate the performance of the proposed method, the accuracy of fingerprint identification is calculated [33].

3. Results and Discussion

The experiment was carried out in MATLAB R2018a (The MathWorks, Natick, MA, USA), using the proposed approach and the image processing toolbox. The CNN was implemented using Python (Jupyter Notebook) and the open-source platform Keras for the TensorFlow machine learning toolbox. It is run in Google Colaboratory (Colab).

The image datasets were stored in Google Drive and the workspaces were connected. Of the total dataset, 60%, 20%, and 20% were used as the training set, validation set, and test set, respectively. The performance of the CNN model training and validation classification accuracy rate over the 10, 20, 30, and 50 epochs are shown in Figures 4–7. The classification accuracy is defined as the ratio between the correct predictions and the total number of predictions in the training or validation data.

As shown in Figures 4–7, during the training of the CNN, the accuracy of the training set (blue line) continued to increase and the network was learning constantly. The validation set (orange line) first increased, then overfitting occurred and the accuracy showed an unstable variation. The same behavior was observed for loss curves. Consequently, we investigated the number of epochs and selected the best number to solve the overfitting problem.

The number of epochs was set to 10, 20, 30, and 50 in order to keep the training time at an acceptable value of 1.8 s/epoch, on average. Prior to each training epoch, the training data was randomly shuffled. The performance of the proposed model is summarized in Table 4.

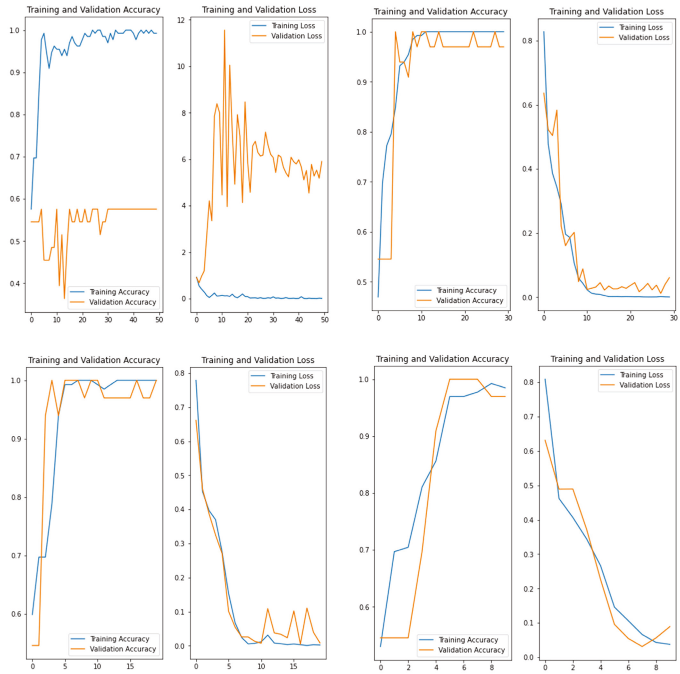

Figure 4. Illustration of model accuracy rate for 50, 30, 20, and 10 epochs for DB1 dataset acquired using an optical sensor "V300" by CrossMatch.

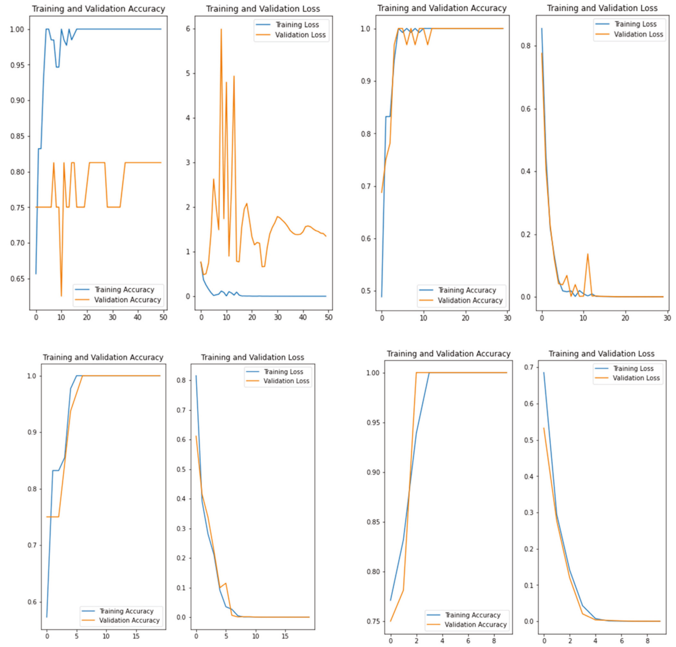

Figure 5. Illustration of model accuracy rate for 50, 30, 20, and 10 epochs for DB2 dataset acquired using an optical sensor "U.are.U 4000".

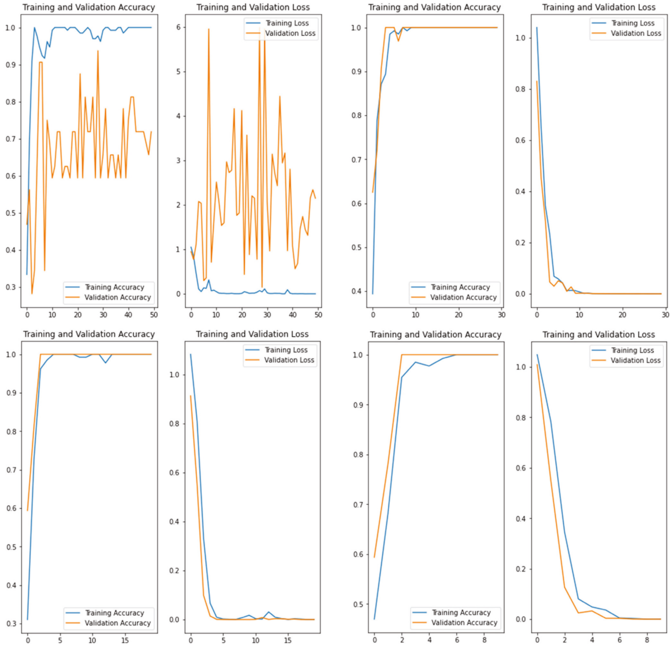

Figure 6. Illustration of model accuracy rate for 50, 30, 20, and 10 epochs for DB3 dataset acquired using a thermal sweeping sensor "FingerChip FCD4B14CB" by Atmel.

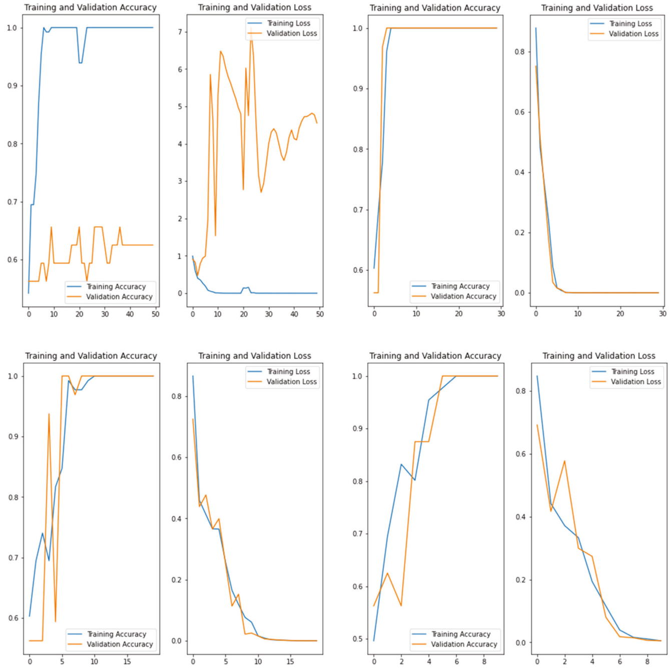

Figure 7. Illustration of model accuracy rate for 50, 30, 20, and 10 epochs for DB4 dataset generated as synthetic fingerprints.

Table 4. The performance of the proposed model.

Database	Number of Test Samples	Validation Accuracy (%)	Validation Loss	Test Accuracy (%)	
				Prewitt Filter	*LoG* Filter
BD1	144	98.7	0.0586	69.8	75.6
BD2	187	67.6	3.1061	62.5	70.2
BD3	187	94.7	0.1931	71.6	73.4
BD4	187	98.7	0.0344	69.8	75.6

The results in Figures 4–7 indicate that, while the accuracy and loss of the training data have very good values, the accuracy and loss of the validation dataset is influenced by the epoch number, indicating the existence of overfitting or underfitting. Our data indicates the overfitting of the model starting with the seventh epoch. In this case, it is necessary to stop the model early by tuning the hyperparameter. The CNN performance is strongly influenced by the quality of a fingerprint image and by its local and global structures. The accuracy of the proposed CNN model depends on the amount and quality of the training images, which in our case show an important variability from dataset to dataset. The performance on the test data (20% of each dataset) is lower than the accuracy provided by the training data, with the amendment that the number of samples is reduced for the test set. However, the LoG filter increased the accuracy compared to the Prewitt filter, and it is a better solution to enhance the edges in the fingerprint images. Additionally, the raw images in the DB2 dataset that were acquired using the optical sensor "U.are.U 4000" had a low quality that affected the performance of the classification.

According to the data in Table 4, the accuracy values determined in the training and validation sets are in line with the reported results in the literature. In [3], an accuracy of 85% was reported for images belonging to the FVC2004 database which were processed using a CNN-based automatic latent fingerprint matching system which uses the local minutiae features. Mohamed et al. [14] reported a 99.2% classification accuracy for the training set in an experiment which used the NIST DB4 dataset and 4000 fingerprint images. Militello et al. [15] reported an accuracy value of 91.67% for a pre-trained CNN, used together with the PolyU and NIST fingerprint databases.

The accuracy values determined for the test set were slightly worse, thus indicating a smaller drop in performance. However, we have mentioned that our proposed method used the whole fingerprint images and the computation time is small compared to the other reported method. As an example, in [34], an accuracy of 94.4% and a testing time of 39 ms/image were reported for a pre-trained CNN architecture of the VGG-F network type, and an accuracy of 95.05% and a testing time of 77 ms/image for the VGG-S network.

In addition, CNN architectures have some drawbacks, such as a poor generalization capacity, a requirement for a huge training dataset, and a low stability to geometrical deformation and rotation. In the proposed study, the low generalization capacity was overcome by increasing the training data size to allow the network to train on as many samples as possible. The obtained results indicate that the CNN performance is greatly influenced by the quality of the fingerprint images. The low stability of the network is due to the diversity of finger scanners which were used to acquire the fingerprints, such as optical and thermal sweeping sensors, and synthetic fingerprints as well. Finding a solution to provide a good performance of classification for this variety of data was a big challenge for our method. Our approach integrates the monitoring of training and validation by setting the number of epochs as a form of regularization, and learning curve graphs to decide on the model convergence.

4. Conclusions

The work conducted in this paper is mainly devoted to fingerprint identification using a CNN network that can perform fingerprint classification by considering whole fingerprint images. The proposed algorithm uses poor-quality original raw fingerprint images. These were processed using Prewitt and Laplace filters to enhance the edges and, in order to reduce the expensive training cost, data resizing was applied. Hyper-parameter tuning, using various epoch numbers, was considered to improve the performance of classification. Our results indicate the overfitting of the model starting with the seventh epoch. The classification accuracy varied from 67.6% to 98.7% for the validation set, and from 70.2% to 75.6% for the test set. Following these considerations, we would argue that the proposed method can achieve a very good performance compared to the traditional hand-crafted features method, despite the fact that it uses raw data and does not perform any handcrafted feature extraction operations.

For future developments, we are interested in improving the performance of classification by using other pre-processing techniques correlated to extensive hyper-parameter tuning. Additionally, other fingerprint databases will be used to assess the generalization capabilities of CNN architectures.

Author Contributions: Conceptualization, S.M. and L.M.; methodology, S.M. and L.M.; software, S.M., A.-M.D.L. and L.M.; validation, S.M. and A.-M.D.L.; formal analysis, A.-M.D.L.; investigation, S.M. and A.-M.D.L.; writing—original draft preparation, S.M., A.-M.D.L. and L.M.; writing—review and editing, S.M. and L.M. All authors have read and agreed to the published version of the manuscript.

Funding: This research received no external funding.

Institutional Review Board Statement: Not applicable.

Informed Consent Statement: Not applicable.

Data Availability Statement: Not applicable.

Acknowledgments: The authors thank the anonymous referees whose comments helped to improve the paper.

Conflicts of Interest: The authors declare no conflict of interest.

References

1. Jain, A.K. An Introduction to Biometric Recognition. *IEEE Trans. Circuits Syst. Video Technol.* **2004**, *14*, 4–20. [CrossRef]
2. Maltoni, D.; Maio, M.; Jain, A.K.; Prabhakar, S. Fingerprint analysis and representation. In *Handbook of Fingerprint Recognition*; Springer Professional Computing; Springer: New York, NY, USA, 2003; pp. 83–130.
3. Deshpande, U.U.; Malemath, V.S.; Patil Shivanand, M.; Chaugule Sushma, V. A Convolution Neural Network-based Latent Fingerprint Matching using the combination of Nearest Neighbor Arrangement Indexing. *Front. Robot. AI* **2020**, *7*, 113. [CrossRef] [PubMed]
4. Militello, C.; Conti, V.; Sorbello, F.; Vitabile, S. A novel embedded fingerprints authentication system based on singularity points. In Proceedings of the Second International Conference on Complex, Intelligent and Software Intensive Systems (CISIS 2008), Technical University of Catalonia, IEEE Computer Society, Barcelona, Spain, 4–7 March 2008; pp. 72–78.
5. Conti, V.; Militello, C.; Sorbello, F.; Vitabile, S. Introducing pseudo-singularity points for efficient fingerprints classification and recognition. In Proceedings of the 4th International Conference on Complex, Intelligent and Software Intensive Systems (CISIS-2010), Krakow, Poland, 15–18 February 2010; pp. 368–375.
6. Saponara, S.; Elhanashi, A.; Zheng, Q. Recreating Fingerprint Images by Convolutional Neural Network Autoencoder Architecture. *IEEE Access* **2021**, *9*, 147888–147899. [CrossRef]
7. Deshpande, U.U.; Malemath, V.S.; Chaugule, S.V. Automatic latent fingerprint identification system using scale and rotation invariant minutiae features. *Int. J. Inf. Tecnol.* **2022**, *14*, 1025–1039. [CrossRef]
8. Wang, T.; Zheng, Z.; Bashir, A.K.; Jolfaei, A.; Xu, Y. FinPrivacy. A privacy-preserving mechanism for fingerprint identification. *ACM Trans. Int. Technol.* **2021**, *21*, 56. [CrossRef]
9. Dhar, R.; Gupta, R.; Baishnab, K.L. An analysis of Canny and Laplacian of Gaussian image filters in regard to evaluating retinal image. In Proceedings of the International Conference on Green Computing Communication and Electrical Engineering (ICGCCEE), Coimbatore, India, 6–8 March 2014.
10. Kumar, S.N.; Fred, L.; Haridhas, A.K.; Varghese, S. Medical image edge detection using gauss gradient operator. *J. Pharm. Sci. Res.* **2017**, *5*, 695–704.
11. Szegedy, C.; Ioffe, S.; Vanhoucke, V.; Alemi, A. Inception-v4, Inception-Resnet and the impact of residual connections on learning. In Proceedings of the AAAI Conference on Artificial Intelligence, San Francisco, CA, USA, 4–9 February 2017.

12. Zhu, Y.; Yin, X.; Jia, X.; Hu, J. Latent fingerprint segmentation based on convolutional neural networks. In Proceedings of the IEEE Workshop on Information Forensics and Security, Rennes, France, 4–7 December 2017; pp. 1–6.
13. Shrein, J.M. Fingerprint classification using convolutional neural networks and ridge orientation images. In Proceedings of the IEEE Symposium Series on Computational Intelligence (SSCI), Honolulu, HI, USA, 7 November–1 December 2017.
14. Mohamed, M.H. Fingerprint Classification Using Deep Convolutional Neural Network. *J. Electr. Electron. Eng.* **2021**, *9*, 147–152. [CrossRef]
15. Militello, C.; Rundo, L.; Vitabile, S.; Conti, V. Fingerprint Classification Based on Deep Learning Approaches: Experimental Findings and Comparisons. *Symmetry* **2021**, *13*, 750. [CrossRef]
16. Wang, J.-W.; Tuyen Le, N.; Wang, C.-C.; Lee, J.-S. Enhanced ridge structure for improving fingerprint image quality based on a wavelet domain. *IEEE Signal Process. Lett.* **2015**, *22*, 390–394. [CrossRef]
17. Yang, J.; Xiong, N.; Vasilakos, A.V. Two-stage enhancement scheme for low-quality fingerprint images by learning from the images. *IEEE Trans. Hum. Mach. Syst.* **2013**, *43*, 235–248. [CrossRef]
18. Borra, S.R.; Jagadeeswar Reddy, G.; Sreenivasa Reddy, E. Classification of fingerprint images with the aid of morphological operation and AGNN classifier. *Appl. Comput. Inform.* **2018**, *14*, 166–176. [CrossRef]
19. Listyalina, L.; Mustiadi, I. Accurate and low-cost fingerprint classification via transfer learning. In Proceedings of the 2019 5th International Conference on Science in Information Technology, Yogyakarta, Indonesia, 23–24 October 2019.
20. Tertychnyi, P.; Ozcinar, C.; Anbarjafari, G. Low-quality fingerprint classification using deep neural network. *IET Biom.* **2018**, *7*, 550–556. [CrossRef]
21. Pandya, B.; Cosma, G.; Alani, A.A.; Taherkhani, A.; Bharadi, V.; McGinnity, T.M. Fingerprint classification using a deep convolutional neural network. In Proceedings of the 2018 4th International Conference on Information Management, Oxford, UK, 25–27 May 2018.
22. Nur-A, A.; Ahsa, M.; Based, M.A.; Kowalski, M. An intelligent system for automatic fingerprint identification using feature fusion by Gabor filter and deep learning. *Comput. Electr. Eng.* **2021**, *95*, 107387. [CrossRef]
23. Trabelsi, S.; Samai, D.; Dornaika, F.; Benlamoudi, A.; Bensid, K.; Taleb-Ahmed, A. Efficient palmprint biometric identification systems using deep learning and feature selection methods. *Neural Comput. Appl.* **2022**, 1–23. [CrossRef]
24. Oleiwi, B.K.; Abood, L.H.; Farhan, A.K. Integrated different fingerprint identification and classification systems based deep learning. In Proceedings of the 2022 International Conference on Computer Science and Software Engineering (CSASE), Duhok, Iraq, 15–17 March 2022; pp. 188–193.
25. Kumar, S.; Singh, M.; Shaw, D.K. Comparative Analysis of Various Edge Detection Techniques in Biometric. *Int. J. Eng. Technol.* **2016**, *8*, 2452–2459. [CrossRef]
26. Moldovanu, S.; Moraru, L.; Stefanescu, D.; Bibicu, D. Edge-preserving filters in a boundary options context. *Ann. Dunarea Jos Univ. Galati Math. Phys. Theor. Mech.* **2017**, *1*, 51–57.
27. Sun, Q.; Hou, Y.; Tan, Q.; Li, C.; Liu, M. A robust edge detection method with sub-pixel accuracy. *Optik JLEO* **2014**, *125*, 3449–3453. [CrossRef]
28. Baareh, A.; Al-Jarrah, A.; Smadi, A.; Shakah, G. Performance Evaluation of Edge Detection Using Sobel, Homogeneity and Prewitt Algorithms. *J. Softw. Eng. Appl.* **2018**, *11*, 537–551. [CrossRef]
29. Cui, S.; Wang, Y.; Qian, X.; Deng, Z. Image Processing Techniques in Shockwave Detection and Modeling. *J. Signal Inf. Process.* **2013**, *4*, 109–113. [CrossRef]
30. Moraru, L.; Moldovanu, S.; Pană, L. Edges identification based on the derivative filters and fractal dimension. *Ann. Dunarea Jos Univ. Galati Math. Phys. Theor. Mech.* **2019**, *1*, 34–42. [CrossRef]
31. FVC2004: Third Fingerprint Verification Competition. Available online: http://bias.csr.unibo.it/fvc2004/databases.asp (accessed on 10 February 2022).
32. Canziani, A.; Paszke, A.; Culurciello, E. An analysis of deep neural network models for practical applications. *arXiv* **2016**. [CrossRef]
33. Damian, F.; Moldovanu, S.; Moraru, L. Color space influence on ANN skin lesion classification using statistics texture feature. *Ann. Dunarea Jos Univ. of Galati Math. Phys. Theor. Mech.* **2021**, *1*, 53–62. [CrossRef]
34. Michelsanti, D.; Ene, A.; Guichi, Y.; Stef, R.; Nasrollahi, K.; Moeslund, T.B. Fast fingerprint classification with deep neural networks. In *Proceedings of the 12th International Joint Conference on Computer Vision, Imaging and Computer Graphics Theory and Applications, VISAPP, Porto, Portugal, 27 February–1 March 2017*; Scitepress: Setúbal, Portugal, 2017; Volume 5, pp. 202–209.

inventions

MDPI

Article

Study on the Design Stage from a Dimensional and Energetic Point of View for a Marine Technical Water Generator Suitable for a Medium Size Container Ship

Catalin Faitar [1,2,*] and Eugen Rusu [1]

[1] Department of Mechanical Engineering, Dunărea de Jos University of Galaţi, 47 Domnească Street, 800201 Galaţi, Romania
[2] Faculty of Naval Electromechanics, Maritime University of Constanta, 104 Mircea cel Batran Street, 900663 Constanta, Romania
* Correspondence: catalin.faitar@cmu-edu.eu

Abstract: The purpose of this study is to provide an overview of the development of the modern low-speed marine two-stroke diesel engine from the point of view of the technical water cooling plant, taking into account and starting from the market requirements for power and speed, with information and design options relevant to the entire shipping industry. Thus, through the ideas of this project, we analyze notions and relevant aspects of systems related to marine slow turning engines, including the basic thermodynamic structure of the technical water system designed for a marine engine. This study also presents the design criteria that define the size and design concept of the engine structure components, with a focus on the technical water cooling installation. The concepts for the main engine hot parts served by the technical water cooling installation play a vital role in the marine technical water generator. The choices the engine designer must make regarding basic auxiliary systems, such as fuel injection and exhaust valve actuation, are important factors to keep in mind when installing a technical water generator onboard a ship. The automation and control systems that govern the modern electronic engine, which drive the supply pump of the technical water cooling system can provide a simplified view of the engine development process. In order to point out the contributions of this study, it is important to focus on the calculations used to determine the main parameters of a technical water generator especially designed for a midsized container ship.

Keywords: technical; desalination; marine; seawater; operation; generator

Citation: Faitar, C.; Rusu, E. Study on the Design Stage from a Dimensional and Energetic Point of View for a Marine Technical Water Generator Suitable for a Medium Size Container Ship. *Inventions* **2023**, *8*, 22. https://doi.org/10.3390/inventions8010022

Academic Editor: Said Al-Hallaj

Received: 21 November 2022
Revised: 4 January 2023
Accepted: 9 January 2023
Published: 12 January 2023

Copyright: © 2023 by the authors. Licensee MDPI, Basel, Switzerland. This article is an open access article distributed under the terms and conditions of the Creative Commons Attribution (CC BY) license (https://creativecommons.org/licenses/by/4.0/).

1. Introduction

The requirements for the hot components of marine main engines are diverse and often conflict with each other. The temperatures of the components can reach values of 600 °C and even above, and these factors presuppose the correct choice of material and adequate cooling of these parts. Thermal stresses caused by temperature gradients must be considered in the analysis of low cycle behavior [1]. The components around the combustion space are bolted together with elastic pins, which are pre-tensioned so that there is no leakage and no dynamic sliding between the components.

Finding the adequate cooling principle is one of the main challenges for the piston designer. With the so-called jet cooling principle, which is applied to most marine main engines, it is possible to keep temperatures below the limit on the side of the combustion space as well as in the cooling holes. High temperatures (above expected values) for the piston tip would lead to material loss due to corrosive attack generated by the combustion gases. Excessive temperatures in the cooling space can lead to the accumulation of carbon deposits in solid form, with negative consequences for the cooling efficiency of the piston. For reliable engine operation, it is also necessary to maintain the temperatures around the piston rings within a certain predefined range.

It is important to keep in mind the basic knowledge regarding the cooling principles of the main components of a marine engine, especially when the main cooling fluid is salt water, which can damage sensitive parts built out of special materials and alloys. That is why technical water generators play such a crucial role in the operation of marine engines in an environment where fresh water is quite scarce. These systems have progressed in such a manner that they can sustain the optimal operation of 15.000 kW to 20.000 kW marine engines [2]. Technical water generators, also known as desalination systems/plants, have been used in the marine industry for quite some time now, but companies always try to improve their design and increase the degree of their usability [3].

Nevertheless, the authors would like to point out that the concept discussed in this paper represents a generalized configuration, one that could be applied to many similar systems that already exist in the technical water generating field as well as in the marine domain. Thus, the analysis and reinterpretations tend towards a generalized system customized for certain operating conditions onboard a commercial ship. That is why we have based our concept on the dimensioning of a technical water generator using established calculation principles to identify an optimal solution for a medium-sized container ship.

Similar concepts have also been addressed by other engineers, one patent relating to a marine water tank, and more particularly, to a marine water tank comprising an evaporation unit producing fresh water using the latent heat of steam [4]. This concept has been proposed a Korean scientist, via the application PCT/KR2013/010944.

The well-known Japanese marine systems company Mitsubishi, through application JP56164324A, developed a concept used to construct a water-making device for ships which uses the heat of heating fluid without the need for any evacuating means by providing a nozzle for ejecting supplied seawater directly toward the heat transfer tubes on the upper stage side of a heater. The concept provides an evacuating means such as orifice to a pipeline for supplying the seawater to said nozzle. This concept was used for a technical water generator installed on an oil tanker in 1995 [5].

On a different level, in 2017 a Russian scientist applied (application RU2017100751A) for a patent regarding an invention that relates to the field of machine building, in particular to seawater desalination installations (desalination units). The proposed desalination unit has at least two tanks to be filled with steam. Thermal compression of the steam in these steam tanks is performed by electric heaters [6]. Compressed steam is directed to the evaporator unit periodically from the first and second steam tanks. Removal of the remaining steam from the tanks is carried out in the low-pressure steam supply pipeline, using the heat of this steam to heat seawater. Supply, withdrawal and removal of steam from the steam tanks is regulated by the control system with the help of locking bodies.

More recently, Japanese scientists tried to invent and build a more complex system consisting of plants characterised by more than one engine delivering power external to the plant, the engines being driven by different fluids [7]. The engine cycles use thermally coupled combustion heat from one cycle to heat the fluid in another cycle with exhaust fluid of one cycle heating the fluid in another cycle. The potential of this concept has been presented in the application JP2018513870A.

2. Materials and Methods

In the first part of this study, special attention will be paid to the targeted compromise in terms of reliability, cost, manufacturability and maintainability of technical water generators, these being the aspects that challenge an engine designer (so-called licensor) to develop a competitive product to its customers, which are obviously shipowners, but also (licensed) engine manufacturers and shipyards. In addition, the tools and methods available for designing a technical water generator will be described in the context of the development process.

Furthermore, in subsequent sections, a detailed analysis of technical water generators is provided. Among the installations supporting the operation of a marine engine onboard a medium-sized container ships, we choose to examine the technical water cooling installation since it is not a very complex installation, but one that plays a crucial role in defining the life span of the main engine [8].

The main technical water sources onboard ships are briefly described in the third part of this study. It is important to underscore the fact that these systems have progressed, allowing ships to use additional spaces onboard (such as tanks) for other purposes than transporting fresh water.

Today, there are many types of technical water generators used in various industries. Depending on the main application domain, they vary in operational complexity. A brief classification is provided in the fourth section with a focus on the main processes used onboard ships to generate technical water.

In order to determine the amount of technical water required for a main engine onboard a medium-sized container ship, in the fifth section, we calculate the dimensioning of technical water generator installation, starting from the premise that all the essential data relating to engine power, vessel size, technical water requirements and other relevant data are known. The container ship used is part of the Panamax category.

Assuming that the dimensioning calculation meets our objectives, we establish an optimal model of a technical water generator which meets the requirements of the ship's main engine and which ensures its operation at the nominal parameters during a voyage of normal duration. Afterwards, taking into account the dimensional and energy constraints onboard the ship, in the final part of the study, we present a method to optimize the operation of the technical water generator. In this way, a series of technologies suitable for this type of system are identified after studying similar models already tested in the marine market.

Seawater contains a high percentage of salts, which makes it unusable for the sanitary installations on ships or as a heating agent in the power installations. Overall, seawater salinity is defined as the weight of all ions contained in a liter of water and is expressed in g/L [9]. Salinity depends on the geographical area; its average value can be considered 33–37 g/L.

Obtaining technical water or fresh water from seawater is carried out in complex installations based on various functional principles. The thermal installations for desalination by distillation and by freezing have been known for a long time. For the purpose of This study examines the operation of common commercial marine technical water generator units which are mainly based on commercial thermal units, most of which can be found on cargo ships and in other marine applications (e.g., oil rigs and passenger ships).

The desalination mechanism can be easily explained if we use a simplified representation of the composition of seawater that includes only water molecules, Na^+ and Cl^- ions. Water molecules, considered as dipoles, surround the ions, forming a layer of molecules attached to the ions by electrostatic forces. The ensemble formed by ions and attached molecules is much larger than the free molecules, and for desalination the two parts must be separated. For technical water to be usable, the salt content must be below 10 p.p.m. (parts per million). When the salt concentration is 18–19 p.p.m. the water can be used for cooling, and if this concentration is even lower (1…3) p.p.m., the water can be used to feed the boilers. Desalination of seawater, in order to use it as technical or drinking water, can be carried out industrially through the following different processes [3,10,11]:

- Distillation;
- Freezing, which can be
  - Direct freezing under vacuum, through vapor absorption;
  - Direct freezing under vacuum, by vapor compression;
  - Indirect freezing with secondary refrigerant (classical method);
  - Indirect freezing with n-butane type secondary refrigerant.
- Reverse osmosis [12].

The conceptual process described in this study is designed to produce boiler feed water with a salinity of <5 p.p.m. The first methods those listed above can be achieved by applying the phase-changing process, which involves high energy consumption and are already considered classics. All processes related to desalination are based on the physical and sometimes chemical properties of both pure water and aqueous solutions (electrolytes), as seawater is considered to be an electrolytic solution.

Taking into account the low energy consumption and the easy maintenance of a technical water generator (or the marine plant) that operates on the basis of reverse osmosis, the quality of the water thus obtained will be reviewed [8,13].

Reverse osmosis is essentially a special process of ultrafiltration of a saline solution using semipermeable synthetic membranes with an appropriate chemical constitution instead of a filter with a porous structure. If appropriate pressure is applied to the saline water in a vessel, which is in contact with such a membrane, the pure water will pass through it, the hydrated ions being retained. Reverse osmosis has practical applications in technical water generators used onboard ships [14].

The principle of reverse osmosis can be better understood if we know the phenomenon of osmosis, which is explained as follows: when two aqueous solutions of unequal concentrations (one concentrated and the other diluted) or a solution and pure water are separated by a membrane of a certain type, water molecules from pure water, or the dilute solution, pass through the membrane into the concentrated solution [15,16].

The principle behind the operation of the electrodialysis process of a marine technical water generator is shown in Figure 1:

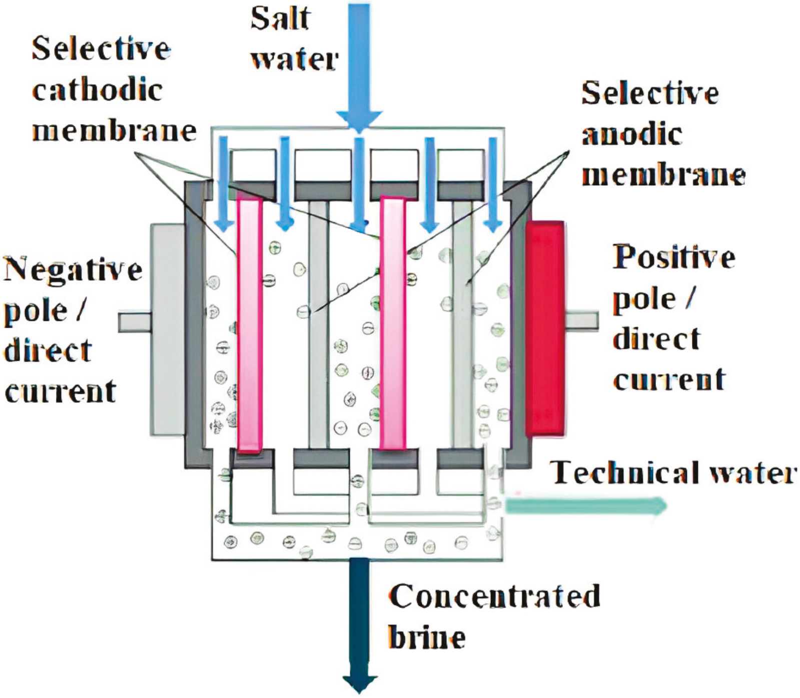

Figure 1. The principle of operation of the electrodialysis process of a marine technical water generator [drawn by the authors].

For many years, increasing interest has been shown in the conversion of seawater into drinking or technical water. To meet the growing need for technical water both onshore and onboard ships, much research has been conducted to find effective methods of removing salt from seawater [17]. Maritime ships have a great need for drinking water, as well as for technical water for washing, for cooling the engines and for many other activities. In the past, ships carried large quantities of fresh water in barrels or specially built tanks because there was no source of fresh water when the ship was at sea except when it rained. Nowadays, despite the fact that fresh water is produced onboard, ships still have to load tons of fresh water. Although technological methods of converting seawater to fresh and technical water exist, they cannot meet the needs onboard ships [18].

The potential lack of technical water is also due to the fact that it is very difficult to control and limit consumption, and it is also impossible to avoid the consumption of this vital element. Research has been conducted and several processes have been developed to obtain technical water from seawater. These processes are distillation, electrodialysis, reverse osmosis, direct freezing evaporation and vapor compression distillation [19,20].

The term reverse osmosis derives from a well-known process inspired by nature itself. This means that if we put a concentrated and a diluted solution in two containers separated by a very fine membrane, the system will try to balance itself in a natural manner due to the fact that the diluted solution will pass through the membrane and mix with the concentrated solution until the same concentration is reached in both containers. The height of the liquid column in the container which holds the concentrated solution will increase until the column becomes too high, and the pressure exerted by it will stop the flow of the diluted solution. The balance point of the water column is called the osmotic equilibrium. If a force is applied to this column, the direction of flow of the solution through the membranes can be changed. This is actually reverse osmosis [21].

In Figure 2 below, the process of the reverse osmosis installation is shown. Seawater is drawn in by a low-pressure pump which in turn feeds a high-pressure pump (with a nominal pressure set over 60 bar). The high-pressure pump then circulates the seawater into the membrane, and due to this process combined with high pressure and the density of the seawater, the brine will be separated from the potable water, so at the other end of the membrane, two circuits will be generated, one of fresh water and one of brine (that will be pumped overboard). As seen in Figure 2, the installation can also be equipped with sand filters and micron filters used to separate impurities from the water, needed to protect the membranes [22].

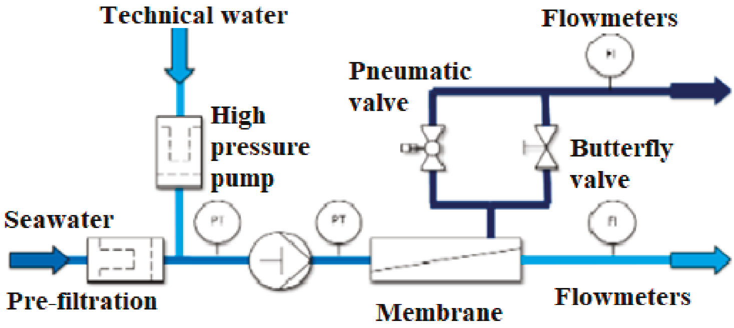

Figure 2. Diagram and model of a marine osmosis installation [drawn by the authors].

3. Results

As a general rule, water installations and sanitary installations (drinkable or technical), installed onboard ships are similar. The only element that differs is the type of installation chosen. The only types of ships for which stricter conditions are imposed are passenger ships, which must meet a series of very demanding quality parameters, both in terms of drinking water and ballast and wastewater. This can be an issue if the system is being installed onboard a smaller ship because in order to keep potable water onboard in storage, the ship must be equipped with at least two tanks [23].

Onboard the ship, the water installation has three well-defined roles, namely: supplying drinking water to the crew and passengers, supply technical water to power the power units and cabins, and supply seawater to flush the toilets and use in washing machines. Corresponding to the three roles, the water supply installation onboard the ship will be composed of three installations that operate according to the same principle and have the same common elements, with a few differences: the technical water installation can use structural tanks not covered on the inside as storage tanks, and it includes a boiler for heating domestic hot water; the seawater installation takes water directly from the seawater main system in a similar concept as that drawn in Figure 3.

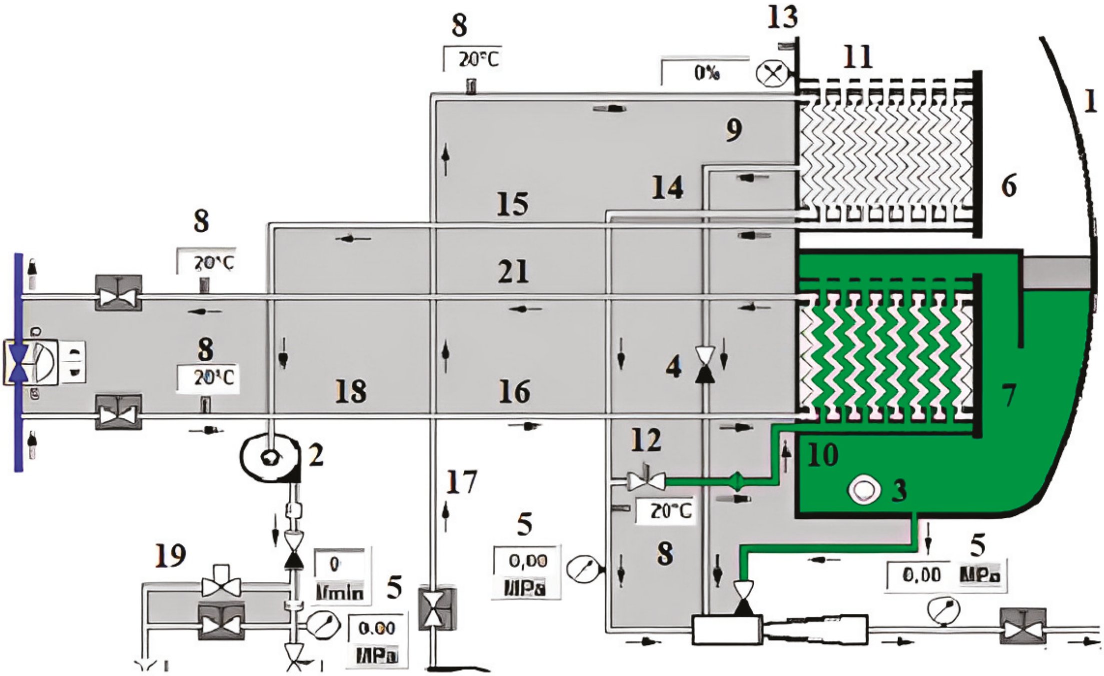

Figure 3. Typical diagram for the water installation onboard a ship [drawn by the authors].

The general technical water system contains the following elements in its composition:

1. Technical water storage tank;
2. Water supply pumps;
3. Water pump for water (potable, technical, sea);
4. Retaining flap;
5. Pressure relay;
6. Technical water treatment module;
7. Technical water module cooling mode;
8. Temperature transducer;
9. Technical water consumption equalization tank;
10. Circulation pump;
11. Boiler (with steam);
12. Valve controlled by transducer for steam input;
13. Tank ventilation equipment;
14. Supply piping coming from the technical water generator;
15. The distribution network for cold technical water;

16. The distribution network for hot technical water;
17. Main seawater supply;
18. Distribution network for seawater;
19. The main piping line of the compressed air installation;
20. Hydrophore safety valve;
21. The distribution network for technical water [24].

Regarding technical water, the installation and operation are similar with the difference that cold technical water is distributed to consumers through parallel pipes and hot technical water through adjacent pipes. This principle has already been pointed out in Figure 2, illustrating the process flow for a similar RO (reverse osmosis) unit. The water is heated in the boiler, which can be with steam, hot water, burner or electric. Regardless of the type of boiler, the installation includes: a circulation pump, an equalization tank and a temperature transducer that controls the start/stop of the pump and the control of the steam valve in order to obtain the preset temperature [25].

The flow rate of technical water pumps is determined as follows [25]:

$$Q_p = \sum_i (n_i \alpha_i q_i) \tag{1}$$

where n is the number of consumers of the same kind, α is the simultaneity coefficient of the operation of consumers of the same type, and q is the consumption norm in [L/s] specific to each type of consumer.

The values of the coefficient and the consumption norm depending on the type of consumer are as it follows:

- For category 1 consumers: $\alpha = 0.3$ and $q = 0.07$ L/s;
- For category 2 consumers: $\alpha = 0.2$ and $q = 0.2$ L/s;
- For category 3 consumers: $\alpha = 0.4$ and $q = 0.15$ L/s;
- For category 4 consumers: $\alpha = 0.5$ and $q = 0.3$ L/s;
- For category 5 consumers: $\alpha = 0.25$ and $q = 0.2$ L/s [25].

Therefore, according to the above values, we will consider:

$$\alpha_1 = 0.3; \alpha_2 = 0.2; \alpha_3 = 0.4; \alpha_4 = 0.5; \alpha_5 = 0.25$$
$$\mathrm{q}_1 = 0.07; \mathrm{q}_2 = 0.2; \mathrm{q}_3 = 0.15; \mathrm{q}_4 = 0.3; \mathrm{q}_5 = 0.2$$

The number of consumers are set as:

- For category 1 consumers: $n_1 = 55$;
- For category 2 consumers: $n_2 = 48$;
- For category 3 consumers: $n_3 = 5$;
- For category 4 consumers: $n_4 = 4$;
- For category 1 consumers: $n_5 = 4$.

The required flow of the installation will be (Equation (3) [25] and Equation (5) [25]):

$$\mathrm{Q_p} = \mathrm{n_1}\alpha_1\mathrm{q_1} + \mathrm{n_2}\alpha_2\mathrm{q_2} + \mathrm{n_3}\alpha_3\mathrm{q_3} + \mathrm{n_4}\alpha_4\mathrm{q_4} + \mathrm{n_5}\alpha_5\mathrm{q_5} \tag{2}$$

$$\mathrm{Q_p} = 4.175\frac{1}{\mathrm{s}} \tag{3}$$

$$\mathrm{Q'_p} = \mathrm{Q_p}3.6 \tag{4}$$

$$\mathrm{Q'_p} = 15.03\frac{\mathrm{m}^3}{\mathrm{h}} \tag{5}$$

The calculation of the working volume of the hydrophore is performed as follows: if i = 7...9 represents the number of starts per hour, we consider i = 8 for the calculation. Its volume will be [25]:

$$\mathrm{V} = \frac{\mathrm{Q'_p}}{\mathrm{i}} \rightarrow \mathrm{V} = 1.879\ \mathrm{m}^3 \tag{6}$$

Calculation of hydraulic losses [7]:

$$h = \lambda \frac{I_c}{d} \rho \frac{v^2}{2} \tag{7}$$

where $v_{rec} = 1 \ldots 1{,}2 \ \frac{m}{s}$ is the recommended speed in the pipes $v = v_{rec}$, thus $v = 1 \frac{m}{s}$.

Pipe diameter is calculated as [26]:

$$d' = \sqrt{\frac{4Q_p}{\pi v_{rec}}}[m] \to d' = 0.0729 \text{ m} \tag{8}$$

The diameter is standardized, so the number of centimeters is [26]:

$$nr_{cent} = \frac{d_{mm}}{25.4} \to nr_{inch} = 2.87 \text{ cm} \tag{9}$$

Thus, $d_m = d \cdot 10^{-3}$.

The kinematic viscosity is [26]:

$$\upsilon = 1.287 \cdot 10^{-6} \frac{m^3}{s} \text{—at } 12\ ^\circ\text{C} \tag{10}$$

The Reynolds number will be [26]:

$$R_e = \frac{v d_m}{\upsilon} = 5.921 \cdot 10^4 \tag{11}$$

Welded, newly galvanized steel pipes with the height of roughness for this type of piping is considered as [26]:

$$K = 0.1 \ldots 0.2 \text{ mm and } \varepsilon = \frac{k}{d_{mm}} = 2.057 \cdot 10^{-3} \tag{12}$$

Altsul's criterion is applied, and the next values will be calculated [26]:

$$R_{e1} = \frac{10}{\varepsilon} = 4.861 \cdot 10^3 \text{ and } R_{e2} = \frac{500}{\varepsilon} = 2.43 \cdot 10^5 \tag{13}$$

The condition $R_{e1} < R_e < R_{e2}$ is met. It follows that the pipe is hydraulic semi-rough, and we will calculate the coefficient of hydrodynamic friction as follows [26]:

$$\lambda = 0.11 (\varepsilon + \frac{68}{R_e})^{0.25} = 0.026 \tag{14}$$

The value of the calculation length l_c and the equivalent length l_e is calculated according to the technical specification for the tank type ship. For the calculated diameter of the piping, we will consider the following equivalent lengths:

- $l_v = 25$—for the check valve;
- $l_c = 5.2$—for a bent;
- $l_t = 5.2$—for normal tee conjunction;
- $l_{ct} = 14$—for sip;
- $l_{CT} = 0.55$—for fully open valve [6].

The equivalent length is [26]:

$$l'_e = 2l_v + 7l_c + 2l_t + 1l_{ct} + 5l_{CT} = 113.55 \text{ m} \tag{15}$$

The calculation length is [26]:

$$l_c = (10 + 2 + 1 + 0.7) \cdot 12 = 164.4 \text{ m} \tag{16}$$

The pump load given by linear and local losses will be [26]:

$$h = (\lambda \frac{l_c}{d_m} + \lambda \frac{l'_e}{d_m}) \rho \frac{v^2}{2} = 4.774 \cdot 10^4 \text{ Pa} \tag{17}$$

The total load of the installation is given by the sum of the losses on the piping and the losses given by the height at which it discharges [26]:

$$H_i = \rho g z + h = 1000 \cdot 9.81 \cdot 16.4 + 4.774 \cdot 10^4 = 2.086 \cdot 10^5 \text{ Pa} \tag{18}$$

The minimum pressure in the hydrophore is [26]:

$$p_1 = H_i = 2.086 \cdot 10^5 \text{ Pa} \tag{19}$$

The maximum pressure in the hydrophore is [26]:

$$p_2 = \alpha p_1 = 1.6 \cdot 2.086 \cdot 10^5 = 3.755 \cdot 10^5 \text{ Pa} \tag{20}$$

The pump load is equal to the maximum pressure in the tank [26]:

$$H_{pump} = P_2 = 3.755 \cdot 10^5 \text{ Pa} \tag{21}$$

$$H'_{pump} = \frac{H_{pump}}{\rho \cdot g} = \frac{3.755 \cdot 10^5}{1000 \cdot 9.81} = 29.773 \text{ m water column} \tag{22}$$

The flow rate of the feed pump is [26]:

$$Q_{pump} = \frac{Q'_p}{0.85} = 17.682 \frac{m^3}{h} \tag{23}$$

4. Discussions

According with the calculation at the end of the previous section, the main technical characteristics of the water installation onboard the container ship were determined. The data obtained through this calculation is essential to establish the component elements within the system framework. Further, on the basis of the same calculation, the technical water generator that serves this installation and for which the operation optimization study will be carried out will be established.

The chosen concept of a technical water generator has an optimized operation, being designed under the "start-and-forget" operational concept ("start it and forget it") and being easily arranged in compartments with machines that do not require constant human supervision. It can also be easily integrated into fully automated operations. This technical water generator is specially designed for operation onboard ships or onboard oil platforms. [27] The operating principle of the desalinator is based on a type of technology unique to this market that uses 3-in-1 type plates that allow desalination to take place in a single pack of plates without the need to install an external plate [27]. Evaporation, separation and condensation processes will all occur within this single plate pack, as represented in Figure 4. The construction of the plates is optimized from the start by the nature of the metal used for their construction, a titanium alloy.

Depending on the needs and configuration of the ship, it can be customized as any type of project that involves the integration of a technical water generator with a wide range of configurations [28].

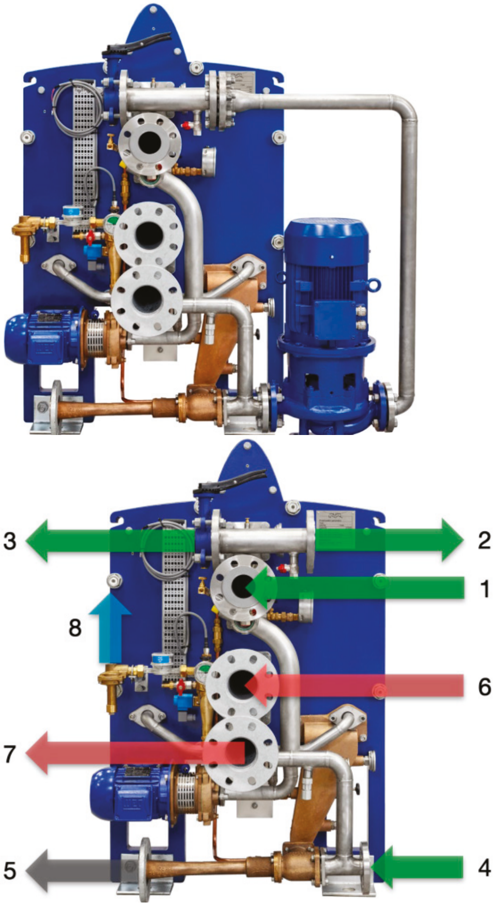

Figure 4. The technical water generator with the main component elements [drawn by the authors].

The figure above shows the technical water generator onboard the reference ship with its main component elements as follows:

○ 1—Suction of seawater/cooling water;
○ 2—Ejector discharge/feed water;
○ 3—Discharge of seawater/cooling water;
○ 4—Ejector suction/feed water;
○ 5—Brine discharge;
○ 6—Suction heating medium (hot water or steam);
○ 7—Discharge of heating medium (hot water or steam);
○ 8—Freshwater discharge.

The equipment onboard the midsize container ship has the following additional equipment intended to optimize its exploitation:

- Supply or ejector pipes;
- Technical water discharge bypass system;
- “Built-in” control panel;
- “Built-in” water treatment equipment. This is to support its three main roles;
- Special valves for manometers;
- Pressure gauges on the ejector, water pump and hot water pump;

- Filling line with dosing system and counter-flanges;
- Protective cover for plates;
- Distance indicators on the fixing bolts;
- Hot water pump;
- Hot water loop for connecting an additional heat source;
- Self-cleaning unit (CIP);
- Spare parts kits;
- UV sterilization unit of the treated water;
- pH adjustment filter;
- Chlorination unit;
- Dechlorination unit;
- Sterilizer with silver ions;
- Additional mode for measuring the purity of technical water [29].

4.1. Optimizing the Operation through the Installation Mode

The technical water generator is very easy to install, as Figure 5 demonstrates. Since the time required for repairs or maintenance work is limited (and this is a positive aspect, taking into account the limitations onboard ships), the installation is very compact. The heating medium in which the still operates is hot water, such as water coming from the main engine, but it can also be steam. The cooling liquid of the condenser is sucked directly into the cooling system of the main engine, to which it is also returned after passing through the distiller system. The feed water is sent by means of a pump or an ejector, this being necessary for the evaporation process, as well as the water that must reach the ejector of brine combined with air. This water can be drawn from the condenser discharge, or it can come from an alternative source.

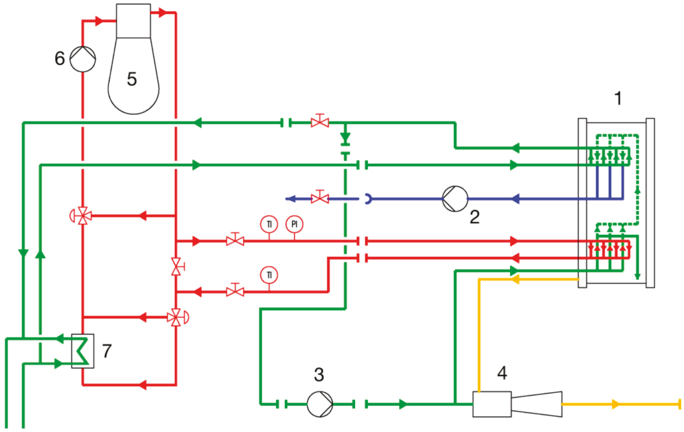

Figure 5. The arrangement of the AQUA Blue S-type technical water generator in the framework of the cooling water installation [drawn by the authors].

The technical water generated is pumped to a storage tank. The control panel provides electrical power to the feed pump, to the ejector, to the water pump and to the metering pump and also provides the control voltage to the hallometer and the drain valve. The components of the diagram above are as follows:

○ 1—Technical water generator;
○ 2—Technical water pump;
○ 3—Water supply pump;
○ 4—Brine/air ejector;
○ 5—The main engine of the ship;

- ○ 6—Cooling water system;
- ○ 7—The central cooler of the main engine.

4.2. Optimization of Electricity and Water Consumption

The technical water generator has an optimized technology that allows it to convert a higher percentage of technical water from salt water. More than that, it cuts the amount of salt water needed for cooling in half. This means that a halved amount of electricity is consumed for pumping, representing half of the electricity consumption dedicated to the operation of the entire system. For cooling, it is possible to opt for the still to be cooled directly by the open cooling circuit of the main engine, and this would further reduce electricity consumption [30]. This difference is highlighted in the diagram in Figure 6.

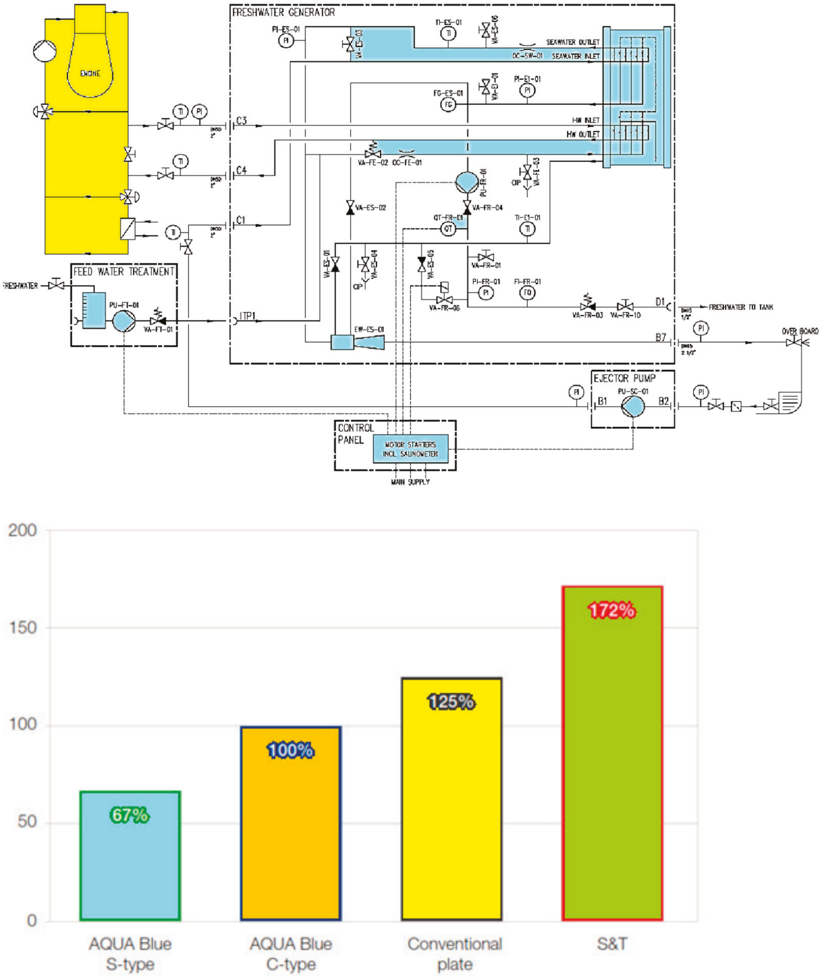

Figure 6. Figure of electricity consumption compared to other types of technical water generators—with aqua blue C type diagram shown above [18] [drawn by the authors].

4.3. Optimization through the Use of Membranes with Special Construction

As mentioned, the system is composed of titanium plates with a 3-in-1 design, the main differences between these plates being marked in Figure 7. They are provided with two types of gaskets, and the whole configuration allows evaporation, separation and condensation in a single package uncovered by the plates. At the same time, this specific configuration enhances the evaporation process and allows the conversion of a larger amount of salt water.

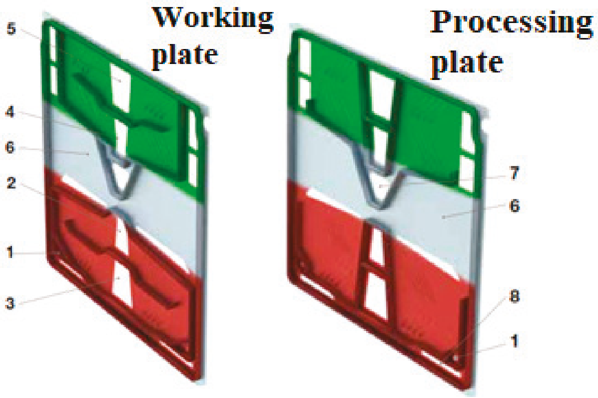

Figure 7. Model of titanium plates used in the configuration of the freshwater generator [drawn by the authors].

In the figure above, the colors associated with the areas of the titanium plates denote the following processes:

○ Green—condensation;
○ Gray—separation;
○ Red—evaporation.

The constructive elements of the plates, as they are numbered in the figure above, are:

○ 1—Saltwater supply;
○ 2—Input of the heating medium;
○ 3—Evacuation of the heating environment;
○ 4—Suction of sea/cooling water;
○ 5—Discharge of sea/cooling water;
○ 6—Evaporated steam;
○ 7—Evacuation of technical water;
○ 8—Brine evacuation [31]

The salt water passes through the lower part of the plate pack, where it is evaporated at a temperature of 40–60 °C in a vacuum process of 85–95% [32]. As the steam increases its pressure and density between the plates, it passes through the separation zone, which locks the brine and makes it fall into the pool at the base of the technical water generator. Thus, only technical water vapor reaches the upper part, which is cooled and condensed into fresh water. The result of the whole process is the generation of good quality water with a maximum salinity of 5 ppm [33]. Due to the optimized flow distribution along the plates, any form of calcareous deposit is avoided.

4.4. Optimizing by Ensuring Correct Exploitation and Compliance with the Installation Maintenance Schedule

Although the technical water generator does not require a high level of maintenance, its operation depends in many ways on the way the installation it serves is maintained. For these reasons, the maintenance of these types of devices is closely related to the maintenance technical water installation onboard the ship [34]. In general, the maintenance and upkeep of the installations onboard ships must focus on the following directions:

- General visual check;

- Checking pump operating parameters;
- Checking the degree of corrosion;
- Check/maneuver valves and taps;
- Checking connections;
- Checking the fixing supports of the component parts (especially in the case of the hydrophore);
- Checking the water reserve and level;
- Verification of the expansion vessel;
- Checking of measuring and control devices;
- Check dashboards;
- Periodic function tests, especially when the installation is not turned on for long periods of time;
- AMC metrological verification (measurement and control devices) of the installation;
- Checking the external/internal water tank and control and signaling devices, cleaning, periodic repainting;
- Ensuring safety lighting in the spaces that serve such installations by checking the electrical lighting installations and lighting fixtures [35].

The control and checks of the installation have a permanent character, being part of the current follow-up regarding the technical condition of the construction, which, correlated with the maintenance and repair activity, has as its objective the maintenance of the installation at the designed parameters. The control and verification of the installation is performed by the operating personnel on the basis of a program. The program will include provisions regarding the entire installation, the categories of installation elements and functional operations, recorded in the operating instructions of the installation.

5. Conclusions

Desalination of ocean water requires a huge amount of energy and of course produces greenhouse gases. Moreover, desalination plants endanger marine ecosystems. In a report dedicated to ocean water desalination plants, representatives of the environmental organization WWF were quite concerned about this issue. Seawater desalination is far from the ideal solution. This technology is a potential threat to the environment and will only make climate change worse [36]. The recourse to these new technologies, which are increasingly accessible, will not remain without consequences for the environment.

Technical water systems or plants can also have a negative impact on coastal areas, amplifying the destruction of marine ecosystems specific to these areas. In addition, the risk of disturbing the balance of these wetlands and the purification and protection functions against catastrophes increases greatly.

Specialists in marine pollution and ecotoxicology have also sounded the alarm about the dire consequences that could occur after the commissioning of the desalination unit onboard the ships [37]. The process of desalination and drinking water production plays a critical role when it comes to navigation and making long-distance and long-duration journeys.

At the same time, the desalination process plays an important role in many other fields, totally different from maritime transport. Many countries in arid areas use seawater as a source of drinking water for their coastal cities, subjecting it to expensive desalination processes. Obviously, the oldest and largest desalination plant is nature itself through evaporation from the seas. More than 30 water desalination processes are known, including condensation, freezing, extraction, electrodialysis, reverse osmosis, ion exchangers, etc.

Author Contributions: Conceptualization, C.F. and E.R.; methodology, E.R.; software, Microsoft Office Word; validation, C.F. and E.R.; formal analysis, E.R.; investigation, E.R.; resources, C.F.; data curation, C.F.; writing—original draft preparation, C.F.; writing—review and editing, C.F. and E.R.; visualization, C.F. and E.R.; supervision, E.R.; project administration, E.R.; funding acquisition, C.F. All authors have read and agreed to the published version of the manuscript.

Funding: This research was funded by PROINVENT – POCU Programme grant number PN-III-P4-ID-PCE-2020-0008 And The APC was funded by Romanian Executive Agency for Higher Education, Research, Development and Innovation Funding—UEFISCDI.

Data Availability Statement: Further data on author work can be studied by accessing the following links, for additional information: https://iopscience.iop.org/article/10.1088/1757-899X/1182/1/012024/meta, https://iopscience.iop.org/article/10.1088/1757-899X/1182/1/012023/meta, https://www.gup.ugal.ro/ugaljournals/index.php/mtd/article/view/4028, https://www.gup.ugal.ro/ugaljournals/index.php/mtd/article/view/4028.

Acknowledgments: The work of Faitar Catalin was supported by the project "PROINVENT", Contract no. 62487/03.06.2022—POCU/993/6/13—Code 153299, financed by The Human Capital Operational Programme 2014–2020 (POCU), Romania, the work of E.R. was carried out in the framework of the research project DREAM Dynamics of the Resources and technological Advance in harvesting Marine renewable energy), supported by the Romanian Executive Agency for Higher Education, Research, Development and Innovation Funding—UEFISCDI, grant number PN-III-P4-ID-PCE-2020-0008.

Conflicts of Interest: The authors declare no conflict of interest.

References

1. Faităr, C.; Novac, I. A new approach on the upgrade of energetic system based on green energy. A complex comparative analysis of the EEDI and EEOI. In Proceedings of the ModTech International Conference Modern Technologies in Industrial Engineering, Iasi, Romania, 15–18 June 2016.
2. Available online: http://engine.od.ua/man-90mc (accessed on 5 December 2022).
3. Available online: http://www.machineryspaces.com/cooling.html/ (accessed on 5 December 2022).
4. Available online: https://patents.google.com/patent/WO2015016432A1/en (accessed on 15 December 2022).
5. Available online: https://patents.google.com/patent/RU2652369C1/en (accessed on 15 December 2022).
6. Available online: https://patents.google.com/patent/JPS5867390A/en (accessed on 21 December 2022).
7. Available online: https://patents.google.com/patent/JP6746692B2/en (accessed on 22 December 2022).
8. Faităr, C.; Novac, I. Basic aspects and contributions to the optimization of energy systems exploitation of a super tanker ship. In Proceedings of the ModTech International Conference—Modern Technologies in Industrial Engineering V, Sibiu, Romania, 14–17 June 2017.
9. Kakac, S.; Kakac, L.S.; Liu, S. *Heat Exchangers Selection, Rating and Thermal Design*; CRC: Boca Raton, FL, USA, 2002.
10. Abu-Khader, M.M. Better thermal calculations using modified generalized Leveque equations for Chevron plate heat exchangers. *Int. J. Green Energy* **2007**, *4*, 351–366. [CrossRef]
11. Muley, A.A.; Manglik, R.M. Experimental study of turbulent flow heat transfer and pressure drop in a plate heat exchanger with chevron plates. *ASME J. Heat Transfer* **1999**, *121*, 110–117. [CrossRef]
12. Çengel, Y. *Heat and Mass Transfer: A Practical Approach*, 3rd ed.; McGraw-Hill: New York, NY, USA, 2011.
13. Wright, A.D.; Heggs, P.J. Rating calculation for plate heat exchanger effectiveness and pressure drop using existing performance data. *Trans. Inst. Chem. Eng.* **2002**, *80*, 309–312. [CrossRef]
14. Demirel, K.; Er, I.D. *Gemimühen Dislerii çin Pomp au Ygulamaları*; BirsenYayınevi: Istanbul, Turkey, 2007.
15. Kralj, P.; Martinović, D.; Tudor, M. Analysis of thermodynamic and technological basics of the marine fresh water generator model. *Desalination Water Treat.* **2017**, *95*, 180–185. [CrossRef]
16. Lior, N. *Measurements and Control in Water Desalination*; Elsevier: Amsterdam, The Netherlands, 1986.
17. Bahar, R.; Hawlader, M.N.A. Desalination: Conversion of Seawater to Freshwater. In Proceedings of the 2nd International Conference on Mechanical, Automotive and Aerospace Engineering, Kuala Lumpur, Malaysia, 2–4 July 2013.
18. Faităr, C. Concepte de Modernizare Energetică a unui VLCC de 305,000 t.d.w. Calculul şi Proiectarea Sistemelor Energetice Auxiliare. Master's Thesis, Maritime University of Constanța, Constanța, Romania, 2016.
19. Sanchez Rosario, R.; Hildenbrand, Z.L. Produced water treatment and valorization: A tehno-economical review. *Energies* **2022**, *15*, 4619. [CrossRef]
20. Alkinani, S.S.; El-Amin, M.F. Numerical modeling and analysis of harvesting atmospheric water using porous materials. *Separations* **2022**, *9*, 364. [CrossRef]
21. Date, A.; Traiask, O.; Ward, M.; Rupakheti, E.; Hu, E. Experimental and theoretical study on mechanical performance of a sustainable method of simultaneously generate power and fresh water. *Sustainability* **2022**, *14*, 14039. [CrossRef]
22. Keriwala, N.; Patel, A. Innovative roadmap for smart cities: A global perspective. *Mater. Proc.* **2022**, *10*, 1.
23. *ISO 19458:2006*; Water Quality (Calitatea apei)—Mostre Pentru Analiza Microbiologică. International Organization for Standardization: Geneva, Switzerland, 2006.
24. *ISO 15748-1:2002*; Ships and marine Technology (Nave și tehnologii marine)—Alimentarea cu apă potabilă a navei și Structurilor Navale. International Organization for Standardization: Geneva, Switzerland, 2006.

25. Scupi, A.A.; Dinu, D. *Fluid Mechanics. Numerical Approach*; Nautica Publishing: Constanța, Romania, 2015.
26. Dinu, D. *Mașini Hidraulice și Pneumatice Utilizate în Domeniul Naval*; Nautica Publishing: Constanța, Romania, 2019.
27. Micale, G.; Rizzuti, L.; Cipollina, A. (Eds.) *Seawater Desalination: Conventional and Renewable Energy Processes*; Springer Science & Business Media: Berlin/Heidelberg, Germany, 2009.
28. Foldrage, R.A. Economics of Desalination Concentrate Disposal Methods in Inland Regions: Deep-Well Injection, Evaporation Ponds, and Salinity Gradient Solar Ponds. Bachelor's Thesis, New Mexico University, Los Cruces, NM, USA, 2017.
29. Khordagui, H. *Environmental Aspects of Brine Reject from Desalination Industry in the ESCWA Region*; ESCWA: Beirut, Lebanon, 2017.
30. Svensson, M. Desalination and the environment: Options and considerations for brine disposal in inland and coastal locations. Ph.D. Thesis, Swedish University of Agricultural Sciences, Uppsala, Sweden, 2015.
31. Leijon, J.; Boström, C. Freshwater Production from the Motion of Ocean Waves—A review. *Desalination* **2018**, *435*, 161–171. [CrossRef]
32. *MJ12-FW Generator (Including Instruction Book)*; Mitsubishi Heavy Industry Ltd.: Tokyo, Japan, 2012.
33. Cieslinski, J.T.; Fiuk, A.; Typinski, K.; Siemienczuk, B. Heat transfer in plate heat exchanger channels: Experimental validation of selected correlation equations. *Arch. Thermodyn.* **2016**, *37*, 19–29. [CrossRef]
34. Soto, J.A.; Martinez, M.T.; Magana, J.L. Theoretical-experimental study of the effect of the external plates on the thermal performance of a plate heat exchanger. *Chem. Eng. Sci.* **2015**, *3*, 12–18.
35. Stan, L.C. *Seas and Oceans, Suppliers of the New and Innovative Renewable Energy*; Constanța Maritime University Annals; Constanța Maritime University: Constanța, Romania, 2015; Volume 24.
36. ACCES (Arctic Climate Change, Economy and Society). Calculation of FW Water Consumption for Various Ship Types and Ice Conditions in Past, Present and Future. Collaborative Project. 2011. Available online: https://nanopdf.com/download/calculation-of-fuel-consumption-per-mile-for-various-ship-types-and_pdf (accessed on 15 December 2022).
37. Available online: https://www.academia.edu/central-cooling-system-lt-with-low/high-temperature (accessed on 12 December 2022).

Disclaimer/Publisher's Note: The statements, opinions and data contained in all publications are solely those of the individual author(s) and contributor(s) and not of MDPI and/or the editor(s). MDPI and/or the editor(s) disclaim responsibility for any injury to people or property resulting from any ideas, methods, instructions or products referred to in the content.

inventions

Article

Optimization of the Parameters Influencing the Antioxidant Activity and Concentration of Anthocyanins Extracted from Red Onion Skins Using a Central Composite Design

Florina Stoica, Oana Emilia Constantin, Nicoleta Stănciuc, Iuliana Aprodu, Gabriela Elena Bahrim and Gabriela Râpeanu *

Integrated Center for Research, Expertise and Technological Transfer in Food Industry, Food Science, Food Engineering, Biotechnology and Aquaculture Department, Faculty of Food Science and Engineering, Dunarea de Jos University of Galati, 111 Domnească Street, 800201 Galati, Romania

* Correspondence: gabriela.rapeanu@ugal.ro; Tel.: +40-0336-130-177

Abstract: This study aimed to extract bioactives from red onion skins for use as edible colorants that are both natural and functional. The extraction of bioactive chemicals from red onion skins using a conventional solvent extraction was optimized using a Central Composite Design (CCD). The influence of extraction parameters, such as ethanol and citric acid concentrations, extraction temperature, and time, on anthocyanin content and antioxidant activity (DPPH method) was studied. A quadratic model was suggested for all of the parameters examined and employed. Citric acid concentration (0.05–2.64%), ethanol concentration (6.36–73.63%), operation temperature (16.47–58.52 °C), and extraction duration (10–234.54 min) were the variables studied in the coded form of the experimental plan. The best conditions for maximum anthocyanins and antioxidant activity recovery were: 60% ethanol, 0.87% citric acid, 179.99 min, and 25 °C. The anthocyanins concentration varied from 0.45 to 1.43 mg C3G/g DW, while the antioxidant activity varied from 24.29 to 37.20 mM TE/g DW, according to the experimental design. Overall, it should be emphasized that the extraction process can be enhanced by settling the operating factors to maximize the model responses. The current findings demonstrate that extracts from red onion skins would be useful in developing functional food products.

Keywords: anthocyanins; extraction; antioxidant activity; red onion skins; CCD

Citation: Stoica, F.; Constantin, O.E.; Stănciuc, N.; Aprodu, I.; Bahrim, G.E.; Râpeanu, G. Optimization of the Parameters Influencing the Antioxidant Activity and Concentration of Anthocyanins Extracted from Red Onion Skins Using a Central Composite Design. *Inventions* **2022**, *7*, 89. https://doi.org/10.3390/inventions7040089

Academic Editor: Monique Lacroix

Received: 6 September 2022
Accepted: 28 September 2022
Published: 3 October 2022

Publisher's Note: MDPI stays neutral with regard to jurisdictional claims in published maps and institutional affiliations.

Copyright: © 2022 by the authors. Licensee MDPI, Basel, Switzerland. This article is an open access article distributed under the terms and conditions of the Creative Commons Attribution (CC BY) license (https://creativecommons.org/licenses/by/4.0/).

1. Introduction

Since ancient times, the onion (*Allium cepa* L.) has been one of the most important vegetable crops and it is the world's second most developed agricultural crop after the tomato. Onions are grown in various shapes, colors, sizes, and pungency to fulfill specific culinary and nutritional needs and have become a nearly universal ingredient in food preparation worldwide [1]. Onion production has grown over the last decade and it now reaches about 98 million tons around the world. More than 550,000 tons of by-products (onion skins) are produced yearly, causing various biological and environmental problems [2]. Valorization is widely applied to managing agro-industrial by-products, in which by-products are considered valuable secondary raw materials with potential functional constituents for developing value-added products [3]. Onion by-products have been an intriguing challenge for researchers aiming to create efficient reuse strategies for its bioactive compounds due to onion increased production and a relatively substantial amount of generated by-products without acceptable disposal.

Onion by-products have generally been recognized as a source of non-structural carbohydrates, dietary fibers, polyphenols, and flavor compounds. Bioactive compounds such as phenolics, flavonoids, and anthocyanins are abundant in red onions and their dry outer layers. Their quantities in the skin of red onion are higher than in the edible portion because of their preventive properties against soil microorganisms [4]. The phenolic compounds in the red onion skin mainly consist of flavonoids. They include two main groups, namely, flavonols (such as quercetin, kaempferol, and its glucoside derivatives) and anthocyanins (especially cyanidin derivatives) [5]. Flavonols are generally found in glycosylated forms; the two most frequent quercetin forms in red onion skin are quercetin 4′-O-β-D-glucoside and quercetin 3,4′-O-β-D-diglucoside, which account for 80–85% of the total flavonoid content [1]. Cyanidin 3-glucoside is the major anthocyanin found in red onion skin. Smaller quantities of cyanidin 3-laminaribioside, peonidin, and pelargonidin glucosides are also present [6]. Red onion skins may be a source of natural colorants that can be extracted using various methods and utilized in foods as a substitute for synthetic compounds. These red onion skins can be a natural, low-cost, and widely available source of beneficial ingredients, including antioxidants [7].

Anthocyanins form an important group of water-soluble plant pigments and are used as food colorants. Additionally, anthocyanins have health-promoting effects such as anti-cancer, anti-inflammatory, antidiabetic, anti-obesity, and enzyme inhibitory effects, contribute to the prevention of cardiovascular disease, and have powerful antioxidant properties [8].

Different methods have been used to obtain phytochemicals, and extraction is the most important stage in providing bioactive compounds. Developing effective extraction procedures is crucial to improve the extraction of valuable compounds in terms of cost-effectiveness and environmental friendliness. The principal elements to consider in extraction processes include matrix properties, solvent selection, temperature, liquid-to-solid ratio, pressure, and extraction time. The most common method for the extraction of bioactive compounds is solvent extraction (such as extraction based on ethanol and methanol) [9].

Solvent extraction is used to increase the extraction efficiency, extraction time, extraction quality, and solvent consumption. Anthocyanins are more soluble in polar solvents than in non-polar solvents. In addition, because anthocyanins are unstable in alkaline solutions, highly acidic aqueous solvents are used. Due to the swelling of the tissue walls, adding acid to a solvent enhances the extraction yield [10]. Aqueous ethanol (50 to 75%) is often used to extract flavonoids from onion skin waste. Temperature, extraction duration, and the solvent-to-raw material ratio also affect the extraction of flavonoids from onion skin waste [11].

In the current study, a conventional solvent extraction method with four variable factors was developed (ethanol concentration, citric acid, temperature, and time). Furthermore, a central composite design (CCD) was employed to optimize the extraction technique and enhance the antioxidant activity. Anthocyanins extraction from red onion skin extracts under stirring was also studied for a more efficient solid/liquid extraction of bioactive compounds. This research offers new insights into the impact of conventional extraction methods on and the determination of the optimal extraction conditions for anthocyanin-rich by-products.

2. Materials and Methods

2.1. Reagents and Chemicals

HPLC-grade methanol, ethanol, Folin–Ciocalteu reagent, glacial acetic acid, 2,2-diphenyl-1-picrylhydrazyl (DPPH), 6-hydroxy2,5,7,8 tetramethylchromane-2-carboxylic acid (Trolox), gallic acid, potassium chloride, sodium nitrite, sodium hydroxide, sodium bicarbonate, sodium acetate, sodium carbonate, aluminum chloride were obtained from Sigma Aldrich Steinheim (Darmstadt, Germany). All other reagents used in the experiments were of analytical grade.

2.2. Red Onion Skins Preparation

Red onions were purchased from a local market in Galați, Romania. The outer layers of the red onions were collected, washed with ultrapure water, and dried for 2 h at 40 °C in a typical oven (Stericell 111, MMM Medcenter, München, Germany) to a moisture content of 11.0%. The red onion skins were powdered (mean particle diameter of 1 mm), stored at room temperature in an airtight glass jar in the dark, and utilized for extraction.

2.3. Conventional Solvent Extraction

The extraction was carried out using 1 g of red onion skin and 15 mL of ethanol in various concentrations, ranging from 6.36 to 73.63%. The plant material-to-solvent ratio was 1 to 15. Each extraction was acidified with a citric acid solution (ratio 14:1, *v*/*v*), using varying quantities from 0.05 to 2.64%. The extractions were carried out using an orbital shaker (SI-300R Medline Scientific, Chalgrove, UK) at 150 rpm at 16.47–58.52 °C for 10 to 234.54 min. The samples were centrifuged for 10 min at 14,000 rpm and 4 °C using a Hettich Universal 320R equipment, Germany, and the supernatant was phytochemically examined.

2.4. Determination of the Total Anthocyanins Content (TAC)

TAC was calculated using the pH differential method with two reagents, i.e., potassium chloride buffer (pH 1.0) and sodium acetate buffer (pH 4.5). The absorbances at 520 and 700 nm were measured using a UV–VIS spectrophotometer (Libra S22, Biochrom, Cambridge, UK).

The total anthocyanin content (TAC) was expressed in mg cyanidin 3-O-glucoside (C3G)/g dry weight (DW) and was calculated according to Equation (1) as described by Lee et al. [12], with slight modifications.

$$\text{TAC mg/g} = \frac{A \times MW \times DF \times Vt}{\varepsilon \times 1 \times \mathrm{M}} \tag{1}$$

where *A* is the difference between (*A*520–*A*700) at pH 1.0 and (*A*520–*A*700) at pH 4.5, *MW* is the molecular weight (449.2 g/mol) of cyanidin-3-glucoside, *DF* is the dilution factor, *Vt* is the total volume (mL), ε is the molar extinction coefficient (26,900) of cyanidin-3-glucoside, l is the path length, and M is the weight of red onion skins (g).

2.5. Determination of the Antioxidant Activity (AA)

The DPPH free radical-scavenging method was used to determine the antioxidant activity, which was expressed as mM Trolox Equivalents (TE)/g DW [13]. To measure the in vitro antioxidant activity, 100 µL of the extract was mixed with 3.9 mL of a DPPH stock solution. The mixture was then kept at room temperature for 30 min in complete darkness. The absorbance was measured at 515 nm, and the results were quantified using a Trolox calibration curve.

2.6. Experimental Design

The Central Composite Design (CCD) method was used to determine experimentally the antioxidant activity and optimize the TAC in the red onion skins extract. A central component of five factors, three central points, and the design of 21 experimental variants were used in an experimental factorial model. Table 1 shows the maximum and minimum values of the variables explored in the experimental plan in their current and coded forms. In addition, for response variables, the CCD creates a quadratic model.

Table 1. Range of values for the factors investigated and encoded values.

Code	Independent Variables	Units	Minimum	Maximum	Coded Low	Coded High
A	Citric acid	%	0.0500	2.64	−1 = 0.10	+1 = 2.00
B	Ethanol	%	6.36	73.63	−1 = 20.00	+1 = 60.00
C	Temperature	°C	16.47	58.52	−1 = 25.00	+1 = 50.00
D	Time	min	10.00	234.54	−1 = 20.00	+1 = 180.00

A second-order polynomial model (2) can be used to represent the software used to test the experimental conditions:

$$R = b_0 + \sum_{i}^{n} b_i \cdot x_i + \sum_{i=1}^{n} b_{ii} \cdot x_{ii}^2 + \sum b_{ij} \cdot x_i \cdot x_{jd} \quad (2)$$

where R is the predicted response, b_0 is the intercept, b_i, b_{ii}, and b_{ij} are the regression coefficients, x_i and x_{jd} are the independent variables analyzed, n is the number of factors.

2.7. Statistical Analysis

In the study, we utilized the statistical software Design Expert (v. 13) from Design-Expert® to examine the experimental model (Stat-Ease, Inc., Minneapolis, MN, USA). All analyses were carried out in triplicate, and the findings are expressed as mean ± standard deviation.

3. Results

A Central Composite Design (CCD) and surface response modeling were utilized to establish the ideal parameters for optimizing the extraction process. Additionally, the content of anthocyanins and the antioxidant activity were determined. The complete CCD matrix used to optimize the principal variables evaluated and the corresponding values are shown in Table 2.

Table 2. Actual values of the principal variables analyzed in the CCD matrix.

Run	Factor 1 A: Citric Acid %	Factor 2 B: Ethanol %	Factor 3 C: Temperature °C	Factor 4 D: Time min	Response 1 AA mM TE/g DW	Response 2 TAC mg C3G/g DW
1	1	40	37	100	26.92	1.02
2	1	40	16.47	100	27.71	1.05
3	2	60	50	20	27.24	1.34
4	1	73.63	37	100	37.2	1.43
5	1	40	37	100	26.84	1.03
6	0.1	20	50	20	28.7	0.6
7	2	60	25	20	25.01	1.32
8	0.1	60	25	180	32.53	1.18
9	1	40	37	100	26.74	1.02
10	1	40	58.52	100	26.73	1.09
11	2.64	40	37	100	25.32	1.11
12	0.1	20	25	20	30.39	0.62
13	2	20	25	180	29.51	0.52
14	1	6.36	37	100	29.41	0.45
15	0.1	60	50	180	31.07	1.21
16	1	40	37	10	24.29	0.52
17	1	40	37	100	26.73	1.04
18	0.05	40	37	100	26.63	1.05
19	1	40	37	234.54	31.14	1.22
20	1	40	37	100	27.64	1.01
21	2	20	50	180	27.24	0.51

3.1. Influence of the Extraction Parameters on AA

This research aimed to determine the effect of a suitable optimal pattern of variables on the antioxidant activity of the extract from red onion skins. The antioxidant activity varied from 24.29 to 37.20 mM TE/g DW depending on the values of the various variables (Table 2). According to the variables of the extraction environment, the regression equations developed after the ANOVA explained the antioxidant activity values of the red onion skin extract obtained (Table 3). For the AA, the Model F-value of 112.73 implied the model was significant. In this case, B, C, D, AB, AC, AD, BC, BD, CD, A^2, and B^2 were significant model terms. According to the regression model used for the DPPH free radical-scavenging potential, the determination coefficient of R^2 was 0.99, indicating that only 0.01 of the variation of the antioxidant activity could not be specified by the current model.

The predicted determination coefficient R^2 of 0.95 was in reasonable agreement with the adjusted determination coefficient R^2 of 0.98.

Table 3. ANOVA for the reduced quadratic model for AA and TAC.

AA						TAC					
Source	**SS**	**df**	**MS**	**F-Value**	***p*-Value**	**Source**	**SS**	**df**	**MS**	**F-Value**	***p*-Value**
Model	172.39	14	12.31	112.73	<0.0001 [a]	Model	1.84	14	0.1316	868.48	<0.0001 [a]
A-Citric acid	0.1126	1	0.1126	1.03	0.3491	A-Citric acid	0.0001	1	0.0001	0.9003	0.3793
B-Ethanol	32.49	1	32.49	297.46	<0.0001	B-Ethanol	0.5410	1	0.5410	3569.82	<0.0001
C-Temperature	1.63	1	1.63	14.91	0.0083	C-Temperature	0.0006	1	0.0006	3.65	0.1045
D-Time	19.45	1	19.45	178.09	<0.0001	D-Time	0.3096	1	0.3096	2043.28	<0.0001
AB	4.22	1	4.22	38.59	0.0008	AB	0.3111	1	0.3111	2052.61	<0.0001
AC	1.19	1	1.19	10.92	0.0163	AC	3.422×10^{-7}	1	3.422×10^{-7}	0.0023	0.9636
AD	19.08	1	19.08	174.65	<0.0001	AD	0.0049	1	0.0049	32.31	0.0013
BC	2.80	1	2.80	25.60	0.0023	BC	0.0008	1	0.0008	5.28	0.0613
BD	4.54	1	4.54	41.59	0.0007	BD	0.0000	1	0.0000	0.1077	0.7540
CD	2.28	1	2.28	20.87	0.0038	CD	0.0001	1	0.0001	0.3299	0.5866
A^2	1.27	1	1.27	11.59	0.0144	A^2	0.0042	1	0.0042	27.54	0.0019
B^2	76.35	1	76.35	698.99	<0.0001	B^2	0.0144	1	0.0144	95.30	<0.0001
C^2	0.1926	1	0.1926	1.76	0.2325	C^2	0.0033	1	0.0033	21.48	0.0036
D^2	0.0442	1	0.0442	0.4045	0.5483	D^2	0.1175	1	0.1175	775.31	<0.0001
Residual	0.6554	6	0.1092			Residual	0.0009	6	0.0002		
Lack of Fit	0.0767	2	0.0383	0.2649	0.7797 [b]	Lack of Fit	0.0004	2	0.0002	1.50	0.3271 [b]
Pure Error	0.5787	4	0.1447			Pure Error	0.0005	4	0.0001		
Cor Total	173.05	20				Cor Total	1.84	20			

Sum of Squares—SS; Mean Square—MS; [a] Significant; [b] Not significant.

After eliminating the minor model terms, a model reduction was accomplished. Equation (3) illustrates the model equation for the relationship between the antioxidant activity (R1) and the variables in coded units.

$$\text{R1 (AA)} = +26.92 + 2.41B - 0.3454C + 2.50D + 1.37AB + 2.41AD + 0.5912BC + 1.51BD - 0.5337CD - 0.4301A^2 + 2.26B^2 \tag{3}$$

The regression equation's b coefficients showed that the temperature had a minor negative effect on the antioxidant activity. Additionally, the interactions between temperature and time (CD) and temperature (C) and quadratic citric acid concentration (A^2) significantly negatively affected the antioxidant activity of the red onion skins extract. Additionally, the antioxidant activity of the extract was enhanced by ethanol concentration (B) and extraction time (D). The interaction between citric acid concentration and ethanol concentration (AB), between citric acid concentration and time (AD), and between ethanol concentration and extraction time (BD) also had a favorable impact on the antioxidant activity. In contrast, citric acid concentration and temperature (AC) and ethanol concentration and temperature (BC) moderately affected the antioxidant activity.

The correlation between the independent and dependent variables was predicted using second-order contour plots (Figure 1A), which were also used to show the synergistic effects of the independent variables on the antioxidant activity of the extract obtained. The three-dimensional response area describes the correlative impact of the chosen parameters on the extract's antioxidant activity.

Figure 1A displays the 3D surface and second-order contour plots for the AA determination. Figure 1A(a,b) show that the ethanol concentration and time influenced the antioxidant activity; AA increased as the citric acid concentration decreased. The maximum antioxidant activity could be attained at a nearly 60% ethanol concentration and about 180 min extraction time. Further, as the plots show, lower extraction times and higher percentages of citric acid led to a decreased DPPH free radical-scavenging potential. Additionally, reducing the temperature and ethanol concentration decreased the red onion skin extract's antioxidant activity (Figure 1A(c)). As shown in Figure 1A(d), the AA increased when the ethanol concentration increased at a constant extraction temperature. Higher temperatures may improve phenolic component solubility, resulting in an AA increase. Still, as temperature and time continued to rise, the extracted phenolic compounds started to degrade and stopped showing AA after reaching equilibrium, reducing AA levels.

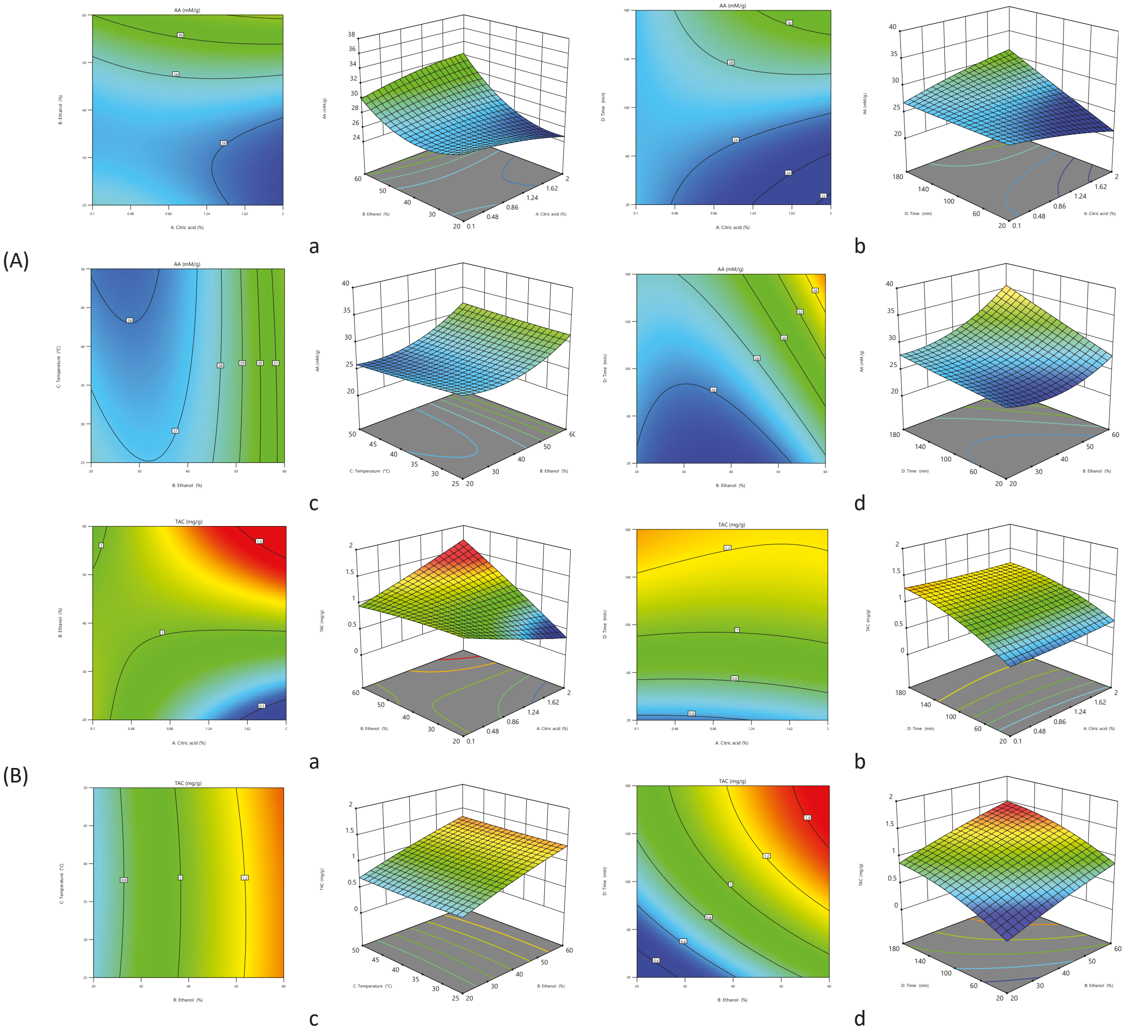

Figure 1. Second-order contour and 3D surface plots screening the variables' effect on the antioxidant activity (**A**) and extraction yield of anthocyanins (**B**).

The perturbation plot for several parameters illustrates how each element affected the current response (Figure 2a). When analyzing the deviation from a reference point, a slope with a large or curved inclination for a specific factor shows that the response is sensitive to this factor. At the same time, a relatively flat line demonstrates insensitivity to changes in this factor. In the perturbation graph, curve B appeared to be critical in determining AA, indicating that the impact of the ethanol value was very substantial. The curves A and C, corresponding to citric acid and temperature, respectively, indicated a lesser effect of these factors on the extraction than ethanol.

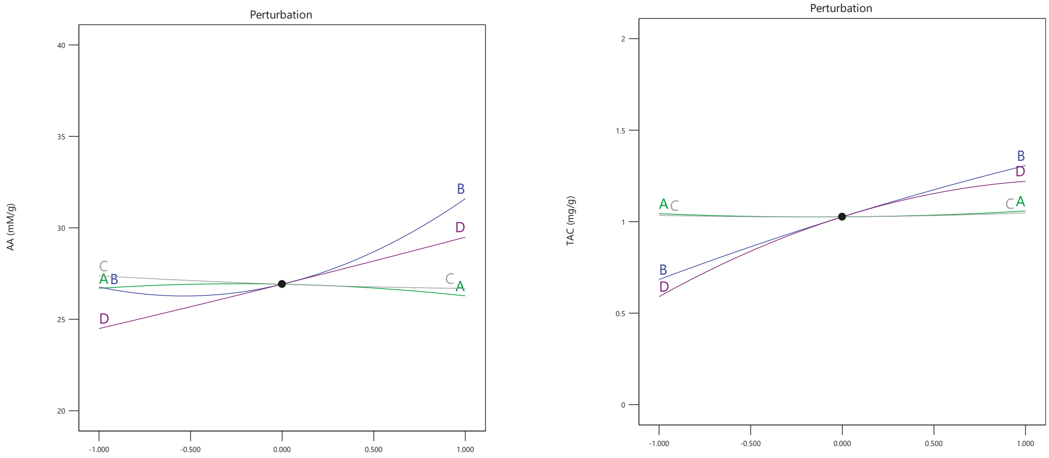

(**a**) (**b**)

Figure 2. Perturbation graphs representing the effect of each independent variable (A, B, C, and D) on AA (**a**) and TAC (**b**) of the red onion skins extract.

3.2. Influence of the Extraction Parameters on TAC

This study aimed to find the best parameters for extracting anthocyanins from red onion skins. The TAC ranged from 0.45 to 1.43 mg C3G/g DW, based on the experimental design (Table 2). Subsequently, from Table 3, it was noticed that for TAC, a Model F-value of 868.48 implied the model was significant, and *p*-values less than 0.05 implied that the model terms were significant. The ANOVA revealed that the significant model terms were B, D, AB, AD, A^2, B^2, C^2, and D^2. Only a 0.01 variation in TAC could not be explained by the existing model, according to the determinant coefficient of $R^2 = 0.99$. Moreover, the predicted R^2 of 0.98 agreed with the adjusted R^2 of 0.99.

$$\text{R2 (TAC)} = +1.03 + 0.3114\text{B} + 0.3152\text{D} + 0.3727\text{AB} - 0.0386\text{AD} + 0.0247\text{A}^2 - 0.0311\text{B}^2 + 0.0148\text{C}^2 - 0.1208\text{D}^2 \quad (4)$$

A model reduction was achieved by neglecting the insignificant model terms. Equation (4) represents the model equation showing the correlation between the TAC (R2) and the variables in coded units. The regression equation's b coefficients showed that the ethanol concentration and extraction time positively affected the anthocyanins extraction. The interaction between citric acid and ethanol concentration (AB) had an appreciably positive effect on anthocyanins extraction. In contrast, citric acid concentration (A^2) and temperature (C^2) had a more negligible contribution. Furthermore, moderately negative effects on the anthocyanins yield were shown by the interaction between citric acid concentration and extraction time (AD), between ethanol concentration and ethanol concentration (B^2), and between time and time (D^2).

The 3D surface plots of significant interaction effects display the ethanol concentration, acid, time, and temperature of extraction and the interaction among various factors influencing the conventional extraction of red onion skins anthocyanins, characterized by curved surfaces, as exhibited in Figure 1B(a–d).

In examining the effects of ethanol concentration and citric acid, it was noticed that the TAC increased as the ethanol concentration increased to 50% and the citric acid concentration was over 0.86% (Figure 1B(a)). According to the surface graphs, the concentration of anthocyanins was not influenced by temperature variation and extraction time but was influenced by ethanol concentration (Figure 1B(b,c)). The yield of anthocyanins constantly improved as the extraction time and ethanol concentration increased simultaneously, according to an analysis of the impacts of both variables (Figure 1B(d)).

The variation in the output response range concerning the reference point revealed how sensitive the response was to that variable. This plot helped to identify the factor that most influenced the TAC extraction response. The perturbations graph showing each independent variable's impact revealed that time extraction and ethanol concentration significantly affected the TAC. To a lesser extent, the temperature also influenced it (Figure 2b).

3.3. Optimization and Validation of the Extraction Parameters

The model recommended optimal factors based on maximizing the response desirability to validate the model equation. A desirability score of 1 (0.929) indicated that all selected conditions were correct (Figure 3, Table 4). The optimal conditions for generating the highest extraction of anthocyanins and the highest antioxidant activity were 0.87% citric acid, 60% ethanol, 25 °C, and an extraction time of 180 min.

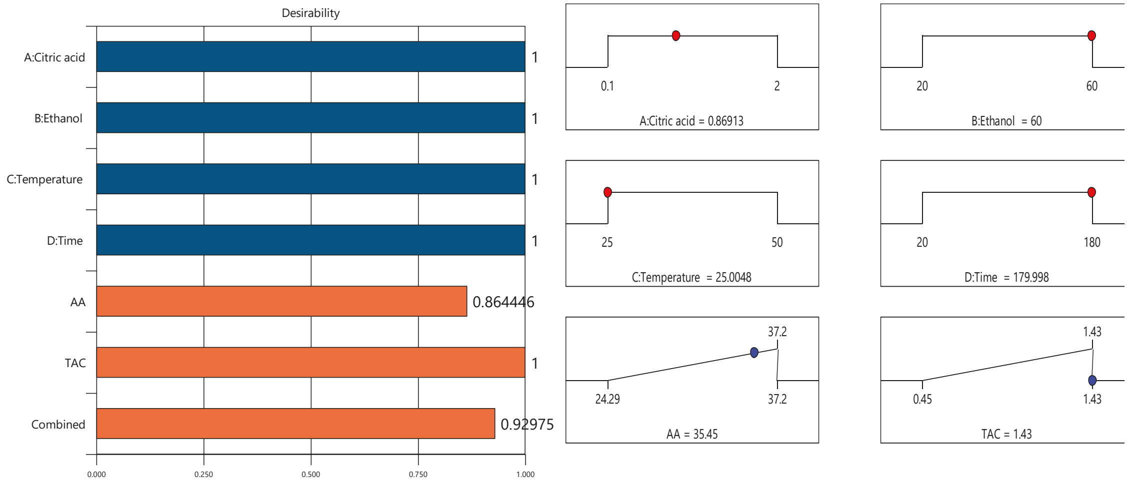

(**a**) (**b**)

Figure 3. Optimization desirability bar chart (**a**) and ramps (**b**).

Table 4. Validation of the mathematical model.

Dependent Variable	Predicted Value	95% Confidence Intervals	Experimental Value
AA (mM TE/g DW)	35.45	24.29–37.20	37.20
TAC (mg C3G/g DW)	1.43	0.45–1.43	1.43

The model predicted the maximum concentration of antioxidant activity and anthocyanins were 35.45 mM TE/g DW and 1.43 mg C3G/g DW, respectively. At the same time, the experimental data showed immediate responses to those predicted by the model, particularly 37.20 mM TE/g DW and 1.43 mg C3G/g DW (Table 4).

4. Discussion

This study optimized the conventional extraction process parameters to extract anthocyanins from red onion skins and enhance their antioxidant activity. Four variables (ethanol concentration, citric acid, temperature, and time) were used to optimize the extraction parameters screened by CCD. Under the optimum conditions, the antioxidant activity was at the highest level at an ethanol concentration of around 60% and a low temperature (25 °C).

However, Corrales et al. [14] reported that extracting red grape skins at 70 °C with 50% ethanol concentration increased the extract's antioxidant activity. These different results could potentially be due to variations in the principles or reaction times used to measure the antioxidant activity [15]. Our findings for red onion skin extracts' antioxidant activity approach those of Viera et al. [16]. The most significant DPPH radical scavenging activity, measured by the authors as 116.58 ± 4.9 mol TE/g DW, was found in red onion skin extracts obtained by conventional extraction under ideal conditions of 80% ethanol and 120 min of extraction at 25 °C. In a different study, Ifesan [17] asserted that the activity to scavenge DPPH radicals was highest in an onion skin extract obtained by conventional extraction (maceration for 24 h at 25 °C with 80% ethanol), reaching a value of 27.76 ± 0.91 µg TE/mL. Prokopov et al. [18] used 70% aqueous ethanol, 15 min as the extraction time, and 45 °C to find that the extract of red onion skins exposed to ultrasound had higher antioxidant activity (490.54 ± 9.43 mM TE/g DW). Additionally, to assess the optimum antioxidant activity of onion solid waste extracts, Khiari et al. [19] utilized a conventional extraction method (40 °C, 6 h). In comparison to our findings, the 90% ethanol acidified with 0.1% HCl produced a decreased antiradical activity (0.32 ± 0.02 mM TE/g DW).

The extraction process is determined by the values of the extraction parameters employed while extracting bioactive compounds from plant matrices. Likewise, the different polarities of the compounds extracted using an experimental model may have an unpredictable effect on the extraction conditions. As a result, the extractions were conducted using solvents with varying polarities and varying the water and ethanol proportions. Adding water to ethanol may enhance the yield of anthocyanins extraction [20], and the resulting extracts are simple to introduce into biological systems. Highly glycosylated phenolics found in red onion skins cannot be extracted entirely only with pure organic solvents and require the application of mixtures containing water and acids. Water plays an important role in the swelling of plant material. In contrast, ethanol is responsible for disrupting the bonding between the solutes and the plant matrix, thus enabling a better mass transfer of the compounds. Therefore, a mixture of water and ethanol as solvent agents displays a synergistic effect that facilitates phenolics extraction. In addition, the citric acid used in a solvent mixture ruptures the cell membranes and releases phenol compounds [21]. The flavylium cation is the dominant species at pH = 3 or lower and contributes to the purple, orange, and red colors. A high solubility of anthocyanins in water is obtained by lowering the pH, increasing the structure transfer to the flavylium cation, and enhancing the stability. Hence, to optimize the extraction, citric acid is added to the extraction blend to acidify the medium [22]. When protic polar solvents such as ethanol are utilized, the acidification of the solvent improves the capacity to extract phenolics. The phenol–phenolate equilibrium moves toward the less polar phenyl form when the medium is acidified, making organic solvent extraction easier [23]. For anthocyanins, acidified ethanol is frequently used, which denatures the cell membranes while dissolving and stabilizing them [24]. Even anthocyanins that are structurally dependent on the medium's pH could be extracted through acidification, which changes their solubility characteristics and affects their stability [23]. Therefore, the use of weak organic acids, such as citric acid, is recommended besides the addition of water to maximize the effectiveness of solvent extraction. As previously noted, acids are typically used for effective anthocyanin extraction. To avoid the degradation or change of the native forms of the phenolic compounds, weak organic acid citric acid at the concentration of 0.05–2.64% was chosen in the experiments. It is also important to mention that the ethanol and citric acid combination was preferred as a food-grade solvent component for phenolics extraction. For example, the extraction of anthocyanins in conditions such as 30% ethanol with 3% of citric acid and 24 h at room temperature has been reported to give good results for blueberry leaves extraction [25]. In the past, mixtures of ethanol and citric acid were employed to extract phenolic compounds, particularly anthocyanins [26–28], and ethanol and its combination with citric acid have been reported to contribute to a successful extraction.

The CCD findings revealed that ethanol concentration and extraction time positively affected anthocyanins extraction. The findings support the results of Khazaei et al. [29], who found that by increasing the ethanol percentage and time, the TAC increased, which indicated a positive effect on anthocyanins extraction. In a Box–Behnken optimization study [30], 90% aqueous glycerol extracts of red onions under optimum sonication conditions with a 90/1 solvent/solid ratio at 45 °C for 60 min generated a high concentration of total pigments (1.87 ± 0.39 mg C3G/g DW). The TAC of the red onion skin extract reported by Bordin Viera et al. [31] was greater than that obtained in the present study, ranging from 0.82 to 4.31 mg C3G/g DW. Using ultrasound extraction, the anthocyanin yield was greater as the ethanol concentration increased (60–80%).

In addition, it was observed that the extraction temperature displayed a minor effect on the extraction yield of anthocyanins. Backes et al. [32] revealed that mild temperatures and a high content of ethanol increased the yield of anthocyanins extraction. Therefore, the authors confirmed that a solvent consisting of ethanol 100% acidified with citric acid, mixed and centrifuged with a powdered sample in a solid/liquid ratio of 50 g/L for 13.74 min at 35.64 °C was the optimal analytical factor to increase the TAC in extracts from fig skin (a by-product of fruit). Higher temperatures damage anthocyanins (may cause their degradation) and result in a loss in yield, according to several earlier studies [33,34].

In our study, the TAC range was close to the one obtained by Oancea and Drághici [20], that reported 0.99 mg C3G/g fresh matter for the outer skins of the Sibiu red onion (*Allium cepa* L.) cultivar after extraction at 4 °C for 2 h with a mixture of ethanol/acetic acid/water (50:8:42, *v*/*v*/*v*), but lower than that reported by Samir et al. [35] (20 mg C3G/100 g), who used acidified ethanol with 1.5 N HCl (85:15, *v*/*v*) by maceration at 4 °C for 24 h.

The concentration of anthocyanins in the red onion skin extracts obtained through conventional extraction was examined by Viera et al. [16]. The extract obtained using 60% ethanol with an extraction time of 60 min at 25 °C yielded a concentration of anthocyanins of 470.2 ± 16.2 mg C3G/100 g DW. Additionally, with 90 min of extraction using 70% ethanol at 40 °C provided a more significant amount of anthocyanins extracted from red onion skins (847.47 ± 34.23 mg C3G/100 g DW) [36]. Makris [37] obtained a higher TAC of 183.85 mg C3G/100g DW by conventional extraction under the optimal conditions of 25 °C and 3.7 h extraction time from onion skins extract using 60% ethanol. Furthermore, the cultivar/origin of the plant material and its extraction conditions impact the amount of the extracted bioactive compounds.

According to the results of the optimization experiment, increasing ethanol concentration and time (up to 2 h) can be favorable to achieve a higher antioxidant activity. These findings are in agreement with the study conducted by Bordin Viera et al. [31], who suggested that ethanol concentration has a significant influence on the DPPH scavenging activity. Therefore, the red onion skin extracts obtained with ethanol at 20%, 40%, and 60% presented antioxidant activities of 26.12, 44.47, and 83.27 µmol TE/g DW, respectively.

5. Conclusions

A CCD and response surface methodology was used to optimize the variables of the conventional solvent extraction process (citric acid concentration—0.87%, ethanol concentration—60%, temperature—25 °C, and extraction time—179.99 min) to obtain red onion skin extracts with a high content of anthocyanins and high levels of antioxidant activity. The interaction of optimal time, temperature and acid and solvent concentrations improved the extraction of the antioxidant compounds yielding higher concentrations of anthocyanins (1.43 mg C3G/g DW) and DPPH radical scavenging activity levels (37.20 mM TE/g DW).

The optimization of the extraction process proved that the conventional solvent extraction could be an effective method for obtaining valuable extracts from natural and inexpensive sources such as food by-products with potential antioxidant and free radical scavenging activities.

These findings display an economically efficient extraction considering the low cost of by-product materials. Due to the high concentration of functional bioactive components in red onion skins, these compounds have a variety of uses in the food, pharmaceutical, and nutraceutical industries.

Author Contributions: Conceptualization, F.S., O.E.C. and G.R.; methodology, F.S. and O.E.C.; software, O.E.C. and I.A.; validation, O.E.C. and I.A.; formal analysis, F.S.; investigation, F.S.; resources, G.E.B.; data curation G.R. and N.S.; writing—original draft preparation F.S. and I.A.; writing—review and editing, G.R. and N.S.; visualization, N.S.; supervision, G.E.B. All authors have read and agreed to the published version of the manuscript.

Funding: This research received no external funding.

Institutional Review Board Statement: Not applicable.

Informed Consent Statement: Not applicable.

Data Availability Statement: The data supporting this study's findings are available from the corresponding author (G.R.) upon reasonable request.

Acknowledgments: The results of this work have been presented to the 10th edition of the Scientific Conference organized by the Doctoral Schools of "Dunarea de Jos" University of Galati (SCDS-UDJG) http://www.cssd-udjg.ugal.ro/ (accessed on 9 April 2022) that will be held on 9th and 10th of June 2022, in Galati, Romania.

Conflicts of Interest: The authors declare no conflict of interest.

References

1. Pérez-Gregorio, R.M.; García-Falcón, M.S.; Simal-Gándara, J.; Rodrigues, A.S.; Almeida, D.P.F. Identification and quantification of flavonoids in traditional cultivars of red and white onions at harvest. *J. Food Compos. Anal.* **2010**, *23*, 592–598. [CrossRef]
2. Sharma, K.; Mahato, N.; Nile, S.H.; Lee, E.T.; Lee, Y.R. Economical and environmentally-friendly approaches for usage of onion (Allium cepa L.) waste. *Food Funct.* **2016**, *7*, 3354–3369. [CrossRef] [PubMed]
3. Galanakis, C.M. Recovery of high added-value components from food wastes: Conventional, emerging technologies and commercialized applications. *Trends Food Sci. Technol.* **2012**, *26*, 68–87. [CrossRef]
4. Benítez, V.; Mollá, E.; Martín-Cabrejas, M.A.; Aguilera, Y.; López-Andréu, F.J.; Cools, K.; Terry, L.A.; Esteban, R.M. Characterization of Industrial Onion Wastes (Allium cepa L.): Dietary Fibre and Bioactive Compounds. *Plant Foods Hum. Nutr.* **2011**, *66*, 48–57. [CrossRef]
5. Zill-e-Huma; Vian, M.A.; Fabiano-Tixier, A.-S.; Elmaataoui, M.; Dangles, O.; Chemat, F. A remarkable influence of microwave extraction: Enhancement of antioxidant activity of extracted onion varieties. *Food Chem.* **2011**, *127*, 1472–1480. [CrossRef]
6. Ali, O.-H.; Al-sayed, H.; Yasin, N.; Afifi, E. Effect of Different Extraction Methods on Stablity of Anthocyanins Extracted from Red Onion peels (Allium cepa) and Its Uses as Food Colorants. *Bull. Natl. Nutr. Inst. Arab. Repub. Egypt* **2016**, *47*, 196–219. [CrossRef]
7. Nile, A.; Gansukh, E.; Park, G.-S.; Kim, D.-H.; Hariram Nile, S. Novel insights on the multi-functional properties of flavonol glucosides from red onion (Allium cepa L) solid waste—In vitro and in silico approach. *Food Chem.* **2021**, *335*, 127650. [CrossRef]
8. Ozkan, G.; Franco, P.; De Marco, I.; Xiao, J.; Capanoglu, E. A review of microencapsulation methods for food antioxidants: Principles, advantages, drawbacks and applications. *Food Chem.* **2019**, *272*, 494–506. [CrossRef]
9. Mourtzinos, I.; Prodromidis, P.; Grigorakis, S.; Makris, D.P.; Biliaderis, C.G.; Moschakis, T. Natural food colorants derived from onion wastes: Application in a yoghurt product. *Electrophoresis* **2018**, *39*, 1975–1983. [CrossRef]
10. Ghareaghajlou, N.; Hallaj-Nezhadi, S.; Ghasempour, Z. Red cabbage anthocyanins: Stability, extraction, biological activities and applications in food systems. *Food Chem.* **2021**, *365*, 130482. [CrossRef]
11. Benito-Román, Ó.; Blanco, B.; Sanz, M.T.; Beltrán, S. Freeze-dried extract from onion (Allium cepa cv. Horcal) skin wastes: Extraction intensification and flavonoids identification. *Food Bioprod. Process.* **2021**, *130*, 92–105. [CrossRef]
12. Lee, J.; Durst, R.W.; Wrolstad, R.E. Determination of Total Monomeric Anthocyanin Pigment Content of Fruit Juices, Beverages, Natural Colorants, and Wines by the pH Differential Method: Collaborative Study. *J. AOAC Int.* **2005**, *88*, 1269–1278. [CrossRef]
13. Horincar, G.; Enachi, E.; Stănciuc, N.; Râpeanu, G. Extraction and characterization of bioactive compounds from eggplant peel using ultrasound—Assisted extraction. *Ann. Univ. Dunarea Jos Galati. Fascicle VI-Food Technol.* **2019**, *43*, 40–53. [CrossRef]
14. Corrales, M.; García, A.F.; Butz, P.; Tauscher, B. Extraction of anthocyanins from grape skins assisted by high hydrostatic pressure. *J. Food Eng.* **2009**, *90*, 415–421. [CrossRef]
15. Etsuo, N. Antioxidant capacity: Which capacity and how to assess it? *J. Berry Res.* **2011**, *1*, 169–176. [CrossRef]
16. Viera, V.B.; Piovesan, N.; Rodrigues, J.B.; Mello, R.; De, O.; Prestes, R.C.; Santos, R.C.; Vaucher, A.; Hautrive, T.P.; Kubota, E.H. Extraction of phenolic compounds and evaluation of the antioxidant and antimicrobial capacity of red onion skin (Allium cepa L.) | Request PDF. *Int. Food Res. J.* **2017**, *24*, 990–999.

17. Ifesan, B.O.T. Chemical Composition of Onion Peel (Allium cepa) and its Ability to Serve as a Preservative in Cooked Beef. *Hum. J.* **2017**, *7*, 25–34.
18. Prokopov, T.; Slavov, A.; Petkova, N.; Yanakieva, V.; Bozadzhiev, B.; Taneva, D. Study of onion processing waste powder for potential use in food sector. *Acta Aliment.* **2018**, *47*, 181–188. [CrossRef]
19. Khiari, Z.; Makris, D.P.; Kefalas, P. An Investigation on the Recovery of Antioxidant Phenolics from Onion Solid Wastes Employing Water/Ethanol-Based Solvent Systems. *Food Bioprocess Technol.* **2007**, *2*, 337. [CrossRef]
20. Oancea, S.; Drághici, O. pH and thermal stability of anthocyanin-based optimised extracts of Romanian red onion cultivars. *Czech J. Food Sci.* **2013**, *31*, 283–291. [CrossRef]
21. Hasbay, I.; Galanakis, C.M. Recovery technologies and encapsulation techniques. In *Polyphenols: Properties, Recovery, and Applications*; Galanakis, C.M., Ed.; Woodhead Publishing: Cambridge, UK, 2018; pp. 233–264. ISBN 978-0-12-813573-0. [CrossRef]
22. Jeya Krithika, S.; Sathiyasree, B.; Beniz Theodore, E.; Chithiraikannu, R.; Gurushankar, K. Optimization of extraction parameters and stabilization of anthocyanin from onion peel. *Crit. Rev. Food Sci. Nutr.* **2022**, *62*, 2560–2567. [CrossRef]
23. Santos-Buelga, C.; Gonzalez-Manzano, S.; Dueñas, M.; Gonzalez-Paramas, A.M. Extraction and Isolation of Phenolic Compounds. *Methods Mol. Biol.* **2012**, *864*, 427–464. [CrossRef]
24. Dai, J.; Mumper, R.J. Plant Phenolics: Extraction, Analysis and Their Antioxidant and Anticancer Properties. *Molecules* **2010**, *15*, 7313–7352. [CrossRef]
25. Routray, W.; Orsat, V. MAE of Phenolic Compounds from Blueberry Leaves and Comparison with Other Extraction Methods. *Ind. Crops Prod.* **2014**, *58*, 36–45. [CrossRef]
26. Gao, L.; Mazza, G. Extraction of Anthocyanin Pigments from Purple Sunflower Hulls. *J. Food Sci.* **1996**, *61*, 600–603. [CrossRef]
27. Nicoué, E.E.; Savard, S.; Belkacemi, K. Anthocyanins in Wild Blueberries of Quebec: Extraction and Identification. *J. Agric. Food Chem.* **2007**, *55*, 5626–5635. [CrossRef]
28. Fan, G.; Han, Y.; Gu, Z.; Chen, D. Optimizing Conditions for Anthocyanins Extraction from Purple Sweet Potato Using Response Surface Methodology (RSM). *LWT Food Sci. Technol.* **2008**, *41*, 155–160. [CrossRef]
29. Khazaei, K.M.; Jafari, S.M.; Ghorbani, M.; Kakhki, A.H.; Sarfarazi, M. Optimization of Anthocyanin Extraction from Saffron Petals with Response Surface Methodology. *Food Anal. Methods* **2016**, *9*, 1993–2001. [CrossRef]
30. Katsampa, P.; Valsamedou, E.; Grigorakis, S.; Makris, D.P. A green ultrasound-assisted extraction process for the recovery of antioxidant polyphenols and pigments from onion solid wastes using Box–Behnken experimental design and kinetics. *Ind. Crops Prod.* **2015**, *77*, 535–543. [CrossRef]
31. Bordin Viera, V.; Piovesan, N.; Mello, R.D.O.; Barin, J.S.; Fogaça, A.D.O.; Bizzi, C.A.; De Moraes Flores, É.M.; Dos Santos Costa, A.C.; Pereira, D.E.; Soares, J.K.B.; et al. Ultrasonic assisted extraction of phenolic compounds with evaluation of red onion skin (Allium cepa L.) antioxidant capacity. *J. Culin. Sci. Technol.* **2021**, *19*, 475–566. [CrossRef]
32. Backes, E.; Pereira, C.; Barros, L.; Prieto, M.A.; Genena, A.K.; Barreiro, M.F.; Ferreira, I.C.F.R. Recovery of bioactive anthocyanin pigments from Ficus carica L. peel by heat, microwave, and ultrasound based extraction techniques. *Food Res. Int.* **2018**, *113*, 197–209. [CrossRef] [PubMed]
33. Pinelo, M.; Rubilar, M.; Jerez, M.; Sineiro, J.; Núñez, M.J. Effect of Solvent, Temperature, and Solvent-to-Solid Ratio on the Total Phenolic Content and Antiradical Activity of Extracts from Different Components of Grape Pomace. *J. Agric. Food Chem.* **2005**, *53*, 2111–2117. [CrossRef] [PubMed]
34. Cacace, J.; Mazza, G. Optimization of Extraction of Anthocyanins from Black Currants with Aqueous Ethanol. *J. Food Sci.* **2003**, *68*, 240–248. [CrossRef]
35. Samir, R.M.; Osman, A.; El-Sayed, A.I.; Algaby, A.M. Physicochemical properties and antimicrobial effects of Roselle corolla, onion peels and peanut skins anthocyanins. *Zagazig J. Agric. Res.* **2019**, *46*, 769–781. [CrossRef]
36. Oancea, S.; Radu, M.; Olosutean, H. Development of ultrasonic extracts with strong antioxidant properties from red onion wastes. *Rom. Biotechnol. Lett.* **2020**, *25*, 1320–1327. [CrossRef]
37. Makris, D.P. Optimisation of Anthocyanin Recovery from Onion (Allium cepa) Solid Wastes Using Response Surface Methodology. *J. Food Technol.* **2010**, *8*, 183–186. [CrossRef]

inventions

MDPI

Article

Event-Based PID Control of a Flexible Manufacturing Process

Octavian Duca [1,2,*], Eugenia Minca [1,3], Adrian Filipescu [1,4], Daniela Cernega [4], Razvan Solea [4] and Claudiu Bidica [1]

[1] Doctoral School of Fundamental Sciences and Engineering, "Dunarea de Jos" University of Galati, 800008 Galati, Romania
[2] Institute of Multidisciplinary Research for Science and Technology, "Valahia" University of Tâgoviste, 130024 Târgoviste, Romania
[3] Department of Automation, Computer Science and Electrical Engineering, "Valahia" University of Tâgoviste, 130024 Târgoviste, Romania
[4] Department of Automation and Electrical Engineering, "Dunarea de Jos" University of Galati, 800008 Galati, Romania
* Correspondence: octavian_duca@yahoo.com

Abstract: In most cases, the system control is made in a sampled manner, measuring the controlled value at a predefined frequency given by the sampling time. However, not all processes provide relevant information at regular intervals, especially in manufacturing. To reduce the costs and complexity of systems, event-based measuring is necessary. To control this kind of process, an event-based controller is needed. This poses some challenges, especially between the event-triggered measurement, as the process runs in an open loop. In the literature, most event-based controllers are based on the comparison of the error value with a predefined value and activate the controller if this value is crossed. However, in this type of controller, the measured value is measured at a predefine interval and is not suited for most event-based processes. In manufacturing systems, the most usual event-based process is represented by the conveyor transportation system. In this process, the product position is measured only in key locations on the conveyor. For the optimal operation of a flexible manufacturing system, the presence of a product in a key location at predetermined intervals is necessary. For this purpose, this article presents an event-based PID controller implemented on a conveyor transportation system.

Keywords: flexible manufacturing; PID; event-based control

Citation: Duca, O.; Minca, E.; Filipescu, A.; Cernega, D.; Solea, R.; Bidica, C. Event-Based PID Control of a Flexible Manufacturing Process. *Inventions* **2022**, *7*, 86. https://doi.org/10.3390/inventions7040086

Academic Editor: Eugen Rusu

Received: 26 August 2022
Accepted: 21 September 2022
Published: 26 September 2022

Publisher's Note: MDPI stays neutral with regard to jurisdictional claims in published maps and institutional affiliations.

Copyright: © 2022 by the authors. Licensee MDPI, Basel, Switzerland. This article is an open access article distributed under the terms and conditions of the Creative Commons Attribution (CC BY) license (https://creativecommons.org/licenses/by/4.0/).

1. Introduction

In a flexible manufacturing environment, most processes need precise control of the output value, especially the transport durations. These values cannot always be measured in a continuous manner, basing the control of the process on a discrete event measurement [1]. Especially in the transportation of the product in the flexible manufacturing system, the measurement of the product position is made based on binary sensors at a predefined location [2]. This determines the necessity for event-based control of the process. In most cases, this event-based control is made in a non-adaptive manner [3]. The control is usually made using a rule-based controller that sets a predefined control value based on an event [4]. In some cases, the controller needs a higher degree of adaptability to cope with variations in the system [5].

In most types of controls, the output value is measured at regular intervals, so the update of the control value is made in a time-triggered manned [6]. Even if studied extensively, the time-triggered control cannot cope with most of the event-based processes, especially because of the asynchronistic behavior of the system and, in some cases, the binary measurements [7]. To compensate for the asynchronistic behavior, some proposals were made in the literature but only for measurement losses, not being suited for an even-based control [8]. In the literature, event-based control, e.g., the arrival of a product to a certain location as an event trigger, has little coverage [6]. In most event-based control studies, the event-trigger is given by arriving at the error level of the output to a certain predefined value [9,10]. This type of even-based control is unsuitable for most event-based processes [11].

Based on event-triggered control, by combining it with impulsive control, further development of event-triggered impulsive control was proposed. In this type of control, the conditions and functions of the event-trigger are pre-set and some specific events determine impulsive instants [12–14].

This type of event-based control has as objective the reduction of control value updates and, as a result, the reduction of computational and power usage, especially in low-power devices [15]. However, to measure the error level, it is necessary to measure the output value at a certain predefine duration [16]. This can be done using an intelligent sensor or allocating controller computational power. This is not suitable for most event-based processes, as the output value cannot be measured at regular intervals.

The differences between the time-triggered mechanism and the event-triggered mechanism, based on the occurrence of a preset event, stirred up research, especially in the state estimation of a system [17–19]. In estimating the state and controlling the system, fuzzy or neural network control is implemented [20–22].

In the manufacturing process, the product position is known only at key locations, usually measured using binary presence sensors. Using this type of sensor, an error-based event-triggering or time-triggering controller cannot be implemented [23]. The inability to implement most types of controllers is due to the measurement of the continuous process in a discreet manner [24]. The number of discreet values measured would be defined by the key locations on the system and would determine the continuous running of most control algorithms [25]. This continuous running would be determined by the error values, but as the measurement is done in a few key points, the controller would run based on the old value [26]. This can determine unintended results due to the small number of input values.

In the literature for event-trigger control, multiple solutions are proposed, such as the event-trigger sliding mode control in [27] or the use of a Markov model in [28]. However, in terms of some advantages, a PID control can be implemented, similar to [29] or [16]. In most cases, the PID controller is adopted for simple structure and adaptability in most control cases. In this article, a control algorithm similar to the error event-based algorithm in [9,16] is proposed, as the computation of the controller will start only at the moment a certain event is happening. As the error level trigger case cannot be implemented in the case of a conveyor, a modification of the event trigger is implemented. An activation of the control algorithm is proposed based on the arrival of the product at a certain point on the conveyor and a sensor is activated. From the perspective of the number of activations, the necessary event-based controller would have fewer activations than the proposed literature controllers. The number of activations is given by the key locations where the position of the product is measured.

This paper is organized as follows: Section 2 presents the time-triggered PID control as a reference base in the event-base controller and details the error variation event-trigger controller. Section 3 presents the flexible manufacturing process in which an event-based controller is necessary. Section 4 presents the proposed event-based algorithm and the expected results of the controller in a transportation system. Section 5 presents the implementation of the controller in a flexible manufacturing system and the results obtained.

2. PID Control

As PID control is one of the most studied types of control, in controlling the event-trigger transportation system, PID event-based control was considered. For better comprehension of the proposed event-based algorithm in this chapter, the time-based PID control and the error trigger event-based PID control found in the literature will be reviewed.

2.1. Time-Based PID Control

For the PID control, the S-domain equation that represents the base for the controller is given by:

$$U(s) = K_P(E(s) + \frac{1}{T_I s} \cdot E(s) + T_D \cdot s \cdot E(s)), \tag{1}$$

defining the command value in the S-domain, $U(s)$, based on the error between the reference and actual value of the output, $E(s)$ [9].

The control equation is composed of three parts: proportional, integral and derivative, represented by U_P, U_I, U_D, defined by the integral gain K_P, the integral time T_I, and derivative time T_D. The parameters of these three parts are modified regarding the controller specifications to obtain the desired performance. In some cases, the weighting of the setpoint can be applied for a more flexible structure. The structure of the three components of the PID controller can be represented as follows:

$$\begin{cases} U_P(s) = K_P \cdot E(s) \\ U_I(s) = \frac{K_I}{s} \cdot E(s) \\ U_D(s) = K_D \cdot s \cdot E(s) \end{cases} \tag{2}$$

with K_I defining the integral component gain, and K_D the derivative component gain [15].

To compensate for the possibility of high-frequency noise from the measurements to the derivative part, a low-pass filter can be added, resulting in:

$$U_D(s) = \frac{N \cdot K_D \cdot s}{K_D \cdot s + N} \cdot E(s) \tag{3}$$

with N as the filter gain [15].

In the case of a real process, the value of the command can increase or decrease until a certain point, as more controlled elements have minimal and maximal values. To corelate the controller with the physical capabilities of the system, a set of command saturation rules needs to be implemented, resulting in the following:

$$\begin{cases} U_{Command}(s) = U_{Inferior},\ U(s) < U_{Inferior} \\ U_{Command}(s) = U(s),\ U_{Inferior} \le U(s) \le U_{Superior} \\ U_{Command}(s) = U_{Superior},\ U(s) > U_{Superior} \end{cases}, \tag{4}$$

with $U_{command}(s)$ representing the command value sent to the executing element, is defined by a minimal value, $U_{Inferior}$, and a maximal value, $U_{Superior}$.

If the command value falls outside the desired interval, in addition to the saturation rules, an anti-windup method must be implemented. This eliminated the delays introduced by the integrator factor. The most commonly used method is the clamping method. This method disengages the integrator factor for the duration in which the command falls outside the desired limits.

Considering the mapping of the PID controller from the S-domain to the discrete-time domain, the following is obtained:

$$u(t_k) = u_P(t_k) + u_I(t_k) + u_D(t_k) \tag{5}$$

with the control value in the time domain $u(t_k)$, and it's components $u_P(t_k)$, $u_I(t_k)$, $u_D(t_k)$, for the proportional, integral and derivative parts, where $t_k = k \cdot \overline{h}$ represents the instant moment of the sampling, having $\overline{h}$ the constant sampling period [15]. Similar to the continuous time controller relation to the S-domain, the relation is similar in the Z-domain with discrete time. The proportional part results in:

$$U_P(z) = K_P \cdot E(z) \tag{6}$$

with the discrete time form as [15]:

$$u_P(t_k) = K_P \cdot e(t_k) \tag{7}$$

In the case of the integrator and derivative parts of the PID controller, several solutions can be applied. One of the solutions, backward difference approximation, is a method based on first-order Taylor series expansion. In this expansion $s = \frac{1-z^{-1}}{\overline{h}}$ resulting in

$$\begin{cases} U_I(z) = \frac{K_I \cdot \overline{h}}{1-z^{-1}} E(z) \\ U_D(z) = \frac{N \cdot K_D(1-z^{-1})}{(N \cdot \overline{h} + K_D) - K_D \cdot z^{-1}} \end{cases}, \tag{8}$$

relating to the time domain as [15]:

$$\begin{cases} u_I(t_k) = u_I(t_k - 1) + K_I \cdot \overline{h} \cdot e(t_k) \\ u_D(t_k) = \frac{K_D}{K_D + N \cdot \overline{h}} \cdot u_D(t_{k-1}) + \frac{NK_D}{K_D + N \cdot \overline{h}} \cdot (e(t_k) - e(t_{k-1})) \end{cases} \tag{9}$$

The approximations in the case of the discrete-time controller are more accurate as the sampling duration, $\overline{h}$, is smaller.

2.2. Error Trigger Event-Based PID Controll

The first proposed event-based PID controller consisted of two main parts: an event detector and an PID controller activated based on the detected event. The event detector, with time-based sampling, ensures that the error value is maintained in a certain range and that the duration since the last controller activation is not over a certain limit. Similar to the time-sampling PID, the event detector samples the controlled value at an $\overline{h}$ sampling period. Based on the setpoint and the measured value, the event detector sends a signal to the PID part of the controller when the error level falls outside a certain predefined limit, considered an event. As presented in the literature cases, the event-trigger is considered to be the absolute error value, $e(t_k)$, crossing a predefined $\overline{e}$ level. As a result, the event condition is [9,15]:

$$|e(t_k)| \geq \overline{e}, \tag{10}$$

with $t_k = \sum_k h_k$, with a variable activation period $h_k = t_k - t_{k-1}$ determined in the moment a new event is taking place.

After an event is detected, the PID event-based controller updates the control signal based on the measurements received from the event detector and the previous controller values. In between the event-triggers, the control signal is constant for the h_k duration. Applying the backward difference method approximation in the case of the integrative and derivative parts results in [16]:

$$\begin{cases} u_I(t_k) = u_I(t_{k-1}) + K_I \cdot h_k \cdot e(t_k) \\ u_D(t_k) = \frac{K_D}{K_D + N \cdot h_k} \cdot u_D(t_{k-1}) + \frac{N \cdot K_D}{K_D + N \cdot h_k} \cdot (e(t_k) - e(t_{k-1})) \end{cases}, \tag{11}$$

having h_k replacing the constant period $\overline{h}$ in Equation (9).

Considering the event-triggering condition from (10), as an event is recorded only when the error value is larger than a certain level, the activation interval can become very long, as the variation of the output can be very small. Some compensations are applied predominantly to the integrator and derivative parts. A diminishing factor for the activation interval is introduced, resulting in the reduction of h_k after a long duration of steady output, reducing its effects on the control values. This approach is very similar to the anti-windup method, compensating for errors in the case of saturation of the control value.

For the integral term, an exponential function determines the decrease in the impact of the activation interval as the steady-state duration increases [15,16]:

$$h^I_{\exp}(h_k) = h_k e^{a_I(h_{old}-h_k)} \tag{12}$$

with a_I used to directly influence the importance of the activation interval. This determines the value to get closer to h_k when the activation duration is small and to get very small when the activation duration gets longer.

In the case of the derivate part, similarly, results in:

$$h^D_{\exp}(h_k) = h_{old} + (h_k - h_{old}) \cdot e^{a_D(h_{old}-h_k)} \tag{13}$$

with a_D used to increase or decrease the influence of the exponential factor. The results show that the $h^D_{\exp}(h_k)$ value will be closer to h_k when the activation value is small and closer to the last activation period h_{old} when the activation duration gets bigger.

Using these improvements, a PID with a forgetting factor is obtained, resulting in the integrator and derivative parts as [15,16]:

$$\begin{cases} u_I(t_k) = u_I(t_k-1) + K_I \cdot h^I_{\exp}(h_k) \cdot e(t_k) \\ u_D(t_k) = \frac{K_D}{K_D+N\cdot h^D_{\exp}(h_k)} \cdot u_D(t_{k-1}) + \frac{N\cdot K_D}{K_D+N\cdot h^D_{\exp}(h_k)} \cdot (e(t_k) - e(t_{k-1})) \end{cases} \tag{14}$$

3. Flexible Manufacturing System

Considering the literature in the event-based control area, the research is centered on the reduction of computation power through the reduction of controller activation and control values. This control is based on the sampled measurement of the output value. This is not always possible in a manufacturing system, for example, as the position of a product is measured only in key positions. In this chapter, the hardware and process structure of the flexible manufacturing system considered in the application of event-based control will be presented.

3.1. Flexible Manufacturing System Hardware

The flexible manufacturing system (FMS) is composed of 7 interlocked workstations arranged in a linear manner (Figure 1). The FMS is equipped with three robotic systems, two robotic arms, placed in two of the workstations and a SCARA robotic transportation system (SRTS) placed parallel to the workstations. Each workstation is equipped with a PLC used in the individual control of the station (Figure 2). This also ensures the flexible integration of equipment into the manufacturing system. All PLCs are interconnected on a ProfiNet network, ensuring fast information transmission between PLCs. Having the possibility of PLC interoperability, decision making is made in two stages. This is composed of centralized decision making, centered on the optimization of production, and local decision making, which ensures the achievement of the proposed production durations.

Figure 1. Flexible manufacturing system.

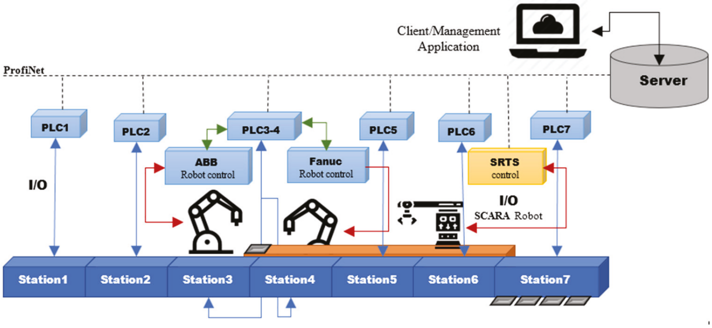

Figure 2. Flexible manufacturing system structure.

Besides the flexibility given by the possibility of integrating new equipment with ease, the FMS presents flexibility in the production process, being able to produce a multitude of products with a minimum of equipment. This is ensured through two production concepts: flexible flow manufacturing (FFM) and flexible manufacturing in cells (FMC). On the FFM, the product travels in a linear manner through 5 workstations of the FMS, schematically represented in Figure 3, each station performing an assembly operation. In FFM production, one of the robotic arms will perform an assembly operation, placing a series of internal parts in a personalized manner, based on the client's request.

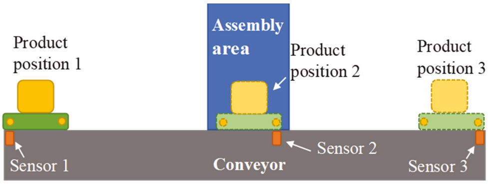

Figure 3. Workstation conveyor sensor placement.

In the FMS, two principal types of products are considered for production: a single internal layer product and a multiple internal layer product. For the multi-layered product, a series of assembly operations are repeated. Both products can be assembled in the FFM process using SRTS. For the multi-layer product, the SRTS transports the product back to one of the previous stations from where a new set of assembly operations are performed. This ensures that the assembly uses a minimal amount of equipment.

For the FMC process, the second robotic arm is used. At workstation 3, the robotic arm can perform some assembly operations on the FFM or perform a competing assembly of a product in a dedicated area. Workstation 3 is equipped with warehouses for each component, allowing for the assembly of any type of product. From the FMC assembly area, the SRTS transports the product on the FFM to the quality control (QC) area at the entry of workstation 6. The FMC is considered only the production of multi-layer products, as robotic arm flexibility gives the possibility of manufacturing more complex products in a much shorter time.

The intersection of the FFM and FMC processes in the QC area and the usage of the SRTS in both processes create some challenges in the optimization of the entire manufacturing system. To ensure the optimal transportation of products on the FMS, the SRTS is placed parallel to the FFM transportation conveyor. This ensures the usage of minimal workstations but also the minimization of some transportation durations.

The placement of the robotic arms is made considering the possibility of increasing the personalization of each product. To compensate for the increased complexity of the assembly process, a robotic arm was introduced in the specific personalization workstation, permitting the manufacturing of a multitude of products based on client requests. The client request is received directly by the FMS, the manufacturing system being connected to a local server. The server receives the client request and processes the information through an optimization algorithm. The output of the algorithm is represented by a production schedule based on assembly and transportation duration. To ensure these durations, a control algorithm is necessary in each station, especially on the transportation side, that can compensate for some of the assembly delays.

3.2. Flexible Manufacturing System Production Process and Control Necessities

Given the production flows of the two considered types of products (Figure 4), in some situations, we have intersecting paths for some products. To ensure optimal manufacturing, the products must arrive at designated locations at a certain time in the process. In the case of the SRTS transport of products, the transport duration is known to be ensured by the robot control system.

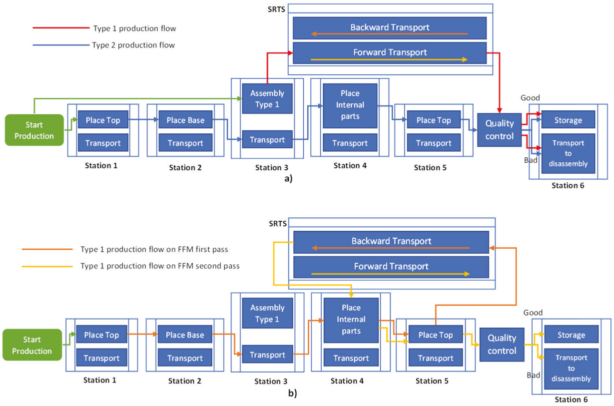

Figure 4. Manufacturing flow for (**a**) single-layer product on FFM and multilayer product on FMC and (**b**) multilayer product on FFM.

In the case of workstation transportation using conveyors, this duration cannot always be guaranteed with sequential control. On a workstation, the position of a product is measured in three key locations using binary location sensors (Figure 3). On a basic conveyor, the position of a product is measured at the entry of the station, the exit and the working area. At a certain moment on the conveyor, only one product is present. In the classic programming of the station PLC, a series of events starts when a certain sensor is activated and continues in a sequential manner until the next sensor is activated. This method of control cannot ensure the transportation of a certain product between two points in a predefined amount of time. To ensure that a product arrives at a certain point at a certain time, an adaptable control algorithm must be implemented.

In the case of a workstation, perturbations on the arrival of a product to a certain location can be introduced mainly by the assembly process. If the process has a longer duration, then the transportation system can compensate for the delay by varying the speed. The control algorithm must also consider some limitations. As a transportation system in a manufacturing process, the direction of transportation should be predefined, meaning that the product cannot travel backwards to a certain location. This can introduce some errors, as the product cannot be positioned at a precise point at the sensor location but position around it. In this case, the error is expected to be lower than the sequential control.

The second factor considered in the control algorithm is the minimal and maximal command values. To ensure that the command value is kept in the desired range, a saturation method is applied. This ensures that the system runs within the desired parameters.

4. Event-Based PID Conveyor Control

As the event-based error triggering method presented in the literature cannot be applied, some modifications were made to this type of control. Considering the number and type of sensors, one of the modifications to the control algorithm needs to be activated if the product is present at one of the sensors. This ensures that the position of the products is known with precision. This leads to a new control algorithm, which is presented in the next pages.

4.1. Event-Based PID Algorithm Structure

Based on the literature on event-based PID with the error level as a trigger event, a new algorithm, Algorithm 1, was designed to replace the error level trigger with a product position trigger. This is accomplished by sending an activation signal to the control part of the algorithm. Based on the product position on the conveyor and the reference set by the production stage, the algorithm calculates the speed of the conveyor and sends it to the conveyor motor. Based on the sensors' positions, in key locations, after the first algorithm activation and arriving of the product to the second sensor, the system will wait for the completion of the production processes and then set the next position reference that starts the transportation. Additionally, between the sensors, the algorithm retains the last known position of the product. In the case of the workstation presented in Figure 3, the activation of the control algorithm is determined by the activation of the sensors present at the entry, assembly area and exit of the workstation. This results in the event-based control algorithm presented below, which calculates the control signal for the transportation of a product between two locations.

Algorithm 1: Algorithm for Event-Based PID Control.

```
Input:      y_ref //position reference given by production stage
            y //product location given by sensor activation
            // actv event triggered by sensors
            actv=      1, if one of the sensors is active
                       0, otherwise
Output: u_com //conveyor speed

//Calculate time between updates: t_pres = t_pres + t_nom
if (actv = 1)
    er = y_ref − y
    up = K * (beta * y_ref − y)
    ud = Td/(N * t_pres + Td) * ud_old − K * Td * N/(N * t_pres + Td) * (y − y_old)
    ui = ui_old + K/Ti − t_pres * e
    u = up + ui + ud
//saturation and anti-windup
        if (u < u_inferior) then //command under a limit
                u_com = u_inferior
                ui = ui_old
        else if (u > u_superior) then //command over a limit
                    u_com = u_superior
                    ui = ui_old
                else
                    u_com = u
                    ui = ui_old + K/Ti − t_pres * e
                end
        end
//update values
        ui_old =ui
        ud_old =ud
        y_old = y
        t_pres = 0 //reset of working time
End
```

4.2. Product Conveyor Transportation Simulation Study

Considering conveyor transportation, the process has as output the product position and as an input the speed of the conveyor. In the S-domain, this translates into a simple transfer function $H(s) = 1/s$. Based on the transfer function, a series of simulations were made to observe the behavior of the system with event-based and continuous PID control. Two situations were considered, one in which the continuous PID controller output is saturated most of the time (Figure 5), resulting in a continuous speed output of the event-based PID (Figure 6). The other situation is considered so that the event-based PID controller changes the output value as the controller is activated the second time the product activates the same sensor.

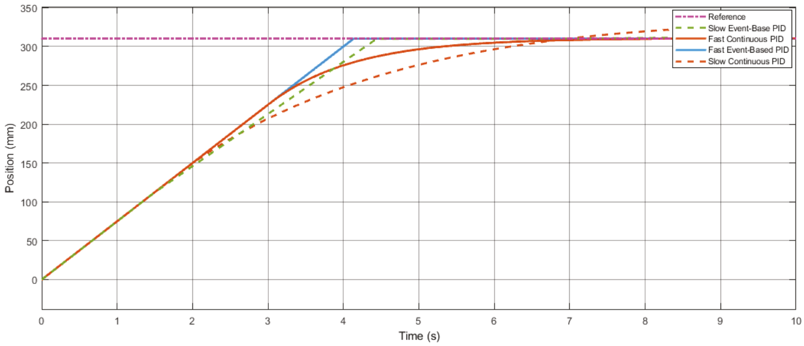

Figure 5. Event-based and continuous PID-measured responses in two different speed conditions.

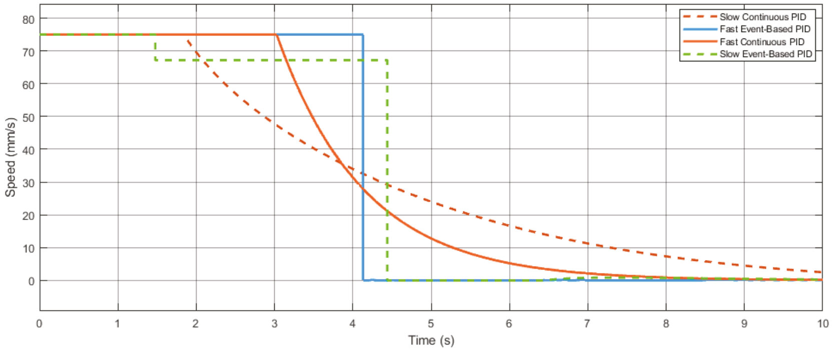

Figure 6. Event-based and continuous PID speed output in two different speed conditions.

The first activation of the event-based PID is determined by the product arriving in the sensor area, determining its activation. The second activation is determined by arriving at the end of the product in the activation area of the sensor. This allowed us to determine the position of the product given by the length of the product. Based on the second activation, a recalculation of the control output is made and an update is made.

It can be observed that the error between the proposed event-based PID and the continuous PID results bets larger with an increase in the transition time. This is determined by the greater speed at the start of the continuous PID, which is similar to the one in the event-based PID. However, in an event-based PID, the speed is calculated only when a sensor is activated; the speed will be kept constant until a new sensor activation occurs.

As the location of the product is usually measured by binary sensors on key locations on the conveyor, in the case of event-based control, the setpoint needs to take values from a discrete interval, given by the number of sensors. This represents the main case of even-based control, as if the setpoint is outside the discrete interval considered, then the product will stop at the next sensor after the setpoint. This is determined by the inability to measure the position of the product between sensors. This could be compensated for by the introduction of digital twins, but this represents future research on this subject. In Figure 7, the error between the setpoint and the event-base PID result can be observed if the setpoint takes a value outside the predefined discrete range. The stabilization of the event-based PID above the setpoint is also given by the introduction of saturation on the command value, assuming that the conveyor can only travel in one direction.

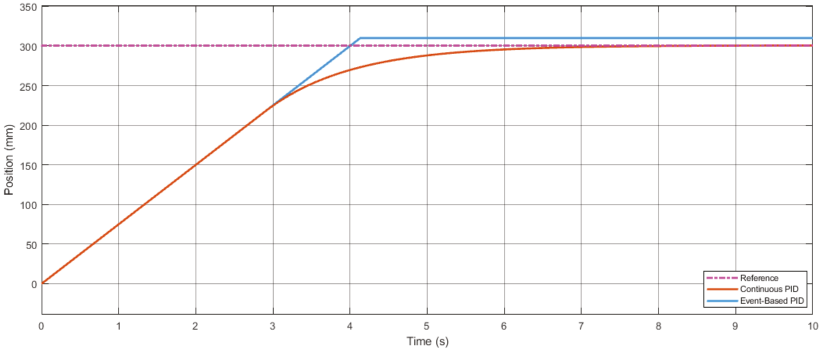

Figure 7. Event-based PID stationary error in the case of reference outside possible discrete points.

If saturation over the control value would not be implemented or the limitation would determine a bidirectional travel of the product, the system would become unstable. In the case of setting a setpoint outside the defined interval, the product would start to travel backward from the sensor after the setpoint to the wone before it. As the product could not settle on the desired setpoint, an infinite oscillation between the two sensors would start. This would also be possible in normal operation, as the setpoint takes values in the desired interval. As the product arrives at a certain sensor, the inertial forces and conveyor error determine the product to overshoot the sensor, triggering an oscillation between sensors (Figure 8). This problem is eliminated by limiting the control value so that the conveyor travels only in one direction, as bidirectional travel is not needed.

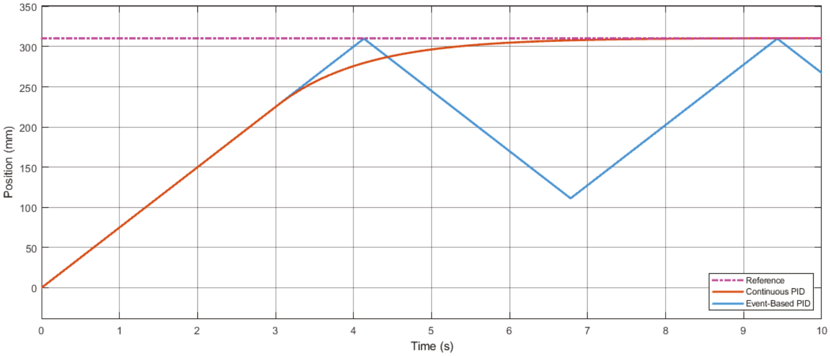

Figure 8. Event-based PID oscillations in the case of negative output signal limits (conveyor moving backward).

5. Flexible Manufacturing System Conveyor Control

Based on the simulation results, an event-based algorithm was implemented, and a series of measurements were made on one of the FMS workstation conveyors. In addition to the calculations of the control value, a series of information transmission durations introduce some delays in system operations. These can be observed in the differences between the algorithm computation durations and the measurements but also by model, using a Petri net (Figure 9). For the simplification of the model, only the first activation of the control algorithm and the corresponding durations for the computation and transport until arriving at the second sensor were considered. This permits more uniform modeling for all situations. The first operation in the conveyor process starts with the previous conveyor, with the transfer of the product and the activation of the first sensor. This is followed by the activation of the control algorithm and the calculation of the control value. This value is sent to the system, and product transportation starts. After the product arrives at the second sensor, assembly operation is started. After the assembly operation is finished, the control value calculation begins. With the control value updated, new transportation of the product is started. As the product arrives at the third sensor, the product is transferred to the next station.

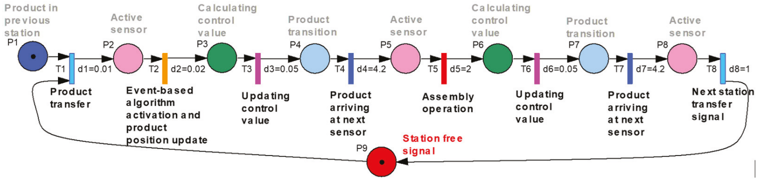

Figure 9. Modeling of the control algorithm in workstation operation.

Figure 10 shows the duration of each step of the conveyor process, from the algorithm activation to the product leaving the workstation. From the control update duration, the time taken by the control value calculation and sending the obtained information to the conveyor can be observed. The value of this duration, even small, can influence the entire production system, especially the production optimization algorithms. This computation and information transmission duration also explain some of the differences between the control algorithm and the measurement duration.

As at a certain moment on the conveyor is present a single product, represented by the station-free signal in the Petri net, a non-Zeno behavior can be ensured. Zeno behavior is defined by the probability of the execution of an infinite number of events in a finite duration. This is represented in most cases as requiring the execution of two or more events at the same moment in time, as presented in [30,31]. As only one product is presented on the conveyor, the activation of the control algorithm is ensured in a sequential manner, as the product arrives at one of the three positions. As one of the sensors is activated, the controller start is triggered. As none of the events that are executed are considered instantaneous and the events are proposed in a sequential manner, the system has a non-Zeno behavior, as illustrated in [30]. Some Zeno behavior can be introduced by faults in the hardware of the system. As certain defects on the sensor side can determine the false activation of certain sensors, the system can interpret the fault as the product being at two positions at the same time, introducing Zeno behavior in the controller. This behavior can be used as a fault detector or eliminated by introducing certain precautions in the system software.

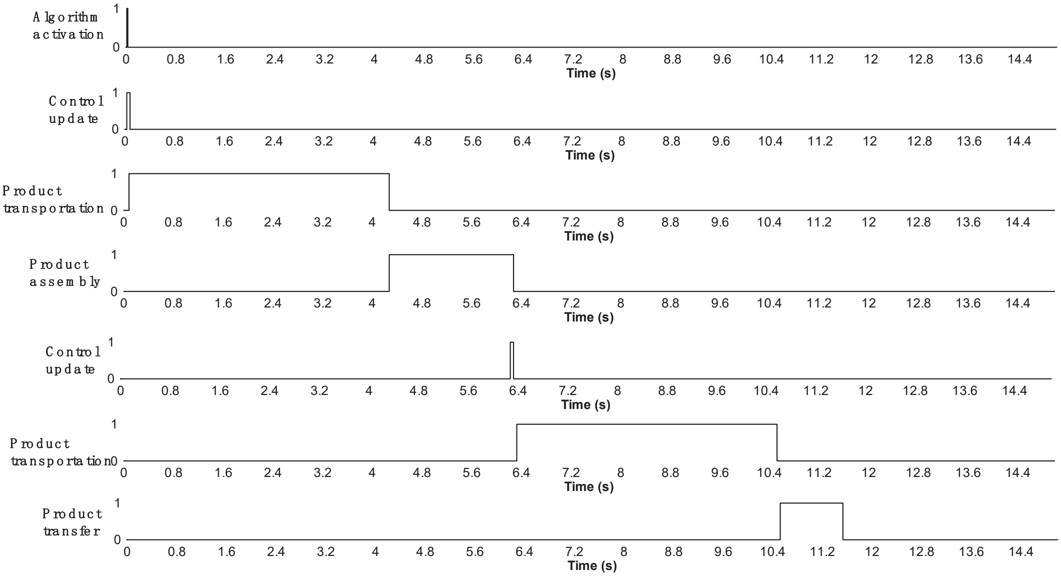

Figure 10. Model simulation duration results.

In Figures 11–13, the control algorithm and model implementation measurements can be observed. Figure 10 represents the control value sent to the conveyor based on the event-based control algorithm. In the graphic, the second update of the control value can be observed as the back of the product crosses the sensor, reducing the conveyor speed. This follows the pattern present in the control algorithm simulation, with minor modifications introduced by data transmission delays and calculation approximations. As the same algorithm is used on the first and second parts of the conveyor and the distances are similar, the results are identical, with minor differences.

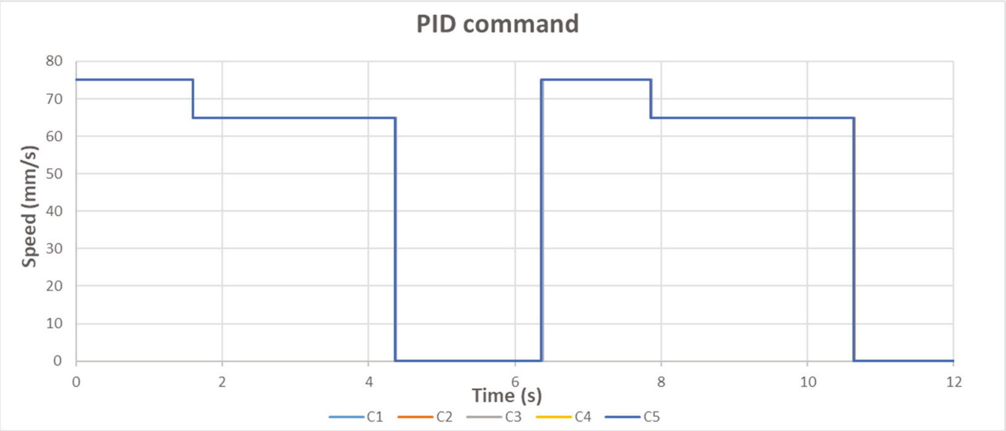

Figure 11. Event-based control speed output in regular cases.

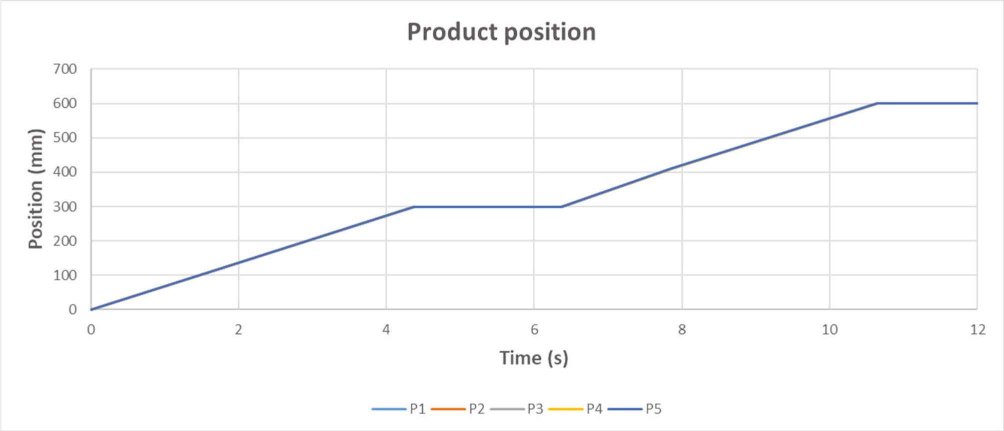

Figure 12. Event-based control product position results in a regular case.

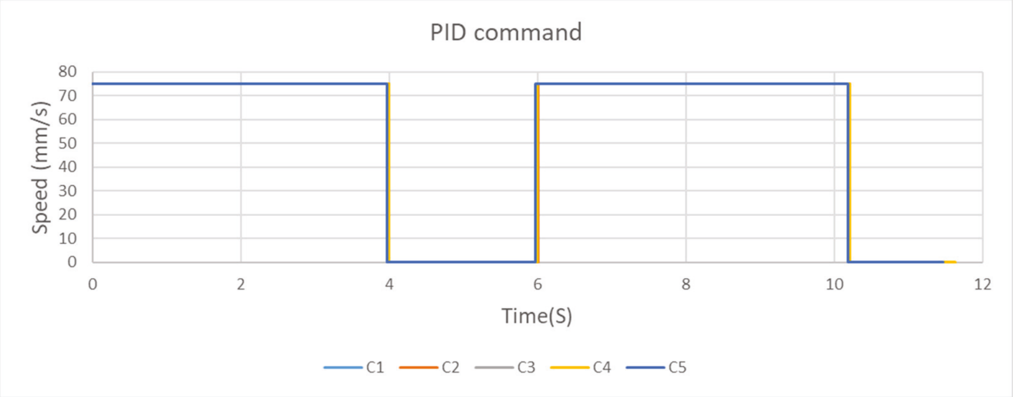

Figure 13. Event-based control speed output in the maximum speed case.

Based on the control value transmitted to the conveyor, Figure 12 shows the position of the product on the duration between entering the workstation and waiting to leave it. Considering the small variation in speed between the product entering and leaving the sensor area, a notable modification in the product transition rate is not visually observable.

In cases in which some durations need to be compensated for based on assembly delays, the controller can set the control value for the conveyor at the maximal value for the entire transport duration between the two locations. These results can be observed in Figure 13, where, for the entire duration of transport, the conveyor speed is kept at the maximum value. This ensures compensation for possible delays.

The proposed algorithm presents control possibilities for a limited number of transportation cases. These cases cannot be controlled in the usual manner, as the measurement of the controlled value is made in a discrete manner. These discrete measurements, done mostly by binary sensors, cannot ensure an optimal number of measurements for a standard PID control. In most cases, and especially in industry, this type of system is controlled using a sequential algorithm. In these usual algorithms, a predefined value is set to the control value, depending on the algorithm step the system is at the given moment. This can be detrimental in some cases if a variable control value is needed.

One type of sequential control algorithm can be based on a Petri net model of the manufacturing system; this determines what actions need to take place at a certain sensor activation. As the resulting actions are predefined, the command values are mostly set at an optimal working speed. This determines a behavior similar to the system, as in the event-based maximal speed case in Figure 13, where the control output is kept at a certain level as the product is transported between the desired positions. This type of control cannot adapt easily to certain disturbances compared to other types of control.

In the case of the proposed event-based algorithm, the best results are obtained if the system is run as a faster process, as the saturation of the control value influences the output of the controller. This brings the event-based controller output closer to the continuous controller.

Another important aspect of the proposed event-based controller is the rapid increase or decrease in the control value. This can further limit the applicability of the controller. In the case of transporting products with a high inertial mass, this type of control can determine big positioning errors and hardware problems. However, in low mas product transportation, this type of problem should not have a definitive impact, permitting the implementation of such a controller.

6. Conclusions

In today's manufacturing environment, most product position measurements are made in an event-triggering manner. As the product arrives in a key position, its location is updated. In most cases, the control of transporting a product between two key locations is carried out by a sequential control algorithm. In this type of control, one sequence of events is activated as the previous sections finish, and some sensors have achieved predefined values. However, using a predefined sequence and value in controlling product transportation limits the possibility of duration compensation in case of product delays. As in flexible manufacturing systems, products need to be at key locations at predefined intervals, so a rigid control algorithm cannot cope with the necessary control requirements.

In this situation, an event-based PID controller is presented for the presented fabrication system. Most of the event-based PID controllers presented in the literature have an event trigger set based on the error value. This means that the output of the system needs to be measured in a sampled manner at regular intervals. This is not possible in most manufacturing systems because the sensors are placed only in key positions.

Starting from the literature algorithms, the main improvement proposed in this article is represented by the modification of the event-trigger from an error level to a position activation event. This is representative of systems where the output of the system, in this case the product position, cannot be measured in a sampled manner. In this case, the error level of the output cannot be determined because the product position is determined only in key positions. This determines the necessity of introducing a new type of event-triggered, as proposed in this paper.

Based on the obtained results, the event-based controller can achieve similar results with the continuous PID in cases in which the control value is limited in a predefined range. In addition, this saturation of the control value results in the stabilization of the event-based controller, as without limitation, the controller would be unstable.

This type of event-based control could be improved by introducing a digital twin in the calculation of the control value and compensating for the error between the digital twin and the real system based on event-triggered measurements. This represents further research on event-based control, with this research being a reference base. Based on the obtained results, further comparisons can be made in developing a digital twin of the system and integrating it into the control loop.

Author Contributions: Conceptualization, O.D., E.M., A.F., R.S., D.C. and C.B.; methodology O.D., E.M., A.F., R.S., D.C. and C.B.; software, O.D.; validation E.M., A.F., R.S. and D.C.; formal analysis E.M., A.F., R.S., D.C. and C.B.; writing—original draft preparation O.D. and E.M.; writing—review and editing E.M., A.F.; supervision E.M., A.F.; project administration E.M.; funding acquisition E.M., A.F. and O.D. All authors have read and agreed to the published version of the manuscript.

Funding: This article (APC) was supported by the Doctoral School of Fundamental Sciences and Engineering, "Dunarea de Jos" University of Galati.

Institutional Review Board Statement: Not applicable.

Informed Consent Statement: Not applicable.

Data Availability Statement: Data availability is not applicable to this article as the study did not report any data.

Acknowledgments: The results of this work were presented to the 10th edition of the Scientific Conference organized by the Doctoral Schools of "Dunarea de Jos" University of Galati (SCDS-UDJG) http://www.cssd-udjg.ugal.ro/ (accessed on 10 May 2022), held on 9th and 10th of June 2022, in Galati, Romania.

Conflicts of Interest: The authors declare no conflict of interest.

References

1. Kamble, S.S.; Gunasekaran, A.; Ghadge, A.; Raut, R. A Performance Measurement System for Industry 4.0 Enabled Smart Manufacturing System in SMMEs—A Review and Empirical Investigation. *Int. J. Prod. Econ.* **2020**, *229*, 107853. [CrossRef]
2. Huang, D.; Lv, J. Run-to-Run Control of Batch Production Process in Manufacturing Systems Based on Online Measurement. *Comput. Ind. Eng.* **2020**, *141*, 106298. [CrossRef]
3. Zhang, D.; Zhang, L.; Yu, Z.; Li, H.; Shu, L. Dynamic Output Feedback Control for Networked Control Systems: A Sum-Based Discrete Event-Triggered Approach. *IFAC-PapersOnLine* **2022**, *55*, 61–66. [CrossRef]
4. Liu, L.; Li, X.; Liu, Y.-J.; Tong, S. Neural Network Based Adaptive Event Trigger Control for a Class of Electromagnetic Suspension Systems. *Control. Eng. Pract.* **2021**, *106*, 104675. [CrossRef]
5. Borase, R.P.; Maghade, D.K.; Sondkar, S.Y.; Pawar, S.N. A Review of PID Control, Tuning Methods and Applications. *Int. J. Dyn. Control.* **2021**, *9*, 818–827. [CrossRef]
6. Visioli, A. Research Trends for PID Controllers. *Acta Polytech.* **2012**, *52*, 144–150. [CrossRef]
7. Durand, S.; Marchand, N.; Guerrero-Castellanos, J.F. Event-Based Stabilization of Nonlinear Time-Delay Systems. *IFAC Proc. Vol.* **2014**, *47*, 6953–6958. [CrossRef]
8. Prabhat Dev, M.; Jain, S.; Kumar, H.; Tripathi, B.N.; Khan, S.A. Various Tuning and Optimization Techniques Employed in PID Controller: A Review. In *Proceedings of International Conference in Mechanical and Energy Technology: ICMET 2019, India*; Yadav, S., Singh, D.B., Arora, P.K., Kumar, H., Eds.; Springer: Singapore, 2020; pp. 797–805. ISBN 978-981-15-2647-3.
9. Åarzén, K.-E. A Simple Event-Based PID Controller. *IFAC Proc. Vol.* **1999**, *32*, 8687–8692. [CrossRef]
10. Durand, S. Event-Based Stabilization of Linear System with Communication Delays in the Measurements. In Proceedings of the 2013 American Control Conference, Washington, DC, USA, 17–19 June 2013; pp. 152–157.
11. Ma, B.; Wang, Y.; Chen, G. Event-Triggered Type-2 Fuzzy-Based Sliding Mode Control for Steer-by-Wire Systems. *Mechatronics* **2022**, *82*, 102704. [CrossRef]
12. Han, X.; Zhao, X.; Sun, T.; Wu, Y.; Xu, N.; Zong, G. Event-Triggered Optimal Control for Discrete-Time Switched Nonlinear Systems With Constrained Control Input. *IEEE Trans. Syst. Man Cybern. Syst.* **2021**, *51*, 7850–7859. [CrossRef]
13. Zhu, W.; Wang, D. Leader-Following Consensus of Multi-Agent Systems via Event-Based Impulsive Control. *Meas. Control.* **2019**, *52*, 91–99. [CrossRef]
14. Bai, Q.-Z. WeiTI-Event-Triggered Impulsive Optimal Control for Continuous-Time Dynamic Systems with Input Time-Delay. *Mathematics* **2022**, *10*, 279. [CrossRef]
15. Durand, S.; Guerrero-Castellanos, J.F. Event-Based Digital PID Control. In Proceedings of the 2015 International Conference on Event-based Control, Communication, and Signal Processing (EBCCSP), Krakow, Poland, 17–19 June 2015; pp. 1–7.
16. Durand, S.; Boisseau, B.; Marchand, N.; Guerrero-Castellanos, J. Event-Based PID Control: Application to a Mini Quadrotor Helicopter. *Control. Eng. Appl. Inform.* **2018**, *20*, 36–47.
17. Heemels, W.P.M.H.; Johansson, K.H.; Tabuada, P. An Introduction to Event-Triggered and Self-Triggered Control. In Proceedings of the 2012 IEEE 51st IEEE Conference on Decision and Control (CDC), Maui, HI, USA, 10 December 2012; pp. 3270–3285.
18. Ge, X.; Han, Q.-L.; Zhang, X.-M.; Ding, L.; Yang, F. Distributed Event-Triggered Estimation Over Sensor Networks: A Survey. *IEEE Trans. Cybern.* **2020**, *50*, 1306–1320. [CrossRef]
19. Qin, J.; Ma, Q.; Shi, Y.; Wang, L. Recent Advances in Consensus of Multi-Agent Systems: A Brief Survey. *IEEE Trans. Ind. Electron.* **2017**, *64*, 4972–4983. [CrossRef]
20. Xu, B.; Li, B. Event-Triggered State Estimation for Fractional-Order Neural Networks. *Mathematics* **2022**, *10*, 325. [CrossRef]

21. Yan, S.; Aly, A.A.; Felemban, B.F.; Gheisarnejad, M.; Tian, M.; Khooban, M.H.; Mohammadzadeh, A.; Mobayen, S. A New Event-Triggered Type-3 Fuzzy Control System for Multi-Agent Systems: Optimal Economic Efficient Approach for Actuator Activating. *Electronics* **2021**, *10*, 3122. [CrossRef]
22. Sun, H.; Yang, Y.; Yu, J.; Zhang, Z.; Xia, Z.; Zhu, J.; Zhang, H. Artificial Intelligence of Manufacturing Robotics Health Monitoring System by Semantic Modeling. *Micromachines* **2022**, *13*, 300. [CrossRef]
23. Yan, J.; Mo, Y.; Ishii, H. Event-Based Control for Synchronization of Stochastic Linear Systems with Application to Distributed Estimation. *IFAC-PapersOnLine* **2022**, *55*, 115–120. [CrossRef]
24. Li, W.; Li, H.; Wang, S. An Event-Driven Multi-Agent Based Distributed Optimal Control Strategy for HVAC Systems in IoT-Enabled Smart Buildings. *Autom. Constr.* **2021**, *132*, 103919. [CrossRef]
25. Krenczyk, D.; Davidrajuh, R.; Skolud, B. An Activity-Oriented Petri Net Simulation Approach for Optimization of Dispatching Rules for Job Shop Transient Scheduling. In *Proceedings of the International Joint Conference SOCO'17-CISIS'17-ICEUTE'17 León, Spain, 6–8 September 2017*; Pérez García, H., Alfonso-Cendón, J., Sánchez González, L., Quintián, H., Corchado, E., Eds.; Springer International Publishing: Cham, Switzerland, 2018; pp. 299–309.
26. Kučera, E.; Nižnanská, M.; Kozák, Š. Advanced Techniques for Modelling of AS/RS Systems in Automotive Industry Using High-Level Petri Nets. In Proceedings of the 2015 16th International Carpathian Control Conference (ICCC), Szilvasvarad, Hungary, 27–30 May 2015; pp. 261–266.
27. Tran, T.D.; Nguyen, T.T.; Duong, V.T.; Nguyen, H.H.; Nguyen, T.T. Parameter-Adaptive Event-Triggered Sliding Mode Control for a Mobile Robot. *Robotics* **2022**, *11*, 78. [CrossRef]
28. Chen, H.; Liu, R.; Xia, W.; Li, Z. Event-Triggered Filtering for Delayed Markov Jump Nonlinear Systems with Unknown Probabilities. *Processes* **2022**, *10*, 769. [CrossRef]
29. Du, S.; Yan, Q.; Qiao, J. Event-Triggered PID Control for Wastewater Treatment Plants. *J. Water Process Eng.* **2020**, *38*, 101659. [CrossRef]
30. Zhang, J.; Johansson, K.H.; Lygeros, J.; Sastry, S. Zeno Hybrid Systems. *Int. J. Robust Nonlinear Control.* **2001**, *11*, 435–451. [CrossRef]
31. Yu, H.; Chen, T. A New Zeno-Free Event-Triggered Scheme for Robust Distributed Optimal Coordination. *Automatica* **2021**, *129*, 109639. [CrossRef]

inventions

MDPI

Article

Sensitivity Analysis of Artificial Neural Networks Identifying JWH Synthetic Cannabinoids Built with Alternative Training Strategies and Methods

Catalina Mercedes Burlacu, Adrian Constantin Burlacu and Mirela Praisler *

Department of Chemistry, Physics and Environment, Faculty of Science and Environment,
"Dunarea de Jos" University of Galati, 47 Domneasca Street, 800008 Galati, Romania
* Correspondence: mirela.praisler@ugal.ro

Abstract: This paper presents the alternative training strategies we tested for an Artificial Neural Network (ANN) designed to detect JWH synthetic cannabinoids. In order to increase the model performance in terms of output sensitivity, we used the *Neural Designer* data science and machine learning platform combined with the programming language *Python*. We performed a comparative analysis of several optimization algorithms, error parameters and regularization methods. Finally, we performed a new goodness-of-fit analysis between the testing samples in the data set and the corresponding ANN outputs in order to investigate their sensitivity. The effectiveness of the new methods combined with the optimization algorithms is discussed.

Keywords: JWH synthetic cannabinoids; artificial neural networks; optimization algorithms

Citation: Burlacu, C.M.; Burlacu, A.C.; Praisler, M. Sensitivity Analysis of Artificial Neural Networks Identifying JWH Synthetic Cannabinoids Built with Alternative Training Strategies and Methods. *Inventions* **2022**, *7*, 82. https://doi.org/10.3390/inventions7030082

Academic Editor: Anastasios Doulamis

Received: 13 July 2022
Accepted: 29 August 2022
Published: 13 September 2022

Publisher's Note: MDPI stays neutral with regard to jurisdictional claims in published maps and institutional affiliations.

Copyright: © 2022 by the authors. Licensee MDPI, Basel, Switzerland. This article is an open access article distributed under the terms and conditions of the Creative Commons Attribution (CC BY) license (https://creativecommons.org/licenses/by/4.0/).

1. Introduction

Artificial neural networks (ANN) contain a set of parameters that can be adjusted to perform different tasks. These structures have universal approximation properties, which means that they can approximate any function in any size and, generally, up to a desired degree of accuracy [1–4].

In this article, we present a series of deep learning training and optimization strategies that have been applied to improve the performance of an ANN identifying JWH-synthetic-cannabinoid-class membership. In order to increase the system sensitivity, we trained and optimized an initial model on four new architectures. For this purpose, we used the data science and machine learning platform *Neural Designer.* The best version was implemented in the *Python 3.10* programming language for further development and improvement.

The classification efficiencies (output results) obtained for several combinations of algorithms, error parameters and regularization methods were compared. The good fit between the test samples and the corresponding ANN outputs was also analyzed. The effectiveness of the methods was analyzed and is presented in detail.

2. Materials and Methods

The initial input database of 150 synthetic chemicals included JWH synthetic cannabinoids, others synthetic cannabinoids and other substances of abuse. These designer drugs were divided into three classes referred to as "Class 1—JWH", "Class 2—non-JWH Cannabinoids" and "Class 3—Others". The group of positives contained 50 JWH synthetic cannabinoids, while the group of negatives included 100 compounds, i.e., 50 non-JWH cannabinoids and 50 other substances of forensic interest [5].

We used the quantitative structure–activity relationship (QSAR) method to estimate and predict the pharmacokinetics, drug-likeness and medicinal chemistry friendliness of each input compound by calculating a number of 300 molecular descriptors in terms of their physical and chemical properties, as well as 50 indices characterizing their chemical absorption, distribution, metabolism, excretion and toxicity activity (ADMET). The descriptors were selected from three blocks, i.e., topological, 3D-MoRSE (molecule representation of structure based on electron diffraction) and toxicity [6].

Only the first 150 most relevant descriptors were selected and used for the final computational and modelling stage. Hence, the input database was a matrix consisting of 150 samples × 150 variables. The shape, feature and target types of the data set, including the list of the computed and tested input molecular descriptors was presented in a previously published article [7].

The data set was divided into three subsets of samples: training, selection and testing. Hence, we used 90 training samples (60%), 30 selection samples (20%) and 30 testing samples (20%). To discover redundancies between the input variables, we used a correlation matrix, which represents a numerical value between -1 and 1 that expresses the strength of the relationship between two variables [8]. The types of layers the most frequently used in our classification model were the perceptron layer, the probabilistic layer and the scaling and bounding layers. The objective of the selection was to find the best-performing network architecture in terms of system sensitivity.

To avoid underfitting and overfitting, the neuron selection algorithm responsible for finding the optimal number of neurons in the networks was the Growing neurons algorithm [9]. The *Neural Designer* data science and machine learning platform was used to generate the mathematical expression represented by ANNs in order to export and incorporate them into the programming language *Python 3.10* in the so-called production mode.

Our general training strategy consisted of two different concepts, i.e., the loss index and the optimization algorithms. The error was the essential term in the loss expression. The most important errors that we estimated were the sum squared error, the mean squared error, the root mean squared error, the normalized squared error and the Minkowski error. We used the L1 and L2 regularization methods, which involve the sum of the absolute values of all parameters and the square sum of all the parameters in the ANN. The loss index was measured on the data set and could be represented as a hyper-surface with the parameters as coordinates (see Figure 1) [10].

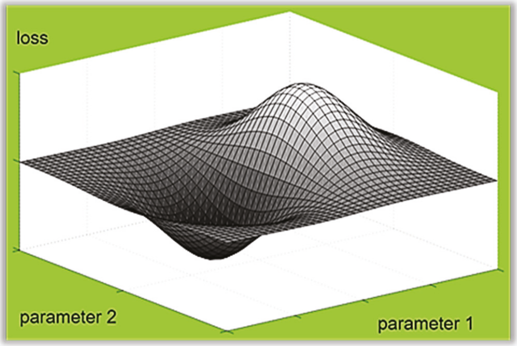

Figure 1. Loss index viewed as a hyper-surface with parameters as coordinates.

In order to train the ANN, we generated a sequence of parameter vectors so that the loss index was reduced at each iteration of the algorithm.

3. Results

Five different optimization algorithms were used and compared, each with a variety of different calculation and storage requirements: gradient descent [11], conjugate gradient, quasi-Newton method, Levenberg-Marquardt algorithm [12] and adaptative linear momentum [13].

In order to scale the inputs, we calculated the following parameters: the minimum, the maximum, the mean and the standard deviation (see Table 1). The ANN architecture is presented in Figure 2 for version 1. The architectures of the following versions (2, 3 and 4) were also with one hidden layer perceptrons and had the same input and output layers as version 1. On the other hand, their hidden layers contained three (version 2), one (version 3) and six (version 4) nodes respectively.

Table 1. Values used for scaling the inputs for all ANN versions.

Input	Minimum	Maximum	Mean	Deviation	Scaler
Topological	4.300000	7.900000	5.843330	0.828066	Mean St. Dev.
3D-MoRSE	2.000000	4.400000	3.054000	0.433594	Mean St. Dev.
ADMET	1.000000	6.900000	3.758670	1.764420	Mean St. Dev.

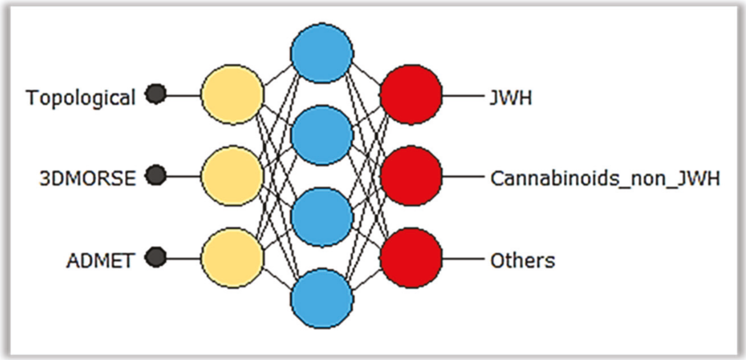

Figure 2. Network architecture, version 1: scaling layer (yellow), perceptron layer (blue), probabilistic layer (red).

We used the adaptive moment estimation (version 1), the Levenberg–Marquardt (version 2), the gradient descent (version 3) and the conjugate gradient optimization algorithms, as well as the growing neuron selection (all versions) method with the L1 (versions 2, 3 and 4) and L2 (version 1) regularization methods.

4. Discussion

The confusion matrices, calculated for each architecture and 30 testing samples, are presented in Tables 2–5 and the error results are highlighted in Table 6. The activation functions used were the hyperbolic tangent (version 1), the rectified linear (versions 2, 3 and 4) and Softmax (all versions).

Table 2. Confusion matrix for the analyzed ANN—version 1: 29 (96.7%) tested compounds were correctly classified and 1 (3.3%) was misclassified.

	Predicted JWH	Predicted Non-JWH Cannabinoids	Predicted Others
Real JWH Cannabinoids	10	0	0
Real non-JWH Cannabinoids	0	7	0
Real Others	0	1	12

Table 3. Confusion matrix for the analyzed ANN—version 2: 27 (90.0%) tested compounds were correctly classified and 3 (10.0%) were misclassified.

	Predicted JWH	Predicted Non-JWH Cannabinoids	Predicted Others
Real JWH Cannabinoids	8	0	0
Real non-JWH Cannabinoids	0	9	1
Real Others	0	2	10

Table 4. Confusion matrix for the analyzed ANN—version 3: 26 (86.7%) tested compounds were correctly classified and 4 (13.3%) were misclassified.

	Predicted JWH	Predicted Non-JWH Cannabinoids	Predicted Others
Real JWH Cannabinoids	8	0	0
Real Non-JWH Cannabinoids	0	9	1
Real Others	0	3	9

Table 5. Confusion matrix for the analyzed ANN—version 4: 27 (90.0%) tested compounds were correctly classified and 3 (10.0%) were misclassified.

	Predicted JWH	Predicted Non-JWH Cannabinoids	Predicted Others
Real JWH Cannabinoids	8	0	0
Real non-JWH Cannabinoids	0	10	0
Real Others	0	3	9

Table 6. Data errors for the analyzed ANNs.

Root Mean Squared Error				
Number of Nodes in the Hidden Layer	ANN	Training Set	Selection Set	Testing Set
1	Version 3	0.187558	0.276155	0.284885
3	Version 2	0.180618	0.276762	0.284408
4	Version 1	0.178430	0.241047	0.213058
6	Version 4	0.173380	0.268222	0.280003

In order to test and compare the performances of the analyzed ANNs, we used the weighted average derived from the confusion matrix, i.e., the accuracy, the recall and the F1 score (see Table 7) [14].

Table 7. Classification metrics for the target variables of each analyzed ANNs.

Weighted Average				
Number of Nodes in the Hidden Layer	ANN	Accuracy	Recall	F1 Score
1	Version 3	0.876667	0.866667	0.866667
3	Version 2	0.903030	0.900000	0.900207
4	Version 1	0.970833	0.966667	0.967111
6	Version 4	0.923077	0.900000	0.899379

5. Conclusions

In terms of the system performance, the results obtained for the four ANNs designed to recognize the class identity of JWH synthetic cannabinoids lead to the following conclusions:

1. Accuracy [(true positives + true negatives)/total instances]:

In comparison with the accuracy (93.3%) obtained for the initial ANN model presented in a previous article, the ANN—amended version 1—generated a higher score (96.7%), while the other three ANNs generated a lower score (86.7% for the amended version 3 and 90.0% for the amended versions 2 and 4).

2. Sensitivity, or true positive rate (true positives/positive instances):

All the ANN architectures (the initial ANN and its four amended versions), had an exceptional sensitivity in detecting JWH synthetic cannabinoids (class I); all the tested JWHs were recognized as such without exception, the rate of true positives (TP) being 100% in all cases.

3. Specificity, or true negative rate (specificity = true negative/negative instances):

Compared to the specificity (90.0%) of the initial ANN model, one of the four new architectures recorded a higher score (95.0% for the amended version 1); the other three were characterized by a lower specificity (81.8% for amended version 3, 86.3% for amended version 2 and 86.3% for amended version 4).

4. Error rate [accuracy = (false positives + false negatives)/total instances]:

While the initial ANN model was characterized by an error rate of 6.6%, its amended version 1 recorded a better (lower) error rate (3.3%), while the other three ANNs recorded a higher error rate (10.0% for amended version 2, 3 and 4).

Regarding the goodness-of-fit analysis, the best results were recorded for the ANN—amended version 1 (99.97%), followed by the amended version 2 (99.94%), amended version 3 (98.41%) and amended version 4 (99.04%). Hence, we may conclude that the best performing ANN architecture was the one that included the following elements:

- Activation function: hyperbolic tangent, Softmax;
- Loss index: normalized squared error;
- Regularization: L2;
- Neuron selection: growing neurons;
- Inputs selection: growing inputs;
- Optimization algorithm: Adaptive Moment Estimation.

The results indicate that very good classification rates were obtained although the data set was complex. We intend to continue this study by applying various metaheuristic algorithms on these data sets and compare the results.

Author Contributions: Conceptualization, C.M.B. and A.C.B.; methodology, M.P.; software, A.C.B.; validation, M.P.; formal analysis, C.M.B.; investigation, C.M.B.; resources, A.C.B.; writing—original draft preparation, A.C.B.; writing—review and editing, C.M.B.; supervision, M.P.; project administration, M.P. All authors have read and agreed to the published version of the manuscript.

Funding: This research received no external funding.

Data Availability Statement: Not applicable.

Acknowledgments: An appreciation of the "Wiley Online Library" and the data science platform and machine learning "Neural Designer", important and useful tools, used in the construction of system architectures presented in this paper.

Conflicts of Interest: The authors declare no conflict of interest.

References

1. Benitez, J.M.; Castro, J.L.; Requena, I. Are artificial neural networks black boxes? *IEEE Trans. Neural. Netw.* **1997**, *8*, 1156–1164. [CrossRef] [PubMed]
2. Doulamis, A.D.; Doulamis, N.D.; Kollias, S.D. On-line retrainable neural networks: Improving the performance of neural networks in image analysis problems. *IEEE Trans. Neural. Netw.* **2000**, *11*, 137–155. [CrossRef] [PubMed]
3. Yeung, D.S.; Cloete, I.; Shi, D.; Ng, W.W.Y. *Sensitivity Analysis for Neural Networks*; Springer: Berlin/Heidelberg Germany, 2010.
4. Montano, J.J.; Palmer, A. Numeric sensitivity analysis applied to feedforward neural networks. *Neural. Comput. Appl.* **2003**, *12*, 119–125. [CrossRef]

5. Burlacu, C.M.; Burlacu, A.C.; Praisler, M. Physico-chemical analysis, systematic benchmarking, and toxicological aspects of the JWH aminoalkylindole class-derived synthetic JWH cannabinoids. *Ann. Univ. Dunarea Jos Galati Fascicle II Math. Phys. Theor. Mech.* **2021**, *44*, 34–45. [CrossRef]
6. Todeschini, R.; Consonni, V. *Handbook of Molecular Descriptors*; Wiley: Weinheim, Germany, 2000; pp. 1–667.
7. Burlacu, C.M.; Gosav, S.; Burlacu, B.A.; Praisler, M. Convolutional Neural Network detecting synthetic cannabinoids. In Proceedings of the 2021 International Conference on e-Health and Bioengineering (EHB), Iasi, Romania, 18–19 November 2021; pp. 1–4.
8. Egger, J.; Pepe, A.; Gsaxner, C.; Jin, Y.; Li, J.; Kern, R. Deep learning-a first meta-survey of selected reviews across scientific disciplines, their commonalities, challenges and research impact. *PeerJ Comput. Sci.* **2021**, *7*, e773. [CrossRef] [PubMed]
9. Gupta, R.; Srivastava, D.; Sahu, M.; Tiwari, S.; Ambasta, R.K.; Kumar, P. Artificial intelligence to deep learning: Machine intelligence approach for drug discovery. *Mol. Divers.* **2021**, *25*, 1315–1360. [CrossRef] [PubMed]
10. Jing, Y.; Bian, Y.; Hu, Z.; Wang, L.; Xie, X.Q.S. Deep learning for drug design: An artificial intelligence paradigm for drug discovery in the big data era. *AAPS J.* **2018**, *20*, 1–10.
11. Smith, S.L.; Dherin, B.; Barrett, D.G.T.; De, S. On the origin of implicit regularization in stochastic gradient descent. *arXiv* **2021**, arXiv:2101.12176.
12. Wang, M.; Xu, X.; Yan, Z.; Wang, H. An online optimization method for extracting parameters of multi-parameter PV module model based on adaptive Levenberg-Marquardt algorithm. *Energy Convers. Manag.* **2021**, *245*, 114611. [CrossRef]
13. Singarimbun, R.N.; Nababan, E.B.; Sitompul, O.S. Adaptive moment estimation to minimize square error in backpropagation algorithm. In Proceedings of the 2019 International Conference of Computer Science and Information Technology (ICoSNIKOM), Medan, Indonesia, 28–29 November 2019; pp. 1–7.
14. Powers, D.M.W. Evaluation: From precision, recall and F-measure to ROC, informedness, markedness and correlation. *arXiv* **2011**, arXiv:2010.16061.

inventions

Article

Wind Variation near the Black Sea Coastal Areas Reflected by the ERA5 Dataset

Victoria Yildirir, Eugen Rusu and Florin Onea *

Department of Mechanical Engineering, Faculty of Engineering, Dunarea de Jos University of Galati, 800008 Galati, Romania; victoria.yildirir@gmail.com (V.Y.); eugen.rusu@ugal.ro (E.R.)
* Correspondence: florin.onea@ugal.ro

Abstract: In the context of the European Green Deal implementation, it is expected that there will be an increase in number of the wind farms located near the coastal areas in order to support this initiative. The Black Sea represents an important source of wind energy, and as a consequence, in the present work the regional wind resources (onshore and offshore) are evaluated by considering a total of 20 years of ERA5 wind data covering the 20-year time interval from January 2002 to December 2021. From a general perspective, it is clear that the offshore areas (100 km from the shoreline) are defined by much higher wind speed values than in the onshore, reaching an average of 8.75 m/s for the points located on the western sector. During the winter, these values can go up to 8.75 m/s, with the mention that the northern sectors from Ukraine and Russia may easily exceed 8 m/s. In terms of the wind turbines' selection, for the offshore areas defined by consistent wind resources, generators will be considered that are defined by a rated wind speed of 11 m/s. Finally, we can mention that a theoretical offshore wind turbine of 20 MW can reach a capacity factor located between 20.9 and 48.3%, while a maximum annual electricity production of 84.6 GWh may be obtained from the sites located near the Romanian and Ukrainian sectors, respectively.

Keywords: Black Sea; coastal environment; wind power; wind turbines; onshore; offshore

Citation: Yildirir, V.; Rusu, E.; Onea, F. Wind Variation near the Black Sea Coastal Areas Reflected by the ERA5 Dataset. *Inventions* **2022**, *7*, 57. https://doi.org/10.3390/inventions7030057

Academic Editors: Shoou-Jinn Chang and Mohammad Hassan Khooban

Received: 1 June 2022
Accepted: 4 July 2022
Published: 7 July 2022

Publisher's Note: MDPI stays neutral with regard to jurisdictional claims in published maps and institutional affiliations.

Copyright: © 2022 by the authors. Licensee MDPI, Basel, Switzerland. This article is an open access article distributed under the terms and conditions of the Creative Commons Attribution (CC BY) license (https://creativecommons.org/licenses/by/4.0/).

1. Introduction

It is well known that human development is directly related to the access to energy sources that subsequently involves the process of some specific types of resources. The foundation of the industrial revolution was built around the use of fossil fuels (oil, coal, and gas) that worked fine until the modern days, when the efficiency and the environmental impact is questioned [1]. The volatility of this sector represents another issue, with significant fluctuations in the prices and stocks during crisis periods that may occur from various causes, such as geopolitical or the pandemic [2,3].

By looking at the near future, it is expected there will be a significant increase in the renewable sources in the energy market, at least on a European level, this being in fact the strategy promoted by the European Union (EU) throughout various agreements, such as the Green Deal. Various priorities are proposed, among those being mentioned an increase in the Europe's offshore wind capacities to 60 GW by 2030 and up to 300 GW at the end of 2050 [4]. The European wind market is an active one, and these targets can be easily achieved. For example, at the end of 2021, an installed capacity of 207 GW was accounted by the onshore sector, while for the offshore one, a value of 16 GW was indicated. The offshore projects have definitely started to gain momentum, with the average power of a newly installed generator being located near 8.5 MW compared to only 4 MW for the onshore turbines. From the EU countries located near the Black Sea, the annual electricity demand covered from wind reached 11% for Romania compared to 4% indicated for Bulgaria. Without doubt, there is room for improvement, taking into account that on a European level the average is close to 14%, to which we can add that most of the countries with coastal regions are already involved in the development of the offshore wind sector [5].

Each wind project is defined by particular features, according to the area of installation (onshore and offshore). For example, Enevoldsen and Valentine [6] highlighted the fact that it is more expensive to build an offshore project, and in some case the wind quality from some regions was similar than the onshore ones. More than this, the authors suggest that an onshore project located close to a forest area may represent a better alternative, if the onshore areas are limited and if the offshore costs are very high. Nevertheless, a marine site may provide multiple advantages, ranging from the development of hybrid projects [7] or suitability for coastal protection [8], with this being viewed as the best option for the expansion of the wind sector.

The Black Sea coastal environment is defined by relevant wind resources that can be used to power a wind farm, this being the case of the western sectors where some major onshore wind farms are located. The best example is probably the Fantanele-Cogealac project, that is defined by an operating capacity of 600 MW and is located at approximately 17 km from the shoreline [9]. By looking at the existing studies focused on the wind conditions from the Black Sea, we can notice that these resources significantly increase as we go from onshore to offshore, with a sharp transition near the shoreline being expected. For example, in the work by Rusu et al. [10], from the spatial distribution of the wind conditions, it was highlighted that the wind resources from the marine areas are constantly exceeding the onshore ones (by at least 2× time). Another interesting aspect is represented by the fact that from this region the best wind resources are noticed in the central part of the Azov Sea, where a maximum of 8.24 m/s may occur during winter ($U10$ values—wind speed at 10 m height). In Kubryakov et al. [11], the regional wind resources ($U10$ values) were evaluated by considering this time satellite measurements. During the winter, average wind speed values of 8 m/s may occur in the north-western areas (e.g., Crimean Peninsula) while minimum average values of 3.5 m/s are associated with the southeastern sector. Although the wind conditions significantly increase from the shoreline to the offshore region, at some point it a stabilization of the conditions is expected. This seems to be the case of the Romanian coastal sector [12], where the average wind conditions ($U10$) may start from 4.37 m/s (shoreline), reach a maximum of 5.89 m/s (at 100 km from the shore), and reduce to 5.75 m/s at a distance of 220 km from the shore. These values are specific to the southern part of this region being based on the ERA5 reanalysis data.

Most of the wind studies focused on the entire Black Sea basin and cover only the marine areas, being designed around various topics such as the analysis of extreme events [13], climate change [14], or as inputs for regional wave models [15]. The results are delivered in terms of spatial maps that may provide relevant information from a meteorological point of view.

In this context, the aim of the present work is to provide a parallel evaluation of the wind resources from onshore and offshore areas of the Black Sea by taking into account some relevant local sites, such as harbors. Throughout specific indicators, the wind conditions at 100 m ($U100$) were processed in order to highlight some new insights of the regional wind energy potential, such as:

(a) What is the range of wind turbines to be installed in this region according to the expected rated wind speed;
(b) Provide a classification of the onshore and offshore sites by using a multicriteria approach that involves various indicators such as average wind speed, monthly variations, or distance from the coast;
(c) Identify the performances of two wind turbines (rated at 2.5 MW and 20 MW) that may involve monopile or floating foundations.

2. Materials and Methods

2.1. Target Area

In Figure 1, the Black Sea target area is illustrated, including the sites considered for analysis. In total, there are nine reference lines, defined along various coastal areas, such as Romania, Russia, Georgia, or Türkiye with the mention that from the sites located near the shoreline (denoted with no. 2), a distance of 100 km was considered to define the onshore sites (no. 1) while a similar distance was associated with the offshore sites (no. 3). More details regarding the sites considered are provided in Table 1.

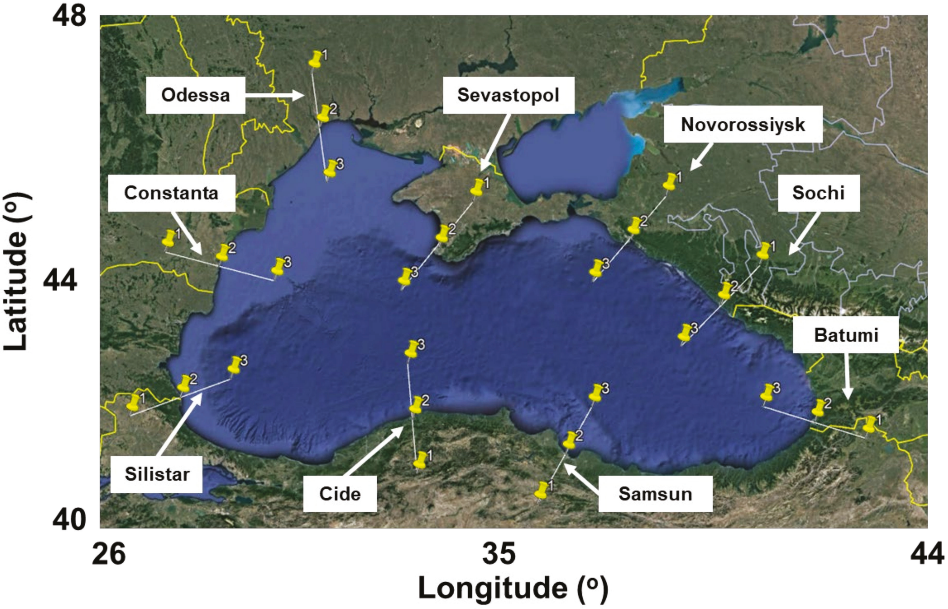

Figure 1. Black Sea target area including the reference points, where: 1—onshore; 2—alongshore; 3—offshore. Map processed from Google Earth, 2022.

Table 1. Characteristics of the reference points located along the shoreline.

Site	Lat (°)	Long (°)	Height/Depth (m)
Constanta (RO)	44.15°	28.66°	−9
Odessa (UA)	46.47°	30.76°	1
Sevastopol (UA)	44.60°	33.55°	47
Novorossiysk (RU)	44.70°	37.81°	63
Sochi (RU)	43.59°	39.75°	78
Batumi (GA)	41.60°	41.66°	47
Samsun (TR)	41.31°	36.29°	0
Cide (TR)	41.87°	33.04°	216
Silistar (BG)	42.01°	28.01°	17

Figure 2 presents in more detail the profile lines, including information related to the sea level (height = 0 m) and the distance to the nearshore sites (distance from the shoreline = 0 km). In general, the water depth significantly increases as we go offshore, and as a consequence it will be necessary to use floating wind platforms, since in most of the cases the areas located near the shoreline will be already allocated for some other maritime activities. The marine sites located near Constanta/Odessa may allow the implementation of a monopile project, since they are located in a plateau area where the water depth is close to 50 m (or below).

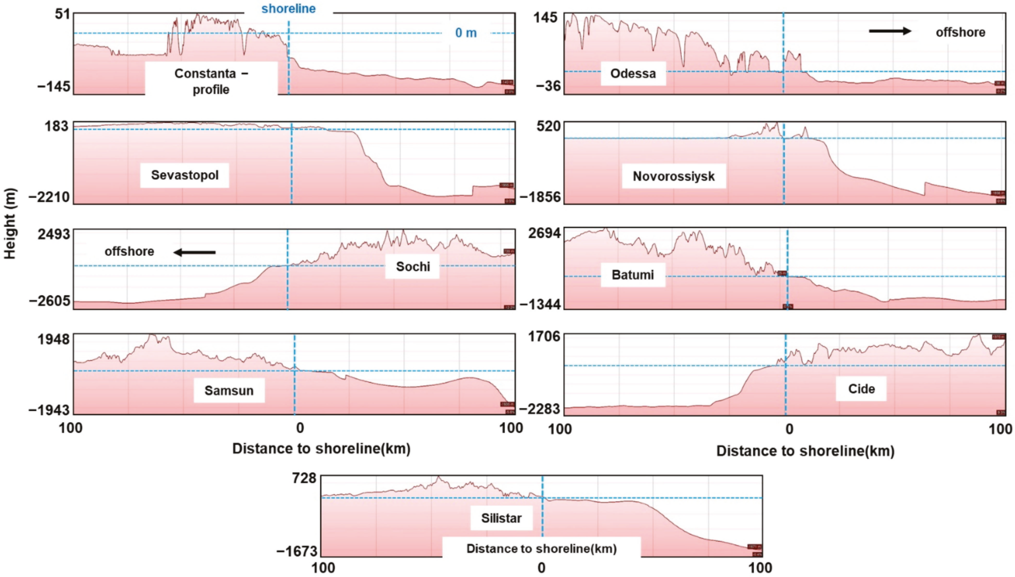

Figure 2. Profile lines represented for each coastal area taken into account. All the values are relative to the seafloor according to the information provided in Google Earth 2022.

2.2. Wind Data and Indicators

The evolution of the regional wind resources is carried out by using the ERA5 dataset [16] that includes wind fields reported directly at 100 m level (denoted with $U100$), this height being frequently considered for the development of onshore and offshore wind generators. A total of 20 years of data covering the interval from January 2002 to December 2021 are processed, the initial dataset being defined by a spatial resolution of 0.25° and by four values per day (00-06-12-18 UTC). This dataset is frequently used for the evaluation of the wind energy all over the world, being also considered for some coastal sectors from the Black Sea [12]. Various analyses are performed, including the seasonal distribution, that are sorted according to: Spring—March, April, May; Summer—June, July, August; Autumn—September, October, November; Winter—December, January, February.

One way to quantify the quality of the wind resources is to use the wind classes. These go from C1 (low energy level) to C7 (ideal conditions) as can be noticed from Table 2. In the present work, only the wind conditions between the classes C4 and C7 are considered, since these are more representative for the development of a wind project.

A more detailed classification of the wind conditions is provided in Costoya et al. [17,18] as can be noticed from Table 3. Several parameters are taken into account, namely: W_{ann} (m/s)—annual average wind speed, related to $U100$; *EWSO* (%)—frequency of occurrence of effective wind speed; *RLO* (%)—rich level occurrence; C_v—coefficient of variation; M_v—monthly variability; *EWS* (m/s)—extreme wind speeds; *WD* (m)—water depth; *DC* (°)—distance to coast. In the first part (denoted with a), a normalized value between 0 and 1 (with a value of 0,25 as interval) is allocated to each indicator. For example, the EWSO indicator is related to the distribution of the wind speed between the cut-in and cut-out values of a turbine (4 and 25 m/s in this case), and if a percentage higher than 80% is noticed, a normalized value of 1 is allocated to each indicator.

Table 2. *U*100—wind classification according to Oh, et al. [19].

Wind class	Indicator	Wind Speed (m/s)	WPD (W/m^2)
C1	Poor	<6.1	<260
C2	Marginal	6.1–7.1	260–420
C3	Fair	7.1–7.8	420–560
C4	Good	7.8–8.3	560–670
C5	Excellent	8.3–8.9	670–820
C6	Outstanding	8.9–9.7	820–1060
C7	Superb	>9.7	>1060

Table 3. Classification of the wind energy resources involving multiple parameters. Results processed from (a) to (c) according to Costoya, et al. [17].

(a) Normalized Criterion							
Normalized Values	**EWSO (%)**	**RLO (%)**	**C_v**	**M_v**	**EWS (m/s)**	**WD (m)**	**DC (°)**
0	<20	<20	>1.75	>1.75	>28	>500	>4
0.25	20–40	20–40	1.25–1.75	1.25–1.75	25–28	100–500	3–4
0.5	40–60	40–60	0.75–1.25	0.75–1.25	20–25	50–100	2–3
0.75	60–80	60–80	0.25–0.75	0.25–0.75	15–20	25–50	0.5–2
1	80–100	80–100	<0.25	<0.25	<15	0–25	<0.5
(b) Importance of each parameter							
	W_{ann} EWSO	RLO	C_v	M_v	EWS	WD	DC
Weight	0.22 0.22	0.1	0.1	0.05	0.14	0.07	0.1
(c) Resources classification							
Class	1	2	3	4	5	6	7
Category	$x \leq 0.4$	$0.4 \leq x \leq 0.5$	$0.5 \leq x \leq 0.6$	$0.6 \leq x \leq 0.7$	$0.7 \leq x \leq 0.8$	$0.8 \leq x \leq 0.9$	$x > 0.9$
Indicator	Poor	Marginal	Fair	Good	Excellent	Outstanding	Superb

This type of analysis was developed to assess only the wind potential of a particular marine site, while in the present work, in a similar way the onshore sites were taken into account, which may be considered as an element of novelty. In the next step (denoted with b), a weight value is applied to each indicator according to their importance, the most important being considered W_{ann} and *EWSO*, while on the opposite side we found water depth (0.07) and monthly variability (0.05), respectively.

The *RLO* indicator is related to the occurrence of the wind power density above 200 W/m^2 and, for example, if a 90% distribution is noticed above this threshold, a normalized value of one is accounted. Regarding the *CV* and *Mv* parameters, if the values reported by a site exceed 1.75, a normalized value of zero is taken into account. In the case of the water depth and distance to coast, if this does not exceed 25 m and 0.5°, a maximum score will be given, while on the opposite side, if the depth exceeds 500 m, a normalized value of zero is obtained. In an ideal scenario, a particular site can be classified as superb (class C7) if for all the criteria mentioned in Table 3 (section a) a normalized value of one is obtained.

Finally, for each site, a number located in the range of 0–1 is obtained that can be included in seven classes (from C1 and C7) according to their attractiveness for a wind project. More details regarding this approach and the definition of the parameters involved are provided in [17].

The wind speed carrying maximum energy parameter (denoted with V_{maxE}) can be used to match a particular wind turbine to a particular site, by considering the available wind resources [20]. In this case, a generator defined by a rated wind speed, which is close to the value of this indicator, is more than recommended. This index can be computed as [21]:

$$V_{maxE} = c\left(1 + \frac{2}{k}\right)^{1/k} \tag{1}$$

where c and k represent the scale and shape parameters of a Weibull distribution function. The Weibull distribution can be defined as [22]:

$$f(u) = \left(\frac{k}{c}\right)\left(\frac{u}{c}\right)^{k-1} exp\left[-\left(\frac{u}{c}\right)^{k}\right] \quad (2)$$

where: c, k—Weibull parameters; u—wind speed ($U100$ in this case).

Another objective of the present work was to assess the performances of some wind turbines that may operate onshore and offshore. In Table 4, two wind turbines are presented, the first one being frequently used in onshore projects such as the one from Fantanele-Cogealac, Romania [23]. The second generator is designed for the offshore areas, being expected to become operational in the near future when the rated capacity of these systems may easily exceed 20 MW [24,25].

Table 4. Characteristics of the wind turbines considered in the present work.

Turbine	Power (MW)	Cut-in Speed (m/s)	Rated Wind Speed (m/s)	Cut-out Speed (m/s)	Tower Range (m)	Reference
GE Energy 2.5 xl	2.5	3.5	13.5	25	75–100	[26]
20 MW model	20	3	10.7	25	160.2	[27]

The annual electricity production of a particular turbine can be defined as [28]:

$$AEP = T \times \int_{cut-in}^{cut-out} f(u)P(u)du \quad (3)$$

where: AEP—is expressed in GWh; T—number of operational hours in a year (8760 in this case); $f(u)$—Weibull function from Equation (2); $P(u)$—power curve of a particular wind turbine, defined by the cut-in/cut-out values. More details regarding the power curves of the two wind turbines used in this work can be found in Figure 3.

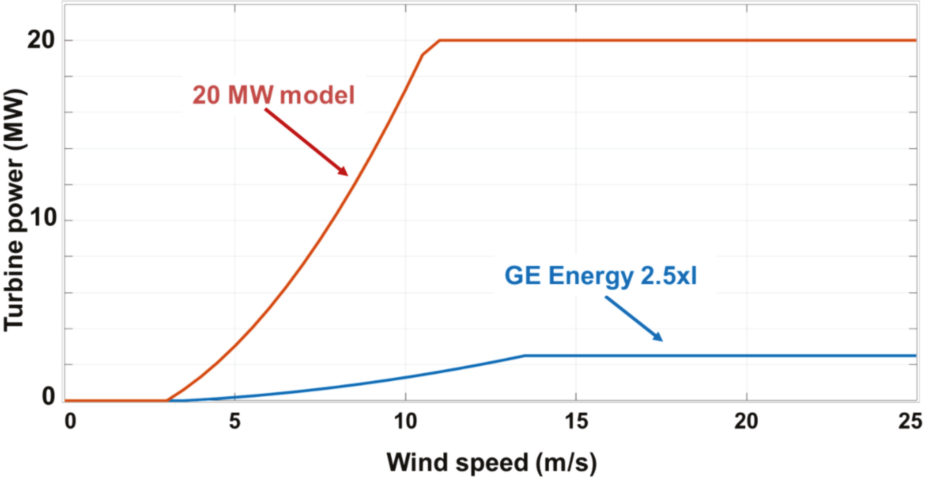

Figure 3. Wind turbines—power curve representation.

Finally, the performance of each generator will be measured by using the capacity factor (Cf), denoted as follows [28]:

$$Cf = \frac{P_{generated}}{P_{rated}} \quad (4)$$

where: $P_{generated}$—expected power to be generated by a wind turbine; P_{rated}—rated power of a generator.

3. Results

In Figure 4, the distribution of the *U*100 parameter (average values) considering the full time distribution is presented. The results are sorted according to different intervals that go from a minimum of 2.45 m/s to a maximum of 7.35 m/s. From this representation, we can clearly notice that the offshore sites are defined by much higher values that frequently exceed 7 m/s in the case of the western region. Considerably lower values are associated with the onshore sites from south and southeast, where for this time period the average wind speed values are below 3 m/s. The shoreline points from line Constanta, Odessa and Sevastopol are defined by similar wind conditions as the offshore points (100 km from the shore) associated with the lines Sevastopol, Novorossiysk, and Cide that present wind resources in the range 6–7 m/s.

The seasonal evolution of the wind speed is presented in Figure 5, where we can observe more impressive values during the wintertime, when the offshore sites from west and north can reach average wind speed values up to 8.75 m/s.

During the spring time, these average wind speed values oscillate in the range 2.44–7.36 m/s, with the mention that this time the offshore site from Silistar is not rated among the most important sites. As for the summertime, we can expect a maximum of 6.02 m/s only from the site associated with Odessa, while a minimum of 2.07 m/s is noticed on the land areas from east and south. During the wintertime, an offshore wind turbine will obtain the best performances near the sites from the north and west sectors, compared to the southeastern site (Georgia) that is on the same energy level as the onshore sites from Constanta and Silistar (100 km onshore).

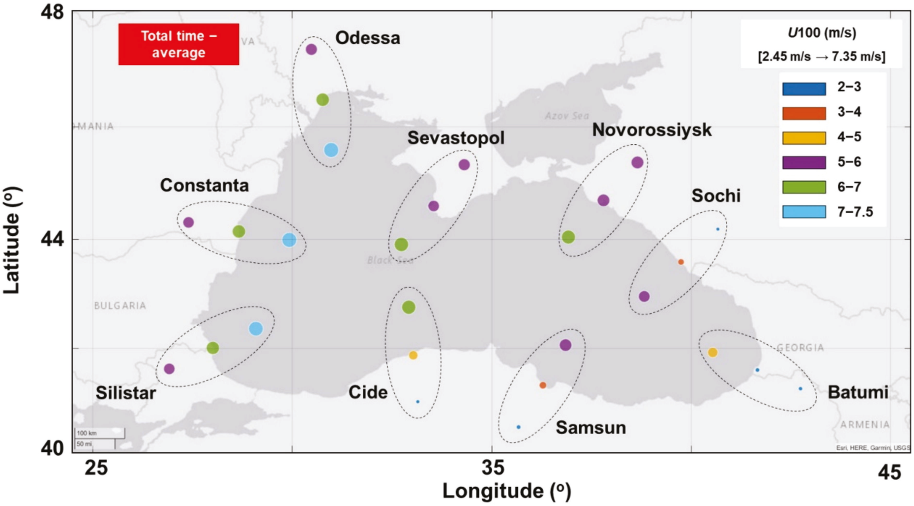

Figure 4. *U*100 average values of the ERA5 wind data corresponding to the 20-year time interval from January 2002 to December 2021. The numbers from the square brackets indicate the minimum and maximum values related to this map.

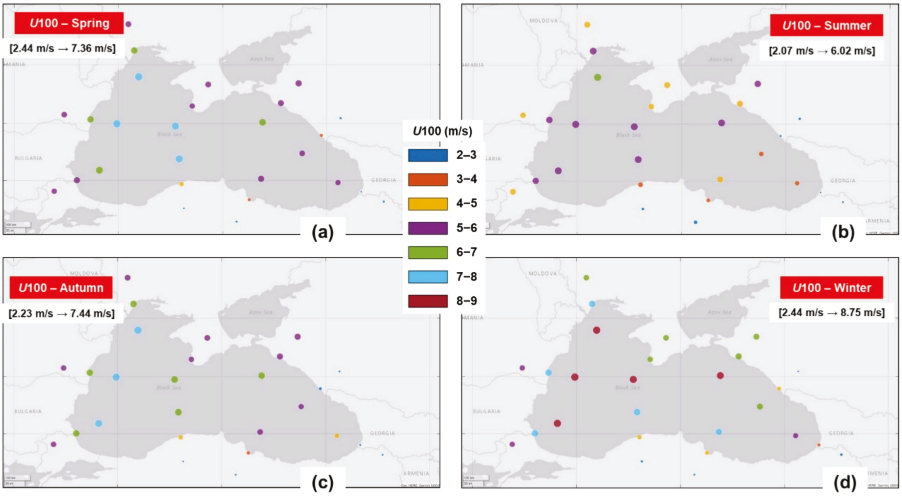

Figure 5. Seasonal distribution of the *U*100 parameter (average values) associated with the 20-year time interval January 2002–December 2021, where: (**a**) spring; (**b**) summer; (**c**) autumn; (**d**) winter. The numbers from the square brackets indicate the minimum and maximum values related to each map.

Figure 6 illustrates the wind distribution by classes (in %), considering only the values from intervals C4 and C7. For the class C4, only the alongshore sites from Constanta and Odessa indicate higher values (>5%), that even exceed the offshore sites where a maximum of 5% is expected. For the class C5, the site from the western sector (alongshore and offshore) presents values in the range 5–5.5%, in this category being included also a marine site from Cide (south sector). The differences between onshore and offshore sites tend to become more significant as we go to higher classes, for example in the case of the class C7 when it goes from 0.021 to 26.1%. For the C7 class, only the Odessa site presents more consistent wind resources, being closely followed by some other reference sites that indicate a distribution in the range 20–25%.

The evolution of the V_{maxE} indicator is provided in Figure 7, considering all the available wind data (*U*100—total time). According to these values, several patterns may occur. For example, the marine sites from the west constantly indicate values in the range 11–11.5 m/s in this section being also included a site from Novorossiysk. On the second place, we have the marine sites from Sevastopol and Cide (north and south) with maximum values of 11 m/s. Most of the onshore sites from west and north can be included in the interval 7.5–8.5 m/s, being expected also an increase to a maximum of 9.5 m/s in the case of the alongshore sites from Constanta and Odessa. The onshore sites from south and east present lower values that reach a minimum of 3.72 m/s, this being relatively close to the cut-in values of some high-capacity wind turbines.

A similar analysis is presented in Figure 8, considering this time the seasonal evolution. As expected, during the wintertime we encounter most of the important wind resources that go in the range 11.5–13 m/s, in this category being included most of the marine sites, except the one from Samsun (southeast), where a maximum of 11 m/s is expected. During spring, these values go from 3.96 to 11.4 m/s, being followed by autumn with values in the interval 3.47–11.3 m/s, while during summer a maximum of 9.44 m/s is expected near the offshore sites.

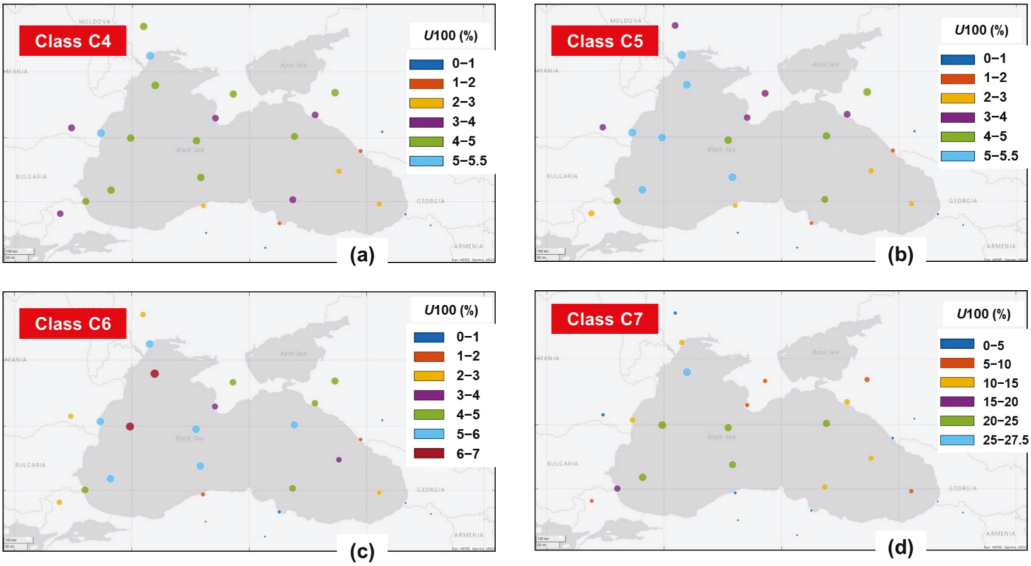

Figure 6. Distribution of *U*100 parameter by wind classes processed for the entire 20-year time period (2002–2021), where: (**a**) class C4; (**b**) class C5; (**c**) class C6; (**d**) class C7. This classification was made according to the information provided in Oh et al. [19].

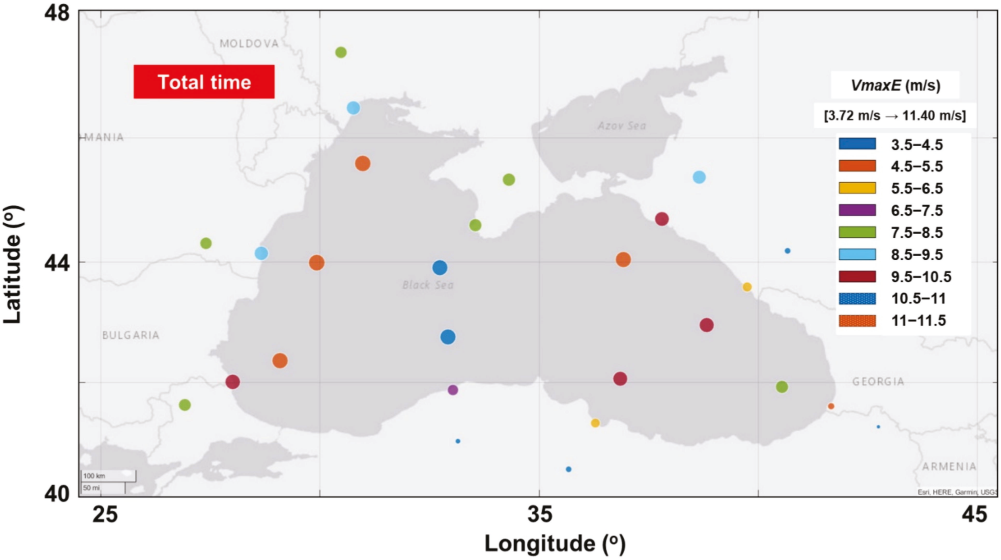

Figure 7. Overview of the V_{maxE} indicator (in m/s) associated with each reference point. Results computed for the entire 20-year time interval (2002–2021) and related to the *U*100 parameter. The numbers from the square brackets indicate the minimum and maximum values related to this map.

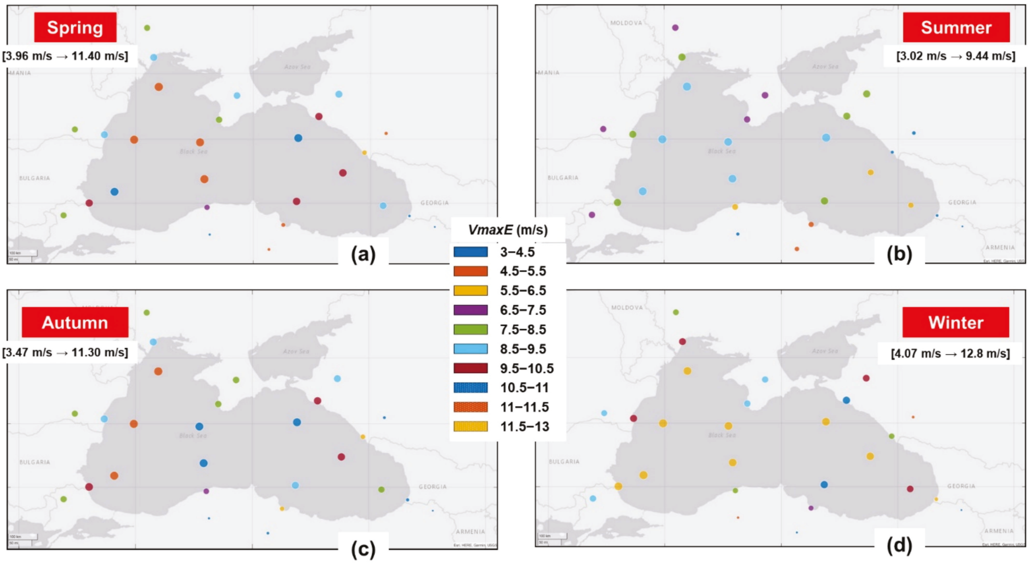

Figure 8. Seasonal distribution of the V_{maxE} indicator (in m/s) based on the $U100$ input, where: (**a**) spring; (**b**) summer; (**c**) autumn; (**d**) winter. The numbers from the square brackets indicate the minimum and maximum values related to each map.

Figure 9 presents a more detailed classification of the site, by taking into account various indicators that present interest for a wind project. From this area, none of the sites are included in the *C7* category (superb) and only the marine site from Odessa is associated with the C6 section (Outstanding). Three of the sites are related to the class C5 (Excellent), this being the case of Constanta and Silistar, to which we add the onshore site from Novorossiysk. For the remaining sites, most of them are included in the class 4 (good), except the western ones that are associated with class 1 (poor).

Figure 10 is focused on a similar evaluation, considering this time the values related to each season. Regardless of the season taken into account, none of the sites are rated as a C7 site, with expected values in the ranges: spring—0.33–0.78 m/s; summer—0.33–0.74 m/s; autumn—0.33–0.84; winter—0.37–0.87 m/s. During spring, a significant part of the sites is included in the classes C4 and C5 (good and excellent), while during summer the balance is shifted to class C4 and C3 (fair). For the autumn season, the marine sites from Constanta and Odessa are included in the class C6, while from the winter interval the onshore sites from Odessa and Novorossiysk may also present interest.

The annual electricity production (AEP) of an individual GE Energy 2.5 xl system is taken into account in Figure 11, by considering all the reference sites (onshore and offshore). By looking at these data, we can notice that the production range goes from 0.159 to 6.84 GWh, with better performances being expected in the western sector. From the marine sites located in the west (Odessa, Constanta, and Silistar), we may expect a production in the range 6–6.84 GWh, that gradually decreases to 4.5 GWh for the shoreline sites and further to 2.3 GWh for the onshore ones. In the case of the eastern sector, only the marine site from Novorossiysk can exceed a production of 5 GWh, while for the onshore sites in this area (east and south) the production does not exceed 1 GWh.

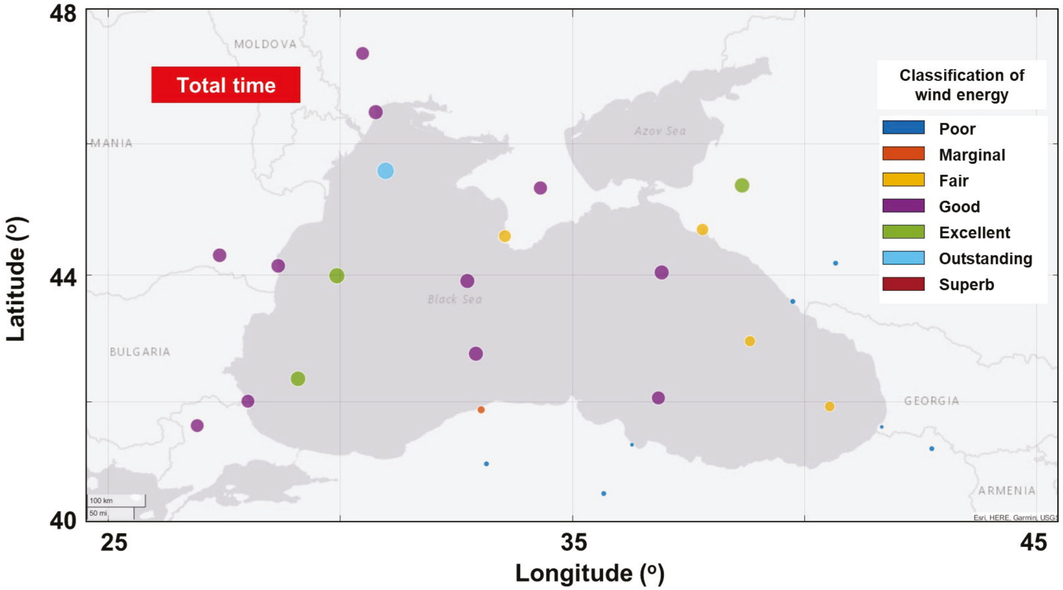

Figure 9. Wind energy classification involving eight parameters (*Wann*, *EWSO*, *RLO*, C_V, M_v, *EWS*, *WD*, *DC*) corresponding to the total time distribution (2002–2021). These results consider the *U*100 parameter and are based on the methodology proposed in Costoya et al. [17].

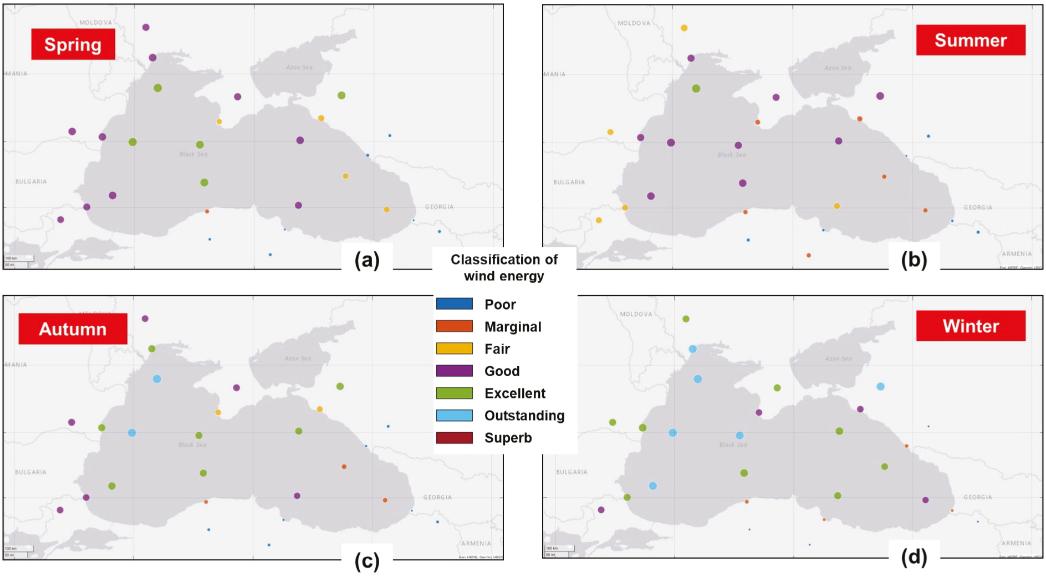

Figure 10. Seasonal values of the wind energy classification index associated with the 20-year time interval January 2002–December 2021, where: (**a**) spring; (**b**) summer; (**c**) autumn; (**d**) winter. These results are using the *U*100 parameter and are based on the methodology proposed in Costoya, et al. [17].

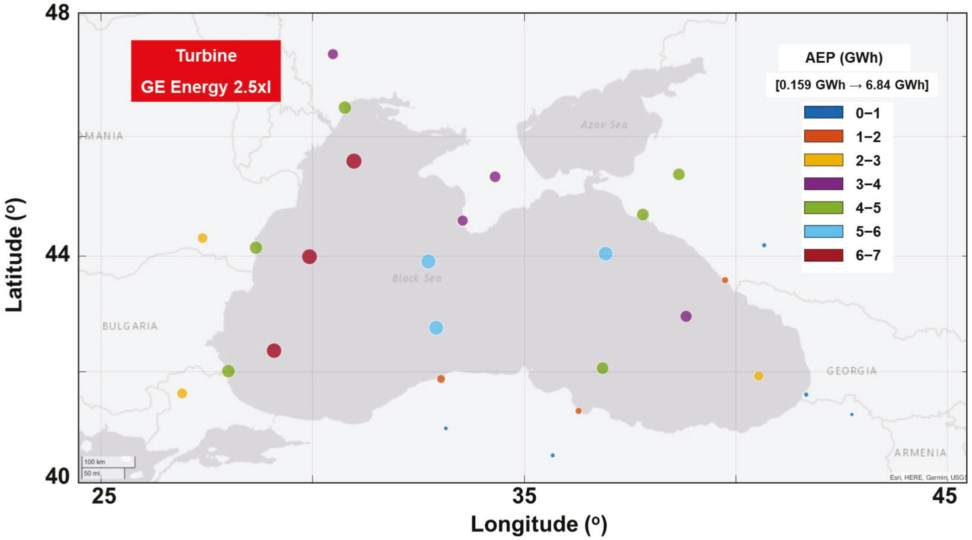

Figure 11. Annual Electricity Production (in GWh) related to the wind turbine GE Energy 2.5 xl.

Figure 12 presents the spatial distribution of the capacity factor reported for this wind turbine. Better performances are expected in the offshore areas, where a maximum value of 31.2% is expected near Constanta and Odessa, while a maximum of 30% may be reached by the marine sites from the central part of the Black Sea. Close to the shoreline, the capacity is relatively close to 25% (western sector) or 20% (northern sector), and does not exceed 5% in the case of the eastern and southern sites. For the onshore sites located on the western sector, a capacity factor in the range 10–15% is expected.

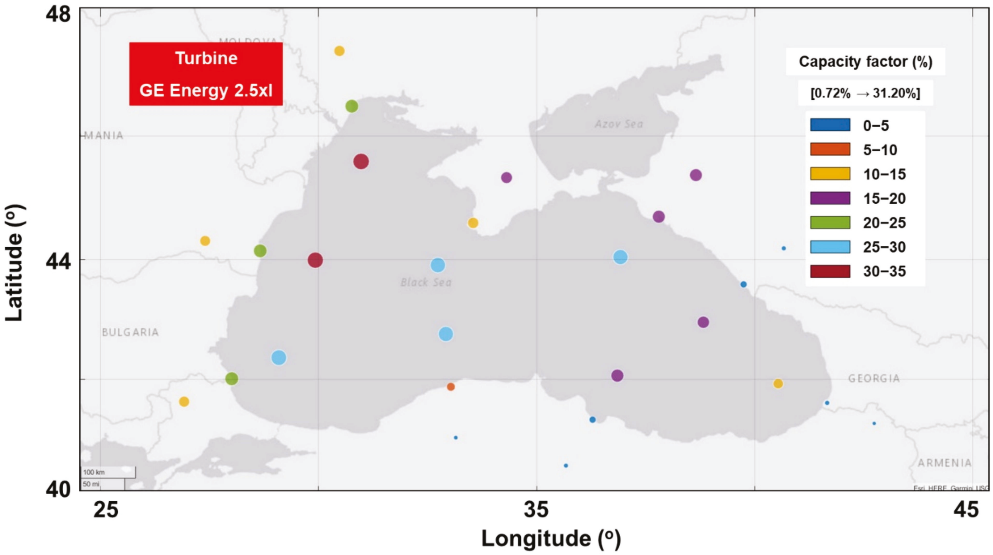

Figure 12. Capacity factor (in %) associated with the wind turbine GE Energy 2.5 xl. The numbers from the square brackets indicate the minimum and maximum values related to this map.

In Figure 13, the performances of the 20 MW wind turbine are presented, considering this time only the marine sites. For the AEP indicator (Figure 13a), the values go in the range 34.6–84.6 GWh, indicating the sites from Constanta and Odessa as the most promising. The performances of this turbine gradually decrease from west to east, in the conditions where the sites from the central parts can reach maximum values of 75 GWh, and drops to 60 GWh in the case of the Samsun site and finally reaches 36.6 GWh near Batumi.

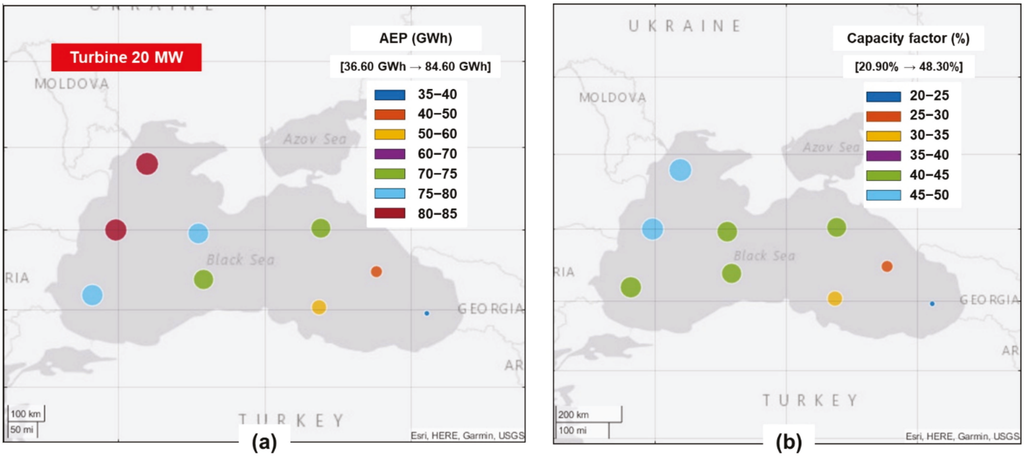

Figure 13. Performances of a theoretical wind turbine defined by a rated capacity of 20 MW, where: (**a**) annual electricity production; (**b**) capacity factor. These results are processed for a hub height of 160.2 m, according to the details mentioned in Ashuri, et al. [27]. The numbers from the square brackets indicate the minimum and maximum values related to each map.

As for the capacity factor (Figure 13b) this turbine is defined by higher values compared to the previous turbine (GE model), the main reasons being related to the lower values of the cut-in and rated wind speed characteristics. Values in the range 45–48.3% are expected for the Constanta and Odessa sites, while on the second place we find the interval 40–45% that defines the central part of the Black Sea. The sites from the southeast represent a particular category that does not exceed the percentage of 35% and can reach a minimum of 20.9% in the case of Batumi.

4. Discussions

The reanalysis dataset represents an important source of information, especially for an enclosed basin such as the Black Sea, where the in situ measurements are limited and in some cases outdated. As a consequence, several research papers focused on the wind energy from this region were published; this is the case for Rusu [14] or Raileanu [29] where an offshore wind farm was proposed to partially cover the energy demand of the Constanta harbor (Romania). In Yildirir et al. [30], the wind resources from the onshore and shoreline area were discussed by making a direct comparison between ERA5 and in situ measurements. According to these results, it was found that for the average values, ERA5 underestimates the onshore wind conditions located below 9 m/s, while as we go near the shoreline, a reverse pattern is noticed (close to Sulina site). A similar trend is observed for the maximum values, where the in situ measurements present peaks in the range 7–13 m/s for the onshore sites, while close to the shoreline this is shifted to the interval 17–25 m/s.

The results provided in this work are related to a hub height of 100 m, with this being frequently used in various projects, such as the one from Fantanele-Cogealac, Romania [31]. As for the 20 MW wind turbine, the performance of this system was evaluated at a hub height of 160.2 m, in the condition where only a single blade has a length of 135 m [27].

For the offshore regions, there are numerous studies focused on the evaluation of the $U100$ parameter, this being the case for Fabiola et al. [32] who was focused on the Porto Santo Island or Archer and Jacobson [33] who provided an analysis on a global scale. Some other studies are dedicated to climatological data, one of which being by Li et al. [34] where some offshore sites from the Yellow Sea were evaluated.

In this work, several reference points were considered for evaluation, among them being mentioned some located at 100 km from the coast. A distance such as this cannot be considered to be exaggerated taking into account that at this moment there are several projects working in similar regions (EnBW Albatros, Germany), with plans to implement projects at 200 km from the shoreline [35]. This may represent good news for the countries located in this region, taking into account that the coastal areas area already used for some other maritime activities are possible for development of wind projects in the nearshore and offshore areas. For example, the exclusive economic zone (EEZ) of Romania is estimated at 22,486 km^2, while for Bulgaria this goes up to 29,052 km^2 [36]. By looking at some other offshore projects, we can notice that the Lincs offshore wind farm has a total capacity of 250 MW and an overall area of 35 km^2, while the London Array project is defined by a capacity of 630 MW developed over 100 km^2 [37]. Comparing these values to the size of the Romania EEZ, the area covered will be less than 0.5%, being possible to find a suitable site that will not be affected by other maritime restrictions.

From the analysis of the ERA5 wind data ($U100$), we can clearly say that the offshore wind resources from the Black Sea are significantly higher than the ones from onshore areas, this being the first time when a study was focused on this issue. In general, the sites from the west and north present more important wind resources that can go to average wind speeds up to 8.75 m/s during the wintertime. The sites from the southern sector (Turkey) can be linked to the second place, easily exceeding the ones from the southeast (Georgia) that are associated with lower wind resources. Nevertheless, the chances that the Turkish authorities will consider developing a wind project in the Black Sea are quite low, taking into account that the wind resources from the Mediterranean Sea are more consistent [38,39].

The V_{maxE} indicator can be used to identify a range of wind turbines suitable for a particular site. In Wen et al. [40], several offshore wind turbines were considered, and based on the power curves of these systems, the first option for the Black Sea area will be the AMSC wt10000dd (7 MW) and Sea Titan (10 MW) generators. At these, we can add that they are defined by a rated wind speed of 12 m/s that have a capacity production in the range 2–7 MW. More than this, the new generation of marine wind turbines are defined by relatively lower rated speeds, which are located in the interval 10.6–11.4 m/s [24,27,41]. During the wintertime, this indicator can reach a value of 12.8 m/s in the case of the offshore sites, but it will not exceed 10.5 m/s if we discuss about onshore areas.

The aim of this work is not to make a direct comparison between the two wind generators (2.5 MW and 20 MW) since they are designed for different projects, this being the reason why in Figure 13 only the offshore sites were considered. On the other hand, the aim of this work is to make a direct comparison between the land and marine areas from the Black Sea region, and for this reason a 2.5 MW generator may represent a suitable solution, since we can find similar generators in the onshore projects (e.g., Cogealac, Romania) or in offshore ones (old technology). As for the marine areas, in the near future we can notice the occurrence of a new generation of wind turbines that may easily exceed 20 MW in terms of rated power, making them a suitable candidate for the Black Sea environment or for a repowering project. At this point, it can be also mentioned that in the work of Girleanu et al. [42], a total of 12 models of wind turbines, ranging from 2 to 10 MW, were evaluated for the Romanian coastal area, and a similar approach can be considered for some other regions of the Black Sea, especially in the case of the marine sites.

A particularity of the marine areas is represented by the possibility to implement high-capacity wind turbines that on a longer term have the capacity to reduce the CO_2 emissions. For example, in Onea et al. [43] such an evaluation was made for the Iberian coast, being estimated that a turbine rated at 9.5 MW could avoid the CO2 emissions with values located in the range 3–15 t/MWh according to the local wind energy. By simply scaling these results for the Black Sea, a maximum of 10.2 t/MWh can be expected from the GE Energy 2.5 xl, while a maximum of 22.8 t/MWh is associated with the 20 MW turbine considered in this work.

At this moment, the geopolitical situation in the Black Sea is not a stable one, with this aspect being reflected in the cost of electricity and due to the fact that some countries from this region (e.g., Romania) are depending on the electricity imports being forced in some cases to reactivate some coal power plants that were closed until now [30]. From all the countries located in the Black Sea area, the best chances to develop an offshore wind project are related to Bulgaria and Romania that may benefit from the initiatives proposed under the European Green Deal [44]. Russia is an important exporter of oil; therefore, there is no interest at this moment to invest in renewable energy, while on a long-term, Ukraine may efficiently use the existing offshore wind resources if a reconstruction plan will be implemented.

5. Conclusions

The present work provides a general picture of the wind energy resources in the coastal environment of the Black Sea (onshore and offshore) ERA5 wind data that cover the 20-year time interval from January 2002 to December 2021.

Besides a general analysis of the wind resources at a hub height level (100 m), some specific analyses related to the wind energy were also performed. These include the distribution by wind classes, a multicriteria classification of the sites, evolution of the V_{maxE} indicator, and performance of a 20 MW wind turbine. Based on these results, we can conclude that the regional offshore wind resources are significantly stronger than onshore regardless of the coastal sector considered. Furthermore, it was also noticed that the wind conditions gradually increase from the land to the marine areas, with the mention that the sites located alongshore may present suitable conditions for the development of a wind project.

Looking now at the initial research questions formulated in the Introduction, the following answers can be provided:

(a) According to the evolution of the V_{maxE} indicator, the rated wind speed of a wind turbine should be located in the range of 3.5–11.5 m/s on a general scale, with higher values being related to an offshore wind generator. During wintertime, a generator operating near a rated speed of 12.8 m/s may be considered efficient for most of the marine areas (100 km from the shore);

(b) By applying a multicriteria decision, it was found that the marine site located close to the Odessa area (Ukraine) presents wind conditions rated as outstanding (class C6), while during autumn and winter, some other sites are included in this category, for example, Constanta, Romania;

(c) As expected, a wind turbine rated at 20 MW (marine version) will have a higher electricity production, compared to a 2.5 MW generator (onshore version), indicating also better performances in terms of the capacity factor.

It has to be also highlighted that the present work has some limitations, of which we can mention the use of the ERA5 wind dataset that is not real, observed data. On the other hand, the ERA5 dataset is considered to be some of the best reanalysis data available at this moment, being frequently used by scientists from various research fields. We need also to mention that there is currently no wind project where a 20 MW generator operates, but on a longer term, this is the philosophy promoted by the European Union that can be achieved throughout projects such as Mobil-Grid-CoP [45].

Finally, we can conclude that the Black Sea area represents an important wind energy source for the implementation of the European Green Deal strategy. From this perspective, a significant contribution is expected from the EU countries (Romania and Bulgaria) that are defined by windy areas and shallow water regions, being possible to develop fixed and floating wind projects.

Author Contributions: V.Y. designed and wrote the manuscript. E.R. drafted and supervised the manuscript. F.O. analyzed the data and performed the interpretation of the results. The final manuscript has been approved by all authors. All authors have read and agreed to the published version of the manuscript.

Funding: This work was carried out in the framework of the research project DREAM (Dynamics of the REsources and technological Advance in harvesting Marine renewable energy), supported by the Romanian Executive Agency for Higher Education, Research, Development and Innovation Funding—UEFISCDI, grant number PN-III-P4-ID-PCE-2020-0008.

Acknowledgments: The results of this work will also be presented to the 10th edition of the Scientific Conference organized by the Doctoral Schools of "Dunărea de Jos" University of Galati (SCDS-UDJG) http://www.cssd-udjg.ugal.ro/ (accessed on 4 June 2022) that will be held on the 9–10 June 2022, in Galati, Romania. The data processed in this work are openly available. The ERA5 wind dataset is freely available through the EU-funded Copernicus Climate Change Service.

Conflicts of Interest: The authors declare no conflict of interest.

References

1. Zou, C.; Ma, F.; Pan, S.; Lin, M.; Zhang, G.; Xiong, B.; Wang, Y.; Liang, Y.; Yang, Z. Earth Energy Evolution, Human Development and Carbon Neutral Strategy. *Pet. Explor. Dev.* **2022**, *49*, 468–488. [CrossRef]
2. Jia, Z.; Wen, S.; Lin, B. The Effects and Reacts of COVID-19 Pandemic and International Oil Price on Energy, Economy, and Environment in China. *Appl. Energy* **2021**, *302*, 117612. [CrossRef] [PubMed]
3. Bento, P.M.R.; Mariano, S.J.P.S.; Calado, M.R.A.; Pombo, J.A.N. Impacts of the COVID-19 Pandemic on Electric Energy Load and Pricing in the Iberian Electricity Market. *Energy Rep.* **2021**, *7*, 4833–4849. [CrossRef]
4. Boosting Offshore Renewable Energy. Available online: https://ec.europa.eu/commission/presscorner/detail/en/IP_20_2096 (accessed on 23 June 2022).
5. Wind Energy in Europe: 2021 Statistics and the Outlook for 2022–2026 | WindEurope. Available online: https://windeurope.org/intelligence-platform/product/wind-energy-in-europe-2021-statistics-and-the-outlook-for-2022-2026/ (accessed on 23 June 2022).
6. Enevoldsen, P.; Valentine, S.V. Do Onshore and Offshore Wind Farm Development Patterns Differ? *Energy Sustain. Dev.* **2016**, *35*, 41–51. [CrossRef]
7. Saenz-Aguirre, A.; Saenz, J.; Ulazia, A.; Ibarra-Berastegui, G. Optimal Strategies of Deployment of Far Offshore Co-Located Wind-Wave Energy Farms. *Energy Convers. Manag.* **2022**, *251*, 114914. [CrossRef]
8. Raileanu, A.; Onea, F.; Rusu, E. An Overview of the Expected Shoreline Impact of the Marine Energy Farms Operating in Different Coastal Environments. *J. Mar. Sci. Eng.* **2020**, *8*, 228. [CrossRef]
9. Dawn, S.; Tiwari, P.K.; Goswami, A.K.; Singh, A.K.; Panda, R. Wind Power: Existing Status, Achievements and Government's Initiative towards Renewable Power Dominating India. *Energy Strategy Rev.* **2019**, *23*, 178–199. [CrossRef]
10. Rusu, L.; Ganea, D.; Mereuta, E. A Joint Evaluation of Wave and Wind Energy Resources in the Black Sea Based on 20-Year Hindcast Information. *Energy Explor. Exploit.* **2018**, *36*, 335–351. [CrossRef]
11. Kubryakov, A.; Stanichny, S.; Shokurov, M.; Garmashov, A. Wind Velocity and Wind Curl Variability over the Black Sea from QuikScat and ASCAT Satellite Measurements. *Remote Sens. Environ.* **2019**, *224*, 236–258. [CrossRef]
12. Onea, F.; Rusu, E.; Rusu, L. Assessment of the Offshore Wind Energy Potential in the Romanian Exclusive Economic Zone. *J. Mar. Sci. Eng.* **2021**, *9*, 531. [CrossRef]
13. Islek, F.; Yuksel, Y.; Sahin, C. Spatiotemporal Long-Term Trends of Extreme Wind Characteristics over the Black Sea. *Dyn. Atmos. Oceans* **2020**, *90*, 101132. [CrossRef]
14. Rusu, E. A 30-Year Projection of the Future Wind Energy Resources in the Coastal Environment of the Black Sea. *Renew. Energy* **2019**, *139*, 228–234. [CrossRef]
15. Amarouche, K.; Akpınar, A.; Soran, M.B.; Myslenkov, S.; Majidi, A.G.; Kankal, M.; Arkhipkin, V. Spatial Calibration of an Unstructured SWAN Model Forced with CFSR and ERA5 Winds for the Black and Azov Seas. *Appl. Ocean Res.* **2021**, *117*, 102962. [CrossRef]
16. Guillory, A. ERA5. Available online: https://www.ecmwf.int/en/forecasts/datasets/reanalysis-datasets/era5 (accessed on 31 May 2019).
17. Costoya, X.; de Castro, M.; Carvalho, D.; Gómez-Gesteira, M. On the Suitability of Offshore Wind Energy Resource in the United States of America for the 21st Century. *Appl. Energy* **2020**, *262*, 114537. [CrossRef]
18. Costoya, X.; de Castro, M.; Santos, F.; Sousa, M.C.; Gómez-Gesteira, M. Projections of Wind Energy Resources in the Caribbean for the 21st Century. *Energy* **2019**, *178*, 356–367. [CrossRef]

19. Oh, K.-Y.; Kim, J.-Y.; Lee, J.-K.; Ryu, M.-S.; Lee, J.-S. An Assessment of Wind Energy Potential at the Demonstration Offshore Wind Farm in Korea. *Energy* **2012**, *46*, 555–563. [CrossRef]
20. Belu, R. *Fundamentals and Source Characteristics of Renewable Energy Systems*, 1st ed.; Series: Nano and energy Series; CRC Press: Boca Raton, FL, USA, 2019; ISBN 978-0-429-29728-1.a.
21. Shu, Z.R.; Jesson, M. Estimation of Weibull Parameters for Wind Energy Analysis across the UK. *J. Renew. Sustain. Energy* **2021**, *13*, 023303. [CrossRef]
22. Al-Nassar, W.K.; Neelamani, S.; Al-Salem, K.A.; Al-Dashti, H.A. Feasibility of Offshore Wind Energy as an Alternative Source for the State of Kuwait. *Energy* **2019**, *169*, 783–796. [CrossRef]
23. Joian, R.; Lung, C.; Horgos, M. The Experimental Determinations at the Wind Farm Fantanel—Cogealac in Dobrogea. In Proceedings of the 2021 IEEE 27th International Symposium for Design and Technology in Electronic Packaging (SIITME), Timisoara, Romania, 27 October 2021; pp. 369–373.
24. Qin, C.; Loth, E.; Zalkind, D.S.; Pao, L.Y.; Yao, S.; Griffith, D.T.; Selig, M.S.; Damiani, R. Downwind Coning Concept Rotor for a 25 MW Offshore Wind Turbine. *Renew. Energy* **2020**, *156*, 314–327. [CrossRef]
25. De Souza, C.E.S.; Bachynski-Polić, E.E. Design, Structural Modeling, Control, and Performance of 20 MW Spar Floating Wind Turbines. *Mar. Struct.* **2022**, *84*, 103182. [CrossRef]
26. GE Energy 2.5xl-Manufacturers and Turbines-Online Access-The Wind Power. Available online: https://www.thewindpower.net/turbine_en_59_ge-energy_2.5xl.php (accessed on 10 March 2019).
27. Ashuri, T.; Martins, J.R.R.A.; Zaaijer, M.B.; Van Kuik, G.A.M.; Van Bussel, G.J.W. Aeroservoelastic Design Definition of a 20 MW Common Research Wind Turbine Model: A 20 MW Common Research Wind Turbine Model. *Wind. Energy* **2016**, *19*, 2071–2087. [CrossRef]
28. Rusu, E.; Onea, F. A Parallel Evaluation of the Wind and Wave Energy Resources along the Latin American and European Coastal Environments. *Renew. Energy* **2019**, *143*, 1594–1607. [CrossRef]
29. Raileanu, A.B.; Onea, F.; Rusu, E. Implementation of Offshore Wind Turbines to Reduce Air Pollution in Coastal Areas—Case Study Constanta Harbour in the Black Sea. *J. Mar. Sci. Eng.* **2020**, *8*, 550. [CrossRef]
30. Yildirir, V.; Rusu, E.; Onea, F. Wind Energy Assessments in the Northern Romanian Coastal Environment Based on 20 Years of Data Coming from Different Sources. *Sustainability* **2022**, *14*, 4249. [CrossRef]
31. Fantanele-Cogealac Wind Farm-Power Technology. Available online: https://www.power-technology.com/projects/fantanele-cogealac-wind-farm/ (accessed on 22 June 2022).
32. Pereira, F.S.; Silva, C.S. Offshore Wind Energy Resource Assessment from Satellite Data Observations and WRF in Porto Santo Island. *Wind. Energy Sci. Discuss.* **2020**, preprint. [CrossRef]
33. Archer, C.L.; Jacobson, M.Z. Evaluation of Global Wind Power. *J. Geophys. Res. Atmos.* **2005**, *110*, 1–10. [CrossRef]
34. Li, D.; Geyer, B.; Bisling, P. A Model-Based Climatology Analysis of Wind Power Resources at 100-m Height over the Bohai Sea and the Yellow Sea. *Appl. Energy* **2016**, *179*, 575–589. [CrossRef]
35. Offshore Wind in Europe-Key Trends and Statistics 2020 | WindEurope. Available online: https://windeurope.org/intelligence-platform/product/offshore-wind-in-europe-key-trends-and-statistics-2020/ (accessed on 23 June 2022).
36. Countries. Available online: https://maritime-spatial-planning.ec.europa.eu/msp-practice/countries (accessed on 23 June 2022).
37. Top 10 Biggest Offshore Wind Farms-Power Technology. Available online: https://www.power-technology.com/analysis/feature-top-10-biggest-offshore-wind-farms-uk/ (accessed on 23 June 2022).
38. Argin, M.; Yerci, V.; Erdogan, N.; Kucuksari, S.; Cali, U. Exploring the Offshore Wind Energy Potential of Turkey Based on Multi-Criteria Site Selection. *Energy Strategy Rev.* **2019**, *23*, 33–46. [CrossRef]
39. Pantusa, D.; Tomasicchio, G.R. Large-Scale Offshore Wind Production in the Mediterranean Sea. *Cogent Eng.* **2019**, *6*, 1661112. [CrossRef]
40. Wen, Y.; Kamranzad, B.; Lin, P. Assessment of Long-Term Offshore Wind Energy Potential in the South and Southeast Coasts of China Based on a 55-Year Dataset. *Energy* **2021**, *224*, 120225. [CrossRef]
41. Sartori, L.; Bellini, F.; Croce, A.; Bottasso, C. Preliminary Design and Optimization of a 20MW Reference Wind Turbine. *J. Phys. Conf. Ser.* **2018**, *1037*, 042003. [CrossRef]
42. Girleanu, A.; Onea, F.; Rusu, E. Assessment of the Wind Energy Potential along the Romanian Coastal Zone. *Inventions* **2021**, *6*, 41. [CrossRef]
43. Onea, F.; Ruiz, A.; Rusu, E. An Evaluation of the Wind Energy Resources along the Spanish Continental Nearshore. *Energies* **2020**, *13*, 3986. [CrossRef]
44. A European Green Deal | European Commission. Available online: https://ec.europa.eu/info/strategy/priorities-2019-2024/european-green-deal_en (accessed on 22 June 2022).
45. Mobil-Grid-CoP. Available online: https://www.iwes.fraunhofer.de/en/research-projects/current-projects/mobil-grid-cop.html (accessed on 22 June 2022).

inventions

MDPI

Article

Mobile Visual Servoing Based Control of a Complex Autonomous System Assisting a Manufacturing Technology on a Mechatronics Line

Georgian Simion [1,2,*], Adrian Filipescu [1,2], Dan Ionescu [1,2], Răzvan Șolea [1], Daniela Cernega [1], Eugenia Mincă [2,3] and Adriana Filipescu [1]

[1] Department of Automation and Electrical Engineering, "Dunărea de Jos" University of Galați, 800008 Galați, Romania; adrian.filipescu@ugal.ro (A.F.); dan.ionescu@ugal.ro (D.I.); razvan.solea@ugal.ro (R.Ș.); daniela.cernega@ugal.ro (D.C.); adriana.filipescu@ugal.ro (A.F.)

[2] Doctoral School of Fundamental Sciences and Engineering, "Dunărea de Jos" University of Galați, 800008 Galați, Romania; eugenia.minca@valahia.ro

[3] Department of Automation, Computer Science and Electrical Engineering, "Valahia" University of Târgoviște, 130024 Târgoviște, Romania

* Correspondence: georgian.simion@ugal.ro; Tel.: +40-770-909-285

Citation: Simion, G.; Filipescu, A.; Ionescu, D.; Șolea, R.; Cernega, D.; Mincă, E.; Filipescu, A. Mobile Visual Servoing Based Control of a Complex Autonomous System Assisting a Manufacturing Technology on a Mechatronics Line. *Inventions* **2022**, *7*, 47. https://doi.org/10.3390/inventions7030047

Academic Editor: Anastasios Doulamis

Received: 15 May 2022
Accepted: 19 June 2022
Published: 22 June 2022

Publisher's Note: MDPI stays neutral with regard to jurisdictional claims in published maps and institutional affiliations.

Copyright: © 2022 by the authors. Licensee MDPI, Basel, Switzerland. This article is an open access article distributed under the terms and conditions of the Creative Commons Attribution (CC BY) license (https://creativecommons.org/licenses/by/4.0/).

Abstract: The main contribution of this paper is the modeling and control for a complex autonomous system (CAS). It is equipped with a visual sensor to operate precision positioning in a technology executed on a laboratory mechatronics line. The technology allows the retrieval of workpieces which do not completely pass the quality test. Another objective of this paper is the implementation of an assisting technology for a laboratory processing/reprocessing mechatronics line (P/RML) containing four workstations, assisted by the following components: a complex autonomous system that consists of an autonomous robotic system (ARS), a wheeled mobile robot (WMR) PeopleBot, a robotic manipulator (RM) Cyton 1500 with seven degrees of freedom (7 DOF), and a mobile visual servoing system (MVS) with a Logitech camera as visual sensor used in the process of picking, transporting and placing the workpieces. The purpose of the MVS is to increase the precision of the RM by utilizing the look and move principle, since the initial and final positions of the CAS can slightly deviate from their trajectory, thus increasing the possibility of errors to appear during the process of catching and releasing the pieces. If the processed piece did not pass the quality test and has been rendered as defective, it is retrieved from the last station of the P/RML and transported to the first station for reprocessing. The control of the WMR is done using the trajectory-tracking sliding-mode control (TTSMC). The RM control is based on inverse kinematics model, and the MVS control is implemented with the image moments method.

Keywords: complex autonomous system; autonomous robotic system; wheeled mobile robot; robotic manipulator; visual servoing system; mechatronics line

1. Introduction

The main contribution of this paper is the modeling and control of a complex autonomous system (CAS) equipped with a robotic manipulator (RM) and a mobile visual sensor (MVS) to achieve precise positioning in a processing technology on a laboratory mechatronics line (ML). The presented technology allows the recovery of products, through reprocessing, if they partially satisfy the quality requirements. The mechatronics line handles the full manufacturing process of a workpiece, and it has buffering, handling, processing (drilling, boring), sorting, and quality testing facilities. Due to the fact that this technology allows the product retrieval operation for reprocessing, the mechatronics line will be further referred to as P/RML.

This paper presents the integration of multiple subsystems for a laboratory mechatronic line: the P/RML is served by a CAS consisting of an ARS equipped with a 7 DOF RM Cyton 1500 and uses an eye in hand type Mobile Visual Servoing (MVS) located on the end-effector. Task planning, simulation, monitoring, and real-time control are some of the tools used to fulfill the objectives of this study, like workpiece recovery for reprocessing or the increase of the automation level o for the P/RML so that a human operator is no longer needed after the program is started. Moreover, the CAS improves the reusability feature of the production line [1–5].

The manufacturing line is characterized by the operations to be performed in the workstations using the monitoring and control systems, CAS, ARS, RM, MVS which give reparability and flexibility features for processing and reprocessing operations [4–8]. The structure of the P/RML highlights the system's overall functions: the automatic processing of parts, transport, handling, storing and the automatic control of all the devices integrated in the system using the PLCs in different configurations: centralized or distributed. The processing/reprocessing tasks are the P/RML actions (drilling, reaming, extrusion, bending), operations which are executed in serial or parallel for manufacturing the workpiece until the final product meets the quality requirements. For this, the processing/reprocessing planning also requires complex operations to be performed such as performance measurement and evaluation, kinematics control, system planning, and resources management. For a P/RML assisted by CAS, a preparing strategy adapted to the characteristics of the system is more effective than the techniques used from domain-independent methods [6–11]. If the final workpiece does not pass the quality test, the task planner will provide the optimal sequence to reprocess the product.

Visual servoing systems are robust systems that enhance the accuracy and adaptability of the control architecture based on optical feedback [12]. The purpose of a servoing system is to close the movement control loop for a robotic arm. The robotic arm has to move from an initial point to a destination point. The aim of a MVS is to provide information, based on a visual sensor, regarding the actual position. Based on this information, the robot control is able to improve the interaction with the working environment. The features extracted from the images represent the actual position and also the input for the control architecture. The control architectures corresponding to the servoing systems are divided into three categories:

- Position Based Visual Servoing (PBVS) [13–15];
- Image Based Visual Servoing (IBVS) [13,16,17];
- Hybrid Visual Servoing (HVS) [4,11,16].

An important factor for a MVS is the visual features selection, which is related to the speed, accuracy, and performance that control the movement of a RM, taking into consideration the degrees of freedom as shown in [10,18,19].

Other elements of originality and contributions are concentrated in the following areas: assigning, planning, and synchronization tasks of P/RML assisted by CAS, RMs, and MVS, designing the architecture of the entire system to allow flexible manufacturing, multifunctionality, communication, synchronization of signals from sensors, distributed control and image processing for precise positioning eye in hand MVS and real-time control, improving the level of automation and increasing the efficiency of the manufacturing lines using the CAS.

The article is structured as follows:

Section 2 is dedicated to the hardware structure and the functional features of the system:

- In Section 2.1, the hardware structure of the P/RML assisted by CAS is presented;
- In Section 2.3, an eye in hand MVS technology is presented;
- In Section 2.3, modeling, and control of MVS, based on the moments of the image, are presented;
- In Section 2.4, assumptions and task planning are presented.
- In Section 3, direct and inverse kinematics model of RM Cyton 1500 are presented;
- In Section 4, trajectory-tracking sliding-mode control of ARS PeopleBot is presented;
- In Section 5, some results regarding real-time control of P/RML assisted by CAS are laid out;
- In Section 6, some final remarks and conclusions are presented.

2. P/RML Assisted by the CAS Equipped with RM and MVS

2.1. The Hardware Architecture of the P/RML Assisted by CAS

The P/RML Festo MPS 200, presented in Figure 1, is a configurable laboratory mechatronic system consisting of four workstations. The four workstations are controlled by an individual Siemens S7 300 PLC that operates in different stages: buffering, handling, processing, and sorting:

- The first station triggers the color tests and then transports the pieces to the warehouse corresponding to the color;
- The second station is where the pieces are buffered for further processing;
- The third station performs drilling and boring operations;
- The fourth station is where the pieces are stored and organized by their colors.

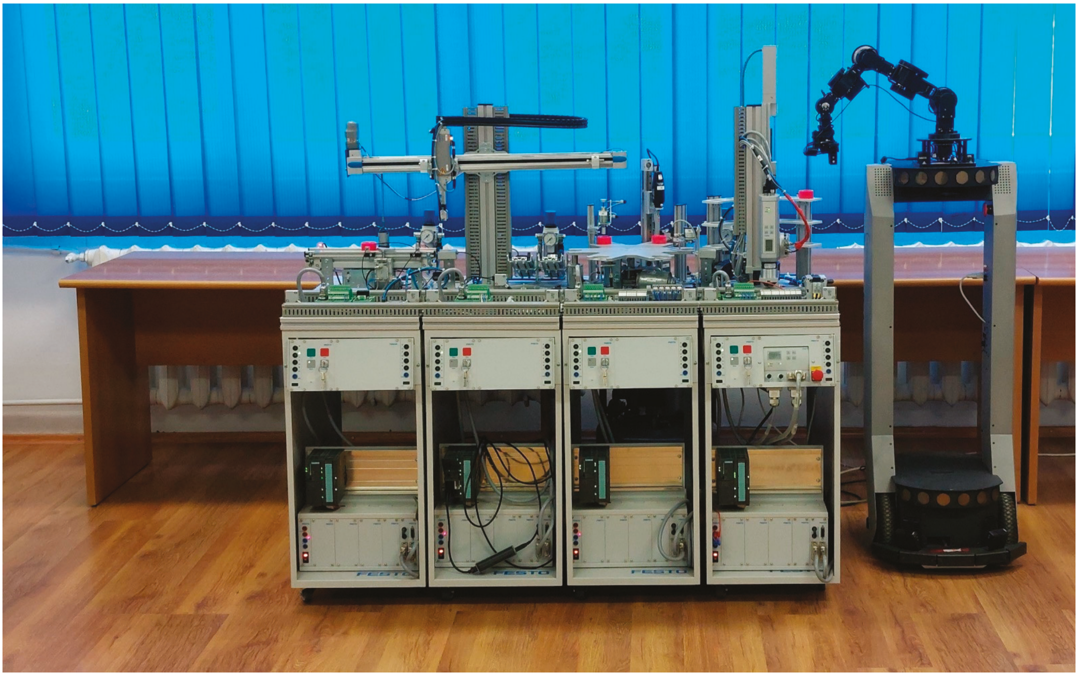

Figure 1. Festo MPS 200 assisted by CAS (ARS PeopleBot equipped with RM Cyton 1500 and MVS).

RM Cyton is used for recovering the pieces which are then transported by the ARS PeopleBot. The RM is equipped with a camera used for the eye in hand subsystem mounted on the end-effector. All the elements are controlled by a computer, the camera via USB connection, ARS PeopleBot, and RM Cyton by Wi-Fi with the help of an Advanced Robotic Interface for Applications (ARIA) package [20–23]. The combined subsystems are presented in Figure 2.

2.2. Eye in Hand MVS

An eye in hand MVS type refers to a system where the visual sensor is placed on the last joint of the RM and the camera movements also affect RM movements. Another type of MVS commonly used is eye to hand, where, contrary to eye in hand, the sensor is fixed in a position relative to the work environment, where both the RM and the workpieces are observed. For image-based visual servoing (IBVS), 2D image information is being used for an estimation of the desired motion of the robot. Standard tasks such as detection, tracking and positioning are realized by minimizing the error between the features extracted from the current image and the visual features of the desired image [13].

In the case of IBVS architecture, the visual sensor that extracts information about the work environment can be either eye in hand implementation, where the movement of the robot induces the movement of the camera, or eye to hand, where the RM and its motions can be examined from a fixed point. A common method used in object detection, classification, and shape identification is called the moments of the image. This method is based on features extraction from a 2D intensity distribution of the image, together with information about the orientation and coordinates of the gravity center. In Figure 3 is presented the complete CAS's transport trajectory, from the last to the first P/RML workstation, from the detection and grabbing to the placing of the workpiece.

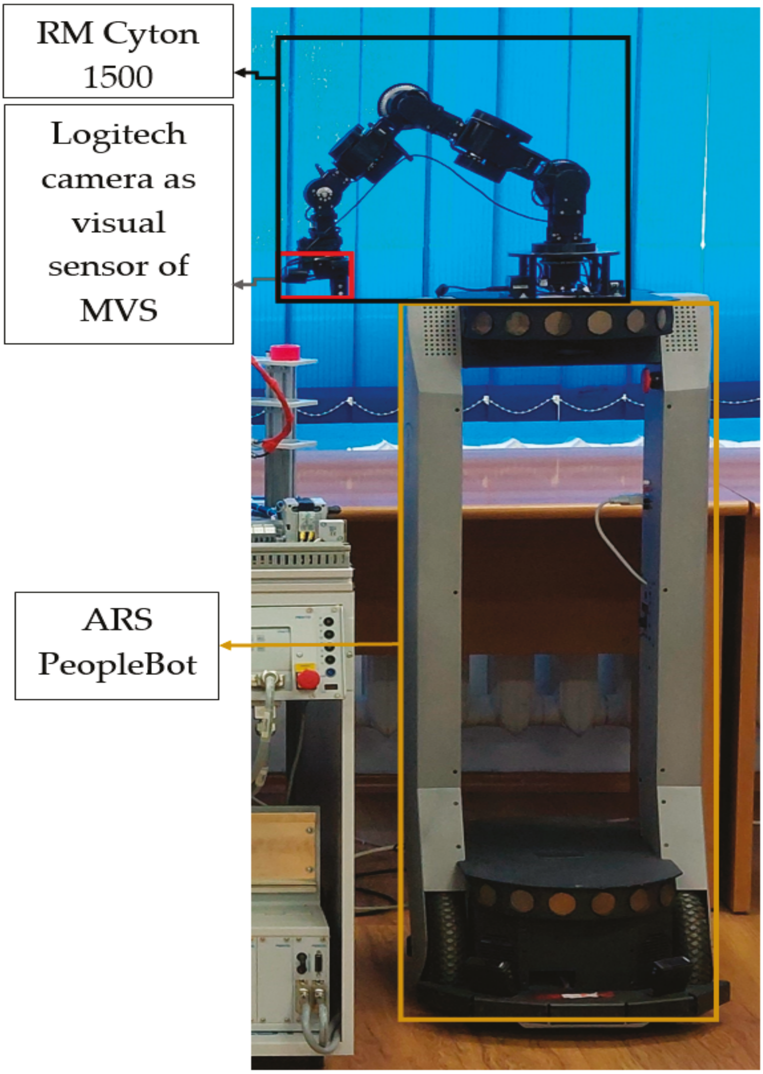

Figure 2. Structure of the CAS: ARS PeopleBot; RM Cyton 1500; eye in hand MVS.

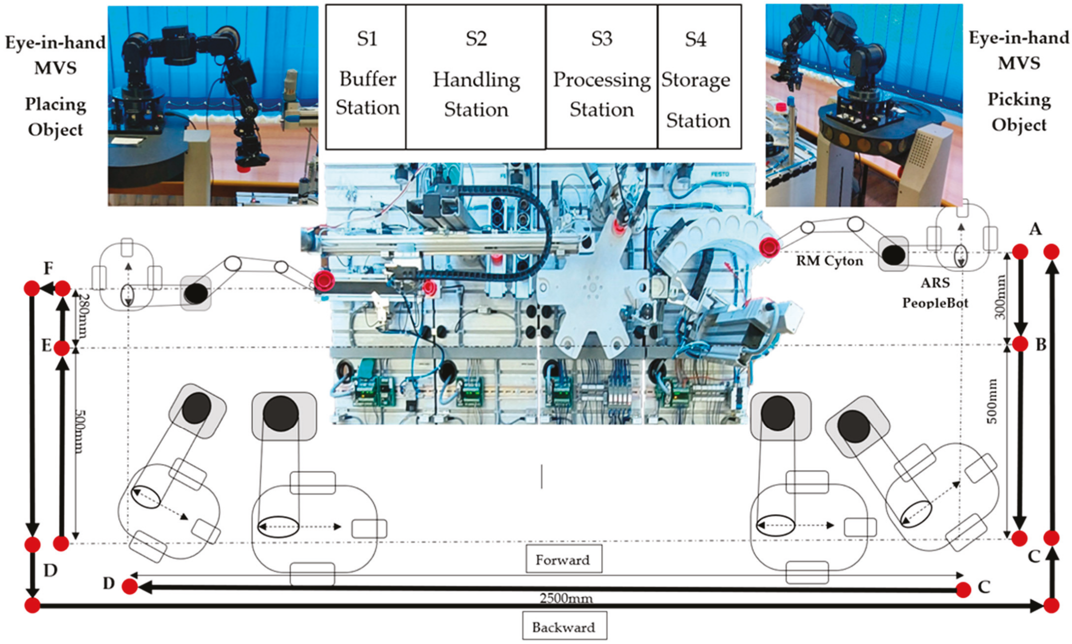

Figure 3. P/RML assisted by CAS.

2.3. Modelling and Control of MVS Based on the Moments of the Image Method

The structure of the eye in hand MVS has the following components: a 7-DOF RM, a visual sensor, and an image-based controller presented in Figure 4.

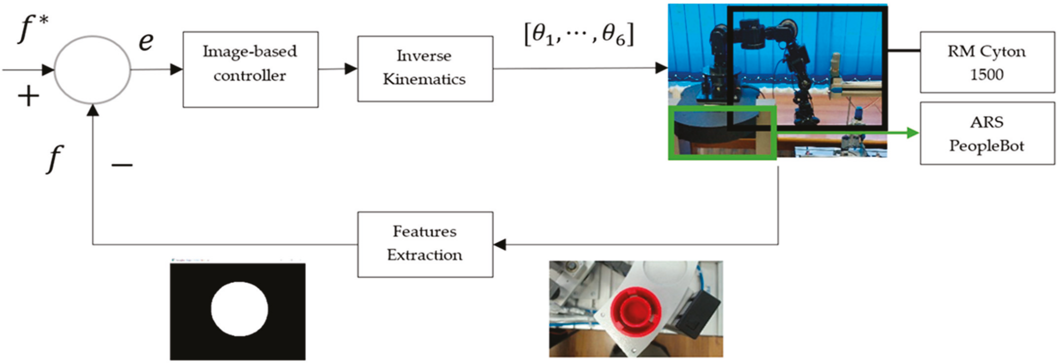

Figure 4. Eye in hand MVS closed-loop control.

One of the most important parts of this design implementation, is that the image-based controller, needs information about the environment of the system to minimize error between the current configuration of the visual features, f, and the desired configuration f^*. For modelling the open loop servoing system, the fixed parts components of the RM and the visual sensor must be analyzed separately. The signal related with the input control of the RM is v_c^*, and it represents the reference speed of the camera with the structure: $v_c^* = (v^*, \omega^*)^T$ where $v^* = \left[v_x^*, v_y^*, v_z^*\right]^T$ and $\omega^* = \left[\omega_x^*, \omega_y^*, \omega_z^*\right]^T$ are defined as the linear and angular speed, respectively. The signal, v_c^* is expressed in Cartesian space and must be transformed to be applied to the RM.

The posture is defined by the v_c^* integration and is noted with $s = [s_1, s_2, s_3, s_4, s_5, s_6]^T$ defining the robot Jacobian as follows:

$$J_r = \left[\partial s_i / \partial q_j\right], i, j = 1, \ldots, 7, \tag{1}$$

where $q_{i,j} = 1, \ldots, 7$ represents the RM's joints' states. The transformation of v_c^* from Cartesian space to robotic joint space is done with J_r^{-1} and the interaction matrix. The moments m_{ij} are a set of visual features with the analytic form for the time variation, $\dot{m}_{ij}$, resultant to the moments of order $(i + j)$, differing depending on the speed of the visual sensor v_c^* corresponding to the following equation:

$$\dot{m}_{ij} = L_{m_{ij}} v_c, \tag{2}$$

where $L_{m_{ij}} = \left[m_{v_x} m_{v_y} m_{v_z} m_{\omega_x} m_{\omega_y} m_{\omega_z}\right]$ is the interaction matrix.

The interaction matrix associated with a set of image moments $f = [x_n, y_n, a_n, \tau, \xi, \alpha]^T$ for n points is processed in this manner [12,13,24–26]

$$L_f = \begin{bmatrix} -1 & 0 & 0 & a_n e_{11} & -a_n(1 + e_{12}) & y_n \\ 0 & -1 & 0 & a_n(1 + e_{21}) & -a_n e_{11} & -x_n \\ 0 & 0 & -1 & -e_{31} & e_{32} & 0 \\ 0 & 0 & 0 & \tau_{\omega_x} & \tau_{\omega_y} & 0 \\ 0 & 0 & 0 & \xi_{\omega_x} & \xi_{\omega_y} & 0 \\ 0 & 0 & 0 & \alpha_{\omega_x} & \alpha_{\omega_y} & -1 \end{bmatrix}. \tag{3}$$

The analytical form of the parameters from (3) can be found in [27].

2.4. Assumptions and Task Planning

The processing/reprocessing tasks can be simplified into a sequence of actions combined in parallel with workpieces positioning and transportation along the cells of the mechatronics line. Shown in Figure 5 is shown the task planning in the form of a block diagram with the actions done by the CAS when a workpiece has failed the quality test. Next, the workpiece is transported from the storage station (last cell) to the buffer station (first cell). The red lines represent the reprocessing tasks done if the piece has been considered faulty, and the black lines represent the normal processing assignments when an initial workpiece has been supplied.

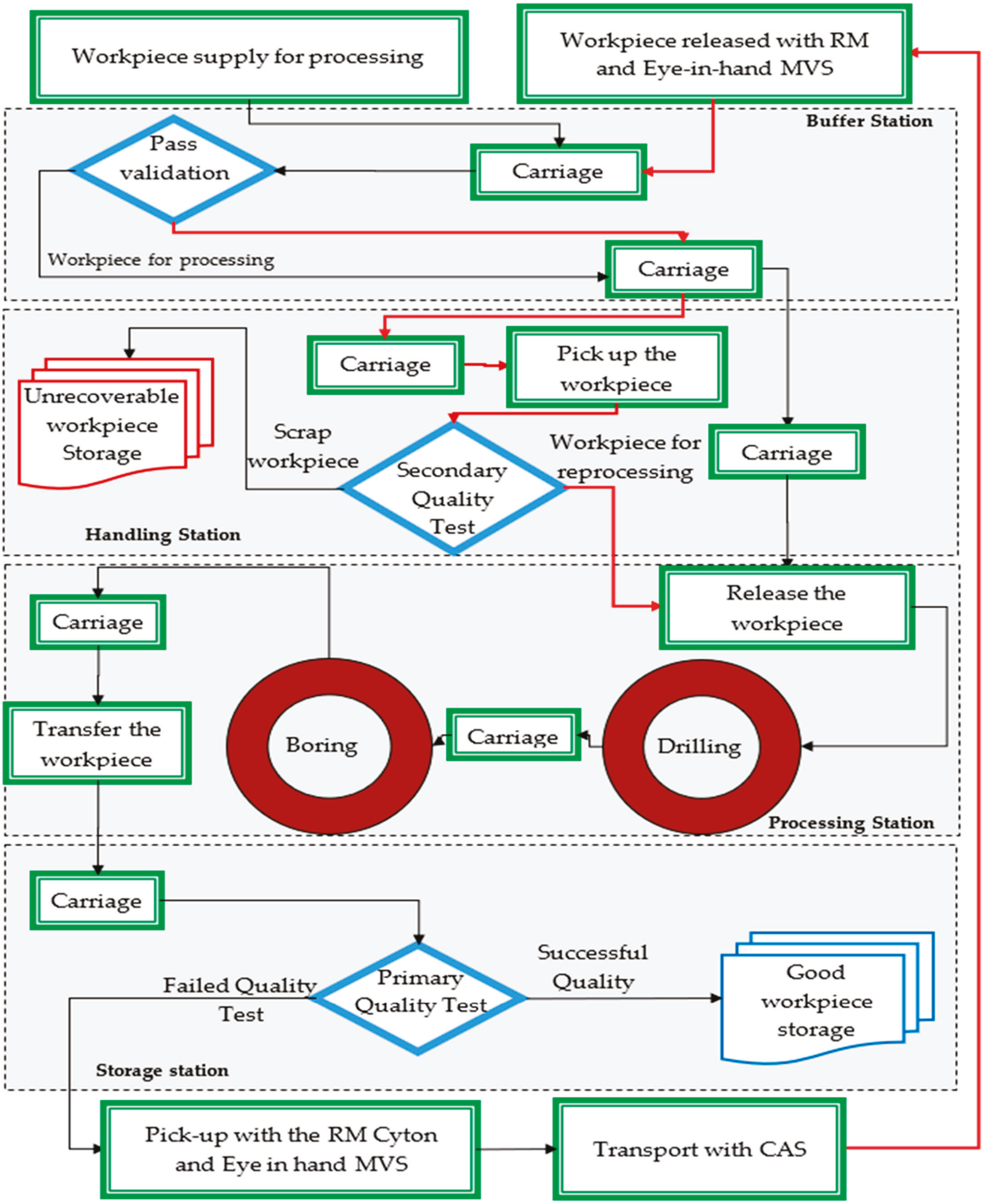

Figure 5. Processing/Reprocessing cycle for a piece that has failed the quality test.

Because the P/RML on its basis is a flexible industrial production line, it is designed to easily adapt to changes in the type and quantity of the product and it has a high range of products that it can provide. Through reprocessing, the faulty products can be retrieved and reworked to the necessary quality standard. Since the technology utilized by the P/RML can be altered by aspects such as process modes, type of finished workpiece, and operations times, some assumptions are needed for the entire system to work as intended:

Assumption 1. *The manufacturing technology processes the workpieces in pipeline mode;*

Assumption 2. *The first station is provided with one piece at a time for processing;*

Assumption 3. *The initial conditions and parameters of the technology are known, such as quantity of pieces and task duration;*

Assumption 4. *Only one type of piece can be processed or reprocessed with different colors since the proposed processing operations are specific to a type of product;*

Assumption 5. *The number of the workstations involved in processing/reprocessing by the P/RML is previously known and unchanged;*

Assumption 6. *The workstations of the P/RML have a linear distribution in the following order: buffer, handling, processing, and storing;*

Assumption 7. *The processing/reprocessing tasks are executed on the same workstation and the pieces can be processed simultaneously in different stages;*

Assumption 8. *A red workpiece will mean that the quality test is not passed and reprocessing is needed;*

Assumption 9. *In the storage, the first level from the top is utilized for rejected workpieces;*

Assumption 10. *One CAS assists the P/RML, which is used for picking up, transporting, and releasing the workpieces;*

Assumption 11. *One eye in hand visual sensor is mounted on the RM Cyton;*

Assumption 12. *To avoid conflict, priority is given to the workpiece for reprocessing;*

Assumption 13. *The technology includes two quality tests, which detect between a scrap workpiece and one recoverable by reprocessing.*

3. Direct and Inverse Kinematics Model of RM Cyton 1500

RM Cyton 1500 offers a robust and precise manipulation for a wide variety of applications. It has been designed to simulate the structure of a human arm; the shoulder has three joints, the elbow has one joint, and the wrist has three joints. All the joints described make up the 7 DOF of the RM. Angle limits of the RM are shown in Table 1.

Table 1. 7-DOF RM Cyton 1500.

Joint	Lower Limit (in Angles)	Upper Limit (in Angles)
Shoulder Roll	−150°	150°
Shoulder Pitch	−105°	105°
Shoulder Yaw	−105°	105°
Elbow Pitch	−105°	105°
Wrist Yaw	−105°	105°
Wrist Pitch	−105°	105°
Wrist Roll	−150°	150°

For testing and simulating the RM, kinematic modeling needs to be performed, with the main objective being the study of RM's mechanical parts, the direct and the inverse kinematics.

The direct kinematics consist of finding the position of the end-effector in space by knowing the movements of the joints, for example $F(\theta_1, \theta_2, \ldots\ldots, \theta_n) = [x, y, z, R]$, and inverse kinematics consist of determining the value of every joint by knowing the position of the end effector and its orientation, $F(x, y, z, R) = [\theta_1, \ldots\ldots\ldots, \theta_n]$.

A RM is composed, in general, of three joints, each defined by one or more degrees. In the case of RM Cyton 1500, it is made of:

- One shoulder type joint, characterized by three angles;
- One elbow type joint, characterized by one angle;
- One wrist type joint, characterized by three angles.

Presented in Figure 6 is a compact diagram block of kinematic modeling [28].

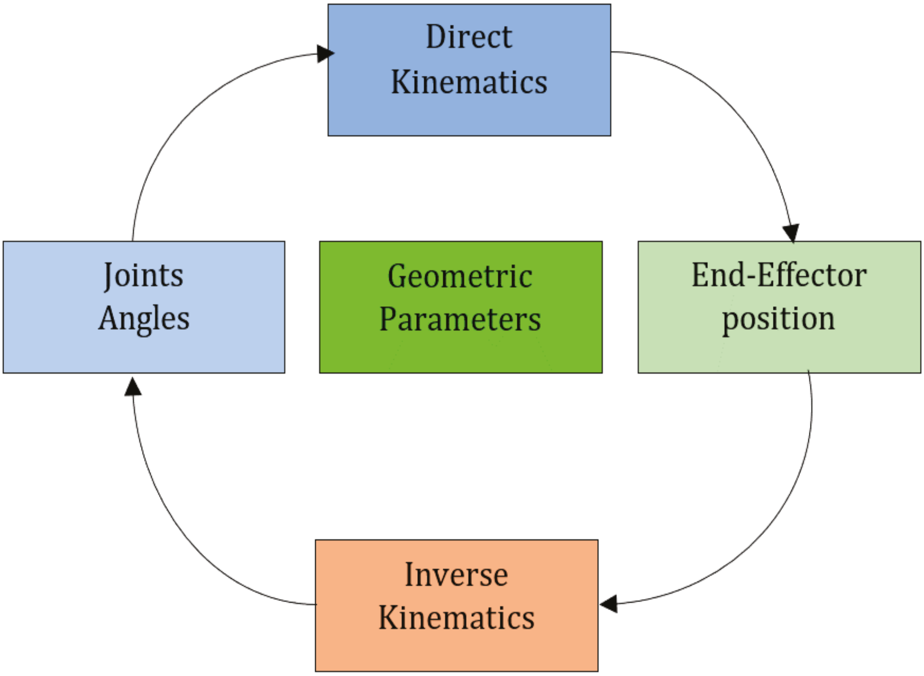

Figure 6. Block diagram of kinematics models.

The configuration of the RM and its joints is presented in Figure 7 [29].

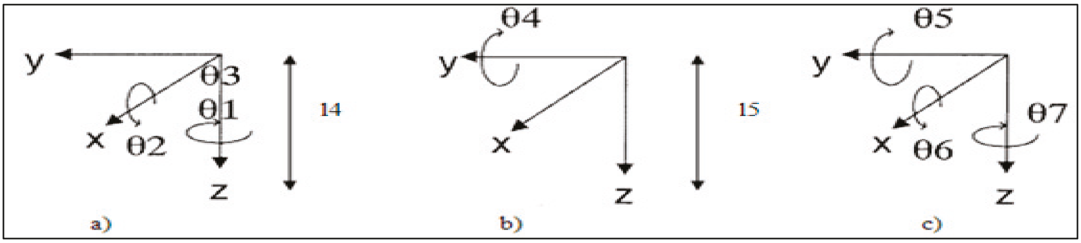

Figure 7. Angles that represent every joint, (**a**) Shoulder type, (**b**) Elbow type and (**c**) Wrist type.

One convention that is used for the selection of reference frames, especially in robotics applications, is represented by the Deavit&Hartenberg (D&H) convention, illustrated in Figure 8 [30], and parameters of the RM Cyton 1500, presented in Table 2.

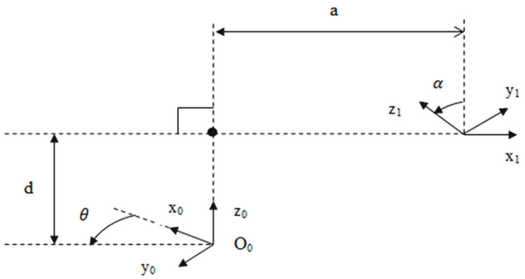

Figure 8. Denavit&Hartenberg Convention.

Table 2. RM Cyton 1500 D&H parameters.

i	*α*	*a*	*d*	*P*
1	90	0	*d*1	*θ*1
2	0	*a*2	0	*θ*2
3	90	0	*d*3	*θ*3
4	0	*a*4	0	*θ*4
5	90	0	*d*5	*θ*5
6	0	*a*5	0	*θ*6
7	−90	*a*6	0	*θ*7

To determine the direct kinematic model, a fixed coordinate system with an index of 0 for the shoulder type joints and, for the other joints, a system with an index of i, $i = 1 \ldots 7$ have been placed. In this convention, every homogeneous transformation A_i is represented as a product of four basic transformations, where the four variables θ_i, a_i, d_i, α_i are the parameters associated with every link and joint.

$$A_i = R_{z,\theta_i} Trans_{z,d_i} Trans_{x,a_i} R_{x,\alpha_i}, \tag{4}$$

$$A_i = \begin{bmatrix} c\theta_i & -s\theta_i & 0 & 0 \\ s\theta_i & c\theta_i & 0 & 0 \\ 0 & 0 & 1 & 0 \\ 0 & 0 & 0 & 1 \end{bmatrix} \begin{bmatrix} 1 & 0 & 0 & 0 \\ 0 & 1 & 0 & 0 \\ 0 & 0 & 1 & d_i \\ 0 & 0 & 0 & 1 \end{bmatrix} \begin{bmatrix} 1 & 0 & 0 & a_i \\ 0 & 1 & 0 & 0 \\ 0 & 0 & 1 & 0 \\ 0 & 0 & 0 & 1 \end{bmatrix} \begin{bmatrix} 1 & 0 & 0 & 0 \\ 0 & c\alpha_i & -s\alpha_i & 0 \\ 0 & s\alpha_i & c\alpha_i & d_i \\ 0 & 0 & 0 & 1 \end{bmatrix}$$

$$A_i = \begin{bmatrix} c\theta_i & -s\theta_i c\alpha_i & s\theta_i s\alpha_i & a_i c\theta_i \\ s\theta_i & c\theta_i c\alpha_i & -c\theta_i s\alpha_i & a_i s\theta_i \\ 0 & s\alpha_i & c\alpha_i & d_i \\ 0 & 0 & 0 & 1 \end{bmatrix}. \tag{5}$$

With the help of the D&H table the A_I matrices have been determined for every DOF of the RM:

$$A_1 = \begin{bmatrix} c_1 & 0 & s_1 & 0 \\ s_1 & 0 & -c_1 & 0 \\ 0 & 1 & 0 & d_1 \\ 0 & 0 & 0 & 1 \end{bmatrix}, A_2 = \begin{bmatrix} c_2 & -s_2 & 0 & \alpha_2 c_2 \\ s_2 & c_2 & 0 & \alpha_2 s_2 \\ 0 & 0 & 1 & 0 \\ 0 & 0 & 0 & 1 \end{bmatrix},$$
$$A_3 = \begin{bmatrix} c_3 & 0 & s_3 & 0 \\ s_3 & 0 & -c_3 & 0 \\ 0 & 1 & 0 & d_3 \\ 0 & 0 & 0 & 1 \end{bmatrix}, A_4 = \begin{bmatrix} c_4 & -s_4 & 0 & \alpha_4 c_4 \\ s_4 & c_4 & 0 & \alpha_4 s_4 \\ 0 & 0 & 1 & 0 \\ 0 & 0 & 0 & 1 \end{bmatrix}, A_5 = \begin{bmatrix} c_5 & 0 & s_5 & 0 \\ s_5 & 0 & -c_5 & 0 \\ 0 & 1 & 0 & d_5 \\ 0 & 0 & 0 & 1 \end{bmatrix}, \tag{6}$$
$$A_6 = \begin{bmatrix} c_6 & -s_6 & 0 & \alpha_6 c_6 \\ s_6 & c_6 & 0 & \alpha_6 s_6 \\ 0 & 0 & 1 & 0 \\ 0 & 0 & 0 & 1 \end{bmatrix}, A_7 = \begin{bmatrix} c_7 & 0 & s_7 & \alpha_7 c_7 \\ s_7 & 0 & -c_7 & \alpha_7 c_7 \\ 0 & 1 & 0 & 0 \\ 0 & 0 & 0 & 1 \end{bmatrix}.$$

The direct kinematics model of the RM Cyton is determined by the decomposition of the seven matrices:

$$T_1^0 = A_1, \tag{7}$$

$$T_7^0 = A_1 A_2 A_3 A_4 A_5 A_6 A_7 = \begin{bmatrix} s_x & n_x & a_x & d_x \\ s_y & n_y & a_y & d_y \\ s_z & n_z & a_z & d_z \\ 0 & 0 & 0 & 1 \end{bmatrix} \tag{8}$$

Figure 9 illustrates an image representing all the joints and angles composing RM Cyton. The kinematic model obtained is utilized in the control structure of RM Cyton:

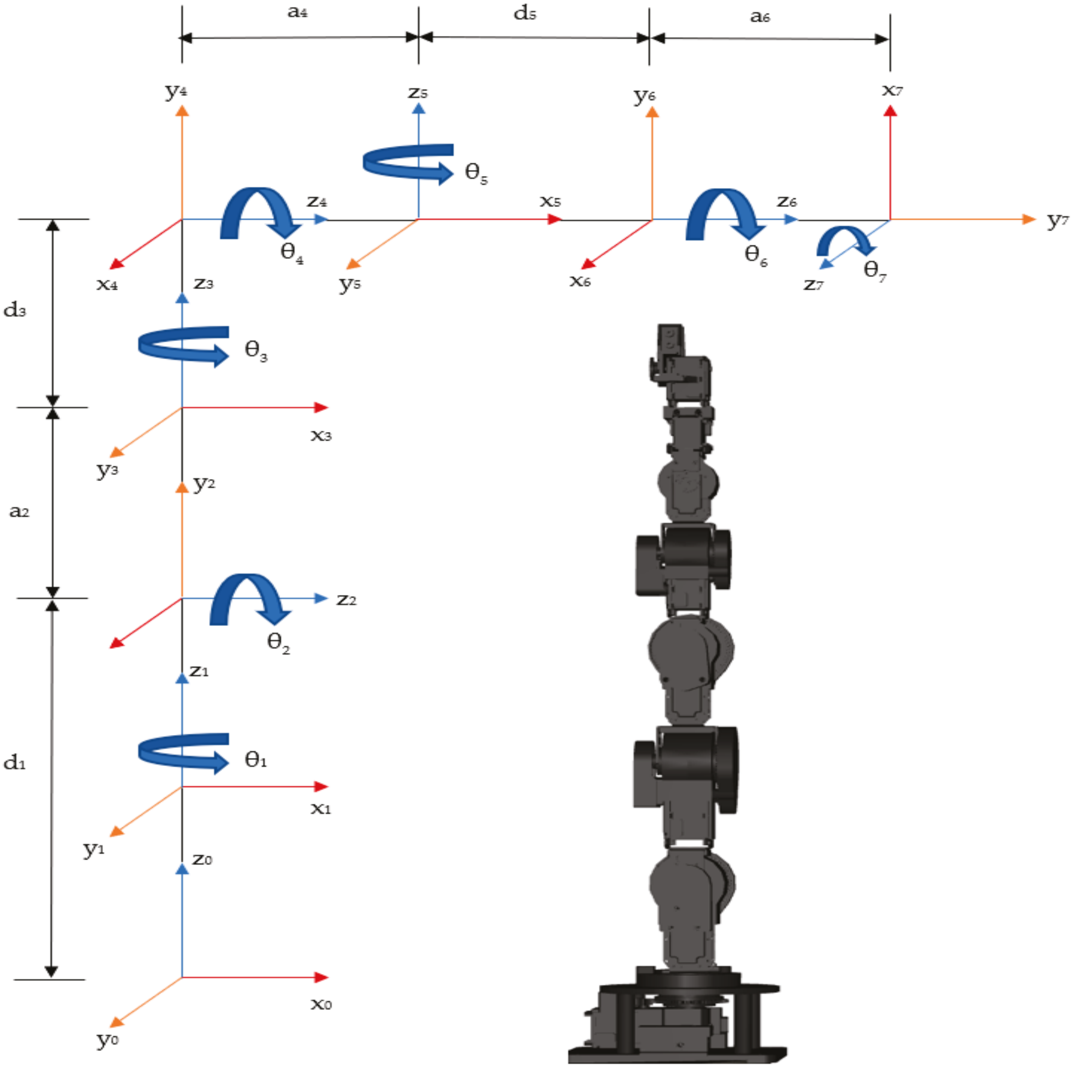

Figure 9. Joints and angles of 7-DOF RM Cyton 1500.

4. Trajectory Tracking Sliding-Mode Control of ARS PeopleBot

The ARS PeopleBot is controlled to follow a desired trajectory based on continuous time sliding-mode control. In TTSMC, the real ARS follows the trajectory of a virtual one, with the desired trajectory generated by the virtual ARS denoted with

$$q_d(t) = \begin{bmatrix} x_d & y_d & \theta_d \end{bmatrix}^T. \tag{9}$$

The kinematic model of the virtual ARS becomes

$$\begin{cases} \dot{x} = v_d \cos\theta_d \\ \dot{y} = v_d \sin\theta_d \,, \\ \dot{\theta} = \omega_d \end{cases} \tag{10}$$

where x_d and y_d represent the cartesian coordinates of the geometric center, v_d represents the linear speed, θ_d represents the orientation, and ω_d represents the angular speed. When the ARS follows the desired trajectory, on X and Y axis appear tracking and orientation errors:

$$\begin{bmatrix} x_e \\ y_e \\ \theta_e \end{bmatrix} = \begin{bmatrix} \cos\theta_d & \sin\theta_d & 0 \\ -\sin\theta_d & \cos\theta_d & 0 \\ 0 & 0 & 1 \end{bmatrix} \begin{bmatrix} x_r - x_d \\ y_r - y_d \\ \theta_r - \theta_d \end{bmatrix}. \tag{11}$$

The error dynamics are given by the following equations

$$\begin{cases} \dot{x}_e = -v_d + v_r \cos\theta_e + \omega_d y_e \\ \dot{y}_e = v_r sin\theta_e - \omega_d x_e \\ \dot{\theta}_e = \omega_r - \omega_d \end{cases}. \tag{12}$$

Since the ARS orientation is not perpendicular on the desired trajectory, it is assumed that $|\theta_e| < \pi/2$. Given the errors' positions (11) and the derivatives (12), the sliding surfaces are

$$\begin{cases} s_1 = \dot{x}_e + k_1 x_e \\ s_2 = \dot{y}_e + k_2 y_e + k_0 sgn(y_e)\theta_e \end{cases}. \tag{13}$$

Presented in Figure 10 are the real and virtual ARS with absolute coordinates and orientation following a desired trajectory:

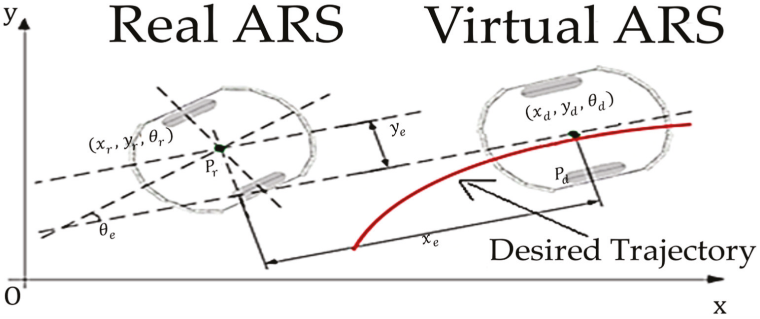

Figure 10. Real ARS, Virtual ARS, Desired trajectory.

The parameters $k1$, $k2$, $k3$ are positive and constant. If s1 converges to zero, then x_e becomes 0 too, and if s_2 tends to 0, then $\dot{y} = -k_2 y_e + k_0 sgn(y_e)\theta_e$. The surface derivatives

$$\begin{cases} \dot{s}_1 = \ddot{x}_e + k_1 \dot{x}_e, \\ \dot{s}_2 = \ddot{y}_e + k_2 \dot{y}_e + k_0 sgn(y_e)\dot{\theta}_e{}' \end{cases} \tag{14}$$

are written in a compact form:

$$\dot{s} = -Qsgn(s) - Ps, \tag{15}$$

where

$$Q = \begin{bmatrix} Q1 & 0 \\ 0 & Q2 \end{bmatrix}, P = \begin{bmatrix} P1 & 0 \\ 0 & P2 \end{bmatrix}, Q \geq 0, P \geq 0, \tag{16}$$

$$s = \begin{bmatrix} s_1 & s_2 \end{bmatrix}^T, sgn(s) = \begin{bmatrix} sgn(s_1) & sgn(s_2) \end{bmatrix}^T. \tag{17}$$

Thus, from (11)–(14), the TTSMC law becomes as follows:

$$\dot{v}_c = \frac{-Q_1 sign(s_1) - P_1 s_1 - k_1 \dot{x}_e - \dot{\omega}_d y_e - \dot{\omega}_d \dot{y}_e + v_r \theta_e + \dot{\dot{v}}_d}{\cos\theta_e}, \tag{18}$$

$$\omega_c = \frac{-Q_2 sign(s_2) - P_2 s_2 - k_2 \dot{y}_e - \dot{v}_r \sin\theta_e + \dot{\omega}_d x_e + \omega_d \dot{x}_e + \omega_d}{v_r cos\theta_e + k_0 sgn(y_e)} \tag{19}$$

5. Real-Time Control of P/RML Assisted by CAS

The assisting technology for P/RML consists of one dynamic robotic system, CAS, used in picking, placing, and transporting the workpieces.

The process is based on 3 main control loops:

- Control loop for the P/RML with Siemens PLCs, programmed in Simatic Step 7;
- Control loop for the ARS PeopleBot based on TTSMC used in workpiece transportation;
- Control loop for the RM Cyton with eye in hand MVS for precise positioning for both picking and placing workpieces.

Presented in Figure 11 are the control loops connected to a single computer that runs the applications which control the P/RML, CAS and its mechanisms with the help of Simatic Step 7, Microsoft Visual Studio, the C programming language, Aria packages, and MATLAB.

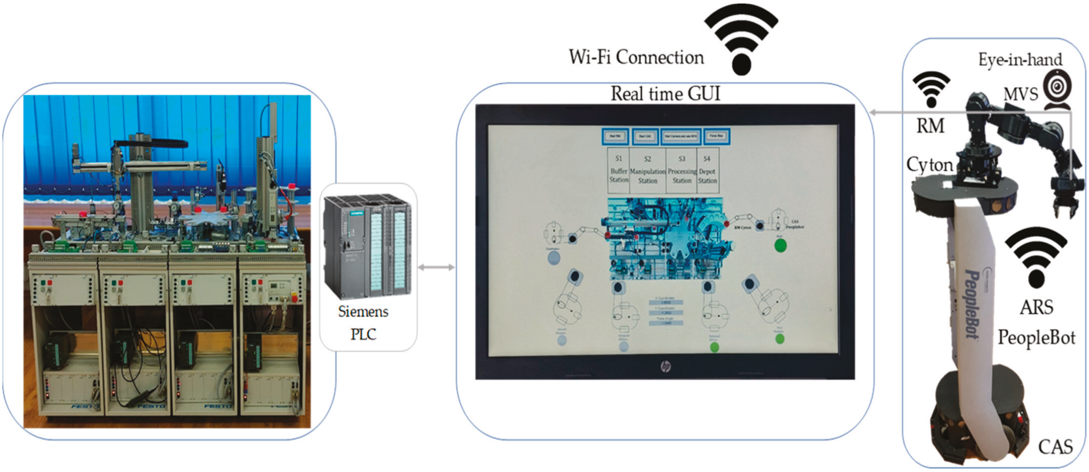

Figure 11. Communication block set of the P/RML, CAS and computer.

Displayed in Figure 12 are a few pictures from real-time with the process of scanning the object, and, if it is detected, it is picked up by the gripper of the RM and transported with the CAS to the first workstation. The process with the main steps done in detecting the objects is presented in Figure 13. In Figure 13a is the conversion from the RGB (Red Green Blue) color model to the HSV (Hue Saturation Value) color model, as it is more robust to changes in light, since, during the experiments, there have been major effects with the type of light used, natural sunlight or laboratory light. Presented in Figure 13b is the detected object if the colors between the HSV limits have been met and the shape (in this case, a circle) has been found using the Ramer–Douglas–Peucker algorithm and Canny Edge detection, which are implemented by using the OpenCV libraries. Finally, in Figure 13c, the object is tracked if the conditions of both the color and shape have been met; the centroid is tracked by using the image moments method for its versatility and efficiency, as deviations appear only in a 2D space, the distance on the Z axis is constant, and the rotations of the object do not exist, since the workpiece always comes to the same place, only the CAS does not have a stable position and a MVS is needed [31].

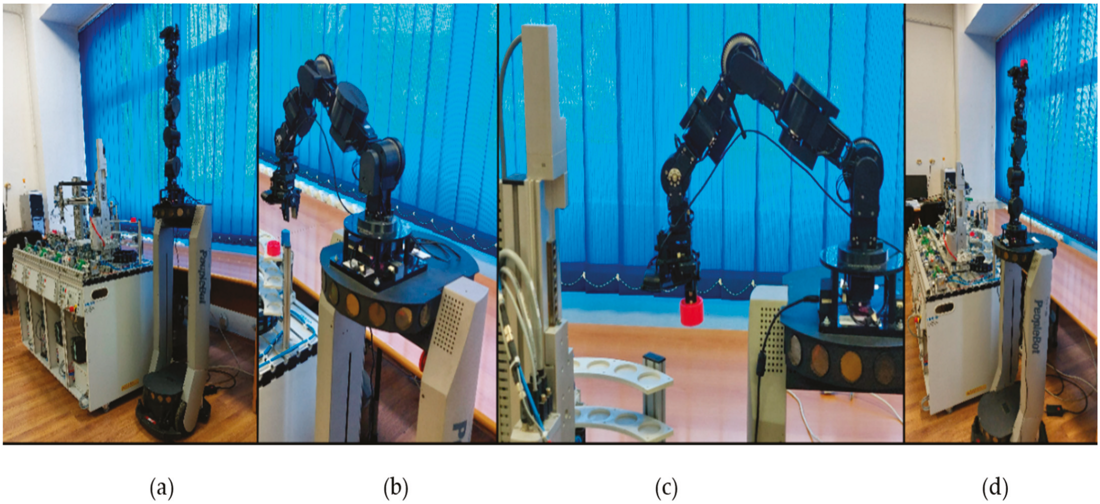

Figure 12. Real-time control of the CAS for picking up workpieces with the following order: (**a**) home position, (**b**) scanning position (**c**) picking up object (**d**) home position with the workpiece picked up in the gripper.

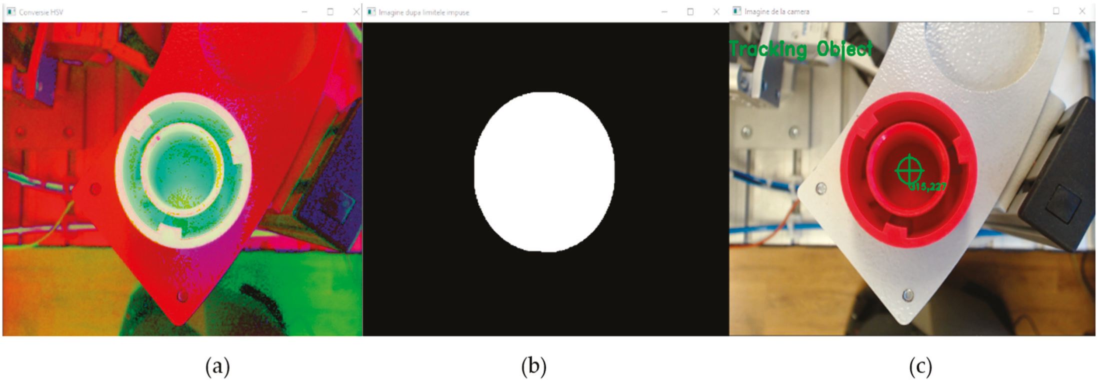

Figure 13. Object Detection of the workpiece with the following steps: (**a**) Conversion from RGB to HSV (**b**) image segmentation after the color has been found between the HSV limits and the shape corresponding to object has been found (**c**) object color and shape has been found and is being tracked.

Likewise, presented in Figure 14 are pictures with a similar process to the previous figure, this time for placing the workpieces rather than pick them up. The biggest difference between Figures 13 and 15 consists of the fact that, in Figure 13, the object itself is detected while, in Figure 15, a reference point specific to the first workstation is detected, and the object is placed. Also, while in the first case the shape detected is a circle, in the second one the shape detected is a rectangle.

(a) (b) (c) (d)

Figure 14. Real time control of the CAS for placing the workpieces with the following order: (**a**) parking position (**b**) scanning position (**c**) placing the object (**d**) RM returning to the home position with the object placed on the workstation.

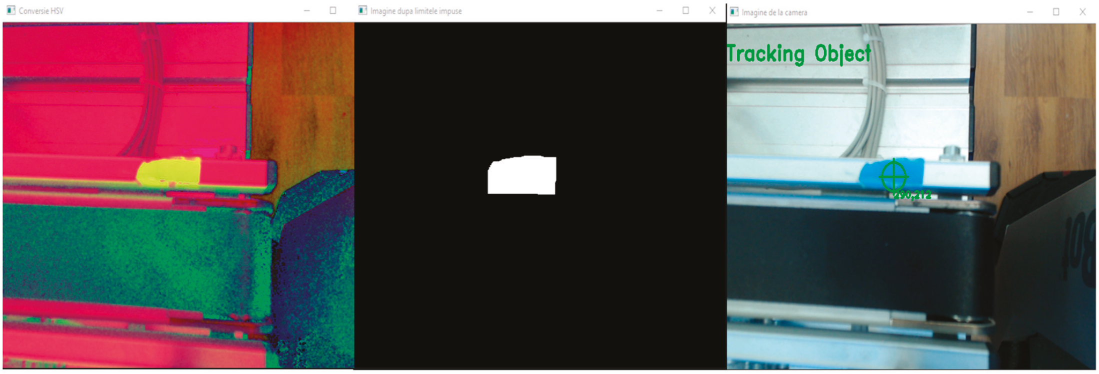

(a) (b) (c)

Figure 15. Object Detection of the reference point with the following steps: (**a**) Conversion from RGB to HSV (**b**) image segmentation after the color has been found between the HSV limits and the shape corresponding to reference has been found (**c**) reference object color and shape has been found and is being tracked.

In Figure 16a, the complete 3D picking up trajectory is presented: the movement from the home position to the scanning, then above the object, picking it, and back to the home position, so that the CAS can transport it to the first workstation for reprocessing if it fails the quality test. Presented in Figure 16b is the 3D trajectory for placing the object.

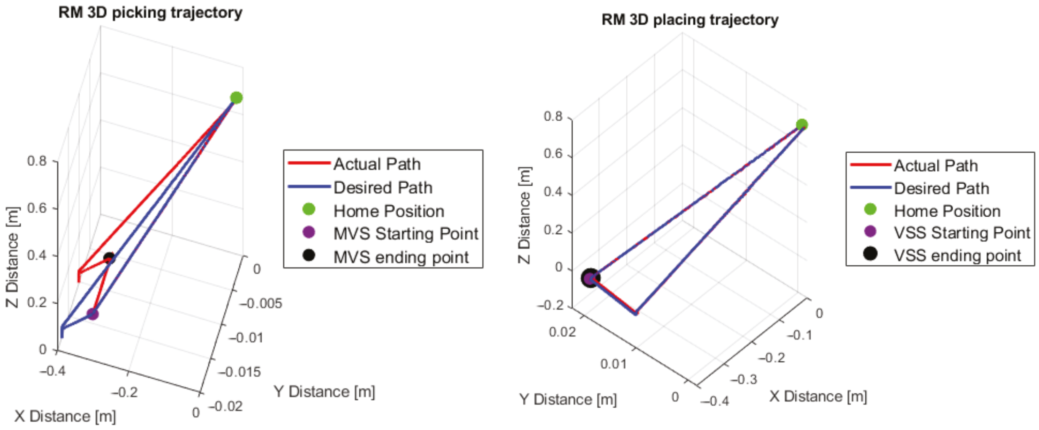

(**a**) (**b**)

Figure 16. 3D Trajectories of the RM for (**a**) picking and (**b**) placing the workpiece.

Although the MVS starting and ending point are present in Figure 16a,b, they are hard to visualize, which is why Figure 17 is needed, in the case of picking the object, having the X and Z axis in Figure 17a and the Y on Figure 17b. The entire MVS process takes ~7 s and it is most apparent in the case of the Y axis, where there is a deviation that goes up to 10 mm from the desired position.

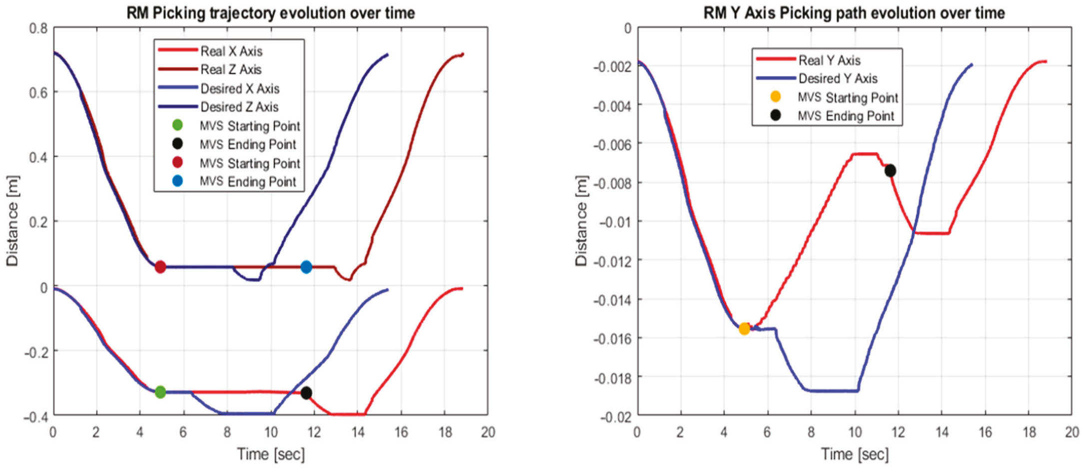

(a) (b)

Figure 17. Trajectories evolution over time for (**a**) X and Z axis and (**b**) Y axis for picking the workpiece.

The time for placing the workpiece, based on MVS control, is about four s due to the fact that difference between the desired and actual features is much smaller than picking up. The X and Z trajectories over time are displayed in Figure 18a. In Figure 18b, only the Y axis trajectory is shown, since the distance is much smaller than the X and Y axis.

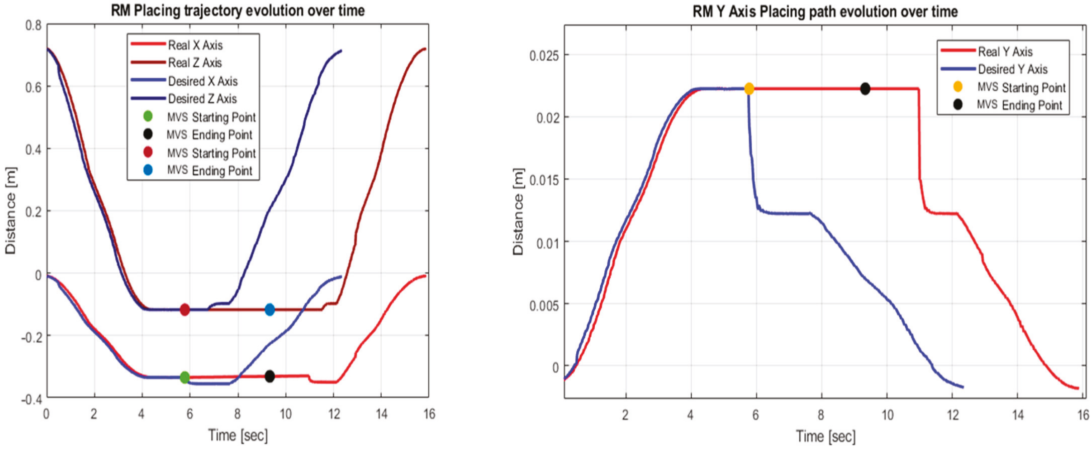

(a) (b)

Figure 18. Trajectories evolution over time for (**a**) X and Z axis and (**b**) Y axis in the case of picking the workpiece.

The PeopleBot trajectory has some deviations on the X and Y axis that can be observed in Figure 19a. Along the X axis, the error is near zero, while on the Y axis the final error is about 4 mm, as shown in Figure 19b.

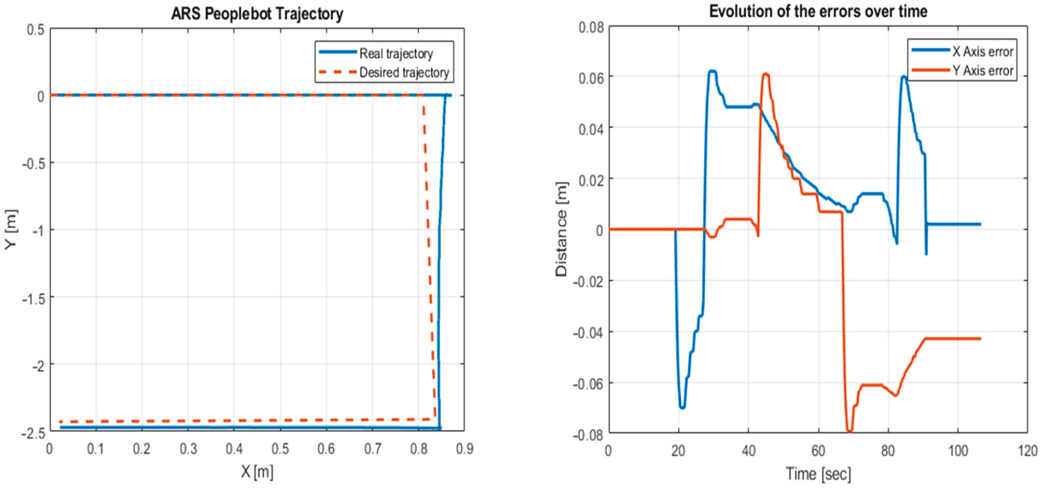

(**a**) (**b**)

Figure 19. (**a**) Real and desired trajectories of the ARS PeopleBot and (**b**) evolution of the errors in time.

The velocity profile of the ARS PeopleBot along the forward trajectory, during transportation of the workpiece, is presented in the Figure 20a, with a maximum of 0.12 m/s. The state transition of the workpiece is shown in Figure 20b. While the RM is active for picking and placing the workpiece, the CAS has zero velocity.

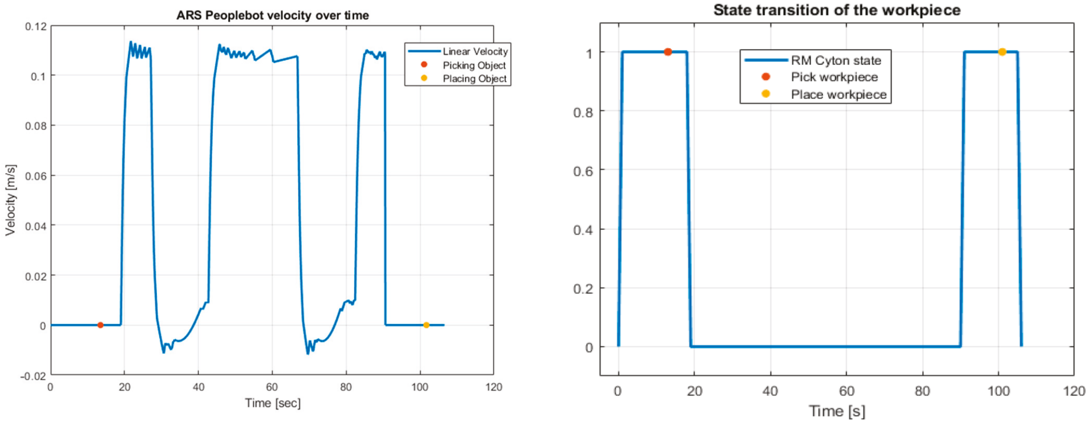

(**a**)

(**b**)

Figure 20. (**a**) ARS PeopleBot velocity evolution over time; (**b**) state transition of the workpiece.

In Figure 21, the X and Y trajectory are displayed, so that the differences between the desired and real trajectories can be identified more easily.

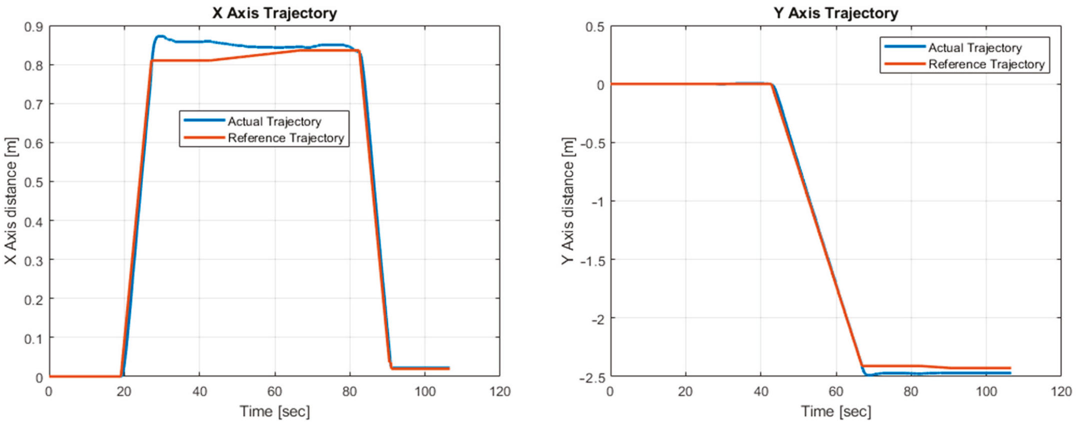

(a)

(b)

Figure 21. ARS PeopleBot trajectory: (**a**) X axis; (**b**) Y axis Trajectories.

6. Conclusions

The presented research is still in the experimental phase, the final step being a fully automated processing technology, allowing the recovery by reprocessing of a given volume of pieces. By using SIMATIC STEP 7, Visual C ++ platforms and MATLAB, real-time control structures have been implemented, allowing automatic processing/reprocessing, assisted by the CAS, ARS equipped with RM, and MVS. Compared to [4], where two autonomous robotic systems and two type visual servoing systems (eye to hand and eye in hand) have been used, in this paper only one CAS, with one type of MVS (eye in hand), assists P/RML. As a result, the reliability, flexibility, and robustness of the technology have been increased due to the uncertainties that might come from the sensors fails, environment conditions, disturbances in data transfer and communications. Although this is a technology that has been used at the level of a laboratory, it can be extended further to real industry, where high accuracy and positioning are needed. In the future, this technology is expected to be improved to be able to satisfy the standards of the Industry 4.0. Through this perspective, the presented manufacturing technology has a dual purpose, one educational and the other to be as close as possible to the real industrial world. The educational goal aims to familiarize the system designer with everything that defines: Industry 4.0, concepts, design, Cloud and IoT communication, real-time monitoring and control. Therefore, we try to improve the presented technology by the integration of the state of the art in the field of Industry 4.0, including smart manufacturing, SCADA systems, tasks communication and synchronization, sensors data fusion, and high precision actuators.

Author Contributions: Conceptualization, G.S., A.F. (Adrian Filipescu), D.I., R.Ș., D.C., E.M. and A.F. (Adriana Filipescu); methodology G.S., A.F. (Adrian Filipescu), D.I., D.C., R.Ș. and E.M.; software, G.S. and D.I.; validation, A.F. (Adriana Filipescu), R.Ș., D.C. and E.M.; formal analysis, G.S., D.I. and A.F. (Adrian Filipescu); writing—original draft preparation, G.S., A.F. (Adrian Filipescu) and D.I.; writing—review and editing, A.F. (Adrian Filipescu), R.Ș. and D.C.; supervision, A.F. (Adrian Filipescu); project administration, A.F. (Adrian Filipescu); funding acquisition, A.F. (Adrian Filipescu), G.S. and D.I. All authors have read and agreed to the published version of the manuscript.

Funding: This article (APC) will be supported by Doctoral School of Fundamental Sciences and Engineering, “Dunărea de Jos” University of Galati.

Institutional Review Board Statement: Not applicable.

Informed Consent Statement: Not applicable.

Data Availability Statement: Data availability is not applicable to this article as the study did not report any data.

Acknowledgments: The results of this work were presented to the 10th edition of the Scientific Conference organized by the Doctoral Schools of “Dunarea de Jos” University of Galati (SCDS-UDJG) http://www.cssd-udjg.ugal.ro/, (accessed on 15 March 2022), that was held on 9th and 10th of June 2022, in Galati, Romania.

Conflicts of Interest: The authors declare no conflict of interest.

References

1. Stoll, J.T.; Schanz, K.; Pott, A. Mechatronic Control System for a Compliant and Precise Pneumatic Rotary Drive Unit. *Actuators* **2020**, *9*, 1. [CrossRef]
2. Syafrudin, M.; Fitriyani, N.L.; Alfian, G.; Rhee, J. An Affordable Fast Early Warning System for Edge Computing in Assembly Line. *Appl. Sci.* **2019**, *9*, 84. [CrossRef]
3. de Gea Fernández, J.; Yu, B.; Bargsten, V.; Zipper, M.; Sprengel, H. Design, Modelling and Control of Novel Series-Elastic Actuators for Industrial Robots. *Actuators* **2020**, *9*, 6. [CrossRef]
4. Filipescu, A.; Mincă, E.; Filipescu, A.; Coandă, H.-G. Manufacturing Technology on a Mechatronics Line Assisted by Autonomous Robotic Systems, Robotic Manipulators and Visual Servoing Systems. *Actuators* **2020**, *9*, 127. [CrossRef]
5. Chen, Z.-Y.; Chen, C.-T. A Remote-Controlled Robotic Arm That Reads Barcodes and Handles Products. *Inventions* **2018**, *3*, 17. [CrossRef]
6. Ciubucciu, G.; Filipescu, A., Jr.; Filipescu, S.; Dumitrascu, B. Control and Obstacle Avoidance of a WMR Based on Sliding-Mode, Ultrasounds and Laser. In Proceedings of the 12th IEEE International Conference on Control and Automation (ICCA), Kathmandu, Nepal, 1–3 June 2016; pp. 779–784, ISBN 978-1-5090-1737-9. [CrossRef]
7. Lupu, C.; Popescu, D.; Florea, G. Supervised Solutions for Precise Ratio Control: Applicability in Continuous Production Line. *Stud. Inform. Control* **2014**, *23*, 53–64. [CrossRef]
8. Radaschin, A.; Voda, A.; Filipescu, A. Task Planning Algorithm in Hybrid Assembly/Disassembly Process. In Proceedings of the 14th IFAC Symposium on Information Control Problems in Manufacturing, Bucharest, Romania, 23–25 May 2012; Volume 45, pp. 571–576. [CrossRef]
9. Minca, E.; Filipescu, A.; Voda, A. Modelling and control of an assembly/disassembly mechatronics line served by mobile robot with manipulator. *Control Eng. Pract.* **2014**, *31*, 50–62. [CrossRef]
10. Filipescu, A., Jr.; Petrea, G.; Filipescu, A.; Filipescu, S. Modeling and Control of a Mechatronics System Served by a Mobile Platform Equipped with Manipulator. In Proceedings of the 33rd Chinese Control Conference, Nanjing, China, 28–30 July 2014; pp. 6577–6582, ISBN 978-988-15638-4-2. [CrossRef]

11. Petrea, G.; Filipescu, A., Jr.; Minca, E. Hybrid Modelling and Simulation of a P/RML with Integrated Complex Autonomous Systems. In Proceedings of the 22nd IEEE, International Conference on System Theory, Control and Computing, (ICSTCC), Sinaia, Romania, 10–12 October 2018; pp. 439–444, ISBN 978-1-5386-4444-7. [CrossRef]
12. Copot, C. Control Techniques for Visual Servoing Systems. Ph.D. Thesis, Gheorghe Asachi Technical University of Iasi, Iasi, Romania, 2012.
13. Song, R.; Li, F.; Fu, T.; Zhao, J. A Robotic Automatic Assembly System Based on Vision. *Appl. Sci.* **2020**, *10*, 1157. [CrossRef]
14. Lan, C.-W.; Chang, C.-Y. Development of a Low Cost and Path-free Autonomous Patrol System Based on Stereo Vision System and Checking Flags. *Appl. Sci.* **2020**, *10*, 974. [CrossRef]
15. Deng, L.; Wilson, W.; Janabi-Sharifi, F. Dynamic performance of the position-based visual servoing method in the cartesian and image spaces. In Proceedings of the IEEE/RSJ International Conference on Intelligent Robots and Systems, Las Vegas, NV, USA, 27–31 October 2003; pp. 510–515. [CrossRef]
16. Gans, N.; Hutchinson, S.; Corke, P. Performance tests for visual servo control systems, with application to partitioned approaches to visual servo control. *Int. J. Robot. Res.* **2003**, *22*, 955–981. [CrossRef]
17. Corke, P.I.; Spindler, F.; Chaumette, F. Combining Cartesian and polar coordinates in IBVS. In Proceedings of the 2009 IEEE/RSJ International Conference on Intelligent Robots and Systems, St. Louis, MO, USA, 11 December 2009; pp. 5962–5967. [CrossRef]
18. Dragomir, F.; Mincă, E.; Dragomir, O.E.; Filipescu, A. Modelling and Control of Mechatronics Lines Served by Complex Autonomous Systems. *Sensors* **2019**, *19*, 3266. [CrossRef] [PubMed]
19. Petrea, G.; Filipescu, A.; Minca, E.; Voda, A.; Filipescu, A., Jr.; Serbencu, A. Hybrid Modelling Based Control of a Processing/Reprocessing Mechatronics Line Served by an Autonomous Robotic System. In Proceedings of the 17th IEEE, International Conference on System Theory, Control and Computing, (ICSTCC), Sinaia, Romania, 11–13 October 2013; pp. 410–415, ISBN 978-1-4799-2228-4. [CrossRef]
20. Gasparetto, A.; Zanotto, V. A new method for smooth trajectory planning of robot manipulators. *Mech. Mach. Theory* **2007**, *42*, 455–471. [CrossRef]
21. Kim, J.; Park, J.; Chung, W. Self-Diagnosis of Localization Status for Autonomous Mobile Robots. *Sensors* **2018**, *18*, 3168. [CrossRef] [PubMed]
22. Brassai, S.T.; Iantovics, B.; Enăchescu, C. Optimization of Robotic Mobile Agent Navigation. *Stud. Inform. Control* **2012**, *21*, 6. [CrossRef]
23. Ravankar, A.; Ravankar, A.A.; Kobayashi, Y.; Hoshino, Y.; Peng, C.-C. Path Smoothing Techniques in Robot Navigation: State-of-the-Art, Current and Future Challenges. *Sensors* **2018**, *18*, 3170. [CrossRef] [PubMed]
24. Chou, C.-Y.; Juang, C.-F. Navigation of an Autonomous Wheeled Robot in Unknown Environments Based on Evolutionary Fuzzy Control. *Inventions* **2018**, *3*, 3. [CrossRef]
25. Filipescu, A.; Ionescu, D.; Filipescu, A.; Mincă, E.; Simion, G. Multifunctional Technology of Flexible Manufacturing on a Mechatronics Line with IRM and CAS, Ready for Industry 4.0. *Processes* **2021**, *9*, 864. [CrossRef]
26. Tolio, T. *Design of Flexible Production Systems—Methodologies and Tools*; Springer: Berlin, Germany, 2009.
27. Tahri, O.; Chaumette, F. Point-based and region-based image moments for visual servoing of planar objects. *IEEE Trans. Robot.* **2005**, *21*, 1116–1127. [CrossRef]
28. Abuqassem, M.R.M. Simulation and Interfacing of 5 DOF Educational Robot Arm. Master's Thesis, Islamic University of Gaza, Gaza, Palestine, June 2010.
29. Badler, N.I.; Tolani, D. Real-Time Inverse Kinematics of the Human Arm. In *Teleoperators and Virtual Environments*; University of Pennsylvania: Philadelphia, PA, USA, 1996; Volume 5, pp. 393–401. [CrossRef]
30. Spong, W.; Hutchinson, S.; Vidyasagar, M. *Robot Modeling and Control*, 1st ed.; Wiley: Urbana, IL, USA, 2005; pp. 71–93, ISBN 978-0471649908.
31. Kromanis, R.; Forbes, C. A Low-Cost Robotic Camera System for Accurate Collection of Structural Response. *Inventions* **2019**, *4*, 47. [CrossRef]

inventions

Article

Communication and Control of an Assembly, Disassembly and Repair Flexible Manufacturing Technology on a Mechatronics Line Assisted by an Autonomous Robotic System

Dan Ionescu [1,2,*], Adrian Filipescu [1,2], Georgian Simion [1,2], Eugenia Mincă [2,3], Daniela Cernega [1], Răzvan Șolea [1] and Adriana Filipescu [1]

[1] Department of Automation and Electrical Engineering, "Dunărea de Jos" University of Galați, 800008 Galați, Romania; adrian.filipescu@ugal.ro (A.F.); georgian.simion@ugal.ro (G.S.); daniela.cernega@ugal.ro (D.C.); razvan.solea@ugal.ro (R.Ș.); adriana.filipescu@ugal.ro (A.F.)
[2] Doctoral School of Fundamental Sciences and Engineering, "Dunărea de Jos" University of Galați, 800008 Galați, Romania; eugenia.minca@valahia.ro
[3] Department of Automation, Computer Science and Electrical Engineering, "Valahia" University of Târgoviște, 130024 Târgoviște, Romania
* Correspondence: dan.ionescu@ugal.ro; Tel.: +40-764-591-764

Abstract: This paper aims to describe modeling and control in what concerns advanced manufacturing technology running on a flexible assembly, disassembly and repair on a mechatronic line (A/D/RML) assisted by an Autonomous Robotic System (ARS), two robotic manipulators (RM) and visual servoing system (VSS). The A/D/RML consists of a six workstations (WS) mechatronics line (ML) connected to a flexible cell (FC) equipped with a 6-DOF ABB industrial robotic manipulator (IRM) and an ARS used for manipulation and transport. A hybrid communication and control based on programmable logic controller (PLC) architecture is used, which consists of two interconnected systems that feature both distributed and centralized topology, with specific tasks for all the manufacturing stages. Profinet communication link is used to interconnect and control FC and A/D/RML. The paper also discusses how to synchronize data between different field equipment used in the industry and the control systems. Synchronization signals between the master PLC and ARS is performed by means of Modbus TCP protocol and OPC UA. The structure of the ARS consists of a wheeled mobile robot (WMR) with two driving wheels and one free wheel (2DW/1FW) equipped with a 7-DOF RM. Trajectory tracking sliding-mode control (TTSMC) is used to control WMR. The end effector of the ARS RM is equipped with a mobile eye-in-hand VSS technology for the precise positioning of RM to pick and place the workparts in the desired location. Technology operates synchronously with signals from sensors and from the VSS HD camera. If the workpiece does not pass the quality test, the process handles it by transporting back from the end storage unit to the flexible cell where it will be considered for reprocessing, repair or disassembling with the recovery of the dismantled parts. The recovered or replaced components are taken over by the ARS from disassembling location and transported back to the dedicated storage warehouses to be reused in the further assembly processes.

Keywords: programmable logic controller; modbus TCP; open platform communications; visual servoing system; wheeled mobile robot; industrial robotic manipulator

Citation: Ionescu, D.; Filipescu, A.; Simion, G.; Mincă, E.; Cernega, D.; Șolea, R.; Filipescu, A. Communication and Control of an Assembly, Disassembly and Repair Flexible Manufacturing Technology on a Mechatronics Line Assisted by an Autonomous Robotic System. *Inventions* **2022**, *7*, 43. https://doi.org/10.3390/inventions7020043

Academic Editor: Luigi Fortuna

Received: 15 May 2022
Accepted: 10 June 2022
Published: 15 June 2022

Publisher's Note: MDPI stays neutral with regard to jurisdictional claims in published maps and institutional affiliations.

Copyright: © 2022 by the authors. Licensee MDPI, Basel, Switzerland. This article is an open access article distributed under the terms and conditions of the Creative Commons Attribution (CC BY) license (https://creativecommons.org/licenses/by/4.0/).

1. Introduction

The continuous development of software and automation in industrial environments brings new concepts for communication, design and control for manufacturing technology. There is a growing need for high-speed robotic assembly and transport of small parts, which often means higher throughput and greater precision than can be achieved using human labor [1].

This study focused on the implementation, simulation and system design of the hybrid communication and control for the advanced flexible manufacturing technology presented on a laboratory system that integrates several subsystems and different field equipment and autonomous robotic systems (ARSs) [2]. A fully automated assembly line assisted by mobile robots is still in its early stages and is not yet widely used. ARSs are extremely flexible because once the facility map is built, they can travel from one destination to the next, autonomously avoiding obstacles along the way, unlike conveyor systems that have limited flexibility, and are quite expensive and time-consuming to reconfigure [3].

The objective of this research is to introduce a new perspective upon the framework of manufacturing technology design where implementation and setup was based more on engineering experience and less on simulations, investigation and validation methods to increase efficiency and to evaluate the performance of the manufacturing lines assisted by ARS [4].

The main elements of originality and contributions are concentrated in the following areas: task scheduling and assigning; planning and synchronization of A/D/RML assisted by ARS, RMs and VSS; Petri Nets modeling; hardware architecture design of the entire system to allow flexible manufacturing, communication concepts, supervisory control and data acquisition (SCADA) [5]; implementation and network topology, synchronization of signals from sensors and between subsystems, distributed control and image processing for precise positioning; VSS and real-time control for implementation of a fully automated manufacturing technology; improving the automation level; security; and increasing the efficiency by using the ARS IRM with VSS technology [6,7]. The presented flexible manufacturing concept allows the assembly of two different products and complete disassembly or repair of the products depending on the quality test. Disassembled components from the rejected products are recovered by ARS and placed back in the designated storage compartments. The recovery process implementation allows the reuse of the products subcomponents through reprocessing, technology that works automatically, completely independent without the operator intervention, increasing efficiency, productivity and safety [8].

The presented technology for flexible assembly, disassembly and repair with components recovery, consists of an assembly/disassembly mechatronics line (A/D/ML), a flexible cell (FC), which is an assembly/disassembly station with an integrated 6-DOF industrial robotic manipulator (IRM), and an ARS which is a WMR equipped with a 7-DOF RM and an eye-in-hand visual servoing system (VSS) [1,2]. Along with the communication concept and real-time implementation, several aspects will be discussed regarding the design of the flexible manufacturing technology, such as: task planning, hybrid modeling, simulation, sensors and actuators, interoperability between field level devices, synchronization, data acquisition, remote monitoring and control [9].

An assembly/disassembly and repair flexible manufacturing line (A/D/R/ML), consists of the following subsystems: IRMs, WMRs, workstations and manufacturing cells, component storage units, transporting system (conveyor belts) and monitoring, control and data acquisition systems, able to perform specific tasks for manufacturing technology such as product assembly, quality check and repair or disassembly operations with components recovery, including a reconfigurable manner that confers reversibility, repeatability, and last but not least, flexibility [3]. The main idea of flexibility added to a manufacturing line, a FML (Flexible Manufacturing Line), means a technology capable to automatically manufacture different products, in small or medium batches, without adding hardware changes or the complete redesign of the system.

The automatic control of all system components and automatic supervision, controls and diagnosis is performed with the help of two PLCs in a hybrid hardware architecture for controlling all the subsystems of the complete A/D/RML and managing the process and operation facilities, thereby coordinating control tasks as well as synchronizing the operations of the ARS with process timings [10]. On top of that, for controlling assembly/disassembly and repair for the flexible manufacturing line, the algorithm architecture is agent-based control, in which the PLC from the FC station acts as a main control unit, or "master PLC", for centrally managing both subsystems of the complete A/D/RML by means of synchronization and confirmation signals [11]. Therefore, master PLC synchronizes with subsystems PLCs to automate their respective areas and for operating and controlling locally their components, after confirmation from the main control unit is applied.

The presented hardware structure includes two Human-Machine Interfaces (HMI) as operator control panels for both major subsystems (A/D/ML and FC) and a SCADA application running on the Remote PC as the main visualization, control and data acquisition system. The information to perform the flexible manufacturing process tasks is obtained from the system using IO Field Devices such as sensors, cameras, measuring devices and transducers and is processed by the PLCs and interfaced via a communication link with Remote PC or SCADA [5].

Industrial development has been evolving rapidly, bringing new smart technologies to automation systems and becoming more dynamic and adaptable production systems. Visual servoing is a commonly used technology in combination with RM and works by processing and implementing the results obtained from several research fields such as real-time image analysis and processing, robotics, control theory and systems and real-time application design. Therefore, a visual sensor—an HD camera—is connected on the end effector, "the eye" of the RM, which allows the visual inspection and investigation of the working environment without contact with its elements. VSS behavior is mainly influenced by the type of visual features used to generate control law [12]. There are several VSS control architectures corresponding to the servoing systems; in this approach, the Hybrid Visual Servoing (HVS) architecture is used for driving the mobile VSS mounted on the ARS robot manipulator [13,14].

The rest of the paper is organized as follows: the proposed hardware technology of the A/D/RML assisted by ARS is presented in Section 2.1 describing FC, ARS and eye-in-hand VSS control architectures; in Section 2.2, Petri Nets modeling is presented and also task planning and scheduling for each of the flexible manufacturing operation; in Section 2.3, the communication concept of the A/D/RML assisted by ARS is described; real-time control results for assembly, disassembly and repair operations are shown in Section 3; Section 4 provides a vision of the experimental laboratory level A/D/RML assisted by ARS, discusses the real-time control results and highlights the laboratory tests limitations of the study and Section 5 is reserved for final conclusions of the approach from this research paper, draws the main research findings and gives an insight to future directions for research/recommendations.

2. Materials and Methods

2.1. A/D/RML Assisted by ARS Technology

2.1.1. Hardware Structure of A/D/RML

An experimental A/D/RML assisted by ARS is developed at the laboratory level that works in real-time, for testing purposes and for the implementation of different methods and techniques for analyzing, optimizing and manufacturing line balancing, to study the actual technology and improve efficiency, reliability and precision. Figure 1 shows the basic design concept of the A/D/RML, consisting of 3 major subsystems, which operate, communicate and synchronize together by means of PLCs and SCADA and act as a single flexible manufacturing line that performs several tasks such as assembly, the disassembly of 2 different products with reprocessing, repair and components recovery functionality.

The main A/D/RML hardware components are:

- Flexible Cell—separate station with ABB RM IRB120 6-DOF and components storage units used for assembly, disassembly and repair of the workpieces, with handling, processing and transport capability;
- A/DML mechatronics line-based on laboratory mechatronic system Hera&Horstmann, used for the assembly and transport of the workpieces with checking and storage facilities;

- ARS—WMR PeopleBot equipped with an RM Cyton 7-DOF used for recovery, transport and return operations for the dismantled components.

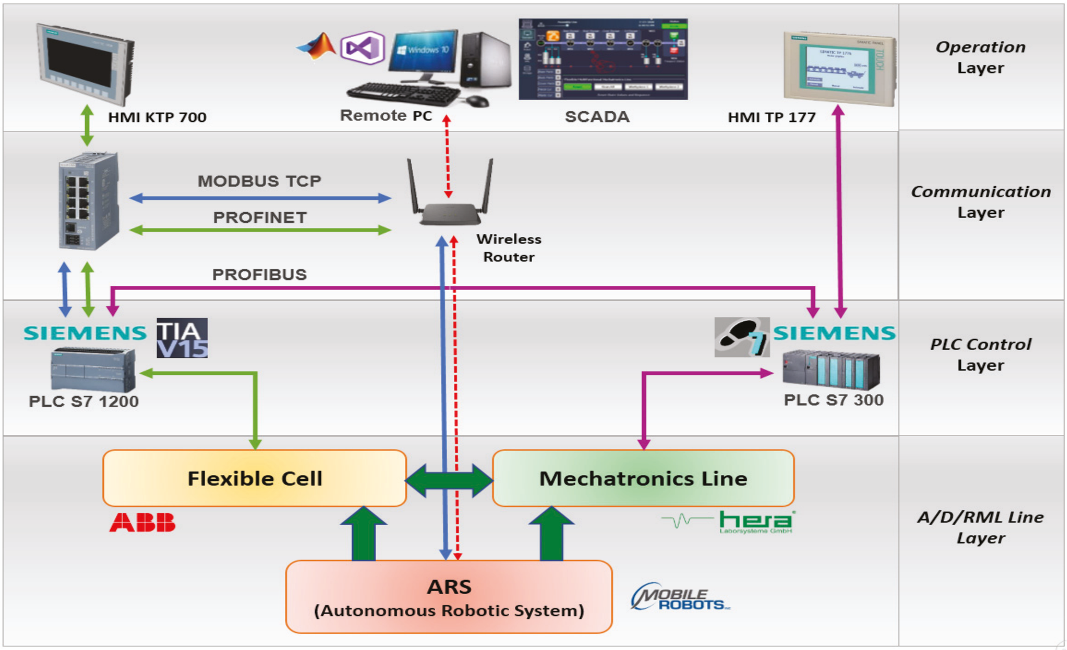

Figure 1. Structure of A/DML Hera&Horstmann and Flexible Cell ABB served by ARS.

The A/D/RML, as described above, is characterized by a modular structure. The hardware structure consists of 2 Siemens PLC controlled subsystems/modules with specific tasks for all the manufacturing operations. FC is a RM pick-and-place station, Siemens S7-1200 PLC controlled assembly/disassembly station, positioned next to mechatronics line, which handles the supply of workparts, assembly and transport for workpiece product type 1 (WP1) on the manufacturing line, acting as a feeding unit and handles the disassembly and repair operation for workpiece product type 2(WP2) upon request. The Hera&Horstmann mechatronics laboratory line is a Siemens S7-300 PLC controlled subsystem that has a predefined role as a logistics unit that assemblies individual workparts into workpiece product type 2(WP2), transports between workstations and stores the assembled workpieces on the final storage place—Storage Rack Tower.

The PLC-based hardware and software design architecture, as seen in Figure 2, is a hybrid structure that features both distributed and centralized topology:

- Distributed structure, by means of separate, individual PLC control for both FC and mechatronics line, to automate their respective areas with visualization and operation facilities;
- Centralized architecture, where the FC station PLC, besides the local control role, acts as "master PLC" for centrally managing both subsystems of the complete A/D/RML, having process and operation facilities, thereby coordinating, controlling and synchronizing the operations tasks with the ARS.

Each PLC hosts several routines for automatic control but the manual, initial task for choosing and starting the manufacturing process operation is made remotely from SCADA or locally from HMIs. The assembly/disassembly and processing/reprocessing routines are managed strictly through Siemens S7-1200 PLC from the FC, which acts as a Central

System that handles visualization and manages the overall operation of the complete A/D/RML [15].

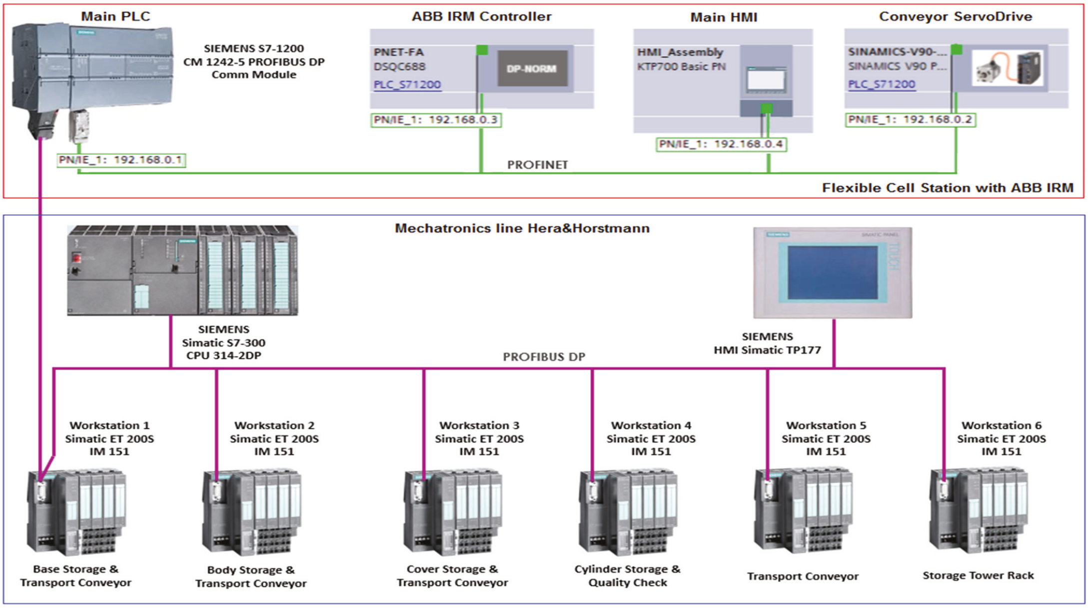

Figure 2. A/D/RML PLC Network hardware structure.

In the mechatronics line, Siemens S7-300 PLC communicates with the I/O field via Profibus (magenta line Figure 2). The Profibus link is used for communicating and the control of the transporting conveyor belts drives, workpiece positioning and PLC to PLC synchronization methods as well as for handshake and signal exchange interface with the FC by means of a Profibus adapter. An additional HMI (Siemens TP 177) is connected for process visualization purposes only. FC communication is based on the industrial Ethernet network Profinet technology (green line Figure 2) for communicating with the main HMI (Siemens KTP 700), ABB IRB120 Robot controller and Intelligent Siemens Servomotor Drives Sinamics V90 with accurate positioning control functionality. The compatibility between the FC and mechatronics line, by means of communication, is performed as mentioned before, via a Profibus adapter to bridge/interconnect the 2 different communication technologies: Profinet (protocol based on the Industrial Ethernet) and Profibus (protocol based on serial communication).

For disassembly or repairing tasks, pick-and-place and transport actions are performed by the ARS with the help of the Cyton RM, which is equipped. First, the FC station with the ABB robot dismantles or repairs the workpiece by replacing the bad components and sliding them on a specific tray. Then, the ARS system will grab the recovered workparts for transporting and place them into the designated storage ML locations. Several synchronization signals will be needed between the master PLC and ARS by means of the Modbus TCP protocol, a standard communications protocol widely used in industrial automation. These signals will be sent when the FC station has ended the repair/disassembly action and the dismantled component (workpart) is released and ready for recovery by the ARS. Synchronization acknowledgment signals will be returned when ARS is busy handling a task such as reprocessing/transport or when placing operation job is completed and ARS becomes available again.

For the developed technology, at the PLC level, several algorithms have been developed by using Siemens programming packages such as TIA Portal, Step7 Manager, as well as WinCC Flexible for the HMIs. SCADA is developed on the Remote PC and also in TIA Portal. In both PLCs, modular programming is used; functions or function blocks are created as an entity, providing a particular functionality or controlling a particular type of device in the system (ABB Robot, conveyors motors, storage, electrical and pneumatic actuators). During each scan, the PLC reads all local and remote inputs, executes every function in a predefined order (using IRQ) and updates all outputs at the end of each scan. PLC programs and algorithms are mainly programmed with Structured Text (ST) or Structured Control Language (SCL) which, according Siemens, corresponds to the IEC 1131-3 language "ST". SCL opens up several new constructs that are unavailable while programming in conventional ladder logic, including the FOR and WHILE loops as well as the CASE statement. These are particularly useful when dealing with large amounts of data in an array form. Using SCL also increases the readability of any sort of arithmetic calculation. The instances of Function Blocks are executed in the cyclical order in every PLC scan (10–12 msec time range). An additional part of the PLC program is the Modbus TCP link between master PLC from the FC station (S7-1200 PLC) and ARS. For that a Modbus TCP Server is configured and programmed, as shown in Section 2.3.3, in the Main Routine of the Siemens master PLC at the beginning of the scan, prior to the program execution, to establish and maintain a stable connection and a quick data exchange/synchronization signals with the ARS.

As shown in Figure 2, a separate Profibus communication link is used to interface data between both PLCs. This data must be sent and received between the master PLC and Siemens S7-300 PLC via the Profibus communication adapter.

2.1.2. Flexible Cell with ABB RM

Flexible Cell (Figure 3) is an Integrated ABB iRB120-Robot Training Station that consists of the following major components:

- RM ABB IRB120 6-DOF, with electric gripper;
- PLC Siemens S7-1200 series, CPU 1214C;
- HMI Siemens KTP700, Color Basic PN;
- Switch Siemens, SCALANCE XB005;
- Conveyor Belt, Sinamics V90 Servo Drive;
- Compact stack storage units for each workpiece component (*S1 to *S4);
- Unloading trays for workpiece component disassembly (*WH1 to *WH5).

The communication link is made with Profinet, protocol standardized in IEC 61158 and IEC 61784, which uses traditional Ethernet hardware and software to define a network that structures the task of exchanging data with PLC and all the above-mentioned devices. For the FC hardware structure, the following profiles are applicable:

- Profinet-IO, interconnecting the PROFINET device with any other fieldbus or industrial Ethernet network. Uses cyclic data transfer to exchange data between PLC over Ethernet with HMI, PLC CPU and ABB Robot Controller;
- PROFI drive, implemented for drives application scenarios, used in FC station to control the conveyor belt with Sinamics V90 Servo Drive.

ABB Robot Controller has the hardware capability to communicate with third party devices via Profinet protocol by means of a dedicated board AnybusCC Profinet slave (DSQC 688) on the ABB Robot Controller DSQC1000 (main computer) (Figure 4). With the Profinet Anybus Device option, the ABB IRM controller can act as a slave on the Profinet network.

2.1.3. Mechatronics Line Hera&Horstmann

The laboratory mechatronics flexible line, from Hera&Horstmann (Figure 5), incorporates five individual workstations with different tasks; each of them handle the line operations in different stages of the manufacturing process such as handling and transporting on conveyor belts, loading and processing workparts with pneumatic workstations, sorting and testing products and storage in the dedicated warehouse unit.

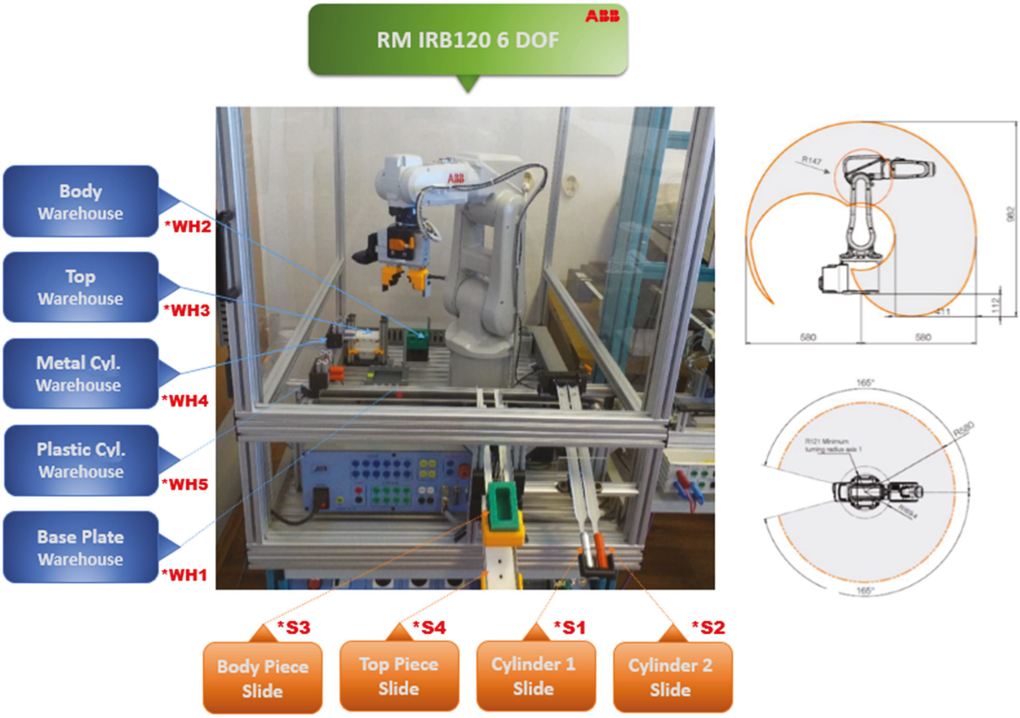

Figure 3. Flexible Cell Station with RM ABB IRB120 6-DOF.

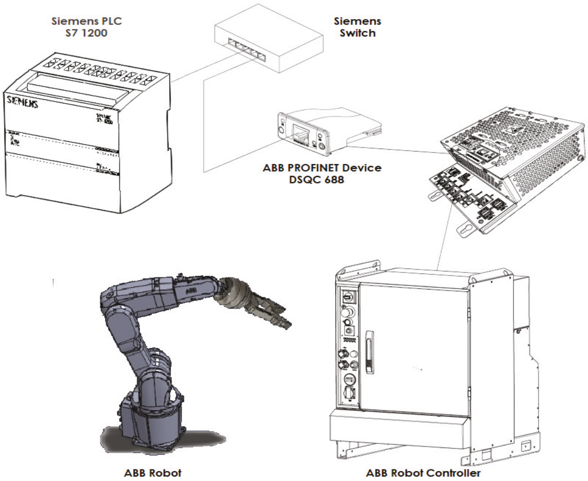

Figure 4. Profinet communication link between Siemens S7-1200 PLC and ABB Robot Controller.

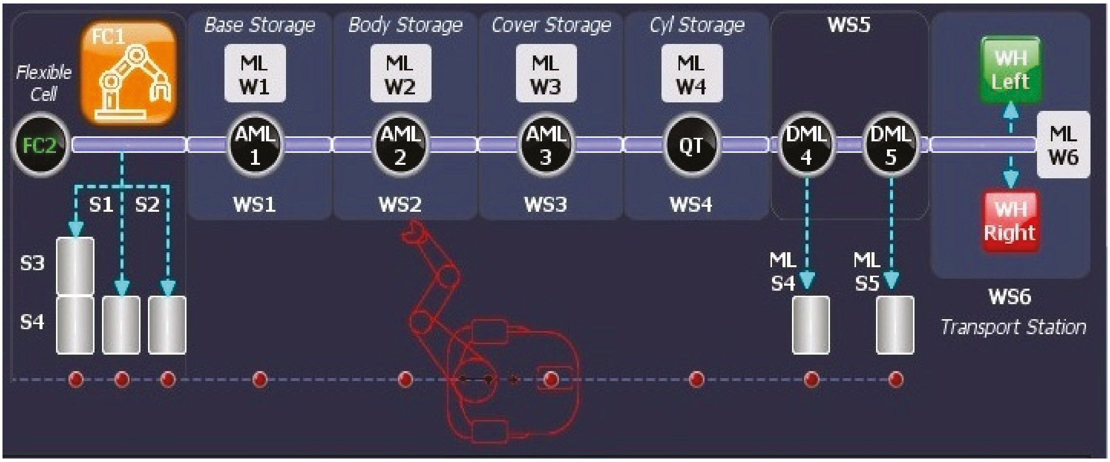

Figure 5. Hera&Horstman assembly/disassembly mechatronics line.

The five-part workpiece enables the complete manufacturing process workflow operations such as assembly, testing, sorting, storage and disassembling. The workparts/components to be assembled into a single product are shown in Figure 6: workpart carrier (base platform), body, top or cover, metal cylinder and plastic cylinder. A/D/RML is a flexible manufacturing line by adding the capability of handling and processing batches of two different products, referred to as workpiece type 1 (WP1) and workpiece type 2 (WP2). WP1 is the workpiece with the triangular edges top part (Figure 6) and is assembled in the FC by ABB IRM. WP2 is the workpiece with round edges, top part (Figure 7a–c), and is assembled on the Hera&Horstmann ML.

The hardware structure of the ML presented on Figure 2 is based on a PLC distributed architecture, integrating the process peripherals such as signals and function modules in Remote I/O stations on the Profibus network, and consists of a Siemens Simatic S7-300 series PLC, processor type CP 314C-2 DP and Siemens CP 343-2 communication module for Profibus link.

Profibus DP interface uses predefined speed up to 12 Mbit/s and connects all 5 workstations and Storage Tower Rack, referred to as Workstation 6, through Remote IO's (Siemens ET200S communication modules), which improves adaptability and execution performance for the flexible assembly/disassembly technology framework inside this decentralized architecture design.

2.1.4. Hardware Structure of the ARS

A/D/RML is served by an ARS, used for the recovery and transport/return operation of the dismantled components, which is a RM-equipped WMR. The ARS, shown in Figure 8, is composed of the following elements:

- 7-DOF Cyton 1500 RM equipped with an eye-in-hand VSS using a high-definition camera, both are connected to the Remote PC via Wi-Fi USB and synchronously communicating with the A/D/RML over Wi-Fi;
- WMR PeopleBot, which is a WMR with two driving wheels and one free wheel (2DW/1FW).

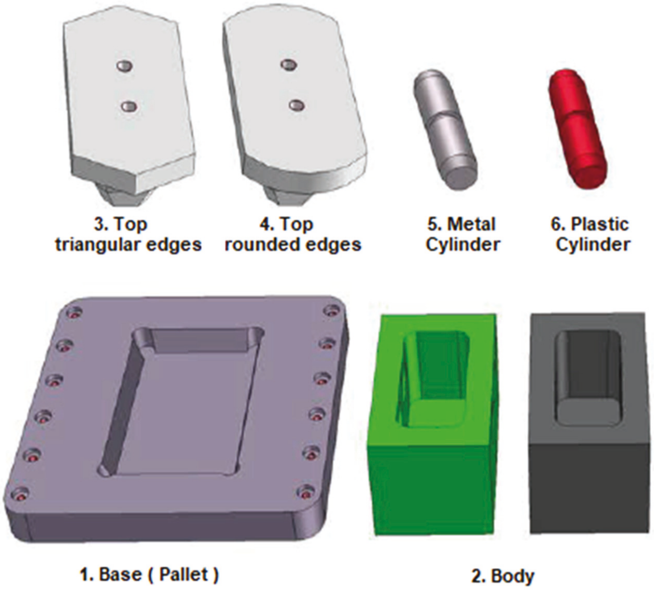

Figure 6. Five-part workpiece components.

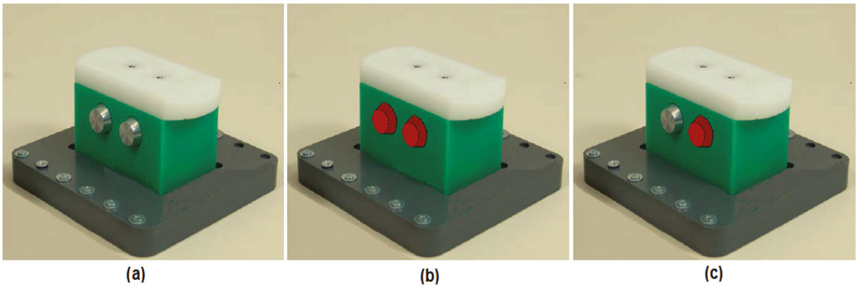

Figure 7. Assembled workpieces: (**a**) workpiece with metal cylinders; (**b**) workpiece with plastic cylinders and (**c**) workpiece with different cylinders.

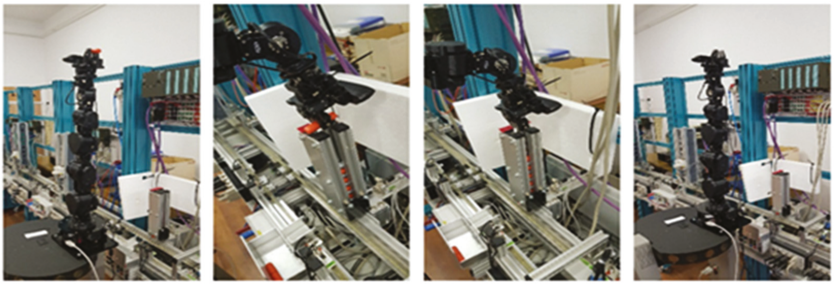

Figure 8. Real-time control of the ARS with RM Cyton.

The ARS is used to pick-and-place the recovered pieces with the help of Cyton 1500 RM in the appropriate storage depots if the assembled workpiece has failed the quality test and has been disassembled or repaired. The control of the ARS is carried out wirelessly using a router that is placed inside the WMR through dedicated functions from Mobile Robots ARIA (Advanced Robotic Interface for Applications), running on the same Remote PC where Cyton RM is connected to.

2.1.5. Eye-in-Hand VSS

In case workparts should be recuperated from the processed bad products, in disassembly and repair, synchronized tasks for pick-and-place actions are executed by ARS by grabbing the recovered dismantled components from the FC station trays. Therefore, ARS is equipped with an RM Cyton 7-DOF (degrees of freedom) with a gripper paddle and HD video camera on the end effector (Figure 8), connected both via Wi-Fi USB with the Remote PC.

For the moving and manipulation of the RM Cyton 7-DOF, signals from gripper video camera are processed, using eye-in-hand VSS technology. RM Cyton, ARS, HD camera and workparts (in this case, cylinders to be recovered) are shown in Figure 8. The eye-in-hand VSS is a system where the HD camera sensor is placed on the last link of the RM, also known as the end effector [1,2,12]. For this type of VSS, real-time computer vision information is processed with OpenCV on the Remote PC to control the motion of the robot in the workspace [16,17]. The objects tracking and the robots positioning are achieved using the comparison between the current visual features, extracted from the images captured by the camera, and the desired visual features. The obtained difference is used to minimize the error the actual configuration of the visual features, the real and the desired features extracted by the video sensor. VSS technology can make robots "smarter" and help to expand their fields of application. Rotational motions influence global image features, translating movements of the end effector result in movements in the eye-in-hand image. Therefore, image moments for the object detection algorithm are used in the Robot Vision fields due to its simplicity and efficiency in implementation. The image moments contain information about the target, the object to be handled, during the positioning task. Thus, ARS localizes and identifies defined objects in advance and decides by itself how to move the WMR on the spot and how to grip the respective part from the FC station trays.

2.2. Modeling the A/D/RML Assisted by ARS

The assembly, disassembly and repair automatic operations can be split up into a logical sequence of basic operational tasks, as seen in the figures below, algorithms that run parallel and synchronized with ARS transportation and positioning tasks assignments along the A/D/RML process. The technology on A/D/RML assisted by ARS and eye-in-hand VSS's basic design approach depends on aspects such as operation modes, operation lengths, distances and manufactured product types [3,5,6]. External events will be interfaced for synchronization between ARS and VSS. Therefore, prior to task scheduling, some assumptions have to be made for FC, A/DML, ARS and VSS in order to control the whole system. For each of the above-mentioned operations, a separate task scheduling strategy has been implemented. The hybrid aspect of the model (A/D/RML assisted by ARS) is given by the continuous aspect, variables associated with the distances covered by the movement of the ARS [2,18,19].

2.2.1. Assembly Process Task Planning

The A/D/RML, as seen in Figure 9, due to the flexibility characteristic, can assemble and process two different products, referred to as workpiece type 1 (WP1) and workpiece type 2 (WP2). WP1 is the workpiece with the top part having triangular edges (Figure 6) and is assembled in the FC station with the ABB IRM. WP2 is the workpiece with top part having round edges (Figure 7a–c) and is assembled on the Hera&Horstmann ML.

The assembly of WP1 is made by the ABB IRM from the FC, picking and placing components in the right order (Figure 6): Base, Body, Top and two cylinders: metal type. Finally, WP1 moves along the Hera&Horstmann ML and is stored on the left side of the

WS6—this product is always considered to be good, with no quality check to perform, although HMI allows operator selection for assembly between plastic and metal cylinders.

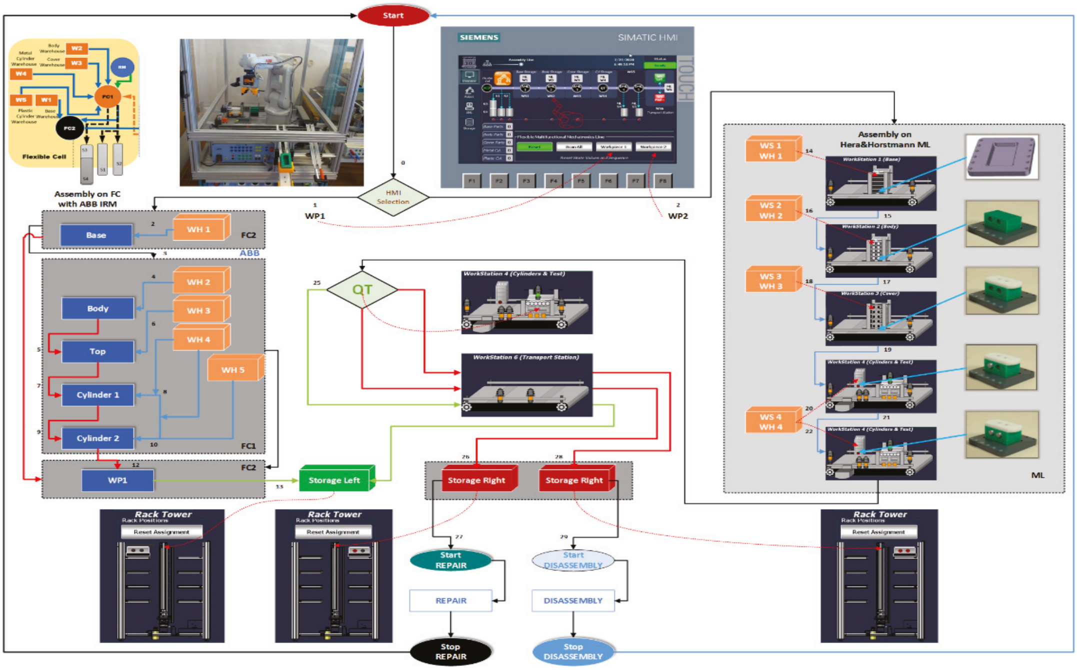

Figure 9. Assembly task planning.

The WP2 product is assembled with randomly picked cylinders and is subjected to the quality test (in mechatronics line, WS4 location, inductive proximity sensor for detecting metal cylinder). To evaluate the quality for the WP2 product, the convention is that an assembled product with both metal cylinders, it is considered of good quality and it is stored on the left side of the WS6 station. The WP2 product that contains both plastic cylinders (Figure 7b) is considered a bad product, unrepairable, and it is stored on the right of the WS6 station. This WP2 will be disassembled for component recovery. The WP2 product with different cylinder types (Figure 7c) is also stored on the right side of the Storage Rack and it will be repaired by replacing the plastic cylinder with a metal one.

2.2.2. Disassembly Process Task Planning

WP2 considered as scrap (two plastic cylinders, Figure 7b) is picked by the WS6 elevator and positioned and transported by the Hera&Horstmann ML back to the FC. The ABB IRM disassembles components in the established order: Cylinder 1 (left), Cylinder 2 (right) and Top and Body, letting them slide on the corresponding trays. The Base is transported back to ML WS1, where the piston pushes it into the storage warehouse. ARS takes over by grabbing each released component in order and transporting it to the appropriate storage on the Hera&Horstmann ML. The complete process of disassembly WP2 with recovering components is presented in Figure 10.

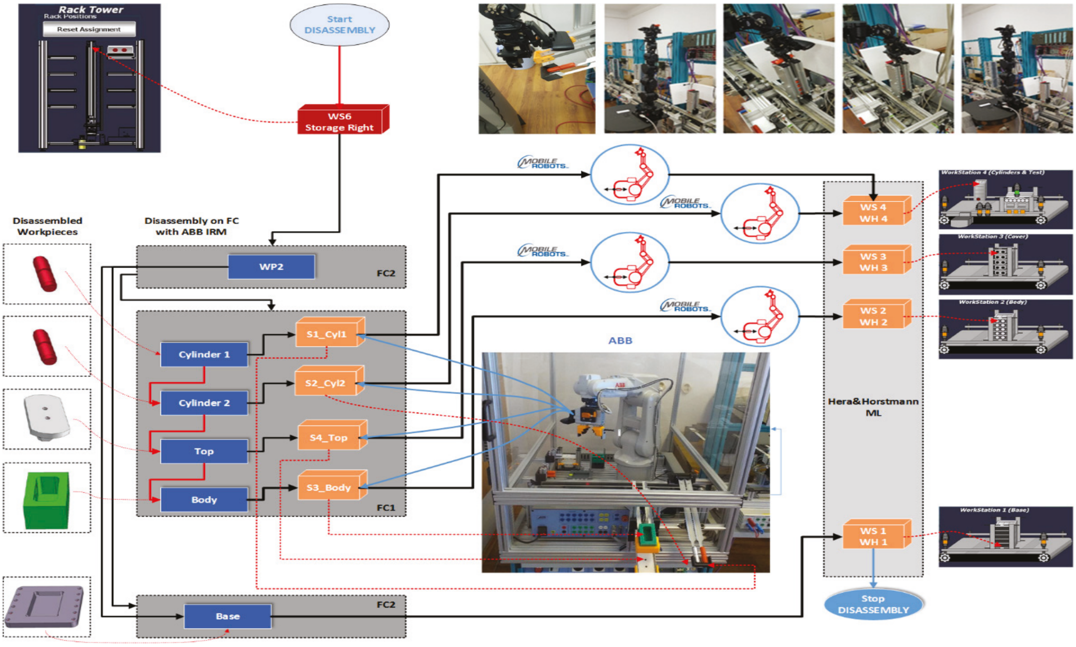

Figure 10. Disassembly task planning.

2.2.3. Repair Process Task Planning

When the assembled workpiece WP2 does not pass the quality test, the process handles it by transporting back from the storage unit (WS6 Storage Rack) to the FC where it will be considered for reprocessing, repair or disassembling—depending on the cylinder types (Figure 7). For repairing process (Figure 11) task scheduling consists of the following tasks:

- Process the WS6 FIFO stack of WP2 with failed quality test—bad product but recoverable (can be repaired);
- Transporting back the workpiece from the Storage Tower Rack to the FC. WP2, having cylinders of different materials (Figure 7c), is taken over by the WS6 elevator and positioned on WS5. It is transported along the Hera&Horstmann ML to the FC;
- The bad cylinder is processed in FC according to the quality state. The ABB IRM disassembles the plastic cylinder, letting it slide on the dedicated external tray compartment and replaces it with a metal one;
- Disassembled component is recovered by ARS. The recovered or replaced cylinder is picked by the ARS RM from disassembling the location tray;
- From this position, ARS handles the recovered plastic cylinder by transporting to the appropriate storage depot from Hera&Horstmann ML to be reused in the further assembly process.
- WP2, now having both metal cylinders, is a good quality product; it is transported from FC along the Hera&Horstmann ML to the WS6 station left side rack.

It is important to mention the following assumption: when on A/D/RML, there is a large volume for assembling, and at a certain moment due to the quality check stage, a bad workpiece may be detected; the repair or disassembly process has priority, so assembly is stopped until the bad workpiece is completely reprocessed. After that, assembly process is restarted for that volume of workpieces from the moment of stopping.

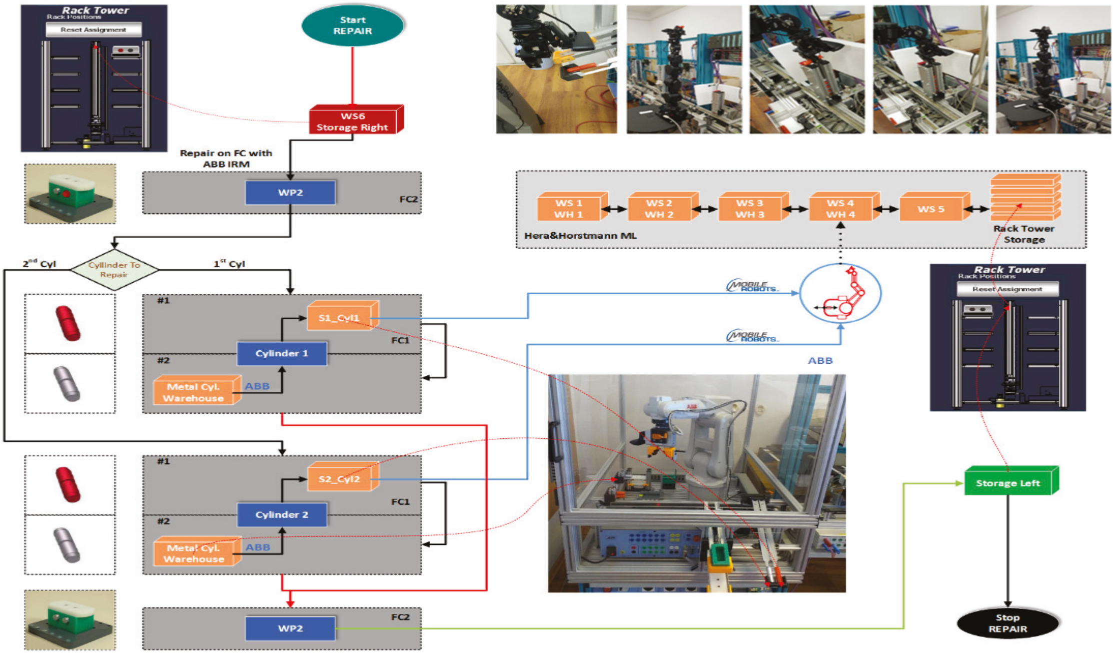

Figure 11. Repair task planning.

2.2.4. SHPN Model Structure and Simulation

The hybrid aspect of the model is determined by variables related to distances travelled by the ARS. These distances are considered between places where disassembly occurs and places where storage warehouses are located. These variables vary according to whether speed is constant or variable, a variation based on the ARS speed between A/D/RML locations. To develop a global assembly and/or disassembly model, we shall consider the hybrid aspect of the assembly/disassembly/repair process served by the platform. For modeling, we shall use Synchronized Hybrid Petri Nets (SHPN) [20], which integrates the discrete appearance of the assembly/disassembly process with the continuous appearance of moving of the WMR and components handling by the RM. The entire model is SHPN type as it is interfaced with external events for synchronization in a modeling/simulation approach useful prior to real-time control. SHPN morphology results in the integration of two PN models, each of which has a specific typology: SPN (Synchronized PN) and SHPN (Synchronized Hybrid PN). The simulation of the SHPN model (non-autonomous HPN model) is used to make and check the compatibility of the discrete dynamics of the ML with the continuous dynamics of the ARS and to be able perform together, synchronized without conflicts. The SHPN overall structure and the SHPN representation by modeling assembly, disassembly and repair operations for 2 different types of products (WP1 and WP2), performed by ARS equipped with RM, is shown in Figure 12.

These models describe the following automatic operations:

- Flexible assembly and storage of 2 different product types (SPN typology);
- Repair products and recover components (SHPN typology);
- Total disassembly of damaged products (SHPN typology).

Based on the SHPN model (Figure 13), Sirphyco simulation results for continuous and discrete places associated with displacements of ARS and FC with IRM are shown in Figures 14 and 15. PN Transitions, task scheduling presentation and steps for disassembly and repair operations on A/D/RML assisted by ARS are shown in Figures 16–18.

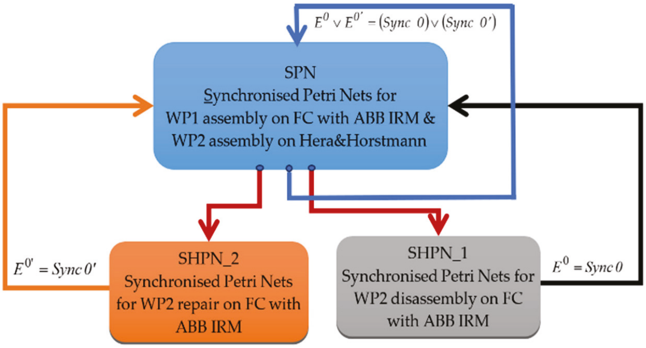

Figure 12. Synchronization and integration of SHPN Model.

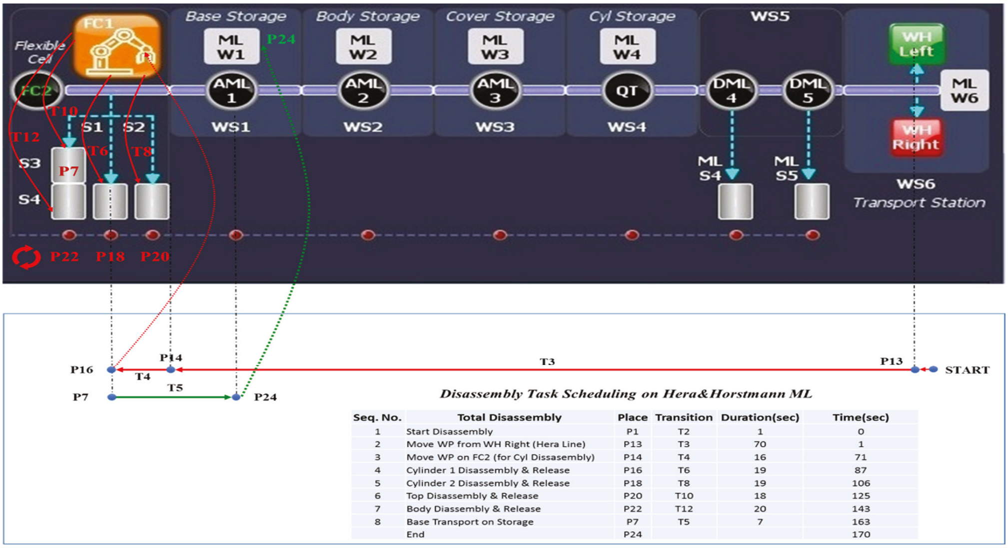

Disassembly Task Scheduling on Hera&Horstmann ML

Seq. No.	Total Disassembly	Place	Transition	Duration(sec)	Time(sec)
1	Start Disassembly	P1	T2	1	0
2	Move WP from WH Right (Hera Line)	P13	T3	70	1
3	Move WP on FC2 (for Cyl Dissasembly)	P14	T4	16	71
4	Cylinder 1 Disassembly & Release	P16	T6	19	87
5	Cylinder 2 Disassembly & Release	P18	T8	19	106
6	Top Disassembly & Release	P20	T10	18	125
7	Body Diassembly & Release	P22	T12	20	143
8	Base Transport on Storage	P7	T5	7	163
	End	P24			170

Figure 13. Task scheduling for disassembly operation on Hera&Horstmann ML.

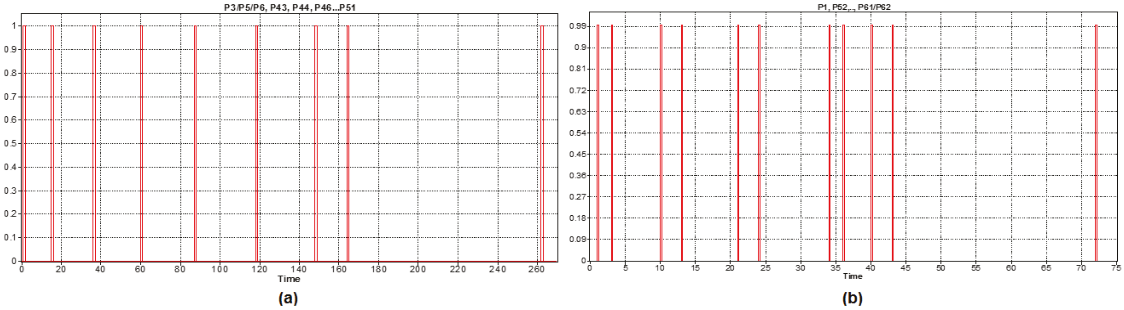

Figure 14. Monitoring signals for assembly operation steps from PN Sirphyco simulation: (**a**) WP 1, (**b**) WP 2.

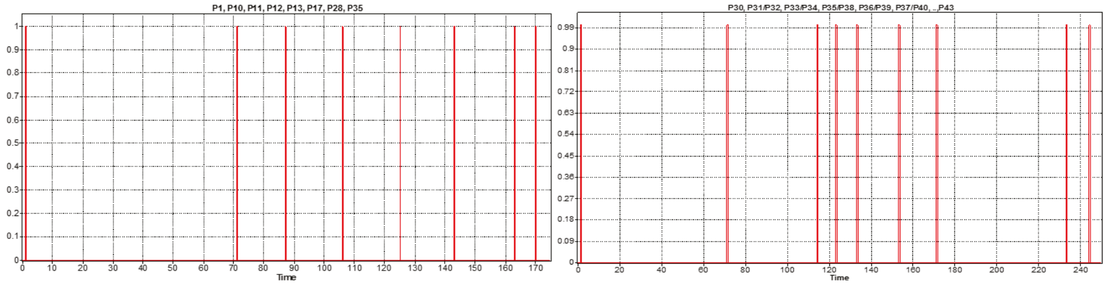

(a) (b)

Figure 15. Monitoring signals in PN Sirphyco simulation: (**a**) disassembly WP2, (**b**) repair WP2.

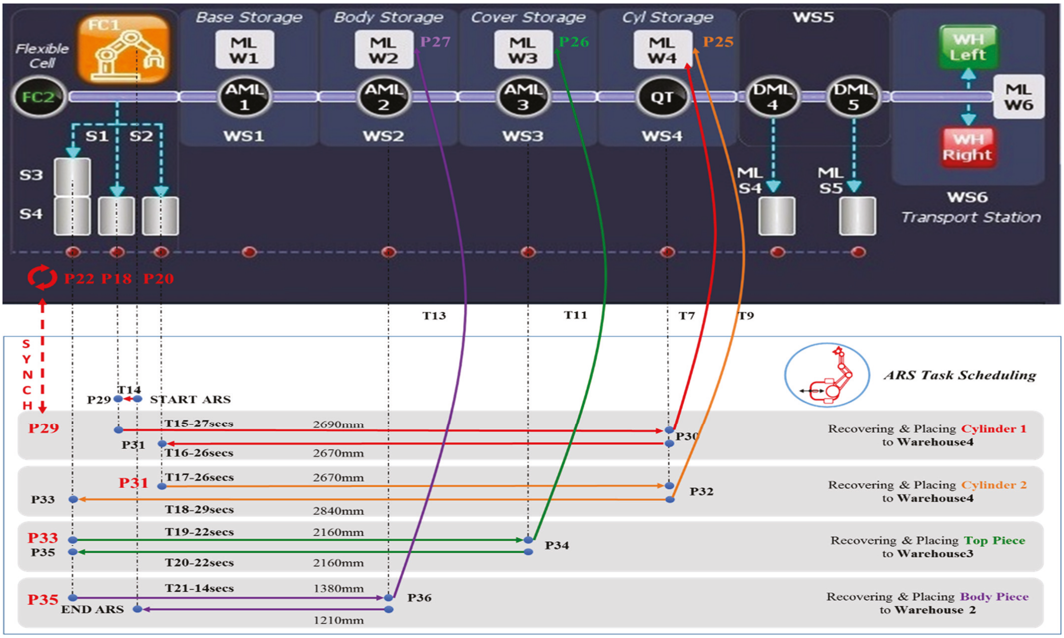

Figure 16. ARS task scheduling for disassembly operation.

2.3. Communication, Synchronization and Control Architecture of Multifunctional Flexible Manufacturing Technology

2.3.1. A/D/RML Control Architecture and Network Topology

SCADA (Supervisory Control And Data Acquisition) systems are used in industrial settings to monitor and control field devices from a distance remotely.

The complete structure of the A/DML real-time control served by ARS is shown in Figure 19. The presented control strategy is a hybrid structure, which consists of two interconnected systems, that features both distributed and centralized topology, with specific tasks for all the manufacturing stages. Moreover, for sequence control and synchronizing of all the routines of the manufacturing line, the control algorithm architecture is agent-based type, managed strictly through Siemens S7-1200 PLC from the FC, which acts as a Central System communicating with all subsystems' PLCs to control the complete manufacturing process by means of signal interface for sending and acknowledging commands or actions. In this control setup, every subsystem or slave from the presented technology of A/D/RML assisted by ARS is considered to be an agent, which includes a separate control, managed by a local agent software synchronized with the master PLC [11].

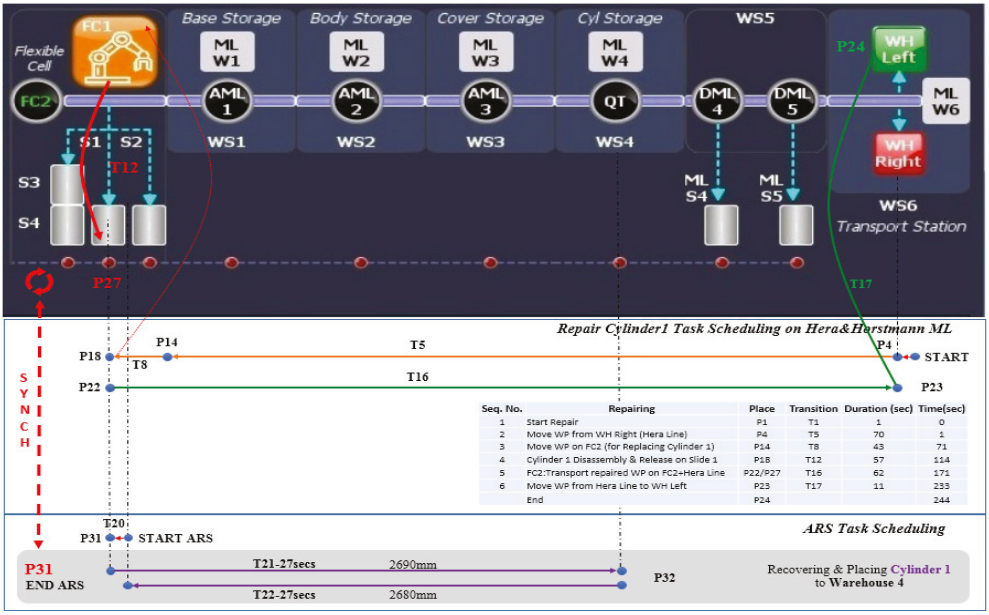

Seq. No.	Repairing	Place	Transition	Duration (sec)	Time(sec)
1	Start Repair	P1	T1	1	0
2	Move WP from WH Right (Hera Line)	P4	T5	70	1
3	Move WP on FC2 (for Replacing Cylinder 1)	P14	T8	43	71
4	Cylinder 1 Disassembly & Release on Slide 1	P18	T12	57	114
5	FC2:Transport repaired WP on FC2+Hera Line	P22/P27	T16	62	171
6	Move WP from Hera Line to WH Left	P23	T17	11	233
	End	P24			244

Figure 17. ARS task scheduling for repair/replace Cylinder 1.

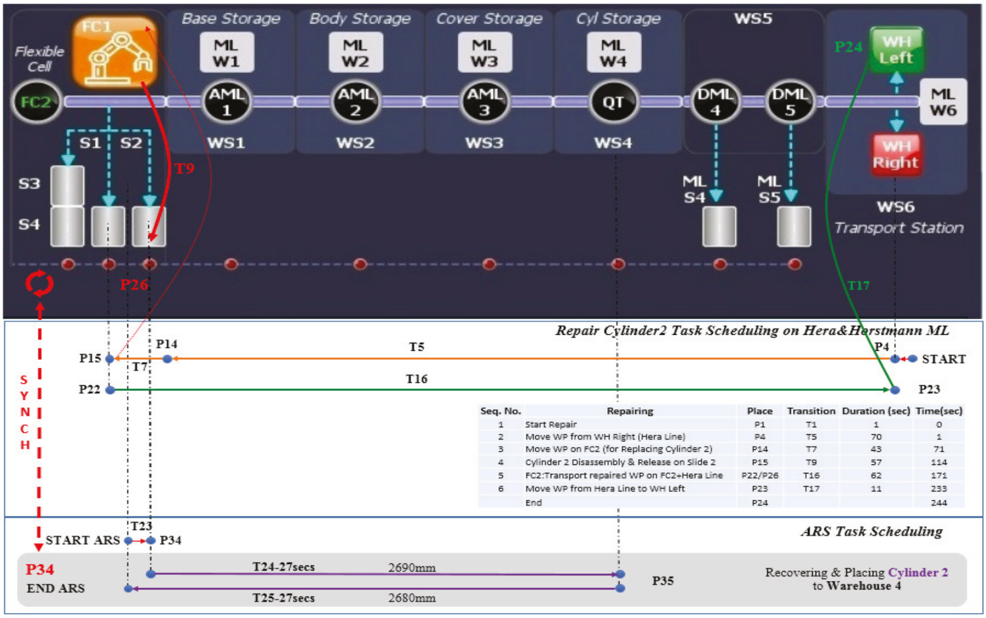

Seq. No.	Repairing	Place	Transition	Duration (sec)	Time(sec)
1	Start Repair	P1	T1	1	0
2	Move WP from WH Right (Hera Line)	P4	T5	70	1
3	Move WP on FC2 (for Replacing Cylinder 2)	P14	T7	43	71
4	Cylinder 2 Disassembly & Release on Slide 2	P15	T9	57	114
5	FC2:Transport repaired WP on FC2+Hera Line	P22/P26	T16	62	171
6	Move WP from Hera Line to WH Left	P23	T17	11	233
	End	P24			244

Figure 18. ARS task scheduling for repair/replace Cylinder 2.

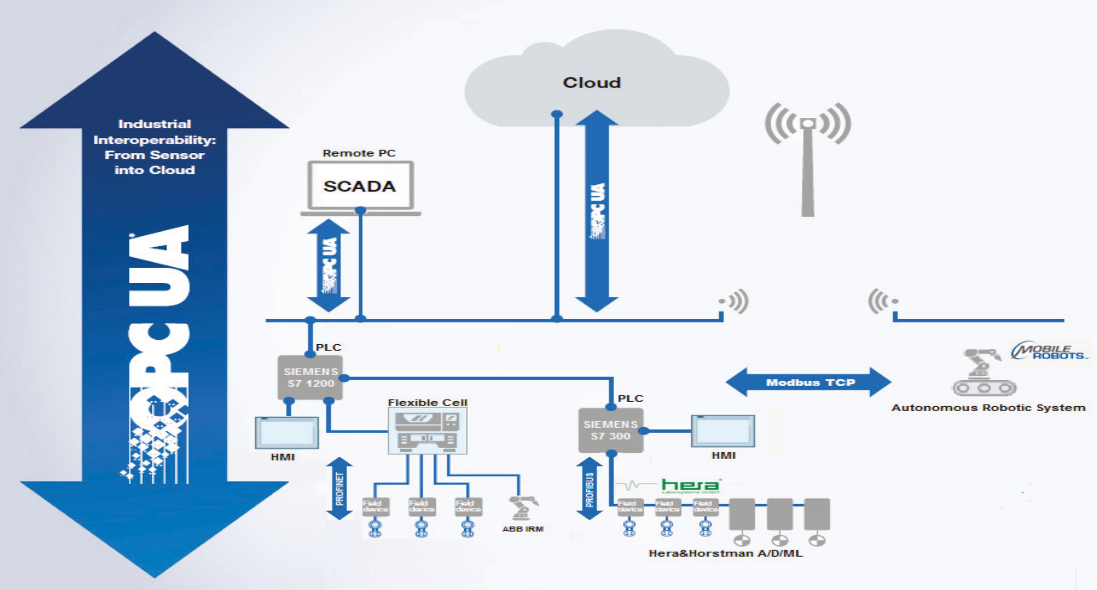

Figure 19. Control structure of A/DML Hera&Horstmann and Flexible Cell ABB served by ARS.

Using SCADA system (Figure 20) along with both HMI's functionality (Figure 21) for controlling, real-time monitoring and visualizing the A/D/RML complete process, it integrates the following major functions:

- Data acquisition, to monitor and control all IO field-sensors from the lower layer of the automation process architecture, conveyor belt sensors, proximity sensors and speed sensors;
- Data communication, involving monitoring the automation process and interacting with all the devices/sensors from a single location via a communications network to bring remotely data from A/D/RML and ARS. A communication adapter (Figure 2) Siemens CM 1242-5 attached to S7-1200 PLC is used for connecting the newer generation Siemens master PLC from FC via the Profibus link to the mechatronics line. This module is used to connect and integrate SIMATIC S7-1200 into an automation solution as a Profibus DP slave. The CM 1242-5 works as a DPV1 slave in accordance with IEC 61158, handles data traffic completely autonomously and thus relieves the CPU of communication tasks. This communication module operates at two levels, the physical layer and data link layer, converting and regenerating the signal it receives or sends and supports cyclic communication for the transfer of process data between Profibus DP slaves and DP master (Mechatronics Line S7-300 PLC). Cyclic communication is handled by the operating system of the PLC;
- Data presentation display information in human readable format in the GUI, suitable for operator needs for easy control and fast response in case of alarms, a solution implemented for both the mechatronics line as well for the ARS and FC (see Figure 21);
- Control the field devices remotely, pending outputs and synchronization commands from SCADA Remote PC and transmitted via the network, improving operator and ARS fast actions and making a quick decision.

2.3.2. ARS Control Input Design

In this approach, the mobile part of the A/D/RML, referred to as ARS with PeopleBot WMR from Mobile Robots, will be used and has an odometric system, two driving wheels and one rear freewheel. Additionally, an onboard embedded microcontroller is able to read the position information and send it, via WI–FI link, to a Remote PC according to a specific protocol. The SCADA application from the Remote PC computes the control input and sends it to WMR. Additionally, the Remote PC sends the data to the A/D/RML PLCs [21,22]. For controlling the ARS and WMR movements between the parking/grabbing and placing positions, dedicated functions from the ARIA (Advanced Robotic Interface for Applications) programming package are used and the TTSMC algorithm is implemented [23–26].

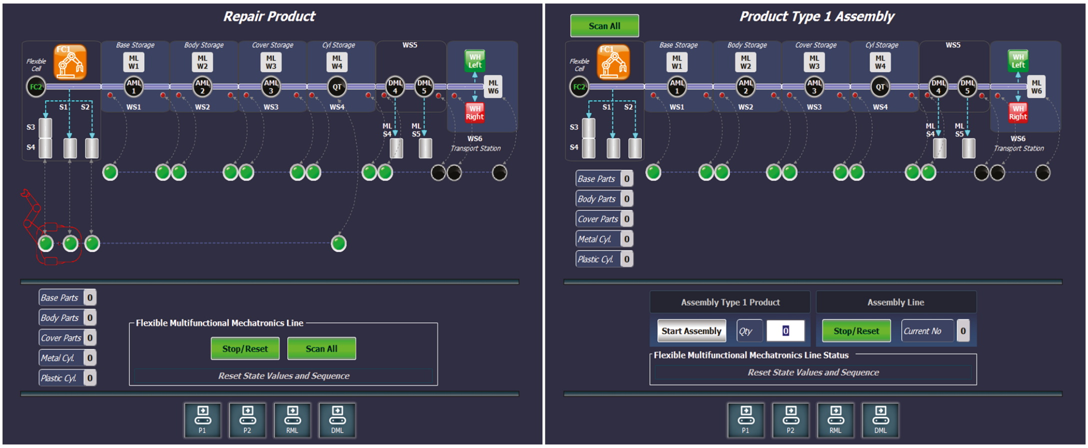

Figure 20. SCADA with Siemens TIA implementation for A/D/RML.

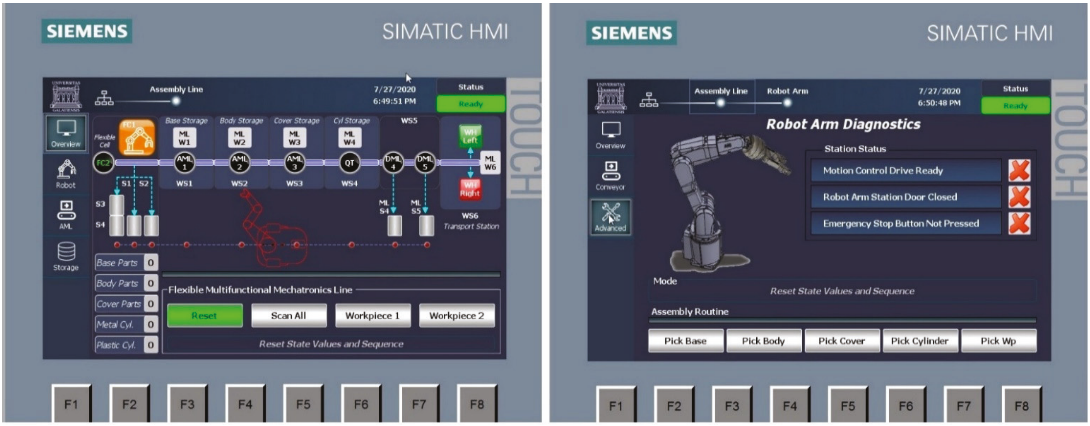

Figure 21. Control and visualization of A/D/RML via Siemens HMI (KTP700).

The ARS is equipped with 7-DOF Cyton 1500 RM and eye-in-hand VSS for picking up the dismantled workpieces from the FC trays in the case of a repair/disassembly process and transporting them to their proper storage warehouses. The control of the ARS is based on 3 control loops:

- Control loop for the synchronization commands between Main PLC and ARS Cyton RM using Modbus TCP signals (Figure 22). As designed, the communication link between the Cyton RM and the Remote PC is performed wirelessly using a USB over Ethernet adapter and a specific TCP/IP protocol;

- Eye-in-hand VSS algorithm, for the Cyton RM, handled wirelessly by Remote PC, for precise robot pick-and-place operations [27]. Cyton RM eye-in-hand VSS control algorithm has been realized using the open-source OpenCV library specialized in image processing;
- ARS WMR control algorithm, for moving the grabbed recovered workparts from the FC and place them on the dedicated storage units on ML, is based on TTSMC [28] with functions from Aria Mobile Robots. Communication with the FC is performed wirelessly using TCP/IP protocol.

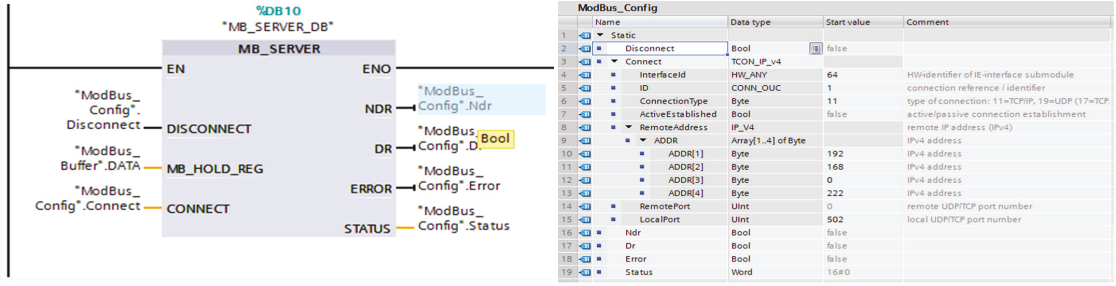

ModBus_Config

	Name	Data type	Start value	Comment
1	Static			
2	Disconnect	Bool	false	
3	Connect	TCON_IP_v4		
4	InterfaceId	HW_ANY	64	HW-identifier of IE-interface submodule
5	ID	CONN_OUC	1	connection reference / identifier
6	ConnectionType	Byte	11	type of connection: 11=TCP/IP, 19=UDP (17=TCP
7	ActiveEstablished	Bool	false	active/passive connection establishment
8	RemoteAddress	IP_V4		remote IP address (IPv4)
9	ADDR	Array[1..4] of Byte		IPv4 address
10	ADDR[1]	Byte	192	IPv4 address
11	ADDR[2]	Byte	168	IPv4 address
12	ADDR[3]	Byte	0	IPv4 address
13	ADDR[4]	Byte	222	IPv4 address
14	RemotePort	UInt	0	remote UDP/TCP port number
15	LocalPort	UInt	502	local UDP/TCP port number
16	Ndr	Bool	false	
17	Dr	Bool	false	
18	Error	Bool	false	
19	Status	Word	16#0	

Figure 22. Siemens Modbus Server configuration in Main PLC.

All three control loops communicate through Remote PC, which also acts as a SCADA server and controls the ARS, eye-in-hand VSS and Cyton 1500 RM and manages the synchronization with the FC, ML and the coordination between them.

2.3.3. Communication and Synchronization between A/D/RML and ARS

As mentioned before, centralized architecture is used, where the Main PLC (Siemens S7 1200) acts as the master PLC and synchronizes the operation with the ARS, which handles the recovering process. The communication between master PLC (Flexible Cell S7-1200 PLC) and ARS is conducted via a Modbus TCP link (Figure 22).

The Modbus protocol was developed in 1979 by Modicon, Incorporated, for industrial automation systems, and it became an industry standard method for the transfer of discrete and analog I/O information and register data between industrial control and monitoring devices. Modbus TCP/IP shares the same physical and data link layers as the traditional IEEE 802.3 Ethernet and uses the same TCP/IP suite of protocols. Therefore, it remains fully compatible with the already installed Ethernet infrastructure of cables, connectors and network-related devices. Unlike traditional Ethernet, which was not considered a viable fieldbus for industrial control, Modbus itself is an a deterministic industrial application protocol, as it defines rules for organizing and interpreting data, but remains simply a messaging structure, independent of the underlying physical layer, and every message is sent or received in a finite and predictable amount of time. Modbus devices communicate using a master–slave (client–server) technique in which only one device (the master/client) can initiate transactions (called queries). The other devices (slaves/servers) respond by supplying the requested data to the master or by taking the action requested in the query. A master's query will consist of a slave address (or broadcast address), a function code defining the requested action, any required data and an error checking field. A slave's response consists of fields confirming the action taken, any data to be returned and an error checking field. Note that the query and response both include a device address, a function code, plus applicable data and an error checking field. A Modbus map is required to know how to interpret the data that is returned. Because TCP is a connection-oriented protocol, a TCP connection must first be established before a message can be sent via Modbus TCP/IP. Following the client–server principle, this connection is established by the client (master). This connection can be handled explicitly by the client user-application software or automatically by the client TCP connection manager. More commonly, this is handled automatically by the client protocol software via the TCP socket interface, and this operation remains transparent to the application. All Modbus TCP/IP message connections are point-to-point communication paths between two devices, which require a source address, a destination address and a connection ID in each direction. Thus, Modbus TCP/IP communication is restricted to unicast messages only. The well-known port 502 has been specifically reserved for Modbus applications. A Modbus server will listen for communication on port 502. When a Modbus client wants to send a message to a remote Modbus server, it opens a connection with remote port 502. As soon as a connection is established, the same connection can be used to transfer user data in either direction between a client and server and may also establish several TCP/IP connections simultaneously [8].

Depending on the task performed by the A/D/RML, Repair process (one cylinder released) (Figure 11) or Disassembly process (all workparts released) (Figure 10), distinct command signals , as shown in Figure 23, will be needed for interfacing between master PLC S7 1200 and ARS:

- Start Job ARS: Recover Cylinder 1;
- Start Job ARS: Recover Cylinder 2;
- Start Job ARS: Recover Body Workpiece;
- Start Job ARS: Recover Top Workpiece;
- Stop Command: stop Job ARS.

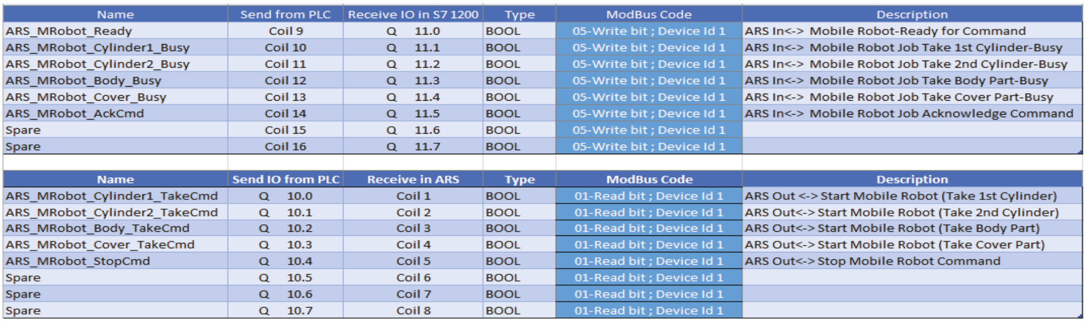

Name	Send from PLC	Receive IO in S7 1200	Type	ModBus Code	Description
ARS_MRobot_Ready	Coil 9	Q 11.0	BOOL	05-Write bit ; Device Id 1	ARS In<-> Mobile Robot-Ready for Command
ARS_MRobot_Cylinder1_Busy	Coil 10	Q 11.1	BOOL	05-Write bit ; Device Id 1	ARS In<-> Mobile Robot Job Take 1st Cylinder-Busy
ARS_MRobot_Cylinder2_Busy	Coil 11	Q 11.2	BOOL	05-Write bit ; Device Id 1	ARS In<-> Mobile Robot Job Take 2nd Cylinder-Busy
ARS_MRobot_Body_Busy	Coil 12	Q 11.3	BOOL	05-Write bit ; Device Id 1	ARS In<-> Mobile Robot Job Take Body Part-Busy
ARS_MRobot_Cover_Busy	Coil 13	Q 11.4	BOOL	05-Write bit ; Device Id 1	ARS In<-> Mobile Robot Job Take Cover Part-Busy
ARS_MRobot_AckCmd	Coil 14	Q 11.5	BOOL	05-Write bit ; Device Id 1	ARS In<-> Mobile Robot Job Acknowledge Command
Spare	Coil 15	Q 11.6	BOOL	05-Write bit ; Device Id 1	
Spare	Coil 16	Q 11.7	BOOL	05-Write bit ; Device Id 1	

Name	Send IO from PLC	Receive in ARS	Type	ModBus Code	Description
ARS_MRobot_Cylinder1_TakeCmd	Q 10.0	Coil 1	BOOL	01-Read bit ; Device Id 1	ARS Out <-> Start Mobile Robot (Take 1st Cylinder)
ARS_MRobot_Cylinder2_TakeCmd	Q 10.1	Coil 2	BOOL	01-Read bit ; Device Id 1	ARS Out<-> Start Mobile Robot (Take 2nd Cylinder)
ARS_MRobot_Body_TakeCmd	Q 10.2	Coil 3	BOOL	01-Read bit ; Device Id 1	ARS Out<-> Start Mobile Robot (Take Body Part)
ARS_MRobot_Cover_TakeCmd	Q 10.3	Coil 4	BOOL	01-Read bit ; Device Id 1	ARS Out<-> Start Mobile Robot (Take Cover Part)
ARS_MRobot_StopCmd	Q 10.4	Coil 5	BOOL	01-Read bit ; Device Id 1	ARS Out<-> Stop Mobile Robot Command
Spare	Q 10.5	Coil 6	BOOL	01-Read bit ; Device Id 1	
Spare	Q 10.6	Coil 7	BOOL	01-Read bit ; Device Id 1	
Spare	Q 10.7	Coil 8	BOOL	01-Read bit ; Device Id 1	

Figure 23. Modbus message interface (Modbus Map).

In the same way, ARS must acknowledge that the received command/action from A/D/RML is handled (Figure 24); therefore, 3 synchronization signals will be used between ARS and master PLC S7 1200:

- ARS Ready for Command-Status;
- ARS Acknowledge Command-Status;
- ARS Job started: Busy Status.

Network topology as shown in Figures 1 and 19 is implemented in the A/D/RML assisted by ARS. OPC UA is the communication data structure between SCADA and main PLC, integrated into an industrial system to provide a standard way for setting a secure and reliable data exchange between industrial devices of multiple vendors and software systems [29], but the other main reason for using this technology for the proposed assisted manufacturing line is that it operates and communicates with other industrial protocols. The flexible manufacturing line also runs with a multitude of protocols such as Profibus, Profinet, Modbus and Ethernet/IP.

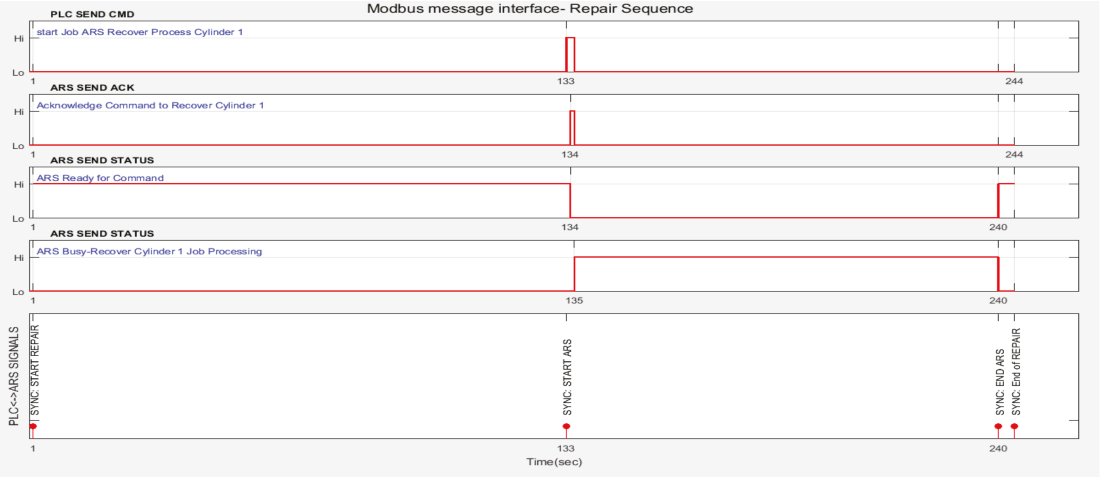

Figure 24. Handshake sequence interfacing master PLC S7 1200 and ARS.

3. Real-Time Results for A/D/RML Control Based on SHPN Model

The SHPN model is transposed via the SCADA platform from Siemens into a real-time application, obtained by interfacing the SHPN model with synchronized signals taken from the real process by means of PLC and sensors [28,30,31].

Following implementation, real-time results within the laboratory setup are shown in Figures 25–28, for continuous and discrete places associated with displacements of ARS and FC, for later comparing and validating data with the simulation framework results as presented in Section 2.2.

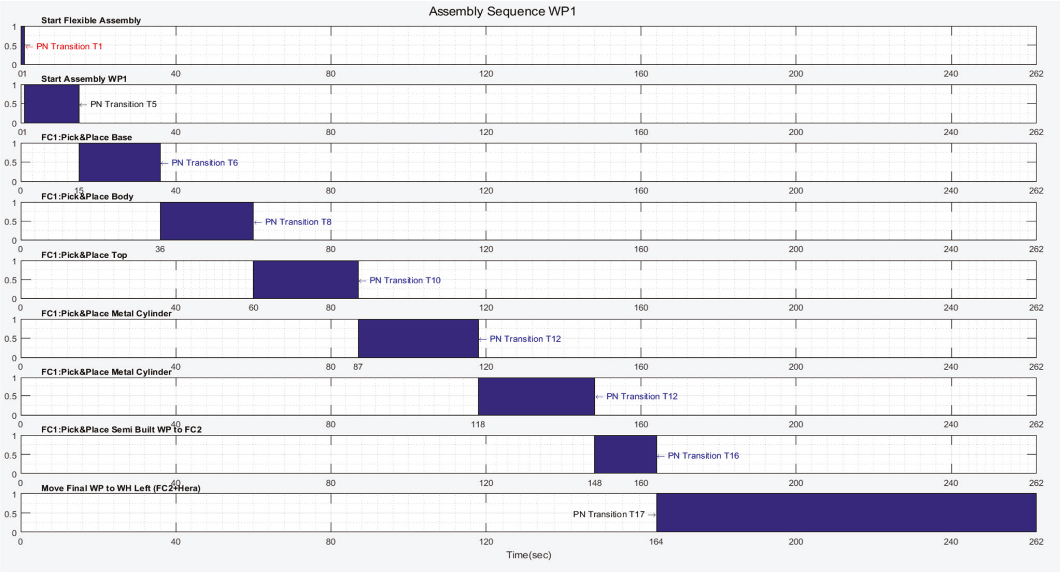

Figure 25. Results for continuous and discrete places associated with displacements of FC with IRM for Assembly WP1.

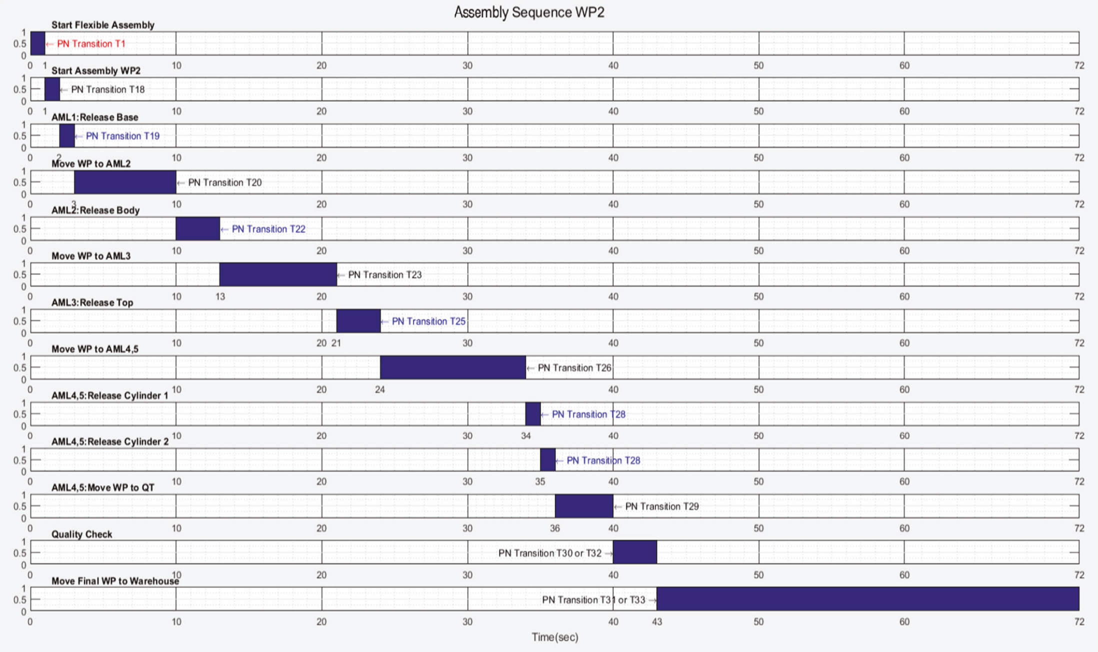

Figure 26. Results for discrete places and transitions on Assembly WP2.

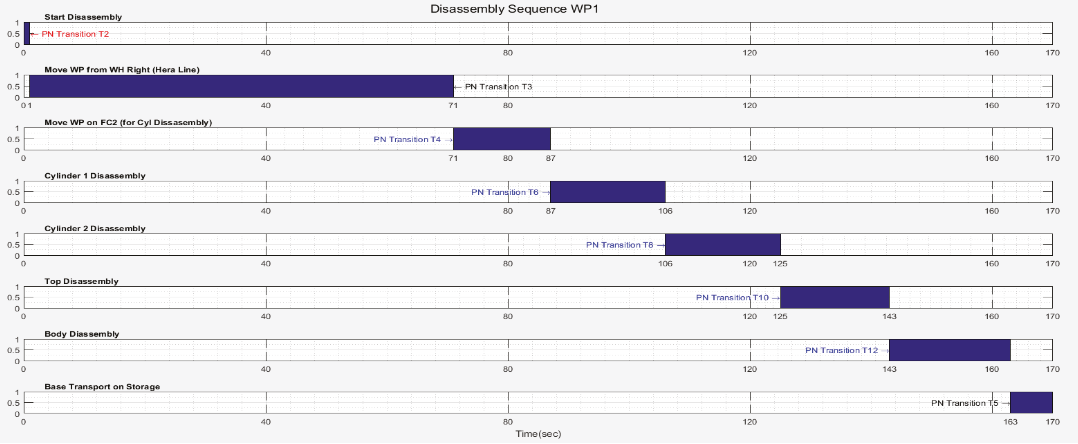

Figure 27. Results for continuous and discrete places associated with displacements of ARS and FC with IRM for Disassembly.

The synchronization signals, used in the real-time control application, validate certain transitions into the SHPN model [32]. These transitions are conditioned by the associated signals for releasing recovered workparts on FC trays or on the ML storage units by the ARS. Synchronization will lead to initializing the robot and to monitoring/controlling assembly/disassembly/repair operations with the ARS. Discrete time and sliding-mode control, in trajectory tracking, based on a kinematic and dynamic model, is used to control WMR. In this way, both ARS and the A/D/RML are controlled so as to achieve a minimum assembly and disassembly time cycle.

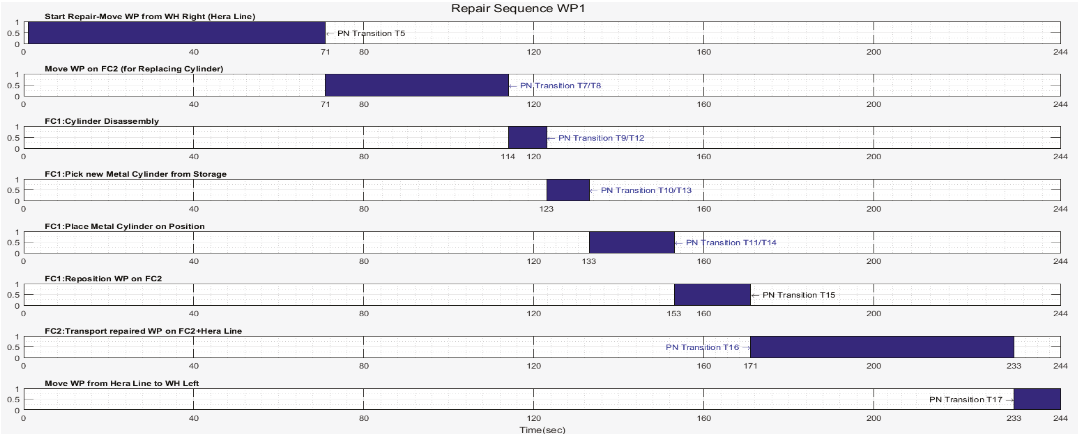

Figure 28. Results for continuous and discrete places associated with displacements of ARS and FC with IRM for Repair.

In order to grab the recovered workparts and place them on the dedicated storage positions, the ARS PeopleBot is equipped with 7-DOF Cyton RM with a gripper paddle and HD video camera on the end effector (Figure 8), connected both via USB with the Remote PC. The gripper is positioned by VSS so as to grab the disassembled component and transport and place it into the dedicated warehouse.

Figure 29 shows the desired and real trajectories of the ARS PeopleBot obtained with the TTSMC in a closed loop control to move from the FC to the storage unit from the mechatronics line and back to the FC in the desired time.

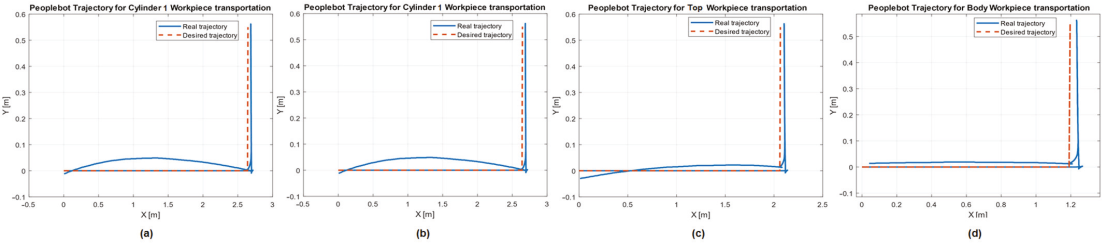

Figure 29. Full disassembly process. Desired and real trajectories of ARS PeopleBot based on TTSMC: (**a**) Cylinder 1, (**b**) Cylinder 2, (**c**) Top and (**d**) Body.

In Figure 30 presents X and Y axis trajectories for a complete disassembly process, both desired and the real one so that the differences between them can be easy distinguished.

Figure 31 illustrates X and Y axis tracking errors in absolute coordinates for the disassembly process as well, where ADRML is served/assisted by ARS for robotic pick-and-place operations for the recovered/dismantled components and transporting them back to the storage units.

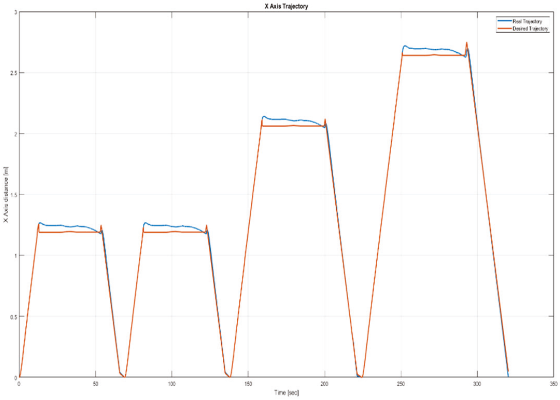

(a) (b)

Figure 30. Full disassembly process. Desired and real trajectories of ARS PeopleBot based on TTSMC: (**a**) X axis, (**b**) Y axis.

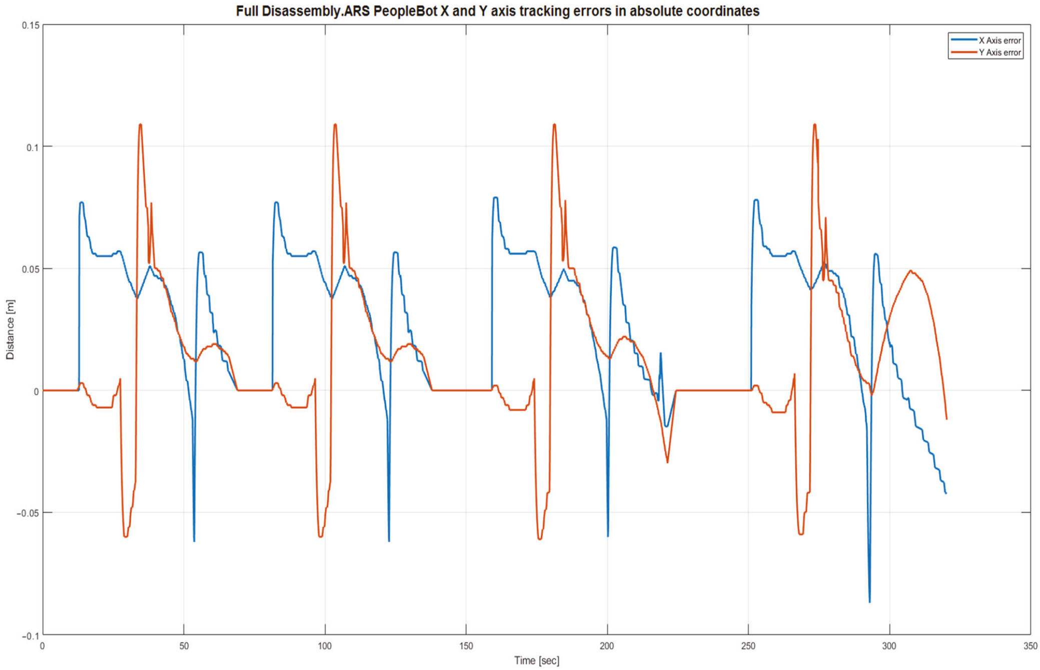

Figure 31. Full disassembly process. Trajectory tracking errors in absolute coordinates.

4. Discussion

The paper proposes an extension both in hardware as well in software, which allows the implementation of a flexible and multifunctional technology able to manufacture different products (Figure 9) and to disassemble (Figure 10), recover components or to repair products that do not correspond to the desired quality (Figure 11). All these functionalities are made with high precision due to the integration of an industrial robotic manipulator (ABB 120 IRM), an autonomous robotic system equipped with a mobile visual servoing system and by using a multi-agent control strategy and communication structure between the flexible cell and the mechatronics line that allows synchronizations of the requested operations. Therefore, the master PLC synchronizes with subsystems PLCs to automate their respective areas and for operating and controlling their local IO devices, after confirmation from the main control unit is applied (Figure 24).

Modeling of the system using hybrid Petri Nets, in which A/D/RML is a hybrid SHPN model having the Hera&Horstmann mechatronics line with discrete states and transitions and the ARS subsystem with continuous dynamics, is presented in the paper and represents only an intermediate stage (Figure 12). Due to the dynamic nature of the system, analytical methods can be used, but are limited; therefore, task scheduling and the simulation of the model, which tackle the compatibility between the two subsystems, is used for studying the evolution of the discrete states of A/D/RML with the physical constraints and continuous states of the ARS.

The real-time research and implementations is followed, comparing and validating data with the simulation framework results. SCADA environment is developed (Figure 20) so that the entire system works autonomously, fully automated to meet the actual industry requirements. The actual results also showed that the actual manufacturing line implementation satisfied the design target. By using the smart and autonomous technologies to operate in a seamless and secured way, this meets also the new requested requirements standards of Industry 4.0, increasing the degree of integration and compatibility with the actual industry needs

The control of the robotic arm Cyton 1500, for handling and precise positioning operations, when gripping or releasing the part, is based on the inverse kinematic model and is robust, having the desired behavior even in presence of uncertainties and external disturbances. Cyton 1500 manipulator is equipped with an anti-collision map tested on the simulation stage; the robotic arm moves until the object detected is in the center, and if the time needed to get to the object is higher than expected or a supplementary torque is detected, for example an obstacle has been placed in the trajectory, the robotic arm returns to the home position and notifies the user that the trajectory path following has been unsuccessful. The implementation of multifunctional flexible manufacturing technology in a laboratory system, to be as close as possible to the real industrial world, draws some limitations as well; we could not gather consistent data regarding the performance of robotic arm in the presence of noise for applying methods to overcome that. A more sophisticated approach has not been implemented, as the deviations that appear are just on the X or Y axis, due to the complex autonomous robot transportation errors.

5. Conclusions

The presented research is still in progress; it is a place for further improvements and fine tunings, and the important benefit and contribution of this research is the implementation of manufacturing technology assisted by autonomous robotic systems at the laboratory level, which works in real-time and which, if used industrially in the real world, would increase efficiency, reliability and precision. This research aimed for a dual purpose, one educational and another to implement, test and adapt this technology to be as close as possible to the real industry world requirements.

The educational goal aims to familiarize the system designer with everything that defines new industry architecture, including Industry 4.0 concepts, and to try to improve the actual technology design with the integration of all new, state of the art aspects of production and engineering, including smart manufacturing products and intelligent material handling systems and technologies.

Regarding the correspondence with the real industrial world, most manufacturing industrial technologies are served by robotic systems that have a fixed position (robotic manipulators). Through this study, we extended the degree of automation and efficiency of these production lines by using new technologies such as autonomous robotic systems equipped with manipulators and visual servoing systems. The goal is to adapt this technology to meet as much as possible the actual industry needs to confirm the feasibility of the line and to keep up the rhythm with the technology development. Therefore, the final purpose is to develop a fully automated multifunctional flexible manufacturing technology without the intervention of the human operator for a predefined production volume with the recovery of components of bad assembled products that did not pass the quality tests and integrating new emerging technologies such as SCADA, IIOT and MQTT protocols for Cloud interface.

Although this is a technology that has been used at the level of a laboratory, it can be extended further to real industry, where high accuracy and positioning are needed. Multispectral video sensors, providing new imaging capabilities without adding size or weight, can be used in order to reduce errors in reflectance estimation for remote sensing on production line inspection or workparts validation and quality checking to more strongly demonstrate the reliability and to increase speed and efficiency by integrating with the ARS of the presented manufacturing line technology, especially for recovery and accurate positioning operations.

The implementation of robust control architectures to uncertainties will be further considered for all systems: ARS, FC and the mechatronics line. As a result, this increases the reliability, flexibility and robustness of the technology to the uncertainties that might come from the sensors from the ARS and VSS.

The presented control architecture is a hybrid structure, multi agent-based control. Unlike using this control strategy, the system can be enhanced with artificial intelligence (AI), which is a combination of situational awareness and creative problem solving, to identify and fix potential assembly problems much faster and can diagnose and prevent further issues by directly alerting through SCADA systems when anomalous units are identified.

Additionally, we will also focus on the time study system performance evaluation and optimization methods of the complete production process to improve the performance and support better product quality [33]. Efficiency requirements are one of the key factor nowadays; therefore, optimization in what concern costs, energy and time will be one of the further purposes of development for manufacturing lines using ARS equipped with robot manipulators and visual servoing systems.

Author Contributions: Conceptualization, G.S., A.F. (Adrian Filipescu), D.I., R.Ș., D.C., E.M. and A.F. (Adriana Filipescu); methodology G.S., A.F. (Adrian Filipescu), D.I., D.C., R.Ș. and E.M.; software, G.S. and D.I.; validation, A.F. (Adrian Filipescu), R.Ș., D.C. and E.M.; formal analysis, G.S., D.I. and A.F. (Adriana Filipescu); writing—original draft preparation, G.S. and A.F. (Adrian Filipescu), D.I.; writing—review and editing, A.F. (Adrian Filipescu), R.Ș. and D.C.; supervision, A.F. (Adrian Filipescu); project administration, A.F. (Adrian Filipescu); funding acquisition, A.F. (Adrian Filipescu), G.S. and D.I. All authors have read and agreed to the published version of the manuscript.

Funding: This article (APC) will be supported by Doctoral School of Fundamental Sciences and Engineering, "Dunărea de Jos" University of Galați.

Institutional Review Board Statement: Not applicable.

Informed Consent Statement: Not applicable.

Data Availability Statement: Data availability is not applicable to this article as the study did not report any data.

Acknowledgments: The results of this work will be also presented to the 10th edition of the Scientific Conference organized by the Doctoral Schools of "Dunărea de Jos" University of Galați (SCDS-UDJG) http://www.cssd-udjg.ugal.ro/ (accessed on 10 May 2022), that will be held on 9th and 10th of June 2022, in Galați, Romania.

Conflicts of Interest: The authors declare no conflict of interest.

References

1. Filipescu, A.; Mincă, E.; Filipescu, A.; Coandă, H.-G. Manufacturing Technology on a Mechatronics Line Assisted by Autonomous Robotic Systems, Robotic Manipulators and Visual Servoing Systems. *Actuators* **2020**, *9*, 127. [CrossRef]
2. Filipescu, A.; Minca, E.; Filipescu, A., Jr. Mechatronics Manufacturing Line with Integrated Autonomous Robots and Visual Servoing Systems. In Proceedings of the 9th IEEE International Conference on Cybernetics and Intelligent Systems, and Robotics, Automation and Mechatronics (CIS-RAM 2019), Bangkok, Thailand, 18–20 November 2019; pp. 620–625, ISBN 978-1-7281-3457-4.
3. Filipescu, A., Jr. Contributions to Electric Drive of the Flexible Manufacturing Lines and Integrated Robots. Ph.D. Thesis, "Dunarea de Jos" University of Galati, Galati, Romania, 2017.
4. Jarrahi, F.; Abdul-Kader, W. Performance evaluation of a multi-product production line: An approximation method. *Appl. Math. Model.* **2015**, *39*, 3619–3636. [CrossRef]
5. Syafrudin, M.; Fitriyani, N.L.; Alfian, G.; Rhee, J. An Affordable Fast Early Warning System for Edge Computing in Assembly Line. *Appl. Sci.* **2019**, *9*, 84. [CrossRef]
6. Stoll, J.T.; Schanz, K.; Pott, A. Mechatronic Control System for a Compliant and Precise Pneumatic Rotary Drive Unit. *Actuators* **2020**, *9*, 1. [CrossRef]
7. de Gea Fernández, J.; Yu, B.; Bargsten, V.; Zipper, M.; Sprengel, H. Design, Modelling and Control of Novel Series-Elastic Actuators for Industrial Robots. *Actuators* **2020**, *9*, 6. [CrossRef]
8. Filipescu, A.; Ionescu, D.; Filipescu, A.; Mincă, E.; Simion, G. Multifunctional Technology of Flexible Manufacturing on a Mechatronics Line with IRM and CAS, Ready for Industry 4.0. *Processes* **2021**, *9*, 864. [CrossRef]
9. Chryssolouris, G. *Manufacturing Systems—Theory and Practice*, 2nd ed.; Springer: New York, NY, USA, 2005.
10. Langmann, R.; Stiller, M. The PLC as a Smart Service in Industry 4.0 Production Systems. *Appl. Sci.* **2019**, *9*, 3815. [CrossRef]
11. Leusin, M.E.; Kück, M.; Frazzon, E.M.; Maldonado, M.U.; Freitag, M. Potential of a Multi-Agent System Approach for Production Control in Smart Factories. *IFAC Elsevier B.V.* **2018**, *51*, 1459–1464. [CrossRef]
12. Copot, C. Control Techniques for Visual Servoing Systems. Ph.D. Thesis, Gheorghe Asachi Technical University of Iasi, Iasi, Romania, 2012.
13. Petrea, G.; Filipescu, A.; Solea, R.; Filipescu, A., Jr. Visual Servoing Systems Based Control of Complex Autonomous Systems Serving a P/RML. In Proceedings of the 22nd IEEE, International Conference on System Theory, Control and Computing, (ICSTCC), Sinaia, Romania, 10–12 October 2018; pp. 323–328, ISBN 978-1-5386-4444-7.
14. Corke, P.; Spindler, F.; Chaumette, F. Combining cartesian and polar coordinates in IBVS. In Proceedings of the IEEE/RSJ Int. Conf. on Intelligent Robots and Systems, IROS'09, St. Louis, MO, USA, 10–15 October 2009; pp. 5962–5967.
15. Maxim, A.; Copot, D.; Copot, C.; Ionescu, C.M. The 5W's for Control as Part of Industry 4.0: Why, What, Where, Who, and When—A PID and MPC Control Perspective. *Inventions* **2019**, *4*, 10. [CrossRef]
16. Chen, Z.-Y.; Chen, C.-T. A Remote Controlled Robotic Arm That Reads Barcodes and Handles Products. *Inventions* **2018**, *3*, 17. [CrossRef]
17. Karimov, A.; Kopets, E.; Kolev, G.; Leonov, S.; Scalera, L.; Butusov, D. Image Preprocessing for Artistic Robotic Painting. *Inventions* **2021**, *6*, 19. [CrossRef]
18. Petrea, G.; Filipescu, A.; Minca, E.; Voda, A.; Filipescu, A., Jr.; Serbencu, A. Hybrid Modelling Based Control of an Processing/Reprocessing Mechatronics Line Served by an Autonomous Robotic System. In Proceedings of the 17th IEEE, Intrenational Conference on System Theory, Control and Computing, (ICSTCC), Sinaia, Romania, 11–13 October 2013; pp. 410–415, ISBN 978-1-4799-2228-4.
19. Filipescu, A., Jr.; Petrea, G.; Filipescu, A.; Filipescu, S. Modeling and Control of a Mechatronics System Served by a Mobile Platform Equipped with Manipulator. In Proceedings of the 33rd Chinese Control Conference, Nanjing, China, 28–30 July 2014; pp. 6577–6582, ISBN 978-988-15638-4-2.
20. David, R.; Alla, H. *Discrete, Continuous and Hybrid Petri Nets*; Springer: Berlin/Heidelberg, Germany, 2010; ISBN 978-3-642-10668-2.
21. Peng, S.; Zhou, M. Sensor-based stage Petri net modelling of PLC logic programs for discrete-event control design. *Int. J. Prod. Res.* **2003**, *41*, 629–644. [CrossRef]
22. Ravankar, A.; Ravankar, A.A.; Kobayashi, Y.; Hoshino, Y.; Peng, C.-C. Path Smoothing Techniques in Robot Navigation: State-of-the-Art, Current and Future Challenges. *Sensors* **2018**, *18*, 3170. [CrossRef] [PubMed]
23. Lee, J.-K.; Park, J.-B.; Choi, Y.-H. Tracking Control of Nonholonomic Wheeled Mobile Robot Based on New Sliding Surface with Approach Angle. 3rd IFAC Symposium on Telematics Applications. In Proceedings of the International Federation of Automatic Control, Seoul, Korea, 11–13 November 2013.
24. Park, B.S.; Yoo, S.J.; Park, J.-B.; Choi, T.-H. Adaptive neural sliding mode control of nonholonomic wheeled mobile robots with model uncertainty. *IEEE Trans. Control Syst. Technol.* **2009**, *17*, 207–214. [CrossRef]
25. Utkin, V.I.; Guldner, J.; Shi, J. *Sliding Mode Control in Electro-Mechanical Systems*, 2nd ed.; CRC Press: Boca Raton, FL, USA, 2009; ISBN 978-1-4200-6560-2.
26. el Youssef, E.S.; Martins, N.A.; De Pieri, E.R.; Moreno, U.F. PD-Super-Twisting Second Order Sliding Mode Tracking Control for a Nonholonomic Wheeled Mobile Robot. In Proceedings of the 19th World Congress the International Federation of Automatic Control, Cape Town, South Africa, 24–29 August 2014.
27. Wei, B. A Tutorial on Robust Control, Adaptive Control and Robust Adaptive Control—Application to Robotic Manipulators. *Inventions* **2019**, *4*, 49. [CrossRef]

28. Ciubucciu, G.; Filipescu, A.; Filipescu, A., Jr.; Filipescu, S.; Dumitrascu, B. Control and Obstacle Avoidance of a WMR Based on Sliding-Mode, Ultrasounds and Laser. In Proceedings of the 12th IEEE International Conference on Control and Automation (ICCA), Kathmandu, Nepal, 1–3 June 2016; pp. 779–784, ISBN 978-1-5090-1737-9.
29. Maia, R.F.; Bálsamo, A.J.; Lopes, G.A.W.; Massote, A.A.; Lima, F. Evaluation of OPC-UA communication in an autonomous advanced manufacturing cell implementation. *Gestão Prod.* **2020**, *27*, e5414. [CrossRef]
30. Minca, E.; Filipescu, A.; Voda, A. Modelling and control of an assembly/disassembly mechatronics line served by mobile robot with manipulator. *Control Eng. Pract.* **2014**, *31*, 50–62. [CrossRef]
31. Dragomir, F.; Mincă, E.; Dragomir, O.E.; Filipescu, A. Modelling and Control of Mechatronics Lines Served by Complex Autonomous Systems. *Sensors* **2019**, *19*, 3266. [CrossRef] [PubMed]
32. SIRPHYCO, Software for Analysis of Hybrid and Continuous Petri Nets. Available online: http://www.lag.ensieg.inpg.fr/sirphyco (accessed on 10 May 2022).
33. Ghafoorpoor Yazdi, P.; Azizi, A.; Hashemipour, M. A Hybrid Methodology for Validation of Optimization Solutions Effects on Manufacturing Sustainability with Time Study and Simulation Approach for SMEs. *Sustainability* **2019**, *11*, 1454. [CrossRef]

inventions

Article

Image Moment-Based Features for Mass Detection in Breast US Images via Machine Learning and Neural Network Classification Models

Iulia-Nela Anghelache Nastase [1,2], Simona Moldovanu [1,3] and Luminita Moraru [1,4,*]

[1] The Modelling & Simulation Laboratory, Dunarea de Jos University of Galati, 47 Domneasca Street, 800008 Galati, Romania; iulia.anghelache@ugal.ro (I.-N.A.N.); simona.moldovanu@ugal.ro (S.M.)
[2] Emil Racovita Theoretical Highschool, 12–14, Regiment 11 Siret Street, 800332 Galati, Romania
[3] Department of Computer Science and Information Technology, Faculty of Automation, Computers, Electrical Engineering and Electronics, Dunarea de Jos University of Galati, 47 Domneasca Street, 800008 Galati, Romania
[4] Department of Chemistry, Physics & Environment, Faculty of Sciences and Environment, Dunarea de Jos University of Galati, 47 Domneasca Street, 800008 Galati, Romania
* Correspondence: luminita.moraru@ugal.ro

Abstract: Differentiating between malignant and benign masses using machine learning in the recognition of breast ultrasound (BUS) images is a technique with good accuracy and precision, which helps doctors make a correct diagnosis. The method proposed in this paper integrates Hu's moments in the analysis of the breast tumor. The extracted features feed a k-nearest neighbor (k-NN) classifier and a radial basis function neural network (RBFNN) to classify breast tumors into benign and malignant. The raw images and the tumor masks provided as ground-truth images belong to the public digital BUS images database. Certain metrics such as accuracy, sensitivity, precision, and F1-score were used to evaluate the segmentation results and to select Hu's moments showing the best capacity to discriminate between malignant and benign breast tissues in BUS images. Regarding the selection of Hu's moments, the k-NN classifier reached 85% accuracy for moment M1 and 80% for moment M5 whilst RBFNN reached an accuracy of 76% for M1. The proposed method might be used to assist the clinical diagnosis of breast cancer identification by providing a good combination between segmentation and Hu's moments.

Keywords: malignant and benign masses; Hu's moments; k-nearest neighbor; radial basis function neural network; breast ultrasound images

Citation: Anghelache Nastase, I.-N.; Moldovanu, S.; Moraru, L. Image Moment-Based Features for Mass Detection in Breast US Images via Machine Learning and Neural Network Classification Models. *Inventions* **2022**, *7*, 42. https://doi.org/10.3390/inventions7020042

Academic Editor: Shoou-Jinn Chang

Received: 3 May 2022
Accepted: 14 June 2022
Published: 15 June 2022

Publisher's Note: MDPI stays neutral with regard to jurisdictional claims in published maps and institutional affiliations.

Copyright: © 2022 by the authors. Licensee MDPI, Basel, Switzerland. This article is an open access article distributed under the terms and conditions of the Creative Commons Attribution (CC BY) license (https://creativecommons.org/licenses/by/4.0/).

1. Introduction

Breast cancer is one of the most common and serious diseases that poses a threat to women's health. According to [1], the female breast cancer (around 2.3 million new cases, which means 11.7% of the total cancer cases in women, and 6.9% of all cancer-related deaths in women, in 2020) and lung cancer (11.4% of the total cancer cases in women and 18% of the cancer-related deaths in women) are the types of cancer with the highest incidence. Breast cancer begins as an uncontrolled multiplication of breast cells which proliferate in the breast tissues. They can be classified as benign (some abnormality of the breast tissues but they do not threaten the patient's life) and malignant (might affect the patient's life).

Breast cancer is examined and investigated through many techniques such as computerized tomography, histopathological imaging, magnetic resonance imaging, mammography, and breast ultrasound (BUS). The BUS is a preferred tool for early breast cancer screening due to the significant amount of information provided in a short time [2]. Breast ultrasound imaging is most suitable for the early detection of breast cancer as it is noninvasive and nonradioactive, resulting in a direct, cost-effective improvement in patient care. Furthermore, breast ultrasound imaging is a practical and feasible approach for the early detection of breast cancer. Early diagnosis based on ultrasound can significantly improve the cure rate. However, the BUS images have poor resolution, show various features, and contain speckle noise. Moreover, to read these images, a high degree of professionalism is required for radiologists to overcome the subjectivity of the analysis.

Techniques that belong to the computer-aided diagnosis and deep learning fields can bring advances in this area and provide more accurate judgment for the clinical diagnosis of breast cancer [3–6]. Automatic segmentation of breast ultrasound images (as a method to delineate anomalies containing suspicious regions of interest) and extraction of the image features devoted to describing the tumor shape, size, and texture provide valuable references on classification for a much-improved clinical diagnosis of breast cancer [7–11]. Furthermore, the best features are then input into a classifier to establish the category of the tumors, followed by an evaluation of the accuracy of the method [12]. The accuracy of the image segmentation directly influences the performance of both feature extraction and classification of the tumors. Even though segmentation is a fundamental task in medical image analysis, the segmentation of BUS images is difficult because (i) BUS images are affected by speckle noise, show low contrast, show low peak signal-to-noise ratio, and contain speckle artefacts that are tissue-dependent, and (ii) a large variability among patients exists related to the breast anatomical structures. Moreover, to evaluate the segmentation performance, the ground-truth images are generated by using a manually delineated boundary.

This paper uses a machine learning- and deep learning-based system to assist doctors in making a more accurate judgment in classifying breast tumors as benign or malignant using BUS images. To test our classification strategy, we propose a method that integrates Hu's moments in the breast tumor analysis as handcrafted and meaningful features [13]. Our method uses the tumor masks provided as ground-truth images in a publicly available BUSI image dataset (Breast Ultrasound Images Dataset (BUSI dataset) https://academictorrents.com/details/d0b7b7ae40610bbeaea385aeb51658f527c86a16, accessed on 1 December 2021). Hu's moments provide attributes that are related to the shape of the tumors regardless of scale, location, and orientation. They are used for the extraction of the shape characteristics from the BUS images. However, Hu's moments incorporate redundant information, and it is necessary to investigate the significance of the diagnosis difference by utilizing different shape features. We performed a statistical test (*t*-test, *p*-value) for testing the differentiation between benign and malignant tumors in the analyzed BUS images according to Hu's moments [14]. The t-test ($p < 0.05$ or 95% confidence interval) is much simpler to apply and provides a quick response if the analyzed features are meaningful for the classification or less relevant. Furthermore, the remaining features are used to train a k-NN classifier for classification purposes. The k-NN technique uses learning processes based on instance [6] to identify the group's membership by exploiting the feature similarity [15]. Moreover, the same selected features are fed into the radial basis function neural network (RBFNN), which allows discriminating between benign and malignant tumors with the highest accuracy. Multiclassification aids gathering the precise information about the cancer's current state and, equally, supports the informed diagnosis decision [16].

The remainder of the paper is organized as follows: Section 2 discusses related studies from the literature; Section 3 presents the proposed work, as well as a concise overview of the proposed method; Section 4 discusses the experimental results obtained by employing the proposed method, as well as its performance evaluation; finally, Section 5 concludes and discusses potential future work.

2. Related Work

Many decision-support technologies based on machine learning and deep learning have been included into experimental investigations devoted to the diagnosis of various kinds of tumors, including breast tumors.

A comparative analysis of watershed, mean shift, and k-means segmentation algorithms to detect microcalcifications on breast images belonging to the MIAS database was reported in [17]. The best results were obtained by using k-means segmentation, which detected 42.8% of breast images correctly and had 57.2% false detections.

Zhang et al. [18] introduced the Hu moment invariant as a feature descriptor to diagnose breast cancer. They used k-fold cross-validation to improve the accuracy of the proposed method and to reduce the difficulty of diagnosis.

A watershed segmentation and k-NN (as a supervised learning method) classification were implemented to detect the tumors in the mammogram images and establish the risk of cancer classification [19]. The breast image classification was performed with an 83.33% overall accuracy rate.

Sadhukhan et al. [20] reported a model used to predict the best features for early breast cancer cell identification. The k-NN and support vector machine (SVM) algorithms were studied in terms of accuracy. On the basis of the contours of the cells, the nuclei were distinctly separated, and an accuracy of 97.49% was determined.

Hao et al. [21] used three-channel features of 10 descriptors to improve the accuracy of benign and malignant breast cancer recognition. An SVM algorithm was used to assess the model's performance. A recognition accuracy of 90.2–94.97% at the image level was reported for the model based on texture features, geometric moments, and wavelet decomposition.

Another study [22] proposed a model which used three-channel features of 10 descriptors for the recognition of breast cancer histopathological images, as well as an SVM to improve the classification of benign and malignant breast cancer. The proposed model showed an increase in the recognition time and little improvement in the recognition accuracy.

Joshi and Mehta [23] analyzed the diagnosis accuracy of the k-NN algorithm using a set of 32 features and with and without dimensionality reduction techniques. The reported results showed 97.06% accuracy for benign vs. malignant classification using k-NN with the linear discriminant analysis technique.

Alshammari et al. [24] extracted intensity-based features (such as average intensity, standard deviation, and contrast between the foreground and background), shape-based features (i.e., diameter, length, degree of circulation, and elongation), or texture-based features for classification purpose. The decision tree, k-NN, SVM, naïve Bayes, and discriminant analysis algorithms were used to maximize the separation between the given groups of data and to produce higher-accuracy results.

Agaba et al. [25] used some handcrafted features such as Hu's moment, Haralick textures, color histogram, and a deep neural network for a multiclassification task devoted to breast cancer classification using histopathological images on the BreakHis dataset. They also used various enlargements for histopathological images analysis. An accuracy score of 97.87% was reported for 40× magnification.

Xie et al. [26] used a combination of SVM and extreme learning machine (ELM) to differentiate between malignant and benign masses in mammographic images. The proposed algorithm included mass segmentation based on the level set method, feature extraction, feature selection, and mass type classification. An average accuracy of 96.02% was reported.

Zhuang et al. [27] proposed a method based on multiple features and support vector machines for the diagnosis of breast tumors in ultrasound images. Their algorithm used both characteristic features and deep learning features and a support vector machine for BUS classification. Hu's moment invariants [13] were used to investigate the characteristics of the posterior shadowing region that were different for benign and malignant tumors. The reported results were as follows: accuracy, sensitivity, specificity, and F1-score of 92.5%, 90.5%, 95%, 90.5%, and 92.7%, respectively, showing superiority to other known methods.

Deep features have played an important role in the progress of deep learning. These features are extracted from the deep convolutional layers of pretrained CNNs or customdesigned CNNs. Shia et al. [28] used transfer learning on a pretrained CNN and trained it using a BUS dataset containing 2099 images with benign and malignant tumors. An SVM with a sequential optimization solver was used for classification. A sensitivity of 94.34% and a specificity of 93.22% were reported for the classification.

Wan et al. [29] used content-based radiomic features to analyze BUS images. This study considered 895 BUS images and three radiomic features (i.e., color histogram, Haralick's texture features, and Hu's moments). The classification was performed using seven well-known machine learning algorithms and a CNN architecture. The best performance in differentiation between benign and malignant BUS was reported for the random forest classifier. The obtained accuracy, sensitivity, specificity, F1-score, and average precision were as follows: 90%, 71%, 100%, 83%, and 90%, respectively.

Moldovanu et al. [30] studied and classified skin lesions using a k-NN-CV algorithm and an RBF neural network. The RBF neural network classifier provided an accuracy of 95.42% in the classification of skin cancer, significantly better than the k-NN algorithm.

Damian et al. [31] used Hu's invariant moments to determine their relevance in the differentiation between nevi and melanomas. The reported results indicated that Hu's moments were good descriptors as they provided a good classification between malignant melanoma and benign lesions.

3. Materials and Method

3.1. Dataset

All images used in this study belonged to the publicly available digital BUSI (breast ultrasound image) database. The images were in a PNG file format with an average image size of 500 × 500 pixels and an 8 bit gray level. The considered dataset contained 780 images classified into normal images (n = 133), images with benign lesions (n = 437), and images with malignant lesions (n = 210). The images were captured at the Baheya Hospital for Early Detection and Treatment of Women's Cancer, Cairo, Egypt [32]. Experts of ultrasonic imaging evaluated their geometry, density, and internal echo contrast levels. Furthermore, ground-truth images were available. The ground-truth images were generated using the MATLAB programming environment and a freehand segmentation method utilized by radiologists and computer science experts (Figure 1).

(**a**) (**b**)

Figure 1. *Cont.*

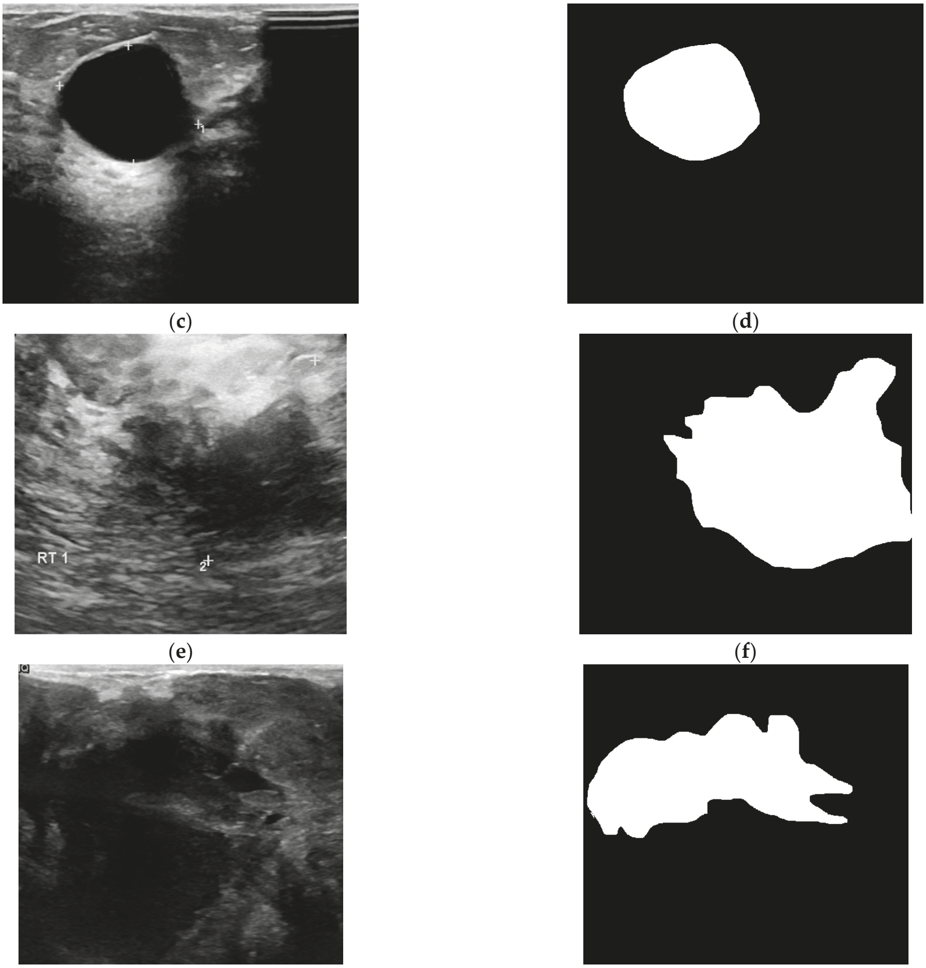
(**c**) (**d**)
(**e**) (**f**)
(**g**) (**h**)

Figure 1. Samples of breast ultrasound images: (**a**,**c**) grayscale image of a benign lesion; (**b**,**d**) ground truth for benign lesion; (**e**,**g**) grayscale image of a malignant lesion; (**f**,**h**) ground truth for malignant lesion [32].

3.2. Feature Extraction and Selection

The extracted features covered the shape of the breast lesions, which can be arranged in the following mathematical form:

$$F = [F1, F2, \ldots, F7]. \tag{1}$$

The $(p + q)$ order of the geometric moment can be defined as follows [13]:

$$m_{pq} = \sum_{y=1}^{N} \sum_{x=1}^{M} x^p y^q f(x, y),\ p,\ q = 1,\ 2,\ 3,\ \ldots, \tag{2}$$

where $f(x, y)$ is the extracted ground-truth region. The central moments are defined as

$$\mu_{pq} = \sum_{y=1}^{N} \sum_{x=1}^{M} (x - \overline{x})^p (y - \overline{y})^q f(x, y),\ p,\ q = 1,\ 2,\ 3,\ \ldots, \tag{3}$$

where $\overline{x} = \frac{m_{10}}{m_{00}}$ and $\overline{y} = \frac{m_{01}}{m_{00}}$ represent the center-of-gravity coordinates of the image. The normalized central moment is

$$\eta_{pq} = \frac{\mu_{pq}}{\mu_{00}^{\rho}},\ \rho = \frac{p+q}{2} + 1. \tag{4}$$

The seven Hu moments were computed using the second- and third-order normalized central moments.

The k-nearest neighbor (k-NN) is a classifier which provides an efficient prediction model based on the closest training examples [15,33]. An object is classified by a majority vote of its neighbors, but the optimal k-value is the most sensitive factor of k-NN. To overcome this drawback, the k-NN algorithm is run many times using various k-values until the optimal value is found. The best performance provided by the validation set indicated k = 3 as the optimal value.

Not all features are useful for improving classification accuracy. In the first step, the *t*-test indicated which features were significant to distinguish between benign masses and malignant ones. Then, the remaining features were independently evaluated by k-NN using a fivefold cross-validation algorithm and an RBFNN. The dataset was split it into training data and test data. The concept of fivefold cross-validation indicates that the training data were randomly split into five equal parts. For each k, the mean accuracy was computed, denoting the final score of each feature. RBFNN is a neural network with a three-layer feedforward architecture (Figure 2). The input layer provides features to the hidden layer in which the nodes use Gaussian functions $f_1, f_2, \ldots, f_n$ as radially symmetric functions. The output layer summarizes the number of possible output classes [30].

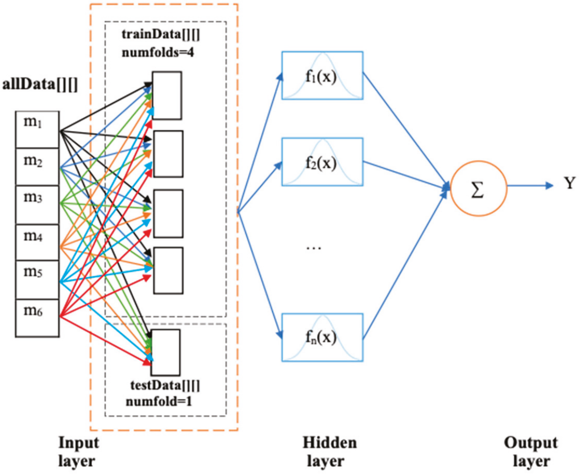

Figure 2. The structure of an RBFNN classifier.

The RBFNN is a nonlinear and three-layer feedforward neural network. There is one unsupervised layer between input nodes and the hidden neurons and one supervised layer between the hidden neurons and output nodes. The RBFNN was trained using four folds, while one fold was used to test the classifier. The net training seeks to determine the centers of the hidden layer in a first step, followed by the computation of the weights connecting the hidden layer to the output layer. RBFNN training was carried out by determining the proper weights and biases to obtain the target output by minimizing the error function, i.e., the root-mean-square error. The training stage of the RBFNN model was terminated once the calculated error reached the goal value of 0.01, and the number of training iterations of 1000 was already completed. Ten neural networks were built by varying the number of hidden neurons from eight to 40, in steps of eight neurons, i.e., eight, 16, 24, 32, and 40 neurons. Furthermore, the spread of radial basis functions (SRBFs) was used. For each number of hidden neurons, two SRBFs (namely, 0.01 and 0.05) were established. Each network was trained until the mean squared error fell below the goal of 0.01. The SRBF of 0.01 reached the imposed goal. The goal/desired value was iteratively compared to the mean squared error. If the goal/desired value was not reached, another eight neurons were added to the structure. A total of 20 trials were run to decide the most suitable number of hidden layer neurons for effective prediction. The best results were obtained for 32 neurons in the hidden layer.

4. Results and Discussion

The dataset we used included ground-truth cases for the normal, benign, and malignant categories. Among these regions, 133 were normal tissue, 210 were malignant masses, and 437 were benign masses.

Before using the k-NN classifier, the penalty *t*-test was used to optimize the feature vector and improve the classification performance (Table 1).

Table 1. Results for *t*-test ($p < 0.05$).

Moments	M1	M2	M3	M4	M5	M6	M7
p-value	0.04	<0.01	<0.01	<0.01	<0.01	<0.01	0.90

The selected features fed a k-NN classifier and RBFNN. We used fivefold cross-validation to select the best features. In fivefold cross-validation, the feature vector (437 benign images, 210 malignant images, and a total of 3882 moments) was randomly divided into five sets. The classifiers were trained using four folds, and one fold was used to test the classifier. The provided average accuracy was considered to evaluate the k-NN and RBFNN classifiers.

The values of accuracy, sensitivity, precision, and F1-score reflect the diagnosis accuracy. Higher values for these metrics indicate a better performance of the system. Figure 3 displays the performance of the k-NN algorithm in the classification of BUS images. The selected moment features with the highest classification accuracy rate were M1 and M5. The M1 moment showed the best accuracy of 0.85, representing the number of correctly classified images. It also had the best precision of 0.87, indicating the proportion of correct positive identifications. The M5 moment provided the best sensitivity of 0.83, indicating a good performance of the classifier. Furthermore, M5 had the second-best accuracy and precision values and the highest F1-score, which denotes the harmonic mean between precision and sensitivity.

The diagnostic performance of the RBFNN is presented in Figure 4. A relatively high classification performance (i.e., accuracy value of 0.76) was obtained for M1. Moreover, M1 had a high precision (0.81), indicating the proportion of correctly positive identifications. The other moments showed lower accuracy but had a good proportion of correctly positive identifications, with precision values around 0.78. The RBFNN model built in this study showed low sensitivity and F1-scores for M2 to M6 moments.

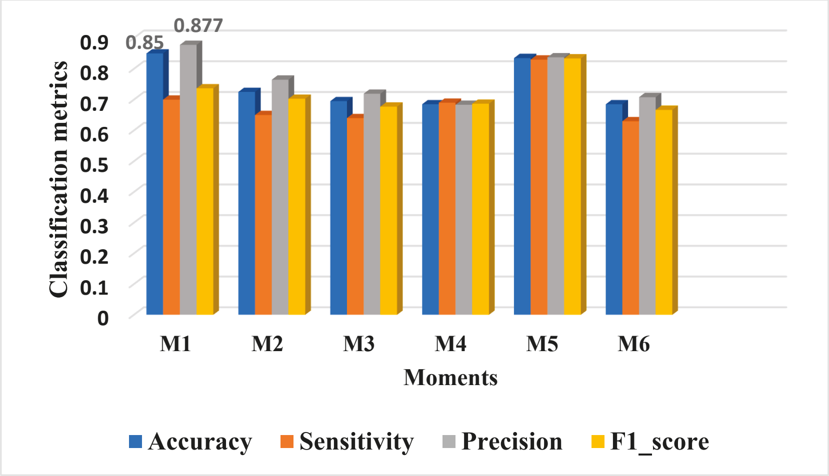

Figure 3. Classification metrics for k-NN.

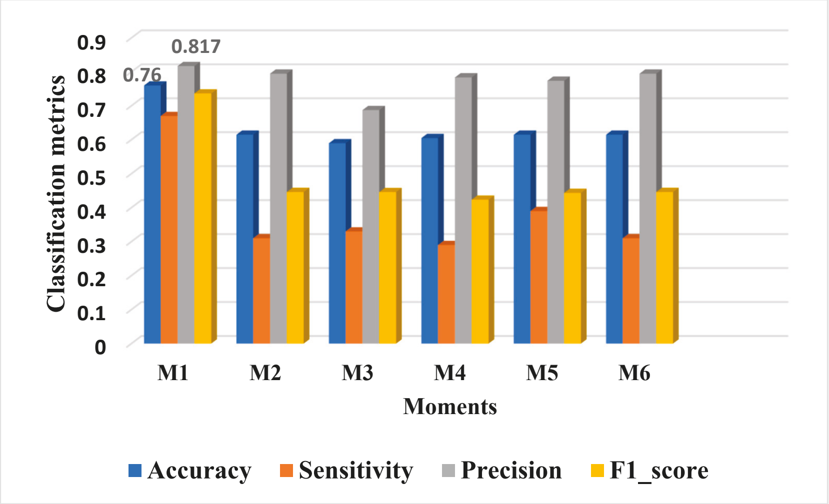

Figure 4. Classification performance of RBFNN from BUSI database.

The diagnostic performance of k-NN and RBFNN classifiers in the differentiation of benign and malignant breast lesions indicated significant differences among the classifiers in the classification performance. The data shown in Figures 3 and 4 indicate the M1 moment as the best feature with relatively high classification performance. When compared to the precision values (i.e., the proportion of correctly positive identifications), the best performance results were provided by the RBFNN. In the case of the M1 moment, there were some differences in the diagnostic performance among these two models. The k-NN was found to have a high accuracy of prediction.

The differentiation ability of our approach is in line with other existing conventional models, as presented in Table 2.

Table 2. Comparison of existing handcrafted approaches and the present handcrafted approach.

Model	Features	Accuracy	Sensitivity	Precision	F1-Scores	Ref.
Hu's moment + colored histogram + Haralick texture + SVM (linear kernel and C = 5) + VGG16	Hu's moment, colored histogram, and Haralick texture	0.8182	0.82	0.85	0.81	[16]
Hu's moment + Haralick texture + colored histogram + DNN	Hu's moment, Haralick texture, and colored histogram	0.98	0.98	0.97	0.97	[25]
Multiple features + SVM	Hu's moment	0.925	0.95	0.905	0.927	[27]
Hu's moment + colored histogram + Haralick texture CNN	Hu's moment, colored histogram, and Haralick texture	0.91	0.82	0.88	0.87	[29]
Hu's moment + K-NN	Hu's moment	0.89	0.83	0.87	0.83	Our model
Hu's moment + RBFNN	Hu's moment	0.76	0.67	0.817	0.73	Our model

The k-NN algorithm is a simple and nonparametric machine learning algorithm built to identify the group's membership by exploiting similarity and to predict the class of the new data. The performance of the k-NN algorithm is related to the complexity of the decision boundary. When the number of neighbors is low, the algorithm chooses only the closest values to the data sample, and a very complex decision boundary is formed. In this case, the model fails at providing an adequate generalization and shows poor results. When the number of neighbors is increased, in an early phase, the model generalizes well; however, when the value is increased too much, it results in a performance drop. RBFNN as a deep learning tool requires several trials in establishing the number of hidden layers and/or choosing the activation function, but it is advantageous as it needs less effort and preprocessing. This is one of the limitations of the present study. Other limitations are related to the small size of the dataset. A neural architecture reaches good performance when handling large amounts of data. However, the recognition accuracy of the proposed method is comparable to some state-of-the-art methods. A future research direction will be devoted to improving the classification performance by combining geometric moments with other feature descriptors.

5. Conclusions

In this paper, we employed both a k-NN algorithm and an RBFNN model, and we investigated their performance in differentiating between benign and malignant breast lesions on BUS images. Both methods highlighted that moment M1 (i.e., correlated with the area of the lesion) was the feature that best differentiated between benign and malignant breast lesions. The k-NN classifier had a classification performance described by an accuracy of 0.85, while RBFNN had a decent score of 0.76. Despite the small difference in classification performance, we believe that RBFNN is a proper tool for the classification task, as the proportion of correctly positive identifications reached higher values.

Author Contributions: Conceptualization, S.M. and L.M.; methodology, S.M. and L.M.; software, S.M., I.-N.A.N. and L.M.; validation, S.M. and I.-N.A.N.; formal analysis, I.-N.A.N.; investigation, S.M. and I.-N.A.N.; writing—original draft preparation, S.M., I.-N.A.N. and L.M.; writing—review and editing, S.M. and L.M. All authors have read and agreed to the published version of the manuscript.

Funding: This research received no external funding.

Institutional Review Board Statement: Not applicable.

Informed Consent Statement: Not applicable.

Data Availability Statement: Not applicable.

Conflicts of Interest: The authors declare no conflict of interest.

References

1. Sung, H.; Ferlay, J.; Siegel, R.L.; Laversanne, M.; Soerjomataram, I.; Jemal, A.; Bray, F. Global Cancer Statistics 2020: GLOBOCAN Estimates of Incidence and Mortality Worldwide for 36 Cancers in 185 Countries. *CA A Cancer J. Clin.* **2021**, *71*, 209–249. [CrossRef] [PubMed]
2. Qi, X.; Zhang, L.; Chen, Y.; Pi, Y.; Chen, Y.; Lv, Q.; Yi, Z. Automated diagnosis of breast ultrasonography images using deep neural networks. *Med. Image Anal.* **2019**, *52*, 185–198. [CrossRef] [PubMed]
3. Evans, A.; Trimboli, R.M.; Athanasiou, A.; Balleyguier, C.; Baltzer, P.A.; Bick, U.; Camps Herrero, J.; Clauser, P.; Colin, C.; Cornford, E.; et al. Breast ultrasound: Recommendations for information to women and referring physicians by the European Society of Breast Imaging. *Insights Imaging* **2018**, *9*, 449–461. [CrossRef] [PubMed]
4. Wu, G.-G.; Zhou, L.-Q.; Xu, J.-W.; Wang, J.-Y.; Wei, Q.; Deng, Y.-B.; Cui, X.-W.; Dietrich, C.-F. Artificial intelligence in breast ultrasound. *World J. Radiol.* **2019**, *11*, 19–26. [CrossRef]
5. Yao, A.D.; Cheng, D.L.; Pan, I.; Kitamura, F. Deep learning in neuroradiology: A systematic review of current algorithms and approaches for the new wave of imaging technology. *Radiol. Artif. Intell.* **2020**, *2*, e190026. [CrossRef]
6. Liu, H.; Cui, G.; Luo, Y.; Guo, Y.; Zhao, L.; Wang, Y.; Subasi, A.; Dogan, S.; Tuncer, T. Artificial Intelligence-Based Breast Cancer Diagnosis Using Ultrasound Images and Grid-Based Deep Feature Generator. *Int. J. Gen. Med.* **2022**, *15*, 2271–2282. [CrossRef]
7. Thummalapalem, G.D.; Pradesh, A.; Vaddeswaram, G.D. Automated detection, segmentation and classification using deep learning methods for mammograms-a review. *Int. J. Pure Appl. Math.* **2018**, *119*, 627–666.
8. Wang, H.-Y.; Jiang, Y.-X.; Zhu, Q.-L.; Zhang, J.; Xiao, M.-S.; Liu, H.; Dai, Q.; Li, J.-C.; Sun, Q. Automated Breast Volume Scanning: Identifying 3-D Coronal Plane Imaging Features May Help Categorize Complex Cysts. *Ultrasound Med. Biol.* **2016**, *42*, 689–698. [CrossRef]
9. Berbar, M.A. Hybrid methods for feature extraction for breast masses classification. *Egypt. Inform. J.* **2018**, *19*, 63–73. [CrossRef]
10. Lou, J.-Y.; Yang, X.-L.; Cao, A.-Z. A Spatial Shape Constrained Clustering Method for Mammographic Mass Segmentation. *Comput. Math. Methods Med.* **2015**, *2015*, 891692. [CrossRef]
11. Liang, X.; Yu, J.; Liao, J.; Chen, Z. Convolutional Neural Network for Breast and Thyroid Nodules Diagnosis in Ultrasound Imaging. *BioMed Res. Int.* **2020**, *2020*, e1763803. [CrossRef] [PubMed]
12. Hassan, S.A.; Sayed, M.S.; Abdalla, M.I.; Rashwan, M.A. Detection of breast cancer mass using MSER detector and features matching. *Multimed. Tools Appl.* **2019**, *78*, 20239–20262. [CrossRef]
13. Hu, M.-K. Visual pattern recognition by moment invariants. *IEEE Trans. Inf. Theory* **1962**, *8*, 179–187.
14. Wason, J.M.; Mander, A.P. The choice of test in phase II cancer trials assessing continuous tumour shrinkage when complete responses are expected. *Stat. Methods Med. Res.* **2015**, *24*, 909–919. [CrossRef] [PubMed]
15. Cherif, W. Optimization of K-NN algorithm by clustering and reliability coefficients: Application to breast-cancer diagnosis. *Procedia Comput. Sci.* **2018**, *127*, 293–299. [CrossRef]
16. Sharma, S.; Mehra, R. Conventional Machine Learning and Deep Learning Approach for Multi-Classification of Breast Cancer Histopathology Images—A Comparative Insight. *J. Digit. Imaging* **2020**, *33*, 632–654. [CrossRef]
17. Podgornova, Y.A.; Sadykov, S.S. Comparative analysis of segmentation algorithms for the allocation of microcalcifications on mammograms. *Inf. Technol. Nanotechnol.* **2019**, *2391*, 121–127.
18. Zhang, X.; Yang, J.; Nguyen, E. Breast cancer detection via Hu moment invariant and feedforward neural network. *AIP Conf. Proc.* **2018**, *1954*, 030014.
19. Mata, B.N.B.U.; Meenakshi, D.M. Mammogram Image Segmentation by Watershed Algorithm and Classification through k-NN Classifier. *Bonfring Int. J. Adv. Image Process.* **2018**, *8*, 1–7. [CrossRef]
20. Sadhukhan, S.; Upadhyay, N.; Chakraborty, P. Breast Cancer Diagnosis Using Image Processing and Machine Learning. *Emerg. Technol. Model. Graph.* **2020**, *937*, 113–127.
21. Hao, Y.; Qiao, S.; Zhang, L.; Xu, T.; Bai, Y.; Hu, H.; Zhang, W.; Zhang, G. Breast Cancer Histopathological Images Recognition Based on Low Dimensional Three-Channel Features. *Front. Oncol.* **2021**, *11*, 2018. [CrossRef] [PubMed]
22. Hao, Y.; Zhang, L.; Qiao, S.; Bai, Y.; Cheng, R.; Xue, H.; Hou, Y.; Zhang, W.; Zhang, G. Breast cancer histopathological images classification based on deep semantic features and gray level co-occurrence matrix. *PLoS ONE* **2022**, *17*, e0267955. [CrossRef] [PubMed]
23. Joshi, A.; Mehta, A. Analysis of K- Nearest Neighbor Technique for Breast Cancer Disease Classification. *Int. J. Recent Sci. Res.* **2018**, *9*, 26126–26130.
24. Alshammari, M.M.; Almuhanna, A.; Alhiyafi, J. Mammography Image-Based Diagnosis of Breast Cancer Using Machine Learning: A Pilot Study. *Sensors* **2022**, *22*, 203. [CrossRef]
25. Agaba, A.J.; Abdullahi, M.; Junaidu, S.B.; Hassan Ibrahim, H.; Chiroma, H. Improved multi-classification of breast cancer histopathological images using handcrafted features and deep neural network (dense layer). *Intell. Syst. Appl.* **2022**, *14*, 200066–200076.
26. Xie, W.; Li, Y.; Ma, Y. Breast mass classification in digital mammography based on extreme learning machine. *Neurocomputing* **2016**, *173*, 930–941. [CrossRef]
27. Zhuang, Z.; Yang, Z.; Zhuang, S.; Joseph Raj, A.N.; Yuan, Y.; Nersisson, R. Multi-Features-Based Automated Breast Tumor Diagnosis Using Ultrasound Image and Support Vector Machine. *Comput. Intell. Neurosci.* **2021**, *2021*, 9980326. [CrossRef]

28. Shia, W.-C.; Chen, D.-R. Classification of malignant tumors in breast ultrasound using a pretrained deep residual network model and support vector machine. *Comput. Med. Imaging Graph.* **2021**, *87*, 101829–101835. [CrossRef]
29. Wan, K.W.; Wong, C.H.; Ip, H.F.; Fan, D.; Yuen, P.L.; Fong, H.Y.; Ying, M. Evaluation of the performance of traditional machine learning algorithms, convolutional neural network and AutoML Vision in ultrasound breast lesions classification: A comparative study. *Quant. Imaging Med. Surg.* **2021**, *11*, 1381–1393. [CrossRef]
30. Moldovanu, S.; Damian Michis, F.A.; Biswas, K.C.; Culea-Florescu, A.; Moraru, L. Skin Lesion Classification Based on Surface Fractal Dimensions and Statistical Color Cluster Features Using an Ensemble of Machine Learning Techniques. *Cancers* **2021**, *13*, 5256. [CrossRef]
31. Damian, F.A.; Moldovanu, S.; Dey, N.; Ashour, A.S.; Moraru, L. Feature Selection of Non-Dermoscopic Skin Lesion Images for Nevus and Melanoma Classification. *Computation* **2020**, *8*, 41. [CrossRef]
32. Al-Dhabyani, W.; Gomaa, M.; Khaled, H.; Fahmy, A. Dataset of breast ultrasound images. *Data Brief* **2020**, *28*, 104863. [CrossRef] [PubMed]
33. Labuda, N.; Seeliger, J.; Gedrande, T.; Kozak, K. Selecting Adaptive Number of Nearest Neighbors in k-Nearest Neighbor Classifier Apply Diabetes Data. *J. Math. Stat. Sci.* **2017**, *2017*, 1–13.

inventions

Article

The Influence of Different Type Materials of Grit Blasting on the Corrosion Resistance of S235JR Carbon Steel

Nicoleta Bogatu [1], Alina Crina Muresan [1], Laurentiu Mardare [1,2], Viorica Ghisman [1], Anca Ravoiu [1,3,*], Floricel Maricel Dima [4,5,*] and Daniela Laura Buruiana [1]

[1] Interdisciplinary Research Centre in the Field of Eco-Nano Technology and Advance Materials CC-ITI, Faculty of Engineering, "Dunarea de Jos" University of Galati, 47 Domneasca Street, RO-800008 Galati, Romania
[2] Amrared Research Consulting, 54 Brailei Street, RO-800201 Galati, Romania
[3] Faculty of Medicine and Pharmacy, "Dunarea de Jos" University of Galati, 35 Al. I. Cuza Street, RO-800010 Galati, Romania
[4] Institute for Research and Development in Aquatic Ecology, Fishing and Aquaculture, 54 Portului Street, RO-800211 Galati, Romania
[5] Faculty of Engineering and Agronomy from Braila, 29 Calea Calarasilor Street, RO-810017 Braila, Romania
* Correspondence: anca.ravoiu@ugal.ro (A.R.); dima.floricel.maricel@asas-icdeapa.ro or dimafloricel@yahoo.com (F.M.D.)

Abstract: The aim of this paper is to evaluate the corrosion rate expressed in material loss per unit of time and the surface properties of carbon steel type S235JR blasted with different types of materials (quartz, alumina, and red garnet with a particle size between 60 and 80 mesh (0.25–0.60 mm)). The estimation of corrosion rate was determined by electrochemical methods, such as open circuit potential (OCP), polarization resistance (R_p), corrosion rate (V_{corr}), and gravimetric method by immersing the samples in 3.5% NaCl solution for a period of 336 h. All surfaces were characterized before and after corrosion tests using ex-situ characterizations, such as optical microscopy and roughness analysis. The results indicate that S235JR non-sandblasted exhibited higher polarization resistance, the lowest corrosion rate, and the lowest roughness values. While for the S235JR sandblasted groups, reduced corrosion resistance and increasing roughness values were noted. From the sandblasted groups, the lowest corrosion resistance and the highest value of roughness are attributed to the S235JR surface sandblasted with quartz. The S235JR surface sandblasted with quartz shows a decrease in corrosion resistance approximately two times lower than the non-sandblasted surface and an increasing of roughness approximately six times greater than the non-sandblasted surface.

Keywords: S235JR carbon steel; corrosion rate; sandblasting; roughness; optical microscopy

Citation: Bogatu, N.; Muresan, A.C.; Mardare, L.; Ghisman, V.; Ravoiu, A.; Dima, F.M.; Buruiana, D.L. The Influence of Different Type Materials of Grit Blasting on the Corrosion Resistance of S235JR Carbon Steel. *Inventions* **2023**, *8*, 39. https://doi.org/10.3390/inventions8010039

Academic Editors: Craig E. Banks and Zhengyi Jiang

Received: 31 December 2022
Revised: 17 January 2023
Accepted: 30 January 2023
Published: 2 February 2023

Copyright: © 2023 by the authors. Licensee MDPI, Basel, Switzerland. This article is an open access article distributed under the terms and conditions of the Creative Commons Attribution (CC BY) license (https://creativecommons.org/licenses/by/4.0/).

1. Introduction

Metals and alloys are widely used as building materials and not only [1]. Steel is a common material widely used for the construction of naval, offshore, mechanical, and civil engineering structures [2]. Carbon steel S235JR is a material mainly intended for the construction of industrial and residential facilities, parts of power transmission towers, equipment elements, offshore structures, car bridges, oil, and gas platforms, as well as other structures [2]. It presents advantages, such as good mechanical resistance and extremely low cost, compared to other types of materials [3,4]. The main disadvantage of these types of materials is their tendency to corrode, which limits their applications [5,6].

Corrosion is a phenomenon that affects the aesthetics of these structures and, more than that, reduces the resistance of the structures over time [7,8].

The surface treatment of metallic materials is one of the most important factors governing their resistance. There are many methods of pretreatment of the surface of the materials. The most common treatments are mechanical, chemical, and electrochemical methods [9,10]. Mechanical methods consist of roughening processes, such as sandblasting, polishing, or abrasion [11]. Sandblasting is a mechanical surface treatment that consists of forcefully propelling a stream of non-metallic or metallic particles onto the surface to be treated, to remove contaminated layers, modify surface roughness, promote mechanical anchoring, and increase free energy of the surface by increasing the thermodynamic interactions at the interface of the bonded materials [12].

Sandblasting could also affect the chemical composition, crystal structure, microstiffness thermal expansion coefficient, resistance, and microstructure on the surface of the material. Sandblasting could also be used as a mechanical surface treatment for various materials, such as titanium alloys, steel, and aluminum, etc. The deformation caused by this type of surface treatment is inhomogeneous [13,14].

As a surface treatment method, sandblasting is commonly used for surface modification, surface strength enhancement, surface cleaning, and rust removal. Therefore, a smoother surface can be obtained by sandblasting in general [15,16].

During the sandblasting process, the surface of metal materials is repeatedly blasted by sand particles or other hard particles at high speed, which leads to the removal of the oxide layer from the surface, at the same time, generating the effect of severe local plastic deformation [12,17].

During sandblasting, the shocks produced between the sand particles and the surface of the steel structure cause serious damage to the surface. This is manifested by the erosion of craters of different shapes and depths present on the surface of the metal material, the thickness of the wall is gradually reduced, and the rupture occurs when the stresses in the crater reach a limiting threshold [12,17]. The sand erosion process improves fatigue strength under tension. This improvement comes from the introduction of compressive residual stresses to the hardened surface layers [18,19].

The aim of this paper is to determine the corrosion resistance by electrochemical and gravimetric methods of carbon steel S235JR sandblasted with different materials (quartz, alumina, and red garnet) over a period of 14 days by immersing the materials in 3.5% NaCl solution. The influence of the roughness, the pH of the solution, and the evolution of the optical micrographs of the surface before and after the corrosion process are also discussed. The novelty of the study consists in adding to the specialized literature a study that has not been reported before. Respectively, the influence of different types of sandblasting materials on the corrosion resistance of S235JR steel immersed for a period of 14 days in the 3.5% NaCl solution simulating the seawater environment will be investigated.

In the specialized literature, there are very few studies that treat the effect of sandblasting on the corrosion resistance of different types of steels, and the results are contradictory [15,20–25]. Some studies show that sandblasting decreases corrosion resistance [21,25], while others claim that sandblasting increases corrosion resistance [15,20,22–24].

The importance of the study consists in the fact that sandblasting is one of the most effective methods of cleaning or finishing the surfaces of any type of solid material with the help of sandblasting grits. The metal surfaces that have been cleaned and from which the oxides have been removed can be covered with anti-corrosive protective films resistant to the action of aggressive environmental factors [25].

Steels sandblasted and covered with anti-corrosive films can be part of maritime structures, civil and industrial architecture structures and elements [2].

Practically, the effective life of an anti-corrosion film depends a lot on the way the steel surface was prepared before painting. The influence of sandblasting on the corrosion resistance of steel before the application of anti-corrosion protection is an important factor.

Because sandblasting also determines the appearance of deep grooves that can capture the corrosion products formed in the upper part of the surfaces, favoring the appearance of micro reactions, generating pitting corrosion, thus affecting the life of the anti-corrosion protections [25].

At the same time, the corrosion under the coating often progresses locally, leading to the collapse of the structures in some cases or to the breaking of the steel elements [4].

Therefore, the surface treatment method before applying anticorrosive coatings is crucial for protecting steel structures against corrosion [4]. In this work, quartz was used as a material for sandblasting because it is a material that consists mainly of quartz (which is a durable crystal) that allows for efficient sandblasting, it is also cheap and very easy to find compared to other types of materials. The main disadvantage of this sandblasting material is the fact that once inhaled, it is harmful to the human body [26].

The red garnet grit used in the sandblasting process was used because it is an ecological material that has the advantage of being able to be recycled several times [27].

Alumina (Al_2O_3) was selected due to the numerous properties that recommend it for use in structural and tribological applications, being a combination of high hardness, heat resistance, chemical inertness, and commercial availability [28].

2. Materials and Methods

In the present experimental study, S235JR steel (purchased from Mairon Galati, Romania) was used, whose chemical composition is indicated in Table 1.

Table 1. Chemical composition of S235JR steel [%].

C	Mn	Si	P	S	N	Cu	Fe
0.17	1.40	0.025	0.028	0.025	0.12	0.45	Balance

The samples used in this study were cut from a steel plate with dimensions of 500 × 500 × 2 mm and brought to the size of 23 × 23 × 2 mm.

Prior to the gravimetric method and electrochemical measurements, the S235JR non-sandblasted were treated with mechanical grinding with 1200 grit SiC emery sandpaper in order to remove the layer of native oxide formed instantaneously on the surface of S235JR steel in contact with the environment. After cutting the samples to the desired dimensions, they were sandblasted with three different types of sandblasting materials that had different chemical compositions. However, with the same grain of the sandblasting grits for quartz, red garnet, and the alumina (ABRAZIV TRADE SRL, Mureș, Romania) used, respectively, 30/60 Mesh [0.25–0.60 mm] and their technical data are listed in Table 2.

Table 2. Technical data of sandblasting grits.

Type of Sandblasting Grit	Hardness [Mohs]	Chemical Composition	Shape of Particles	Grain Size [mm]	Density [g/cm^3]
Quartz	7	SiO_2: 99% Fe_2O_3: 0.2% Other: 0.8%	rounded, yellowish white	0.25–0.60 mm	1.63
Red garnet	8	Almandine: 98% Ilmenite: 1% Quartz: 0.5% Other: 0.5%	angular		2.4
Alumina (white electrocorundum)	9.2	Al_2O_3: 99.52% Fe_2O_3: 0.029% SiO_2: 0.034% Na_2O: 0.26% Other: 0.16%	angular		3.85

The mechanical sandblasting process was done with the help of the Seltech brand-sandblasting equipment, which has a capacity of 80 L, an air flow of 600 L, and a working pressure of 6 bar. The size of the ceramic nozzle was 3.5 mm.

The samples were sandblasted at a 45° angle. The schematic drawing of the blasting process of the S235JR steel samples is illustrated in Figure 1. The sandblasting was done according to the ISO 8501 standard, which is the international standard for dry abrasive blasting, at the S_a (degree of cleaning) $2\,\frac{1}{2}$ blasting level [29].

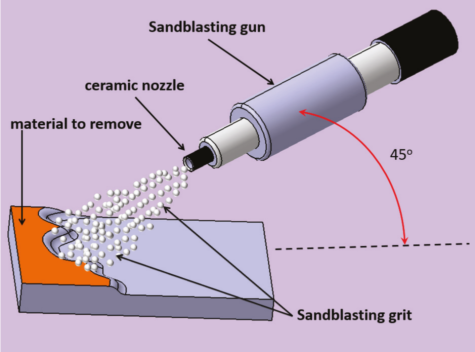

Figure 1. Schematic drawing of the sandblasting process used for S235JR steel samples.

After sandblasting, the samples were blown with air to remove the excess dust formed after the sandblasting process.

For the electrochemical tests, the S235JR non-sandblasted and sandblasted S235JR carbon steel samples were bonded to a copper wire. After that, they were insulated with epoxy resin to obtain an active surface area of 5.29 ± 0.3 cm^2. The electrochemical equipment PGP 201 connected to a PC was used for electrochemical investigations, on which the VoltaMaster version 5.10 software runs.

The electrochemical cell used to evaluate the corrosion behavior of the sandblasted and untreated S235JR carbon steel is a classic cell made of glass with a maximum volume of 250 mL composed of three electrodes where (1) the working electrode (the material to be studied in our case, the steel S235JR sandblasted and non-sandblasted), (2) the reference electrode (Ag/AgCl inside which is saturated KCl solution, which has a potential of +199 mV vs. SHE (standard hydrogen electrode) and (3) an auxiliary electrode made of Pt.

Before and after each experiment, both the analyzed sample and the counter electrode were washed with distilled water, and the volume of electrolyte (3.5% NaCl solution) used for each experiment was kept constant at 150 mL. The 3.5% NaCl solution was prepared with distilled water by dissolving the NaCl p.a reagent (purchased from Sigma-Aldrich).

The physical-chemical parameters of the 3.5% NaCl solution before and after the corrosion process were measured using a Toledo S20k pH meter, and the resulting values are presented in Table 3.

Table 3. Physical-chemical parameters of 3.5% NaCl solution before and after the corrosion process.

Parameters	**3.5% NaCl**			
	before Corrosion Process			
	S235JR—Non-Sandblasted	**S235JR—Sandblasted with Quartz**	**S235JR—Sandblasted with Garnet**	**S235JR—Sandblasted with Alumina**
pH	6.73 ± 0.2			
Conductivity [mS/cm]	42.3 ± 1			
Salinity [ppt]	26.5 ± 0.5			
	after Corrosion Process			
pH	7.11 ± 0.3	7.96 ± 0.5	7.88 ± 0.2	7.80 ± 0.1
Conductivity [mS/cm]	43.5 ± 0.5	43.7 ± 0.9	43.6 ± 0.6	43.1 ± 0.3
Salinity [ppt]	26.8 ± 0.1	26.5 ± 0.4	27.3 ± 0.7	27.1 ± 0.5

The tests were performed at room temperature, respectively 22 ± 1 °C. All studied samples were repeated three times to verify the reproducibility of the experimental data. After immersing the sample in the 3.5% NaCl solution, sequences of electrochemical measurements of OCP (open circuit potential or free potential), $R_{p,}$ and V_{corr} (polarization resistance and corrosion rate) were performed as follows.

(a) At $T_1 = 0$ (immersion):
- OCP_1 with a duration of 60 min, meas period 0.6 s.
- R_{p1}-V_{corr1}, determine 30 points, scan rate = 1 mV/s, over voltage = 40 mV, OCP duration = 1 min

(b) At T_2 = (after 336 h):
- OCP_2 with a duration of 60 min, meas period 0.6 s.
- R_{p2}-V_{corr2}, determine 30 points, scan rate = 1 mV/s, over voltage = 40 mV, OCP duration = 1 min

Each measurement sequence (R_p-V_{corr}) contains 30 value points calculated by using the Stern–Geary equation (Equations (1) and (2)).

$$i_{cor} = \frac{B}{R_p} \tag{1}$$

$$B = \frac{b_a|b_c|}{2.303(b_a+|b_c|)} \tag{2}$$

where i_{cor} = corrosion current density, B = the specific constant, R_p = polarization resistance, b_a = are the Tafel slopes for anodic, and $b_{c\,=}$ Tafel slopes for cathodic reactions.

It should be mentioned that the samples were not taken out of the solution during the experiment until after the passage of 336 h. The obtained results were interpreted with the help of the Origin 2022 program.

In order to determine by the gravimetric method, the loss of material caused by the corrosion process, the sandblasted and untreated S235JR steel samples were weighed before and after immersing the samples for 336 h in 3.5% NaCl. Weighing the samples before and after the corrosion process was done using a Kern EWJ 300-3H analytical balance, which has a measurement accuracy of ±0.1 g. The samples were immersed in a 3.5% NaCl solution in hermetically sealed sterile vials that had a solution volume of 40 mL. The tests were done at room temperature 22 ± 1 °C and repeated three times. The images of the immersed samples before and after 336 h from immersion in 3.5% NaCl are presented in Figure 2.

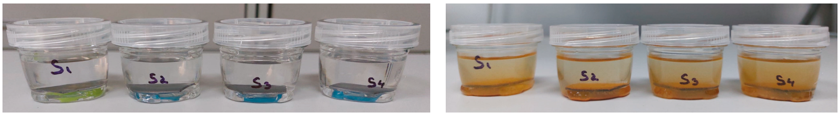

(**a**) (**b**)

Figure 2. Images of S235JR steel samples for (S1)—S235JR—non-sandblasted, (S2)—S235JR—sandblasted with quartz, (S3)—S235JR—sandblasted with garnet, (S4)—S235JR—sandblasted with alumina: (**a**) at T_1 = at immersion, (**b**) T_2 = after 336 h from immersion time.

After weighing, weight loss was evaluated using ASTM G1-90 (1999) with Equations (3) and (4) below, respectively [30,31]:

$$\Delta W = W1 - W2 \tag{3}$$

$$\Delta w = \frac{\Delta W}{S \cdot t} \tag{4}$$

where ΔW is weight loss in g, W_1 is the initial weight of the sample before immersion, W_2 is the final weight of the sample after immersion, Δw is the gravimetric index of the sample in g/m^2 h, S is the surface area of the sample in m^2 and t—is exposure time in hours.

The corrosion rate in mm year^{-1} was evaluated from weight loss data using the relation Equation (5):

$$CR\left(mm\ year^{-1}\right) = \frac{\Delta W \cdot K}{\rho \cdot A \cdot t} \tag{5}$$

where ΔW is weight loss in grams, ρ is metal density in g cm^{-3}, A is the area of the sample in cm^2, t—is exposure time in hours, and K is a constant depending on the unit of measurement of the corrosion speed according to ASTM G1-90 (1999) (=87.600).

To highlight the variations suffered by the studied samples before and after the corrosion process, a Kern OBE114 metallurgical microscope was used.

The topographical characterization in terms of obtaining 2D roughness profiles was measured using a Mitutoyo Surftest SJ-210 Series roughness meter by moving the feeler needle on the surface of the studied samples over a distance of 4 mm and with a speed of 0.20 µm/s. A number of three samples from each set were analyzed, on which three measurements were performed in different areas on each sample. After which the average roughness parameters R_a (arithmetic roughness average), R_q (average maximum peak to valley distance for five sampling lengths within the measurement length), and R_z (the difference between the deepest valley and the tallest peak in the surface) [32] were calculated.

3. Results and Discussion

3.1. Electrochemical Measurements and Gravimetric Method Results Used to Determine the Corrosion of Tested Samples

3.1.1. Open Circuit Potential

The open circuit potential (OCP) method is the first method applied in a protocol for determining the corrosion rate. It should be mentioned that this method is not a quantitative method for determining corrosion but rather a qualitative method that indicates the oxidation tendency of a surface/material studied in an electrochemical environment [31].

Figure 3a,b shows the evolution of the free potential of surfaces studied at (a) (T_1 = immersion time) and (b) after 336 h from immersion (T_2).

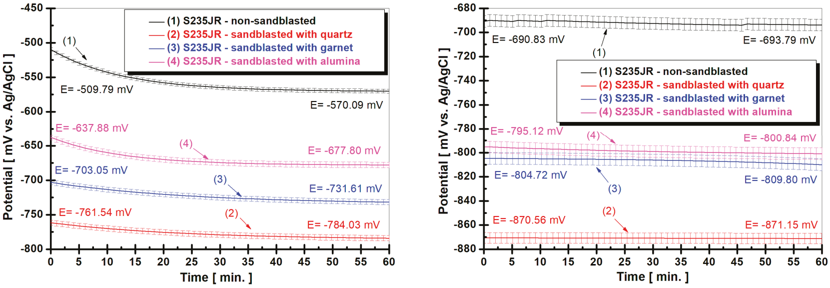

(**a**) (**b**)

Figure 3. Evolution of free potential of S235JR steel samples immersed in 3.5% NaCl solution for (1) S235JR—non-sandblasted, (2)—S235JR—sandblasted with quartz, (3)—S235JR—sandblasted with garnet, (4)—S235JR—sandblasted with alumina: (**a**) at T_1 = at immersion, (**b**) T_2 = after 336 h from immersion time.

From Figure 3, it can be observed that the values of the free potential upon immersion of all studied surfaces have a tendency to move towards more negative values, being more pronounced in the case of sandblasted surfaces compared to the untreated surface.

The movement of the free potential towards more negative values indicates the inability of the material to form a protective oxide film on its surface, while the stationary state indicates that the surface has reached a state of equilibrium (it neither dissolves nor forms the oxide layer on the surface of the samples) [25]. If for S235JR—non-sandblasted (curve 1), the value of the free potential at immersion (Figure 3a) is E = −509.79 ± 24 mV vs. Ag/AgCl at the end of the first measurement period reaches E = −570.09 ± 32 mV vs. Ag/AgCl, the potential difference between the two values being 60.3 mV more negative than the free potential value from immersion.

For the same surface studied, it can be observed that after 336 h from immersion, the value of the free potential decreases compared to the first measurement period (during immersion), however, stabilizing around the value of −693 mV.

For S235JR—sandblasted with quartz (curve 2) it can be observed that at immersion (Figure 3a), it has a value of E = −761.54 ± 17 mV vs. Ag/AgCl reaching the end of the measurement at the value of E = −784.03 ± 31 mV vs. Ag/AgCl, ΔE in this case, being 22.49 mV lower than the value from immersion. Moreover, for the same surface studied (Figure 3b), a decrease in the values of the free potential can be observed compared to the first measurement period. The same tendency of the free potential moving towards more negative values with increasing immersion time is also observed for S235JR—sandblasted with garnet (curve 3) and S235JR—sandblasted with alumina (curve 4).

Comparing all the surfaces studied, it can be seen that the free potential values are more negative for S235JR—sandblasted with quartz, S235JR—sandblasted with garnet, and S235JR—sandblasted with alumina as compared to S235JR—non-sandblasted at both period time measured.

A displacement of the potential towards more negative values (behavior indicating dissolution of the oxide layer) in the case of sandblasted surfaces was observed in the specialized literature also by other authors [25]. This behavior can be attributed to the increase in the roughness of a surface that causes an increase in corrosion processes because the roughness influences the corrosion potential favoring the appearance of corrosion pits [33].

3.1.2. Evolution of Polarization Resistance and Corrosion Rate (R_p-V_{corr})

The Rp method is a corrosion monitoring method that makes it possible to measure the corrosion rate in real time and directly [31].

The corrosion current calculated with this method, represents the current that occurs at the metal-medium (corrosive) interface when the metal is immersed in the electrolyte [31].

The variation of the polarization resistance for the studied surfaces immersed in the 3.5% NaCl solution at (a) (T_1 = immersion time) and (b) after 336 h from immersion (T_2) is presented in Figure 4a,b.

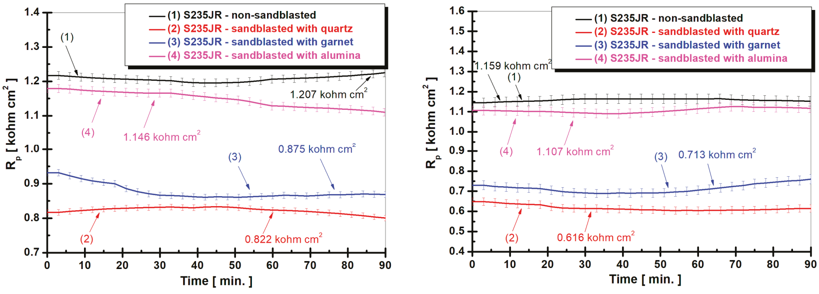

(**a**) (**b**)

Figure 4. Evolution of polarization resistance (R_p) of S235JR steel samples immersed in 3.5% NaCl solution for (1) S235JR—non-sandblasted, (2)—S235JR—sandblasted with quartz, (3)—S235JR—sandblasted with garnet, (4)—S235JR—sandblasted with alumina: (**a**) at T_1 = at immersion, (**b**) T_2 = after 336 h from immersion time.

From Figure 4a, it can be observed that the values of the polarization resistance at both studied times decrease in the case of the sandblasted samples compared to the value obtained for the untreated surface. If for S235JR—non-sandblasted (curve 1) the R_p value after one hour from immersion is 1.207 ± 0.04 kohm cm^2, for S235JR—sandblasted with quartz (curve 2) the lowest R_p value is 0.822 ± 0.06 kohm cm^2, the difference between these

2 values being 0.385 kohm cm^2. A high value of polarization resistance means a low value of corrosion rate.

For S235JR—sandblasted with garnet (curve 3), it is observed that the R_p value = 0.875 ± 0.03 kohm cm^2, a value which is also lower than S235JR—non-sandblasted (curve 1) with 0.332 kohm cm^2 but higher than S235JR—sandblasted with quartz (curve 2) with 0.53 kohm cm^2.

For S235JR—sandblasted with alumina (curve 4), it can be seen that the R_p value is 1.146 ± 0.05 kohm cm^2 with 0.061 kohm cm^2 lower than S235JR—non-sandblasted but higher than S235JR—sandblasted with quartz with 0.324 kohm cm^2 and 0.271 kohm cm^2 compared to S235JR—sandblasted with garnet.

After 336 h from immersion, Figure 4b shows a decrease in all polarization resistance values compared to the values obtained in Figure 4a after one hour from immersion.

If after one hour of immersion, S235JR—non-sandblasted has a value of 1.207 ± 0.04 kohm cm^2, after 336 h of immersion, this sample reaches a value of 1.159 ± 0.06 kohm cm^2, the value decrease in this case is 0.048 kohm cm^2 compared to the first measurement period. In the case of S235JR—sandblasted with quartz, the difference between the first measurement period and the second measurement period is 0.206 kohm cm^2. At S235JR—sandblasted with garnet, the difference between the first measurement period and the second measurement period is 0.162 kohm cm^2. For S235JR—sandblasted with alumina, the difference between the first measurement period and the second measurement period is 0.039 kohm cm^2.

The variation of the corrosion rate expressed as a penetration index for the studied surfaces at (a) (T_1 = immersion time) and (b) after 336 h from immersion (T_2) is shown in Figure 5a,b.

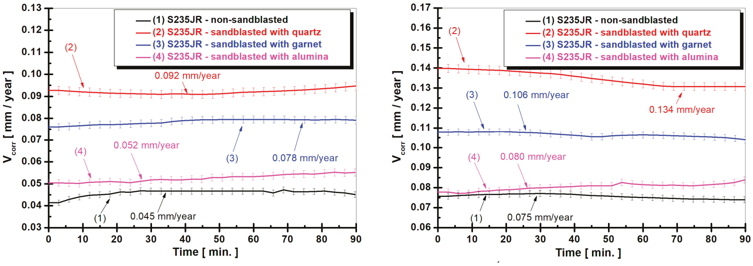

(**a**) (**b**)

Figure 5. Evolution of corrosion rate (V_{corr}) of S235JR steel samples immersed in 3.5% NaCl solution for (1) S235JR—non-sandblasted, (2)—S235JR—sandblasted with quartz, (3)—S235JR—sandblasted with garnet, (4)—S235JR—sandblasted with alumina: (**a**) at T_1 = at immersion, (**b**) T_2 = after 336 h from immersion time.

From the analysis of Figure 5a, it can be observed that the values of the corrosion rate at both studied times increase in the case of the sandblasted samples compared to the value obtained for the untreated surface.

If for S235JR—non-sandblasted (curve 1), the V_{corr} value after one hour of immersion is 0.045 ± 0.02 mm/year, for S235JR—sandblasted with quartz (curve 2) the highest V_{corr} value is 0.092 ± 0.04 mm/year, the difference between these two values being 0.047 mm/year.

It is well known that R_p is inversely proportional to V_{corr}. A high value of polarization resistance means a low value of corrosion rate [31].

For S235JR—sandblasted with garnet (curve 3), it is observed that the V_{corr} value = 0.078 ± 0.05 mm/year, a value which is also higher than S235JR—non-sandblasted (curve 1) with 0.033 mm/year but lower than S235JR—sandblasted with quartz (curve 2) with 0.014 mm/year.

For S235JR—sandblasted with alumina (curve 4), it can be seen that the V_{corr} value is 0.052 ± 0.04 mm/year with 0.007 mm/year higher than S235JR—non-sandblasted (curve 1) but lower than S235JR—sandblasted with quartz (curve 2) with 0.04 mm/year and 0.026 mm/year compared to S235JR—sandblasted with garnet (curve 3).

After 336 h of immersion, Figure 5b shows an increase in all V_{corr} values compared to the values obtained in Figure 5a after one hour of immersion.

If after one hour of immersion, S235JR—non-sandblasted (curve 1) has a value of 0.045 ± 0.02 mm/year, after 336 h of immersion, this sample reaches a value of 0.075 ± 0.05 mm/year, the increase of the V_{corr} value, in this case, being with 0.03 mm/year higher than the first measurement period. In the case of S235JR—sandblasted with quartz (curve 2), the difference between the first measurement period and the second measurement period is 0.042 mm/year.

At S235JR—sandblasted with garnet (curve 3), the difference between the first measurement period and the second measurement period is 0.028 mm/year, and for S235JR—sandblasted with alumina (curve 4), the difference between the first measurement period and the second measurement period is 0.028 mm/year.

A decrease in the corrosion resistance in the case of other sandblasted materials was also observed in the literature by other authors [21,25].

From the electrochemical results, it can be seen that the S235JR non-sandblasted surface shows the highest corrosion resistance. This behavior is possible due to the fact that the non-sandblasted surface has a lower roughness value compared to sandblasted surfaces.

The lowest corrosion resistance is obtained by the S235JR sandblasted with quartz, which has a corrosion resistance approximately two times lower compared to the non-sandblasted surface. This behavior is due to the increase in roughness value approximately six times higher compared to the non-sandblasted surface. Sandblasting increases the roughness and determines the appearance of deep grooves that can capture the corrosion products formed in the upper part of the surfaces, favoring the appearance of micro reactions, thus generating pitting corrosion [33].

Table 4 shows the values of the corrosion rate and the gravimetric index calculated according to the formulas presented in the material and methods chapter.

Table 4. The weight loss of the S235JR steel samples for S235JR—non-sandblasted, S235JR—sandblasted with quartz, S235JR—sandblasted with garnet, and S235JR—sandblasted with alumina during 336 h from immersion time.

Parameters	**Sample Code**			
	S235JR—Non-Sandblasted	**S235JR—Sandblasted with Quartz**	**S235JR—Sandblasted with Garnet**	**S235JR—Sandblasted with Alumina**
$W1$ [g]	6.0982 ± 0.003	5.9829 ± 0.009	5.4550 ± 0.006	5.4520 ± 0.002
$W2$ [g]	6.0875 ± 0.002	5.9630 ± 0.007	5.4394 ± 0.003	5.4393 ± 0.001
S [m^2]	0.0529 ± 0.003			
t [h]	336			
K	87.600			
ρ [g cm^{-3}]	7.87			
Δw [g/m^2 h]	$6.07 \pm 0.03 \times 10^{-4}$	$1.11 \pm 0.06 \times 10^{-3}$	$8.77 \pm 0.04 \times 10^{-4}$	$7.14 \pm 0.02 \times 10^{-4}$
CR [mm year^{-1}]	0.067 ± 0.004	0.124 ± 0.009	0.097 ± 0.005	0.074 ± 0.003

From Table 4, it can be seen that, in the case of the results determined by the gravimetric method, the trend of the samples after 336 h of immersion in the 3.5% NaCl solution remains the same as that determined by the electrochemical method. Thus, it can be seen that the corrosion rate increases in the case of sandblasted samples compared to the non-sandblasted

S235JR sample. This is mainly because the roughness of the surfaces increases compared to the untreated sample, favoring the occurrence of corrosion.

3.2. Surface Roughness Results of Tested Surfaces before and after Corrosion Process

Roughness is an important parameter in understanding the effect that surface topography has on the corrosion resistance of a material [33,34]. Figure 6a–d shows the surface roughness before corrosion, and Figure 7a–d shows the surface roughness after corrosion. Table 5 shows the average values of the obtained roughness parameters.

Table 5. Roughness parameter values for the tested surfaces before and after the corrosion process.

Parameters	**Sample Code**			
	before Corrosion Process			
	S235JR—Non-Sandblasted	**S235JR—Sandblasted with Quartz**	**S235JR—Sandblasted with Garnet**	**S235JR—Sandblasted with Alumina**
R_a [µm]	0.856 ± 0.01	5.548 ± 0.05	4.039 ± 0.02	3.749 ± 0.01
R_q [µm]	1.068 ± 0.1	6.805 ± 0.2	5.209 ± 0.4	4.826 ± 0.2
R_z [µm]	4.652 ± 0.3	31.723 ± 0.9	25.732 ± 0.5	25.291 ± 0.7
	after Corrosion Process			
R_a [µm]	1.153 ± 0.03	5.065 ± 0.03	3.642 ± 0.01	3.349 ± 0.02
R_q [µm]	1.422 ± 0.5	6.452 ± 0.6	4.881 ± 0.4	4.360 ± 0.3
R_z [µm]	6.894 ± 0.1	29.812 ± 0.3	25.571 ± 0.1	24.448 ± 0.5

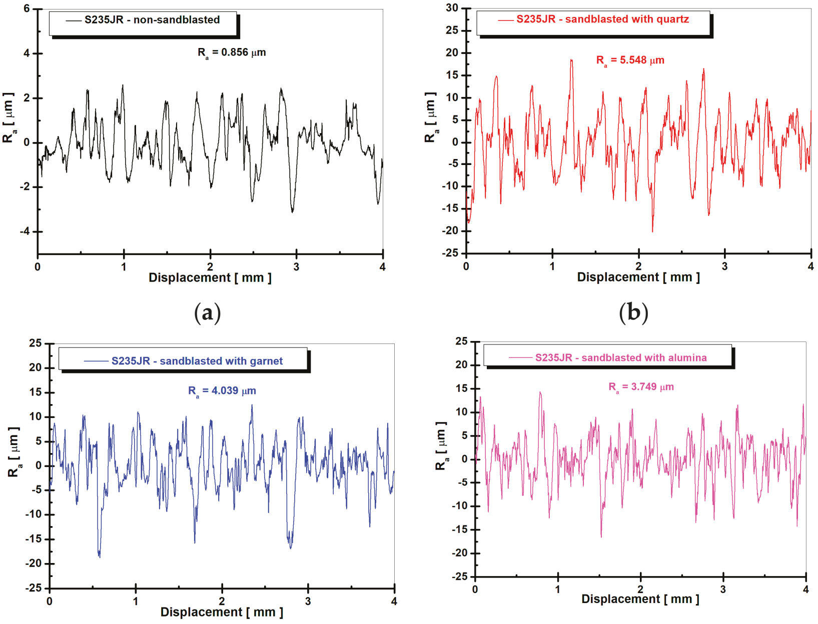

(**a**) (**b**)

(**c**) (**d**)

Figure 6. 2D surface profile of surface roughness before corrosion for: (**a**) S235JR—non-sandblasted, (**b**)—S235JR—sandblasted with quartz, (**c**)—S235JR—sandblasted with garnet, (**d**)—S235JR—sandblasted with alumina.

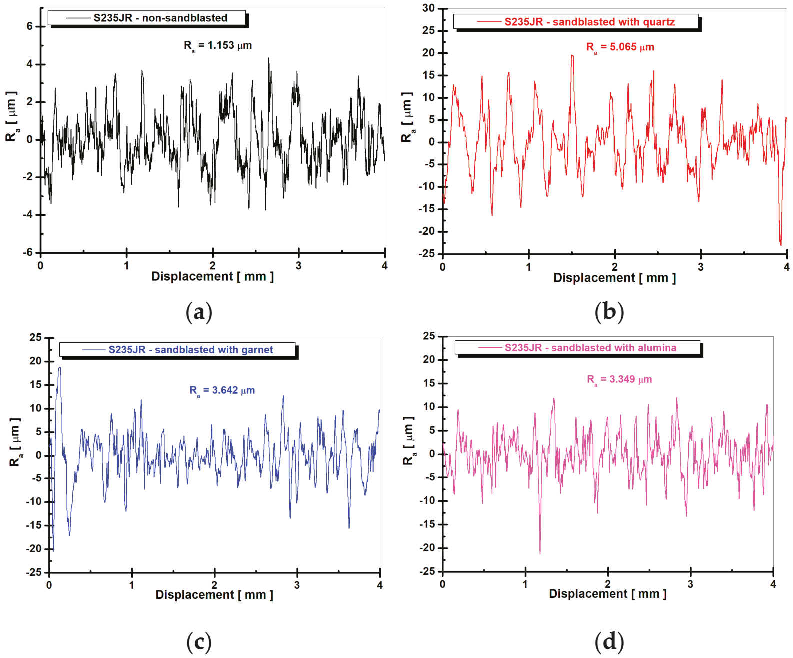

(**a**) (**b**) (**c**) (**d**)

Figure 7. 2D surface profile of surface roughness after corrosion of S235JR immersed during 336 h in 3.5 NaCl solution for: (**a**) S235JR—non-sandblasted, (**b**)—S235JR—sandblasted with quartz, (**c**)—S235JR—sandblasted with garnet, (**d**)—S235JR—sandblasted with alumina.

From the analysis of Figure 6, it can be seen that after the sandblasting process, the roughness of the samples increased compared to the S235JR—non-sandblasted steel sample (Figure 6a). If S235JR—non-sandblasted has a roughness of 0.856 ± 0.01 µm, it can be seen that S235JR—sandblasted with quartz (Figure 6b) has a roughness of 5.548 ± 0.05 µm, the increase of the roughness parameter, in this case, is 4.692 µm.

In the case of S235JR—sandblasted with garnet (Figure 6c), the roughness value has a value of 4.039 ± 0.02 µm, while S235JR—sandblasted with alumina (Figure 6d) has a value of 3.749 ± 0.01 µm. The increase in roughness after the sandblasting process was also observed in the specialized literature by other authors [25,32,35,36].

This behavior is explained in the specialized literature by the fact that during the sandblasting process, the surface of the samples is repeatedly sandblasted with hard particles at a very high speed, which leads to the removal of the superficial oxide layer formed on the surface of the samples generating at the same time a local plastic deformation and a micro cutting process (formation of irregular cavities with random distribution) in the surface layer [25,32].

From the analysis of Figure 7, an increase in roughness after the corrosion process can be observed in the case of S235JR—non-sandblasted (Figure 7a). If before the corrosion process, it had a roughness of 0.856 µm, after the corrosion process, it has a value of 1.153 µm. In this case, the increase of the parameter of roughness (R_a) is higher than the initial value with 0.297 µm.

This is possible due to the appearance of corrosion products on the surface of the sample that generated an inhomogeneous surface. In the case of the sandblasted samples, a decrease in the roughness parameter (R_a) after the corrosion process is observed compared to the values of the roughness parameter before the corrosion process.

In the case of samples sandblasted after the corrosion process, the roughness decreases due to the fact that the corrosion products formed on the surface of the layer fill the voids formed after sandblasting, resulting in a more uniform surface [33].

According to Evgeny Barmatov and his team [33], sandblasting is a process that causes surface defects, plastic deformations, micro deformations, and changes in heterogeneity through the possible fragmentation of the particles used in the sandblasting process that reach the surface of the sandblasted materials [33]. Sandblasting also determines the appearance of deep grooves that can capture the corrosion products formed in the upper part of the surfaces, favoring the appearance of micro reactions, thus generating pitting corrosion [25,33].

Thus, in the same study [33], the authors state that the increase in the roughness of a surface causes an increase in corrosion processes because the roughness influences the corrosion potential favoring the appearance of corrosion pits. While a less rough surface reduces, the occurrence of metastable pits by reducing the sites capable of being activated [33].

The results of the roughness tests presented in this study confirm the results obtained from the corrosion and optical microscopy study.

3.3. Optical Microscopy of Tested Surfaces before and after Corrosion

The surface of untreated S235JR steel, and blasted with quartz sand, red garnet, and white electrocorundum investigated by optical microscopy before and after corrosion tests in NaCl 3.5% to highlight the corrosive attack are shown in Figures 8a–d and 9a–d.

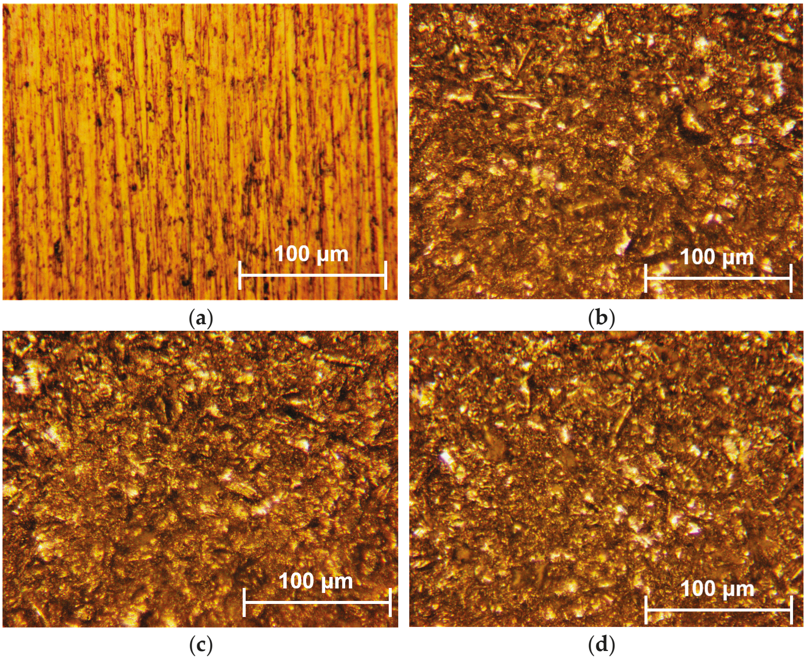

(**a**) (**b**) (**c**) (**d**)

Figure 8. Optical microscopy before corrosion of S235JR for: (**a**) S235JR—non-sandblasted, (**b**)—S235JR—sandblasted with quartz, (**c**)—S235JR—sandblasted with garnet, (**d**)—S235JR—sandblasted with alumina.

From the analysis of the images obtained with the help of optical microscopy before immersing the samples in the 3.5% NaCl solution, it can be observed that the surfaces are clean, without traces of corrosion products and defects.

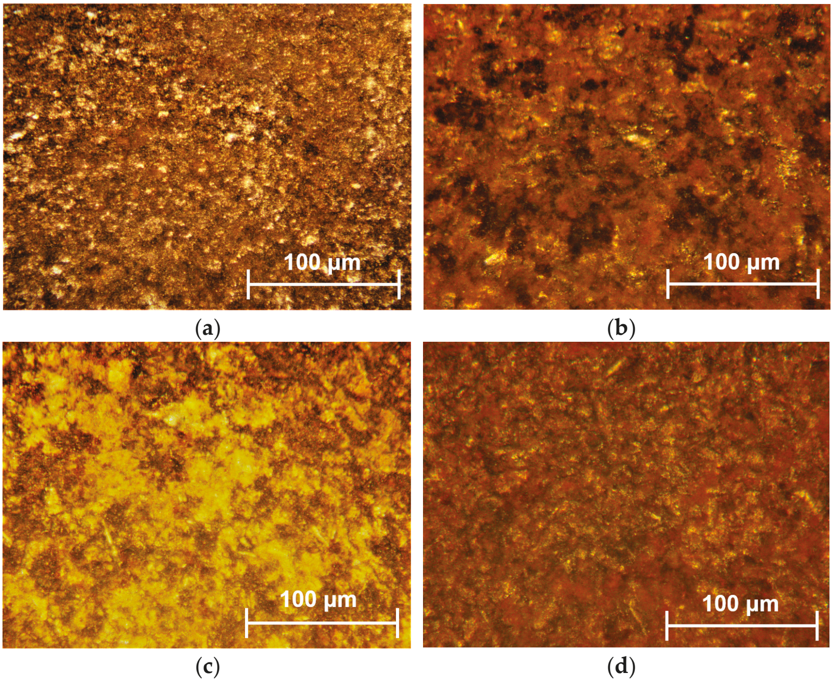

(**a**) (**b**)

(**c**) (**d**)

Figure 9. Optical microscopy after corrosion of S235JR immersed during 336 h in 3.5 NaCl solution for: (**a**) S235JR—non-sandblasted, (**b**)—S235JR—sandblasted with quartz, (**c**)—S235JR—sandblasted with garnet, (**d**)—S235JR—sandblasted with alumina.

From the analysis of the images after immersing the samples in the 3.5% NaCl solution for 336 h, it can be seen that the surfaces show corrosion products (rust products) that formed on the surface of the samples. The surface most affected by corrosion products is the surface of the S235JR—sandblasted with quartz (Figure 9b), which shows pitting corrosion. The pitting corrosion covers a high surface of S235JR—sandblasted with quartz, and the pits are deeper into the substrate. The least affected surface by corrosion products is the surface of the S235JR—non-sandblasted (Figure 9a), which shows more generalized corrosion at the surface of the materials without attacking the substrate. The optical microscopy images are in good agreement with all the measurements analysis presented in this study.

4. Conclusions

The present study describes the influence of different type materials of grit blasting on the corrosion resistance by immersing the samples in 3.5% NaCl solution for 336 h. As a result, the following conclusions were observed:

From the evolution of the free potential, a decrease in the free potential can be observed in the case of sandblasted samples compared to the untreated sample. After one hour from immersion, the studied samples show a shift of the free potential towards more negative values, indicating dissolution of the oxide layer on the surface of the samples.

From the electrochemical and gravimetric methods used to determine the corrosion resistance, it can be seen that sandblasting has a negative effect on the corrosion resistance of the S235JR steel. The highest corrosion resistance is observed for the S235JR non-sandblasted surface, which presents higher values of V_{corr} compared to the sandblasted surfaces. This behavior is possible due to the fact that the S235JR non-sandblasted surface has a lower roughness value compared to sandblasted surfaces.

The lowest corrosion resistance is obtained by the S235JR sandblasted with quartz, which has a corrosion resistance approximately two times lower compared to the non-sandblasted surface. This behavior is possible due to the increase in roughness value approximately six times higher compared to the non-sandblasted surface. Sandblasting increases the roughness and determines the appearance of deep grooves that can capture the corrosion products formed in the upper part of the surfaces, favoring the appearance of micro reactions, thus generating pitting corrosion. In the case of the S235JR steel surface sandblasted with garnet, a decrease in corrosion resistance of approximately 1.4 times less is observed compared to the non-sandblasted surface. For the surface of S235JR steel sandblasted with alumina, it can be seen that it has V_{corr} values, which are close to the V_{corr} values obtained by the non-sandblasted surface, indicating that sandblasting with alumina grit can be chosen as a method of steel preparation in order to prepare the surfaces for possible coatings. It was also observed that as the immersion time increases, the corrosion rate increases, a behavior observed on all studied surfaces.

From the roughness analysis, it can be seen that after the sandblasting process, the roughness of the sandblasted samples increases compared to the untreated surface. This behavior is due to the fact that the oxide layer formed on the surface of the sample is removed by sandblasting process, generating at the same time a local plastic deformation and a micro-cutting process (formation of irregular cavities with random distribution) in the surface layer.

After the corrosion process, the roughness of the sandblasted samples decreases due to the fact that the corrosion products formed on the surface of the layer fill the voids formed after sandblasting, resulting in a more uniform surface, while the roughness of the non-sandblasted surface studied increases. This behavior can be explained by the fact that the appearance of corrosion products on the surface of the sample generated an inhomogeneous surface.

Determining the corrosion behavior of a material used in various industrial applications represents one of the most important properties that determine its choice or replacement in a specific application. Thus, this study offers a deeper understanding of the effect that sandblasting has on the corrosion resistance of carbon steel S235JR, a material of major interest considering its wide range of uses in various industrial sectors.

Further studies will be done regarding the influence of the three presented sandblasting grits on the corrosion resistance of S235JR steel coated with different paints enriched with ceramic nanoparticles. The studies will be completed by the analysis of the corrosion products that appear on the surface of material.

Author Contributions: Conceptualization, N.B., F.M.D. and A.R.; methodology, N.B., A.C.M. and A.R.; software, L.M.; validation, N.B., A.C.M. and A.R.; formal analysis, V.G.; investigation, N.B., F.M.D. and A.R.; resources, D.L.B.; data curation, L.M.; writing—original draft preparation, N.B., A.C.M. and D.L.B.; writing—review and editing, N.B., A.C.M., A.R. and D.L.B.; visualization, V.G.; supervision, A.C.M. and D.L.B. All authors have read and agreed to the published version of the manuscript.

Funding: This research was funded by the project "PROINVENT", Contract no. 62487/03.06.2022—POCU/993/6/13—Code 153299, financed by the Human Capital Operational Programme 2014–2020 (POCU), Romania.

Data Availability Statement: The raw/processed data required to reproduce these findings cannot be shared at this time: as the data also form part of an ongoing study.

Acknowledgments: The work of Nicoleta Bogatu was supported by the project "PROINVENT", Contract no. 62487/03.06.2022—POCU/993/6/13—Code 153299, financed by the Human Capital Operational Programme 2014–2020 (POCU), Romania. In addition, the authors would like to acknowledge of the company ABRAZIV TRADE SRL, Mureș, Romania for donation the sandblasting materials.

Conflicts of Interest: The authors declare no conflict of interest.

References

1. Fang, C.K.; Chuang, T.H. Surface morphologies and erosion rates of metallic building materials after sandblasting. *Wear* **1999**, *230*, 156–164. [CrossRef]
2. Rajput, A.; Paik, J.K. Effects of naturally-progressed corrosion on the chemical and mechanical properties of structural steels. *Structures* **2021**, *29*, 2120–2138. [CrossRef]
3. Chelaru, J.D.; Mureşan, L.M. Study of S235 steel corrosion process in wastewater from the petrochemical industry. *Stud. UBB Chem.* **2019**, *LXIV 2 Tom II*, 323–333. [CrossRef]
4. Kim, A.; Kainuma, S.; Yang, M. Surface characteristics and corrosion behavior of carbon steel treated by abrasive blasting. *Metals* **2021**, *11*, 2065. [CrossRef]
5. Trela, J.; Chat, M.; Scendo, M. Influence of sodium molybdate (VI) on the corrosion of S235 carbon steel. *Chemik* **2015**, *69*, 592–599.
6. Lipiński, T. Corrosion of S235JR steel in NaCl environment at 3 °C. In Proceeding of the 26th International Conference on Metallurgy and Materials, Brno, Czech Republic, 24–26 May 2017.
7. Khalaj, G.; Pouraliakbar, H.; Arab, N.; Nazerfakhari, M. Correlation of passivation current density and potential by using chemical composition and corrosion cell characteristics in HSLA steels. *Measurement* **2015**, *75*, 5–11. [CrossRef]
8. Kiahosseini, S.R.; Mohammadi Baygi, S.J.; Khalaj, G.; Khoshakhlagh, A.; Samadipour, R. A study on structural, corrosion, and sensitization behavior of ultrafine and coarse grain 316 stainless steel processed by multiaxial forging and heat treatment. *J. Mater. Eng. Perform.* **2017**, *27*, 271–281. [CrossRef]
9. Burduhos-Nergis, D.-P.; Vizureanu, P.; Sandu, A.V.; Bejinariu, C. Phosphate surface treatment for improving the corrosion resistance of the C45 carbon steel used in carabiners manufacturing. *Materials* **2020**, *13*, 3410. [CrossRef]
10. Burduhos-Nergis, D.-P.; Vizureanu, P.; Sandu, A.V.; Bejinariu, C. Evaluation of the corrosion resistance of phosphate coatings deposited on the surface of the carbon steel used for carabiners manufacturing. *Appl. Sci.* **2020**, *10*, 2753. [CrossRef]
11. Rudawska, A.; Danczak, I.; Müller, M.; Valasek, P. The effect of sandblasting on surface properties for adhesion. *Int. J. Adhes. Adhes.* **2016**, *70*, 176–190. [CrossRef]
12. Bechikh, A.; Klinkova, O.; Maalej, Y.; Tawfiq, I.; Nasri, R. Sandblasting parameter variation effect on galvanized steel surface chemical composition, roughness and free energy. *Int. J. Adhes. Adhes.* **2020**, *102*, 102653. [CrossRef]
13. Geng, S.; Sun, J.; Guo, L. Effect of sandblasting and subsequent acid pickling and passivation on the microstructure and corrosion behavior of 316L stainless steel. *Mater. Des.* **2015**, *88*, 1–7. [CrossRef]
14. Petrov, Y.M.; Vasiliev, M.O.; Trofimova, L.M.; Filatova, V.S. Layer-by-layer evolution of a microstructure in a Cu–Zn alloy after sandblasting. *Usp. Fiz. Met.* **2006**, *7*, 173–187. [CrossRef]
15. Ding, L.; Torbati-Sarraf, H.; Poursaee, A. The influence of the sandblasting as a surface mechanical attrition treatment on the electrochemical behavior of carbon steel in different pH solutions. *Surf. Coat. Technol.* **2018**, *352*, 112–119. [CrossRef]
16. Multigner, M.; Frutos, E.; González-Carrasco, J.L.; Jiménez, J.A.; Marín, P.; Ibáñez, J. Influence of the sandblasting on the subsurface microstructure of 316LVM stainless steel: Implications on the magnetic and mechanical properties. *Mater. Sci. Eng. C* **2009**, *29*, 1357–1360. [CrossRef]
17. Heikki, R.; Eero, K.; Pauli, L.; Jani, R.; Ari, N.; Pasi, H.; Tuomo, K. Influence of surface integrity on the fatigue strength of high-strength steels. *J. Constr. Steel Res.* **2013**, *89*, 21–29. [CrossRef]
18. Garbatov, Y.; Parunov, J.; Kodvanj, J.; Saad-Eldeen, S.; Guedes Soares, C. Experimental assessment of tensile strength of corroded steel specimens subjected to sandblast and sandpaper cleaning. *Mar. Struct.* **2016**, *49*, 18–30. [CrossRef]
19. Alhussein, A.; Capelle, J.; Gilgert, J.; Dominiak, S.; Azari, Z. Influence of sandblasting and hydrogen on tensile and fatigue properties of pipeline API 5L X52 steel. *Int. J. Hydrog. Energy* **2011**, *36*, 2291–2301. [CrossRef]
20. Krawczyk, J.; Bembenek, M.; Frocisz, Ł.; ´Sleboda, T.; Pa´cko, M. The effect of sandblasting on properties and structures of the DC03/1.0347, DC04/1.0338, DC05/1.0312, and DD14/1.0389 steels for deep drawing. *Materials* **2021**, *14*, 3540. [CrossRef]
21. Wang, X.; Li, D. Mechanical and electrochemical behavior of nanocrystalline surface of 304 stainless steel. *Electrochim. Acta* **2002**, *47*, 3939–3947. [CrossRef]
22. Hou, J.; Fu, X.; Chung, D.D.L. Improving both bond strength and corrosion resistance of steel rebar in concrete by water immersion or sand blasting of rebar. *Cem. Concr. Res.* **1997**, *27*, 679–684. [CrossRef]
23. Ding, L.; Poursaee, A. The impact of sandblasting as a surface modification method on the corrosion behavior of steels in simulated concrete pore solution. *Constr. Build. Mater.* **2017**, *157*, 591–599. [CrossRef]
24. Marina, C.; Vasco, P.P.; Apostolos, N.C.; Spiros, G.P. Effect of corrosion and sandblasting on the high cycle fatigue behavior of reinforcing B500C steel bars. *Frat. Integrita. Strutt.* **2017**, *42*, 9–22.
25. Hammouda, N.; Belmokre, K. Effect of surface treatment by sandblasting on the quality and electrochemical corrosion properties of a C-1020 carbon steel used by an Algerian oil company. *MATEC Web Conf.* **2019**, *272*, 01001. [CrossRef]
26. Hubbs, A.F.; Minhas, N.S.; Jones, W.; Greskevitch, M.; Battelli, L.A.; Porter, D.W.; Goldsmith, W.T.; Frazer, D.; Landsittel, D.P.; Ma, J.Y.; et al. Comparative pulmonary toxicity of 6 abrasive blasting agents. *Toxicol. Sci.* **2001**, *61*, 135–143. [CrossRef]
27. Franziska, K.; Michael, B.; Torsten, G. Potential of garnet sand as an unconventional resource of the critical high-technology metals scandium and rare earth elements. *Sci. Rep.* **2021**, *11*, 5306. [CrossRef]
28. Zadorozhnaya, O.Y.; Khabasa, T.A.; Tiunova, O.V.; Malykhin, S.E. Effect of grain size and amount of zirconia on the physical and mechanical properties and the wear resistance of zirconia-toughened alumina. *Ceram. Int.* **2020**, *46*, 9263–9270. [CrossRef]
29. *EN ISO 8501-1:2007*; Corrosion Protection of Steel Structures by Painting. ISO: Geneva, Switzerland, 2007.

30. Ofoegbu, S.U. Comparative gravimetric studies on carbon steel corrosion in selected fruit juices and acidic chloride media (HCl) at different pH. *Materials* **2021**, *14*, 4755. [CrossRef] [PubMed]
31. Muresan, A.C.; Istrate, G.G. *Elemente de Electrochimie si Coroziune*; Note de curs; Editura Galati, University Press: Galati, Romania, 2021; pp. 170–171.
32. Hagen, C.M.H.; Hognestad, A.; Knudsen, O.Ø.; Sørby, K. The effect of surface roughness on corrosion resistance of machined and epoxy coated steel. *Prog. Org. Coat.* **2019**, *130*, 17–23. [CrossRef]
33. Evgeny, B.; Hughes, T.; Eskin, D. Effect of surface roughness on corrosion behaviour of low carbon steel in inhibited 4 M hydrochloric acid under laminar and turbulent flow conditions. *Corros. Sci.* **2016**, *103*, 196–205. [CrossRef]
34. Toloei, A.; Stoilov, V.; Northwood, D. The relationship between surface roughness and corrosion. In Proceeding of the ASME International Mechanical Engineering Congress and Exposition (IMECE), San Diego, California, USA, 15–21 November 2013.
35. Finger, C.; Stiesch, M.; Eisenburger, M.; Breidenstein, B.; Busemann, S.; Greuling, A. Effect of sandblasting on the surface roughness and residual stress of 3Y-TZP (zirconia). *SN Appl. Sci.* **2020**, *2*, 1700. [CrossRef]
36. Poorna Chander, K.; Vashista, M.; Sabiruddin, K.; Paul, S.; Bandyopadhyay, P.P. Effects of grit blasting on surface properties of steel substrates. *Mater. Des.* **2009**, *30*, 2895–2902. [CrossRef]

Disclaimer/Publisher's Note: The statements, opinions and data contained in all publications are solely those of the individual author(s) and contributor(s) and not of MDPI and/or the editor(s). MDPI and/or the editor(s) disclaim responsibility for any injury to people or property resulting from any ideas, methods, instructions or products referred to in the content.

MDPI
St. Alban-Anlage 66
4052 Basel
Switzerland
Tel. +41 61 683 77 34
Fax +41 61 302 89 18
www.mdpi.com

Inventions Editorial Office
E-mail: inventions@mdpi.com
www.mdpi.com/journal/inventions

MDPI

Academic Open
Access Publishing

www.mdpi.com

ISBN 978-3-0365-7893-4